JPL PUBLICATION 86-26

# The Second Spaceborne Imaging Radar Symposium

## April 28-30, 1986
## Jet Propulsion Laboratory



December 1, 1986

National Aeronautics and
Space Administration

**Jet Propulsion Laboratory**
California Institute of Technology
Pasadena, California

JPL PUBLICATION 86-26

# The Second Spaceborne Imaging Radar Symposium

## April 28-30, 1986
## Jet Propulsion Laboratory

December 1, 1986

NASA
National Aeronautics and
Space Administration

**Jet Propulsion Laboratory**
California Institute of Technology
Pasadena, California

This publication was prepared by the Jet Propulsion Laboratory, California Institute of Technology, under a contract with the National Aeronautics and Space Administration.

CONTENTS

CONTENTS (Contd)

SIR-B REFLIGHT, SIR-C, AND XSAR PLANNING

ABSTRACT

This document contains summaries of the papers presented at the Second Spaceborne Imaging Radar Symposium held at the Jet Propulsion Laboratory, California Institute of Technology, in Pasadena, California, on April 28 - 30, 1986. The purpose of the symposium was to present an overview of recent developments in the different scientific and technological fields related to spaceborne imaging radars and to present future international plans.

This symposium is the second in a series of "Spaceborne Imaging Radar" symposia that are held at JPL every three years. The first was held in January 1983; the third will be held in the 1989/1990 period.

# INTRODUCTION

This document contains summaries of the papers presented at the Second Spaceborne Imaging Radar Symposium held at the Jet Propulsion Laboratory, California Institute of Technology, in Pasadena, California, on April 28 - 30, 1986. The purpose of the symposium was to present an overview of recent developments in the different scientific and technological fields related to spaceborne imaging radars and to present future international plans.

Results from the recent SIR-B mission, and from the SIR-A and Seasat missions, showed that the radar is a powerful tool with a key scientific role in Earth observation. It provides information on the surface and near-surface physical properties that complement information acquired by visible and infrared imagers. In the area of technology, significant advances have been accomplished since the first symposium in 1983, particularly in the areas of real-time processing and distributed transmitters/antennas.

The next five years will see a very high level of activity in this field. The Magellan mission to map Venus with a radar sensor is scheduled for mid-1989. The European ERS-1, with its complement of active microwave sensors, will be launched in late 1989. The U.S. SIR-C and German/Italian X-SAR are scheduled for two flights on the space shuttle in 1990. The Japanese ERS-1 is scheduled for 1991. A number of promising efforts to conduct collaborative scientific experiments are ongoing. One goal of these efforts is a standardized output data format that will facilitate this cooperation. In addition, plans for the Earth Orbiting System (EOS) will be finalized in the next few years thus setting the framework for the activity in the mid-to-late 1990s.

C. Elachi
Symposium Chairman

# Geology and Planetology Research

# TECTONIC GEOMORPHOLOGY OF THE ANDES WITH SIR-A AND SIR-B

Arthur L. Bloom and Eric J. Fielding
Department of Geological Sciences and
Institute for the Study of Continents, Cornell University
Ithaca, New York

Data takes from SIR-A and SIR-B crossed all of the principal geomorphic provinces of the central Andes between 17° and 34°S latitude (Figure 1). In conjunction with TM images and photographs from hand-held cameras as well as from the Large Format Camera that was flown with SIR-B, the radar images give an excellent sampling of Andean geomorphology. In particular, the radar images show new details of volcanic rocks and landforms of late Cenozoic age in the Puna, and the exhumed surfaces of tilted blocks of Precambrian crystalline basement in the Sierras Pampeanas.

SIR-A data take 31 and SIR-B data take 39.6 crossed at about 19°S directly over a volcano 4600 m high in northern Chile (Figure 2). The western wall of the Andes at this latitude is a sheet of volcanic ejecta that drapes down to the west from a line of stratovolcanoes that range from 4500 to 5000 m in height. Volcanic and other sediments fill the tectonic longitudinal valley of northern Chile to a depth of 1000 m or more. The coastal cordillera of uplifted basement rocks forms a tectonic dam about 1 km above sea level, behind which the massive volcaniclastic deposits have been ponded (Bloom, in press).

To the southeast along SIR-B data take 39.6, the Ollague volcanic field on the Chile-Bolivia frontier has andesite stratovolcanoes 12 to 25 million years old that are partly buried by massive ignimbrite sheets. The ignimbrite sheets may be 3 to 5 million years old, and are in turn topped by younger andesite stratovolcanoes. A weathered and possibly wind-eroded fracture pattern in the ignimbrite sheets gives a distinct bright radar signature wherever they appear along the radar tracks (Fielding et al., 1986, esp. Figure 3).

North of 27°S latitude, the eastern flank of the Andes is the Subandean fold and thrust belt, including the Santa Barbara group of deformed sedimentary rocks near Salta, Argentina. The Subandean belt is a region of major petroleum exploration along the entire eastern Andes from Colombia south to Argentina. Ford et al., (1986, p. 24-25) illustrated the geology of the Subandean belt at 5°S latitude on the Peru-Ecuador frontier, farther northwest along SIR-B data take 39.6.

There is no active volcanism in the Andes between 27°S and 33°S. This is the zone of flat-slab subduction where the Pacific Nazca Plate passes under western South America with a dip of less than 10° (Jordan et al., 1983). Here, the Andean orogenic belt narrows abruptly to a width of no more than 200 km. SIR-A data take 29-30 crossed this section of the Andes on a northeastward course at about 30°S latitude, imaging the Cordillera Principal, the Cordillera Frontal, the Precordillera, and several of the Sierras Pampeanas - all of the major tectonic units across the flat-slab zone of the Andes.

 

The Sierras Pampeanas are of great interest to North American structural geologists because they are modern analogs of the Laramide blocks that created the central Rocky Mountains about 60 million years ago (e.g., Fielding and Jordan, in review). Individual Pampean ranges are blocks of igneous and metamorphic Precambrian and Paleozoic basement rocks, 50-100 km wide, uplifted as much as 6 km along thrust faults. They are separated by arid sedimentary basins in which several km of alluvial sediments have accumulated in late Cenozoic time. The surfaces of the tilted Pampean blocks are intricately fractured by ancient tectonic lineaments, which in part have been reactivated by contemporary uplift (Figure 3). They seem to be part of the ancient Gondwana shield and platform that was disrupted when South America separated from Africa in the Mesozoic Era. They were eroded flat and have either been exposed at the surface or slightly buried under alluvium from late Paleozoic time until their rejuvenation by recent involvement in Andean tectonics. They must be one of the world's most remarkable examples of exhumed topography. Their intricate surface patterns of intersecting fractures have been only slightly modified by modern fluvial erosion. They stand out clearly on Landsat TM, SIR-A, and SIR-B images. One of the more remarkable Pampean Ranges, known as Pie de Palo, and the adjacent Precordillera were photographed in color infrared by the Large Format Camera during STS Mission 41-G, and the photograph has been widely reproduced.

South of 33°S latitude, the Andean Cordillera is lower and dominated by a chain of andesite stratovolcanoes that continue into Tierra de Fuego. South of 42°S latitude, this great volcanic chain was covered by the Patagonian mountain ice cap during Pleistocene ice ages, and still supports small valley glaciers. The Chilean volcano Michinmahuida (2400 m high, 43°S, 73°W) was imaged by four data takes of SIR-B radar, and illustrates the definition achievable by shuttle imaging radar over inaccessible, cloud-covered regions (Elachi et al., 1986, Fig. 7; Fielding et al., 1986, Fig. 6; Ford et al., 1986, p. 74-75).

## REFERENCES


Bloom, A. L. (in press), Coastal landforms, in Short, N. M., Editor, Pictoral Atlas of Regional Landforms from Space: NASA Special Publication no. _____, chap. 6.

Elachi, C., Cimino, J. B., and Settle, M., 1986, Overview of the Shuttle Imaging Radar-B preliminary scientific results: Science, v. 232, p. 1511-1516.

Fielding, E. J. and Jordan, T. E. (in review), Active deformation of the boundary between thin- and thick-skinned shortening, Precordillera and Sierras Pampeanas, Argentina, and comparison with ancient Rocky Mountain deformation in North America: submitted for Schmidt, C. J., and Perry, W. J., eds., Interaction of the Rocky Mountain foreland cordilleran thrust belt, Geological Society of America Special Paper _____.

Fielding, E. J., Knox, W. J., Jr., and Bloom, A. L., 1986, SIR-B radar imagery of volcanic deposits in the Andes: IEEE Transactions on Geoscience and Remote Sensing, v. GE-24, p. 582-589.

Ford, J. P., Cimino, J. B., Holt, B., and Ruzek, M. R., 1986, Shuttle imaging radar views the Earth from Challenger: The SIR-B experiment: JPL Publication 86-10, 135 p.

Jordan, T. E., Isacks, B. L., Allmendinger, R. W., Brewer, J. A., Ramos, V. A., and Ando, C. J., 1983, Andean tectonics related to geometry of subducted Nazca plate: Geological Society of America Bulletin, v. 94, p. 341-361.

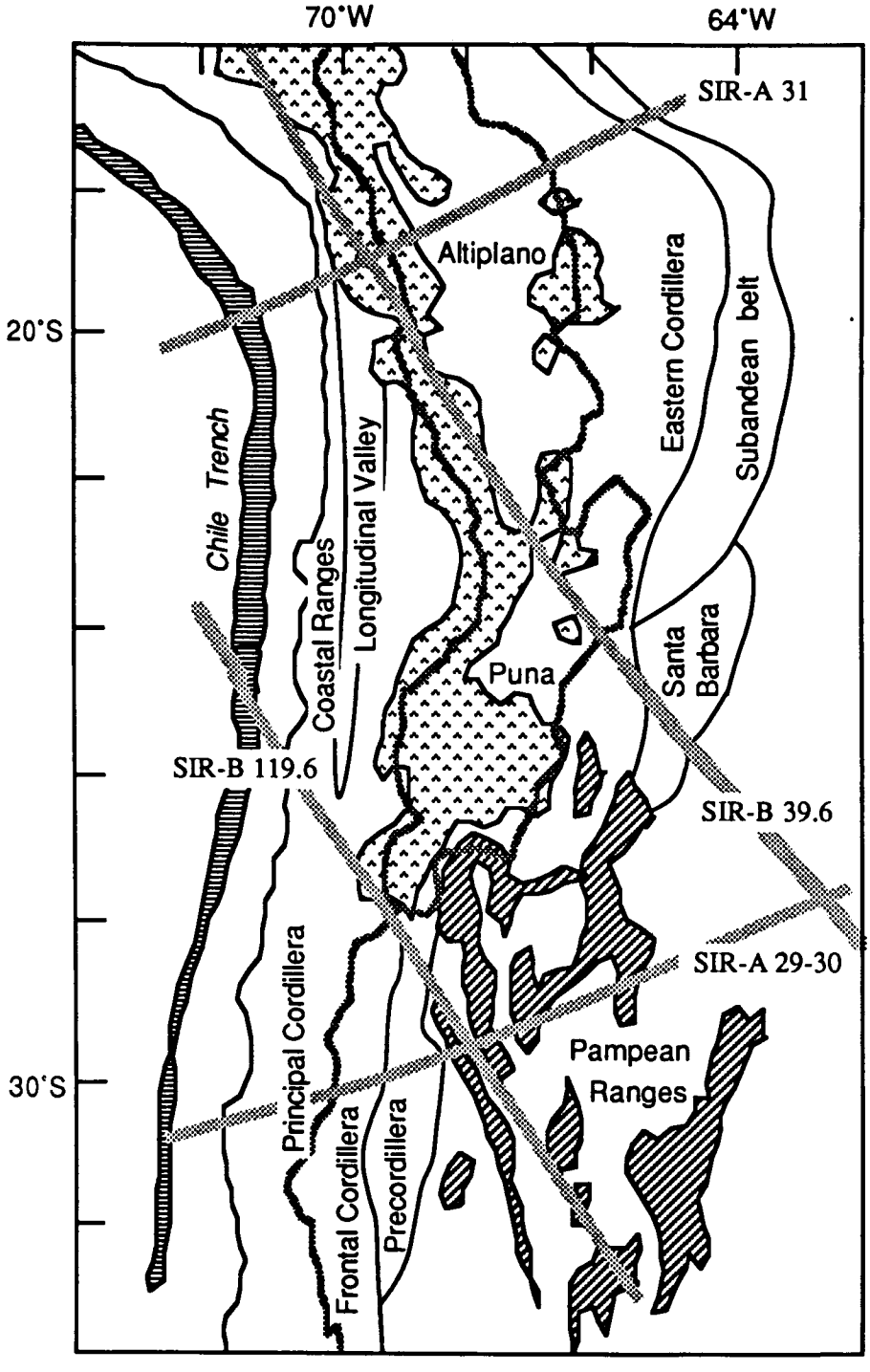


Figure 1. The major geomorphic units of the central Andes with SIR-A and SIR-B ground tracks superimposed. Other SIR-B tracks crossed the southern Andes between 40° and 45° S. Drainage divides (dark grey lines) enclose the Altiplano and Puna regions; late Cenozoic volcanoes shown in triangular pattern; Sierras Pampeanas shown in diagonal shading (modified from Jordan, et al., 1983, Fig. 4).

Figure 2. Stratovolcano at 19°S, 69°25'W in northern Chile. Coastal cliffs are almost 1 km high. This negative copy of SIR-A optical data take 31 makes the ocean appear in light shades, but gives the shadow effects of lighting from the upper right. Scale dots at bottom are spaced at about 7 km.

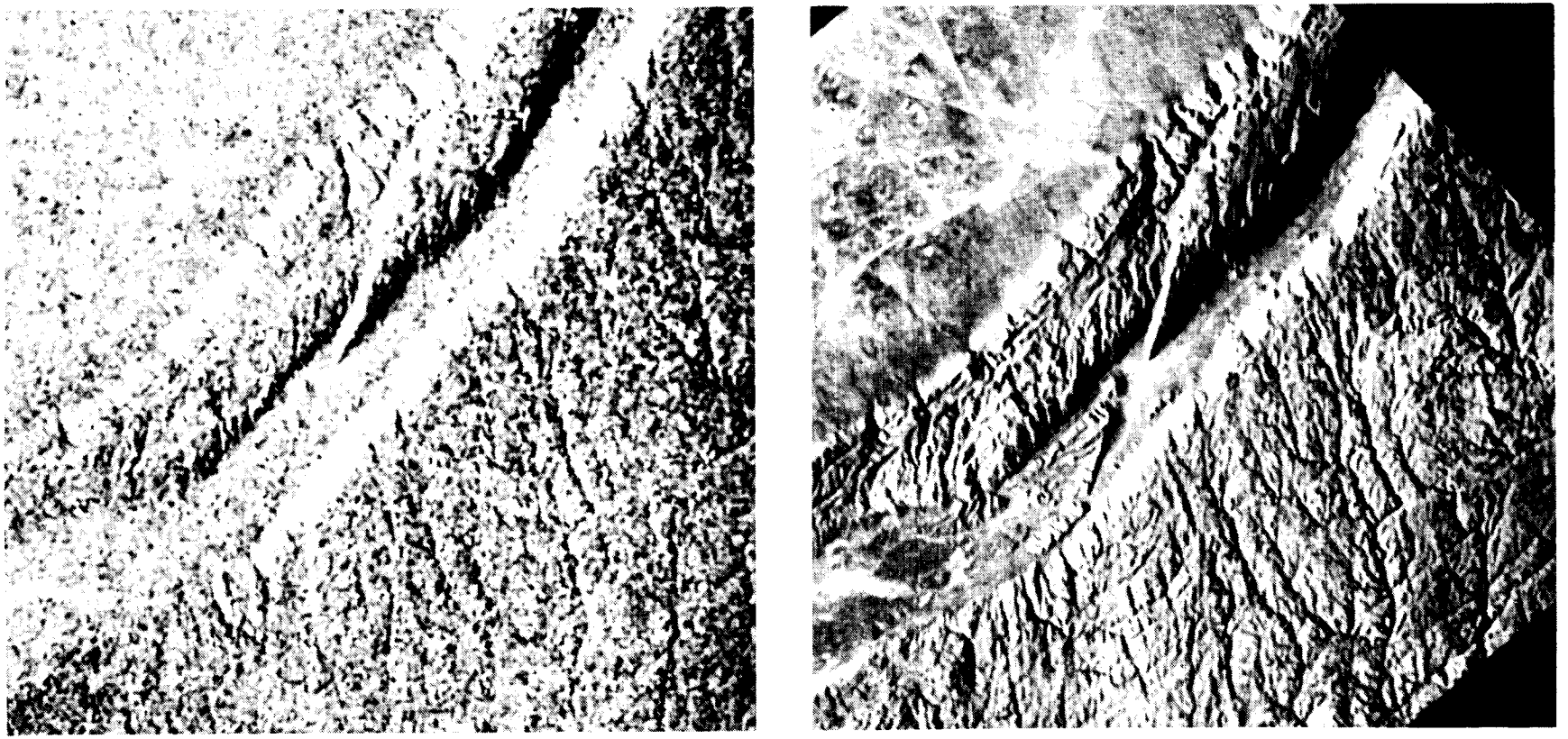

Figure 3. Sierra Ulapes-Sierra Las Minas (31°30'S, 66°30'W). Images by SIR-B (data take 119.5, scene 11) and Landsat (TM 231-82-2) aligned for steroscopic viewing. North to lower left, area about 12.5 x 12.5 km. Radar scene was illuminated toward 041.2°N, look angle 54.4°. By displaying the radar negative, the reversed shading is almost identical to the illumination of the TM scene with sun azimuth 040° and elevation 23°. Resolution is best on the TM scene, but the steroscopic effect is due almost entirely to the oblique look angle of the radar image.

# SPACE SHUTTLE RADAR IMAGES OF INDONESIA

Floyd F. Sabins
Chevron Oil Field Research Company
La Habra, California

John P. Ford
Jet Propulsion Laboratory, California Institute of Technology
Pasadena, California

Sabins (1983) interpreted SIR-A images of Indonesia; Sabins and Ford (1985) interpreted SIR-B images. These investigations had the following major results: (1) major lithologic assemblages are recognizable by their terrain characteristics in the SIR images and (2) both local and regional geologic structures are mappable. This report summarizes these results.

## I. TERRAIN CATEGORIES

Erosion of various rock types produces terrain categories with distinctive features in radar images. The following terrain categories are illustrated in Figure 1 and described below.

Coastal and alluvial plains (Figure 1A) are characterized by low relief and numerous meandering streams. Brightness differences are caused by differences in vegetation cover. Figure 1A along the southeast coast of Kalimantan includes patches of mangrove which produce a distinctive bright tone.

Clastic terrain (Figure 1B) is underlain by sandstone and shale which form distinctive terrain caused by differential erosion of resistant sandstone and nonresistant shale. In areas of horizontal to gentle dips, the sandstones form table lands underlain by shale slopes. In areas of moderate to steep dips, sandstone forms broad dip slopes with narrow, steep antidip scarps. Shale forms linear valleys. Where beds are dipping toward the radar antenna, dip slopes have extensive bright signatures; antidip scarps are shadowed and have dark, narrow linear signatures. Highlights and shadows are reversed where beds dip away from the antenna.

In tropical climates, carbonate rocks (Figure 1C) weather to karst topography which has a characteristic pitted appearance caused by closely spaced pinnacles and depressions caused by solution and collapse. Karst terrain is expressed as closely spaced, irregular highlights and shadows in radar images.

Volcanic terrain (Figure 1D) consists of cinder cones, eroded necks, lava flows, and other landforms that are recognizable by their morphology. These landforms are only recognizable in relatively young volcanic terrain. Older volcanic areas that have been eroded and deformed lack the distinctive morphologic features.

Melange rocks (Figure 1E) form in the collision zones between crustal plates and consist of slabs and blocks of a wide range of oceanic rocks in a shaley matrix. Erosion produces an irregular arrangement of rounded hills and ridges with an unsystematic drainage pattern.

Metamorphic terrain (Figure 1F) formed on metamorphosed clastic strata consists of angular ridges and steep valleys. Metamorphism has obliterated any topographic expression of the original stratification.

## II. GEOLOGIC STRUCTURE

Sabins (1983) illustrated and interpreted SIR-A images of the major types of local and regional geologic structures in Indonesia. Figure 2 shows additional examples of local structures as imaged by SIR-B.

Folds are expressed by attitudes of beds (strike and dip) and by outcrop patterns. An oval-shaped syncline along the Kendilo River, Kalimantan, is shown in the SIR-B image and map (Figure 2A,B). The structure is outlined by ridges of dipping clastic strata with the dip directions oriented radially toward the center of the structure.

A regional unconformity (Figure 2C,D) is expressed by a horizontal erosion surface that truncates underlying folded clastic strata in northwest Borneo. Elsewhere in this area the images show layers of horizontal clastic strata and volcanic flows overlying the unconformity surface which indicates that this is not a modern erosion feature.

Lineaments (Figure 2E,F) are expressed as straight and aligned stream segments and as linear scarps. Many, but not all, lineaments are the expression of faults and fractures that are preferably eroded.

Figure 3A is a SIR-B image strip in southwestern Kalimantan that shows the expression of regional structures. The interpretation map (Figure 3B) shows a moderately eroded anticline and syncline in the southeastern area (right portion) that are well expressed in the image. In the northwest part of the image, folds are more deeply eroded and less prominent. Nevertheless, these subtle features are detectable because of the highlights and shadows in the radar image. The rocks are predominantly sandstone and shale with some limestone beds that form karst topography.

## III. SUMMARY

SIR-A images of Indonesia acquired in 1981 were interpreted earlier to develop criteria for recognizing lithologic terranes and structural features. SIR-B images acquired in 1984 provide the opportunity to study additional areas in Kalimantan and Sumatra. The earlier interpretation criteria are applicable to these new images.

## REFERENCES

Sabins, F. F., 1983, Geologic interpretation of Space Shuttle radar images of Indonesia: American Association Petroleum Geologists Bulletin, v. 67, p. 2076-2099.

Sabins, F. F. and J. P. Ford, 1985, Space Shuttle radar images of Indonesia: Indonesian Petroleum Association, Proceedings, Fourteenth Annual Convention, v. 2, p. 471-476, Jakarta, Indonesia.


A. COASTAL AND ALLUVIAL TERRAIN

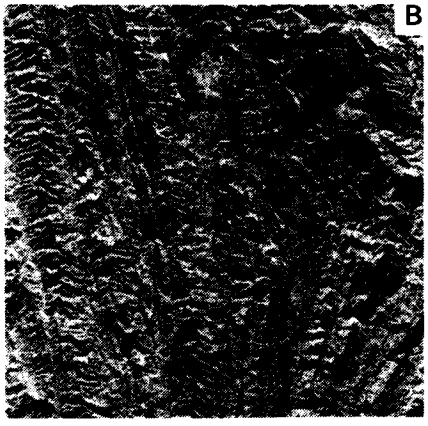


B. CLASTIC TERRAIN

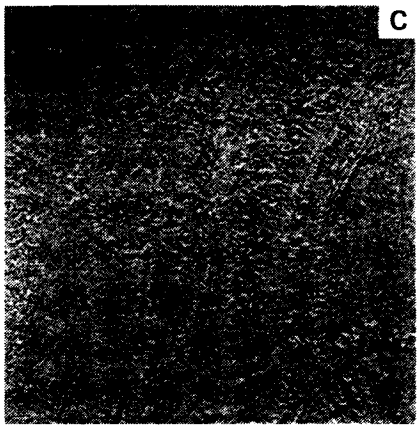


C. CARBONATE TERRAIN

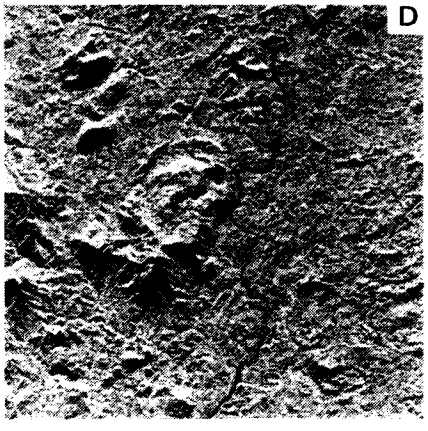


D. VOLCANIC TERRAIN

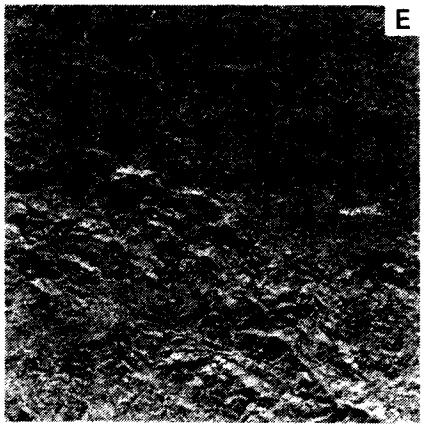


E. MELANGE TERRAIN

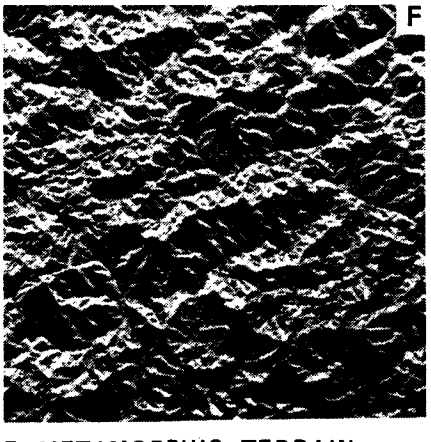


F. METAMORPHIC TERRAIN

Figure 1. Terrain types in SIR-A and -B images of Indonesia; each image covers an area of 30 by 30 km

A. SYNCLINE

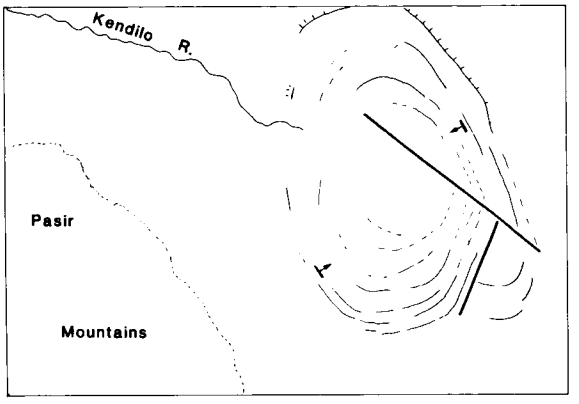


B. MAP

C. UNCONFORMITY

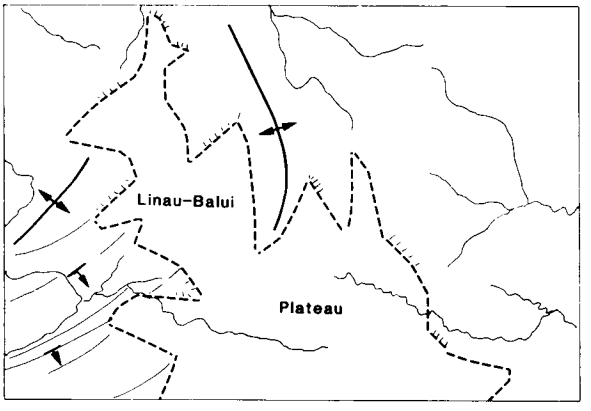


D. MAP

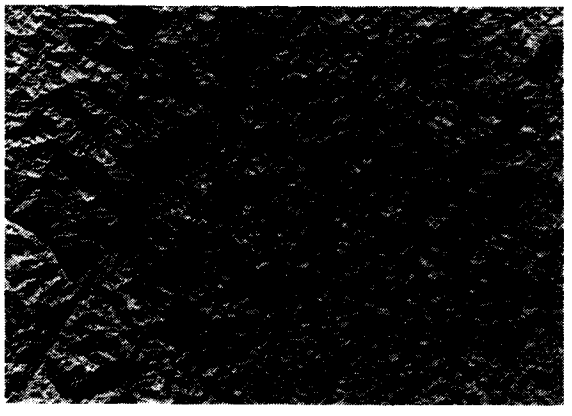

E. LINEAMENTS

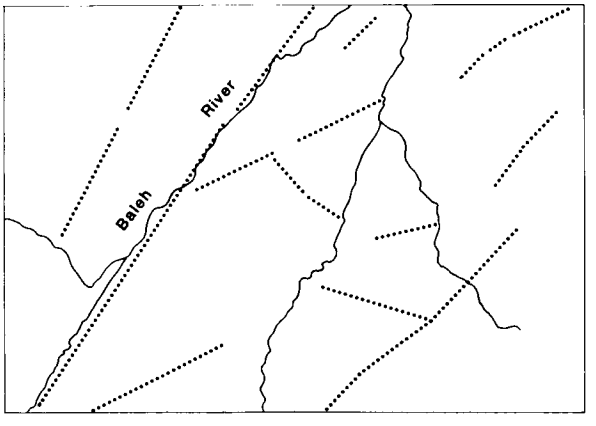


F. MAP

Figure 2. Local structures in SIR-B images of Kalimantan, Indonesia; each image covers an area of 20 by 30 km

A. SIR-B IMAGE ACQUIRED OCTOBER 1984 WITH A 48° DEPRESSION ANGLE.

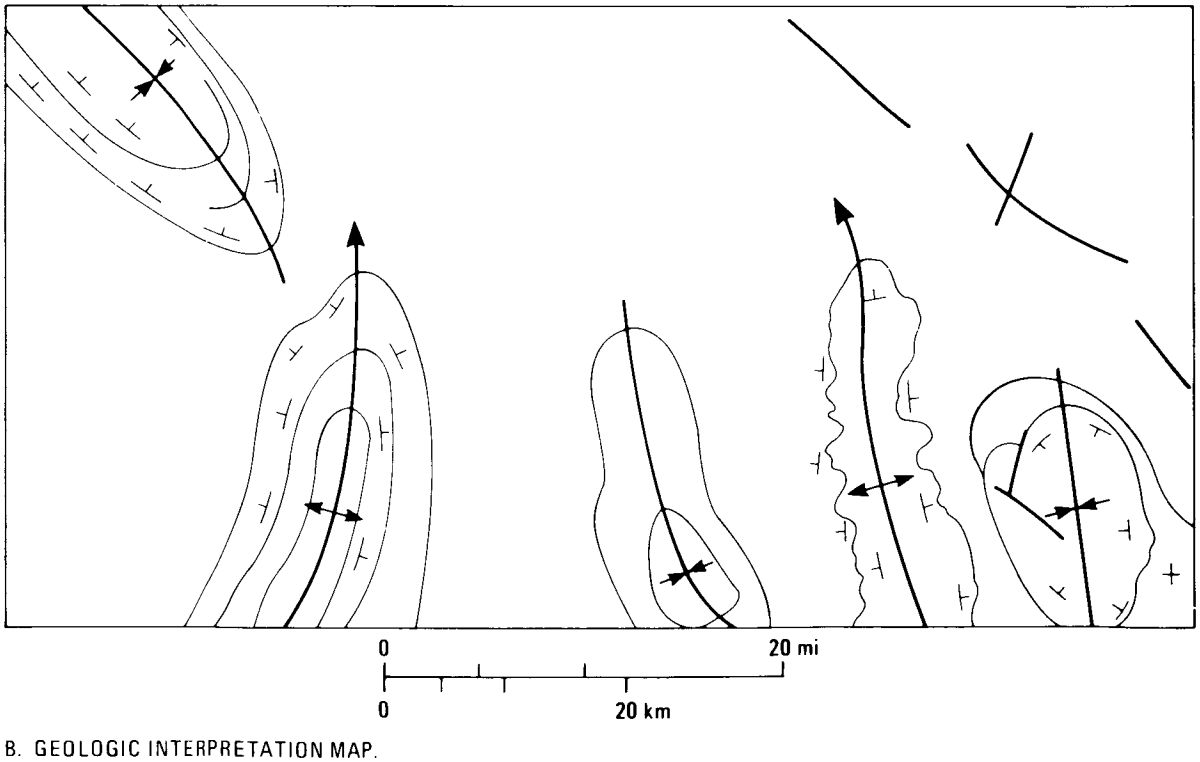


B. GEOLOGIC INTERPRETATION MAP.

Figure 3. Regional geologic structure on SIR-A image of southeast Kalimantan, Indonesia

# DELINEATION OF FAULT ZONES USING IMAGING RADAR

M. N. Toksoz, L. Gulen, M. Prange, and J. Matarese
Earth Resources Laboratory
Department of Earth, Atmospheric, and Planetary Sciences
Massachusetts Institute of Technology
Cambridge, Massachusetts

G. H. Pettengill and P. G. Ford
Center for Space Research
Massachusetts Institute of Technology
Cambridge, Massachusetts

The assessment of earthquake hazards and mineral and oil potential of a given region requires a detailed knowledge of geological structure, including the configuration of faults. Delineation of faults is traditionally based on three types of data: 1) seismicity data, which shows the location and magnitude of earthquake activity; 2) field mapping, which in remote areas is typically incomplete and of insufficient accuracy; and 3) remote sensing, including Landsat images and high altitude photography. Recently, high resolution radar images of tectonically active regions have been obtained by SEASAT and Shuttle Imaging Radar (SIR-A and SIR-B) systems. These radar images are sensitive to terrain slope variations and emphasize the topographic signatures of fault zones. Our objective is to develop techniques for using the radar data in conjunction with the traditional types of data to delineate major faults in well-known test sites, and to extend interpretation techniques to remote areas.

Two study areas in this paper cover the tectonically complex region of Southern California, including the San Andreas and Garlock faults around the Mojave plate, and an equally complex region in Turkey, containing the North Anatolian Fault zone. In both of these areas extensive geological and seismic data are available and are being collected by ongoing studies. An excellent example of the sensitivity of imaging radar to the morphological features of major fault zones is shown by a SEASAT image of the Mojave plate (Figure 1a). A qualitative fault interpretation of Figure 1a is given in Figure 1b. Major fault zones such as the San Andreas, Garlock, and San Gabriel, along with the associated secondary faults, can be clearly identified on SEASAT imagery. The most striking features of these faults on the radar imagery are long, linear valleys and scarps. Also associated with these linear features are discontinuities created by offset streams, ridges, and valleys. These discontinuities are necessary to identify faults among other linear features. Radar imagery yields high resolution textural information unavailable on Landsat images. An example of such textural information is given by the contrast between the Mojave plate and surrounding regions on Figure 1a.

The fault zones on radar imagery can be delineated by identifying the above characteristics using digital techniques. The digital techniques that we use for fault detection consist of edge detectors as pre-processors and line detectors as post-processors. We are currently exploring two techniques: a smoothed directional derivative filter (Canny, 1983), and Kalman filtering. A derivative filter emphasizes various frequency components

of an image along a given direction, making edges appear as spikes. We operate the filter in twelve cardinal directions, yielding directional and edge magnitude information at each pixel. The Kalman filter tracks statistics (such as mean and variance) within an expanding window and indicates edges where the window encounters points which do not match these statistics. The advantage of Kalman filtering is that any statistical parameters may be used for the edge detection criteria; however, no directional information is generated.

The post-processors are methods for finding lines in the edge detector output. We are evaluating three techniques: a gun-sight line finder, a linking line finder (Nevatia and Babu, 1978), and simulated annealing (Geman and Geman, 1984; Derin et al., 1984). The gun-sight line finder examines thresholded edge magnitudes and directional deviations along a given direction, putting linear segments where the point density is above a given value. The linking line finder is a connect-the-dots algorithm which uses directional information at each point to trace curvilinear segments, ending a segment where the directional deviation is above a threshold. The simulated annealing method emplaces line elements using edge magnitude and directional information, and then tests the global energy of this line configuration according to an a priori energy function, and iterates over the line segment configuration to minimize this energy. An efficient line finder will ultimately be a combination of these basic algorithms.

The usefulness of the above techniques was demonstrated by the delineation of a previously unknown active fault zone in a remote area in eastern Turkey using the SIR-A image in Figure 2a. Three large earthquakes ($M_b$>5) and a number of smaller aftershocks were recorded near Olur in 1983 and 1984. For fault detection, the gun-sight line finder was applied to derivative filter output and the result is shown in Figure 2a. The fault, which is difficult to detect by eye on the SIR-A image, is greatly enhanced by the processing. The seismicity data obtained by the seismic network that we set up to monitor this recent earthquake activity is shown in Figure 2b. The alignment of earthquake epicenters along the Olur fault verifies our SIR-A interpretation.

Digital processing is also being applied to a SIR-B image covering an area in Southern California at the intersection of the San Andreas and Garlock fault zones (Figure 3a). A qualitative fault interpretation of this image is shown in Figure 3b. The faults in this area are curvilinear on a small scale, making the gun-sight approach ineffective. An example of the linking line finder applied to the derivative filtered image is shown in Figure 3c. This method successfully delineates the San Andreas, Garlock, and Pine Mountain fault zones. We are currently working to improve the fault detection technique by using a combination of the above algorithms, including a texture sensitive pre-processor.

## REFERENCES

Canny, J. (1983), Finding Edges and Lines in Images, MIT Artificial Intelligence Laboratory, Technical Report No. 720.

Derin, H., H. Elliot, R. Cristi, and D. Geman, (1984), Bayes smoothing algorithms for segmentation of binary images modeled by Markov random fields, IEEE Trans. Pattern Anal. Machine Intell.

Geman, D., and S. Geman, (1984), Stochastic relaxation, Gibbs distribution, and Bayesian restoration of images, IEEE Trans. Pattern Anal. Machine Intell.

Nevatia, R., and K. Babu, (November, 1978), Linear feature extraction, Proceedings of the Image Understanding Workshop, ed. Bauman Lee, Science Applications.

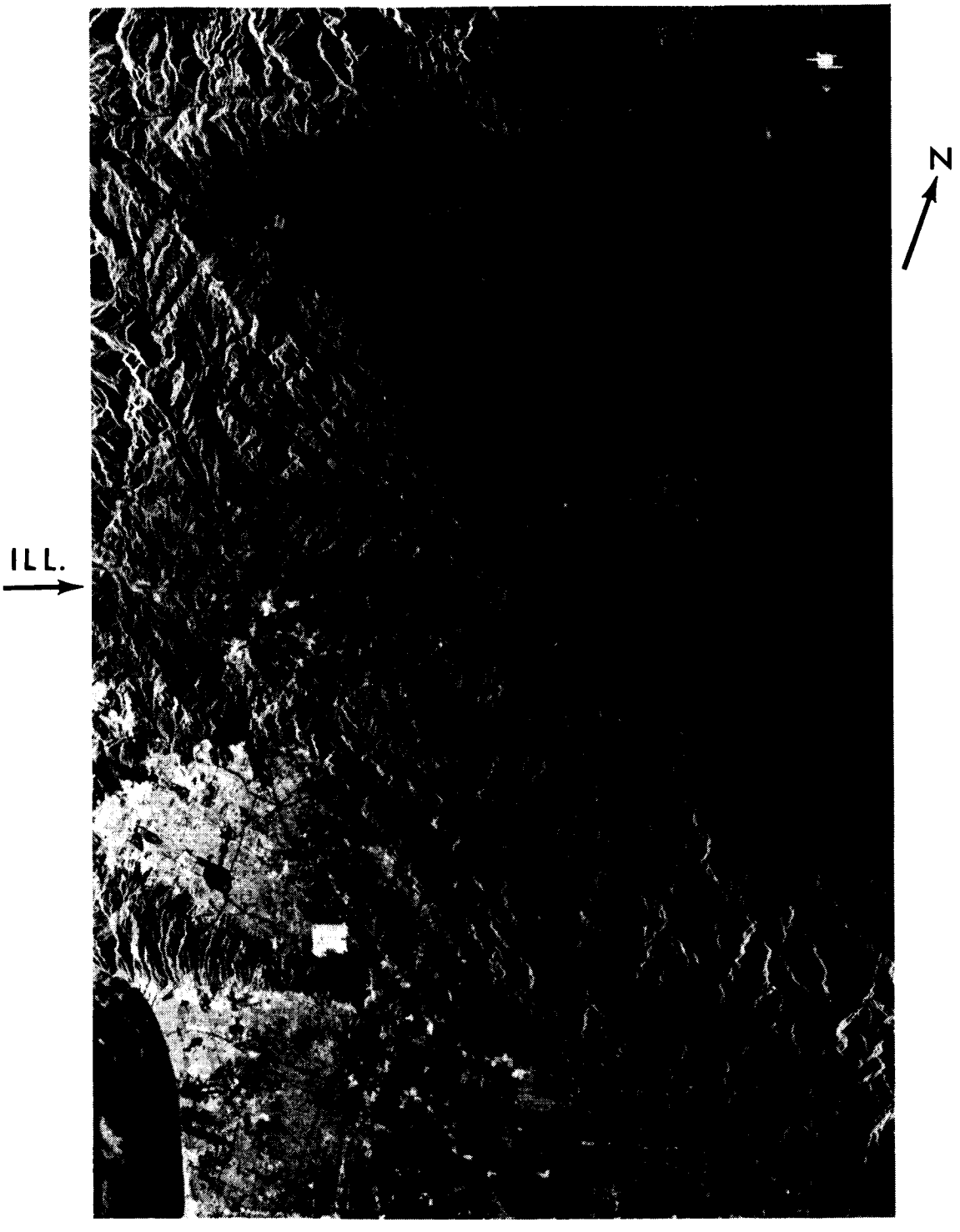


Figure 1a. Composite SEASAT radar (23.5cm wavelength) image of Southern California.

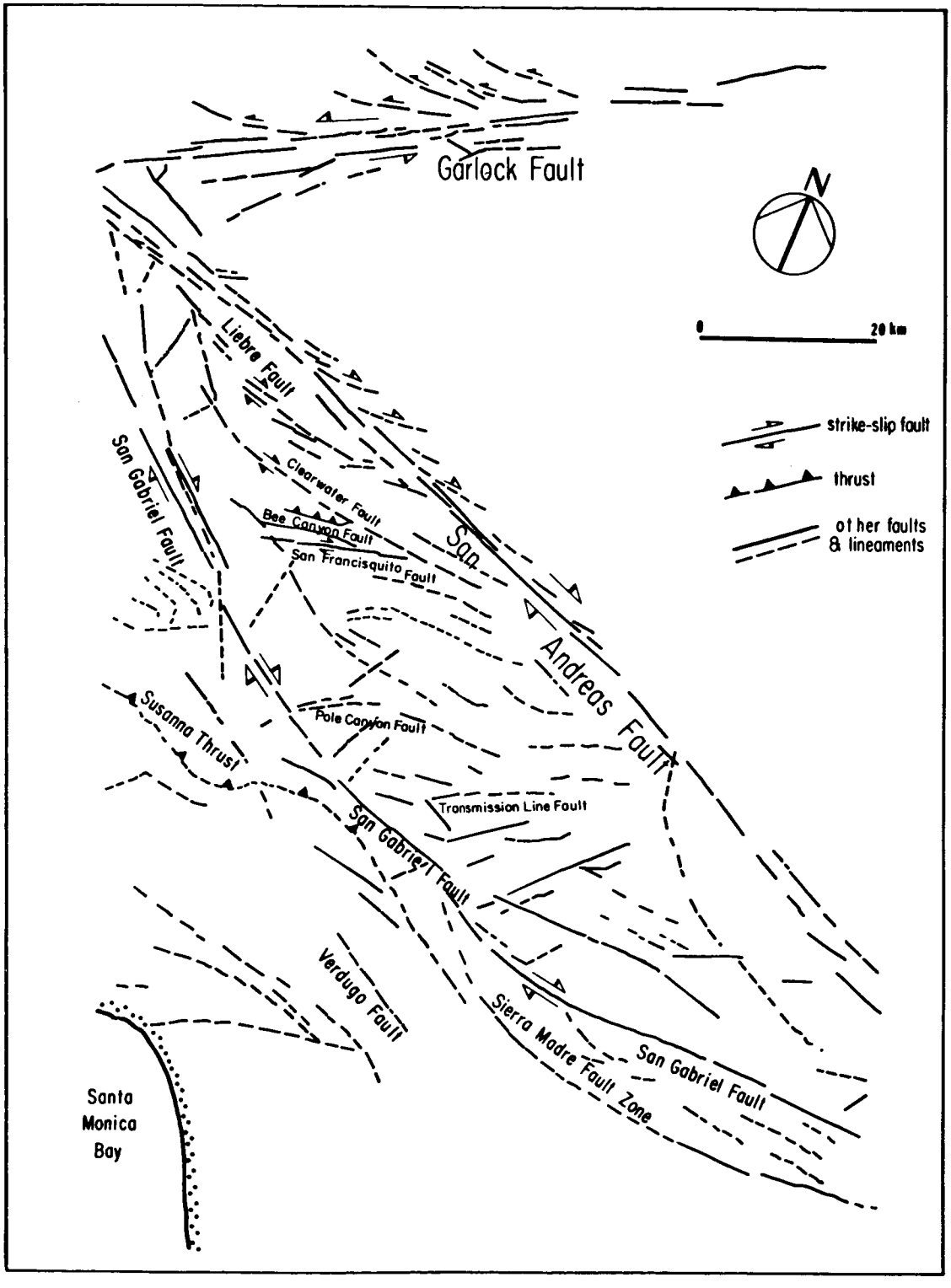


Figure 1b. Qualitative fault interpretation of Figure 1a.

Figure 2a. SIR-A image of Olur area with superimposed digital fault interpretation showing Olur fault.

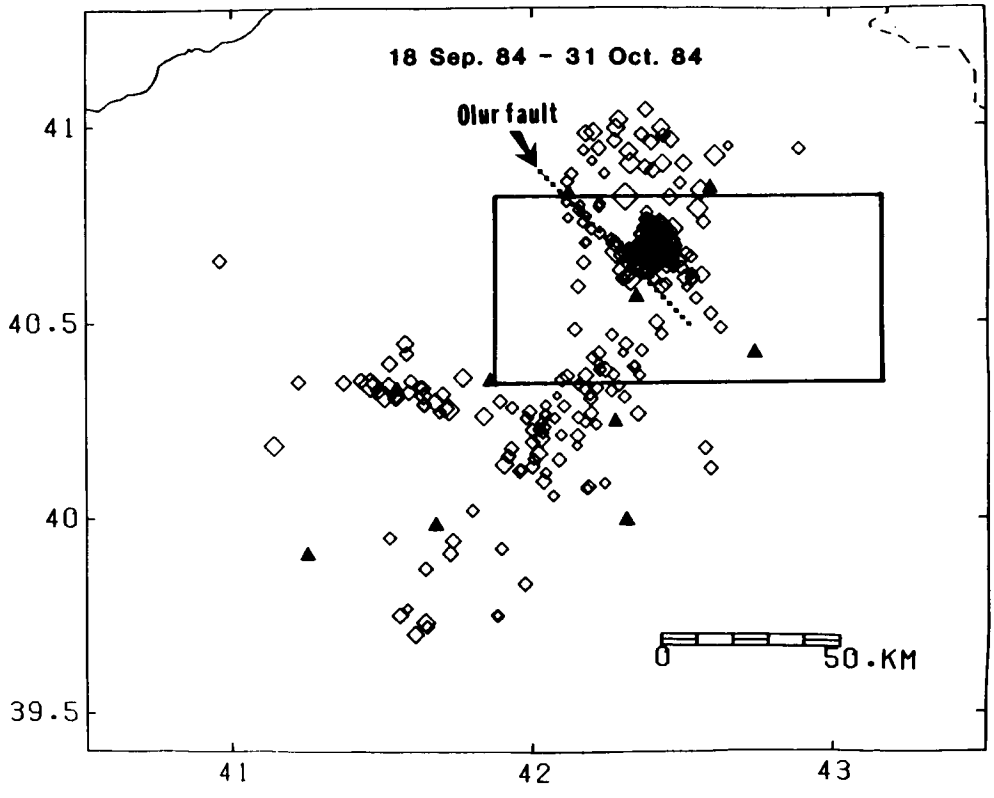


Figure 2b. Distribution of aftershock epicenters in the Olur area in the period 18 Sept. 1984 to 31 Oct. 1984, with the box indicating the area covered by the SIR-A image in Figure 2a. The filled triangles indicate the location of seismic stations. The open diamonds denote the epicenters of aftershocks, and size indicates relative magnitude. The NE-SW alignment of epicenters verifies the digital SIR-A Olur fault interpretation.

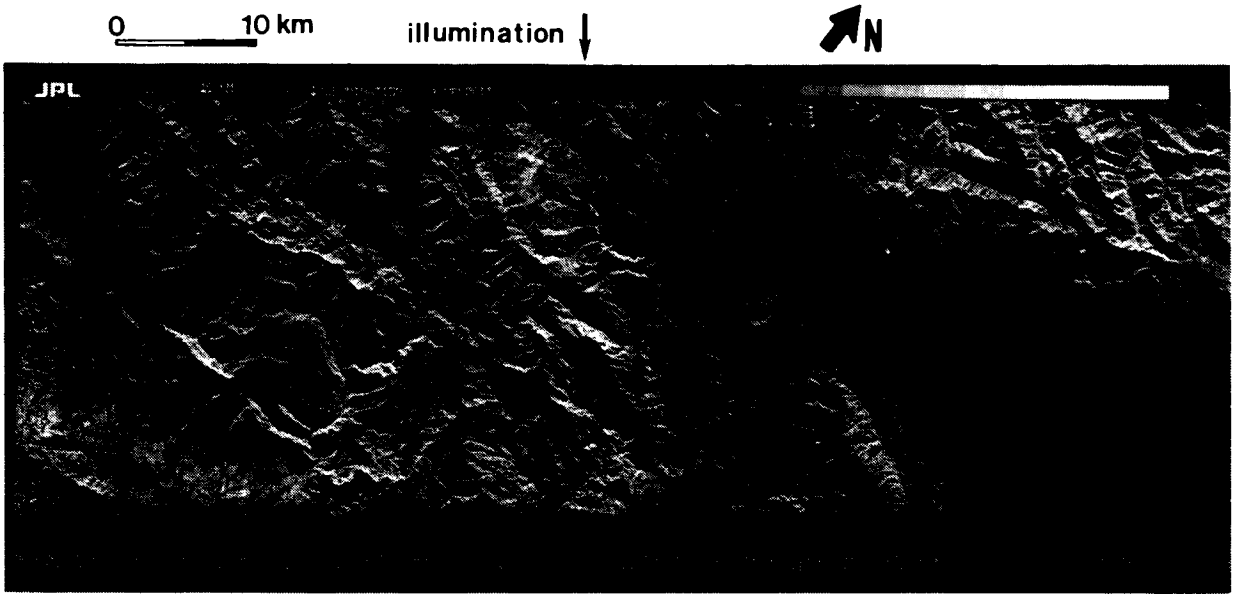


Figure 3a. SIR-B image covering an area in Southern California at the intersection of the San Andreas and Garlock fault zones.

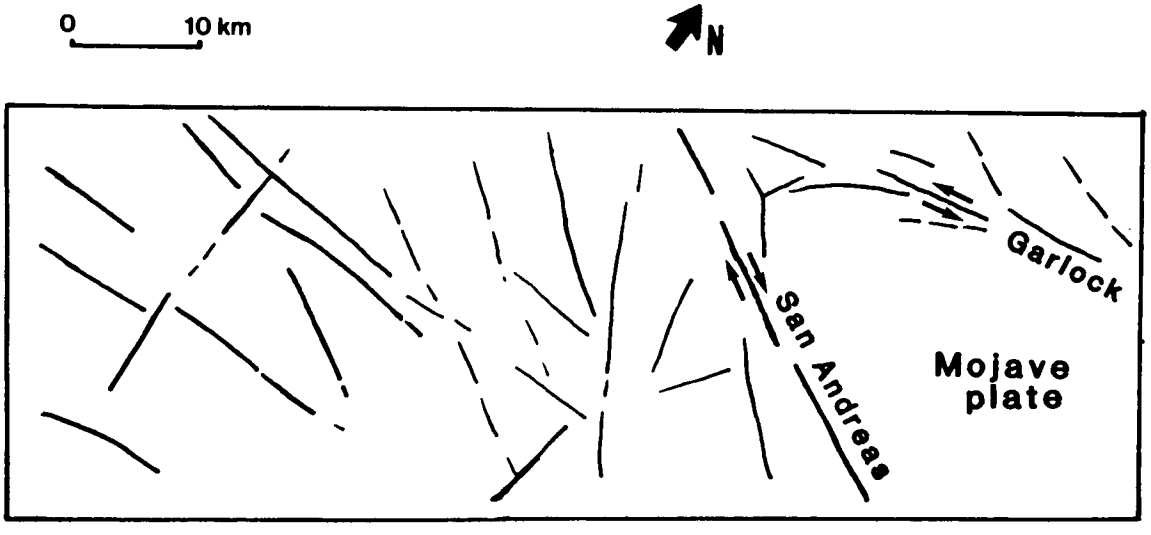


Figure 3b. The qualitative fault interpretation of Figure 3a.

Figure 3c. A digital fault interpretation of Figure 3a using the linking line finder applied to the derivative filtered SIR-B image. The SIR-B image was smoothed by pixel averaging before processing. This method successfully delineates the San Andreas, Garlock, and Pine Mountain fault zones.

# THE MEGAGEOMORPHOLOGY OF THE RADAR RIVERS OF THE EASTERN SAHARA

John F. McCauley, Carol S. Breed, and Gerald G. Schaber
U.S. Geological Survey, Flagstaff, Arizona

## I. SIGNIFICANCE OF THE RADAR RIVERS

The Eastern Sahara (Fig. 1) is devoid of surface drainage -- this unusual characteristic distinguishes its morphology from that of most other desert regions where running water dominates landscape development (Peel, 1939). Cyclic aridity, which is responsible for the obscuring eolian blankets and wind-erosion effects, had set in by the Pliocene-Pleistocene transition, about 2 million years ago (Williams, 1982). SIR-A/B reveals, however, that the "bull's-eye" of aridity in North Africa underwent a long prior history of erosion by southwestward-trending Tertiary streams (McCauley et al., 1986; Schaber et al., 1986).

Figure 2. derived from SIR-A/B and Landsat images and the literature, shows the major presently known paleodrainages in the Eastern Sahara. Of particular importance in this compilation is the presence of the Abu Ballas Divide. This structural arch contains Jurassic continental clastics that crop out discontinuously along a topographically subdued prong and extend eastward from the Gilf Kebir Plateau to the Dakhla-Kharga region, south and west of the Limestone Plateau. Westward-flowing drainages lying to the south of this post-Tethys divide would have been shepherded away from the Mediterranean to take other routes to the sea or to intracontinental basins.

This compilation (Fig. 2) permits consideration of the key questions: Where did the radar rivers come from and where did they go? The detailed work done along the Nile Valley in the past three or more decades (Said, 1981, 1982) is of limited assistance in this effort because the Nile is chiefly a late Tertiary-Quaternary feature. The various rivers that once occupied the Nile Trough are relatively young (late Miocene to Quaternary), and they developed separately from the older (late Eocene) westward-trending radar rivers. The oldest of the Niles, the Eonile (Said, 1981), is relevant to the radar river problem because during the Messinian event it cut a canyon from Cairo to Aswan that was longer and deeper than the Grand Canyon of the Colorado River in Arizona. This deep southward incision by the Eonile in the late Miocene created a new drainage barrier in Egypt that severely affected the subsequent history of the radar rivers.

Analysis of SIR-A data led McCauley et al. (1982) to suggest that the radar rivers, because of their southwestward trends, once flowed into the Chad Basin. This key North African feature is a regional structural low formed in the Early Cretaceous in response to initial opening of the South Atlantic (Browne and Fairhead, 1983). The problem of the origin of headwaters for the radar rivers was less tractable. The idea that the source areas of the radar rivers might originally have been the same as those (The Ethiopian Highlands) later captured by the Nile was proposed tentatively. A more extensive review of the Cenozoic tectonic history of North Africa reveals no reason now to suppose that the Central African tributaries of the present Nile were ever connected to the large alluvial valleys in southwestern Egypt and northwestern Sudan.

New insights into the problem of determining the source areas of the radar rivers are provided by Issawi (1983). An analysis of the relations of wadis such as the Allaqi, the Qena, and those of the Kom Ombo area, all east of the present Nile, points to the Red Sea Hills in Egypt and Sudan as a logical source area for the radar rivers. These valleys mark, in part, the courses of old westward- and southward-flowing consequent streams. They are the descendants of a more ancient drainage system that developed independently of the successive rivers that later occupied the Nile Trough. These streams and other westward-flowing consequent drainages, which came from the flanks of the Red Sea uplift prior to integration of the Nile Trough, in either middle or late Tertiary time must have run out onto the continental slope of a then more simple African landscape. The radar rivers, when put into the context of the plate tectonics of North Africa, prove to be the missing links to a previously unrecognized, now-defunct drainage system of continental proportions.

## II. A TRANS-AFRICAN DRAINAGE SYSTEM

The unusual surficial characteristics of the Eastern Sahara, particularly its present hyperaridity and unique eolian veneer, are products of progressive Quaternary desiccation. The region is not a distinct geologic entity. Its pre-Quaternary history is inseparable from the now-well-documented sequence of Tertiary tectonic and volcanic events that shaped North Africa as a whole. The more detailed picture of the history of the radar rivers than possible in our earlier report (McCauley et al., 1982) results from post-SIR-A field work and a number of recent key papers on the tectonics of North Africa, particularly the Central African Rift System (Bermingham et al., 1983).

Shortly after or simultaneously with the regression of the Eocene Tethys Sea from southwestern Egypt, the Afro-Arabian (Red Sea) Rift began to form, about 30 to 40 million years ago; the first movements occurred as early as lower middle Eocene. A sequence of events involving doming, rifting, sedimentation, magmatism, and tectonism then took place along the northeast edge of Africa and profoundly affected this newly emergent landscape (Table 1). More than 2000 m of uplift of the crystalline basement and the Mesozoic and early Tertiary sedimentary cover occurred in the Red Sea Hills region. A number of large, roughly northward-trending troughs such as the Qena and the Nile, along with east-west structures like the Abu Ballas Divide, formed in response to the opening of this new oceanic rift. The Red Sea Hills (Fig. 1) would have been the highest mountains in northeastern and central Africa during Oligocene to middle Miocene time, because the great intraplate volcanic complexes such as the Darfur and Tibesti had not yet developed. These northward-trending Red Sea massifs sloped to the west, toward the older Cretaceous sedimentary basins of north-central Africa, and the consequent streams emerging from the Red Sea Hills were controlled by these regional slopes (Fig. 3).

The Tertiary climate of Egypt, and by inference that of much of North Africa was wet; a dense vegetation cover and moderate to intense chemical weathering suggest warm temperatures. Discharge would have been substantial off the continental slopes of the Eastern Sahara and the developing Ethiopian-Afar volcanic complex. A family of westward-flowing, vigorous branch streams that extended many hundreds of kilometers downstream from their source areas must have developed. These streams are probably contemporaries

of the streams in northern and central Egypt that deposited the gravel spreads of Oligocene age described by Said (1981, 1983) and Salem (1976). Unlike those streams, however, the consequent streams from the Red Sea Hills would have flowed not only over the marine sediments of the Limestone Plateau, but in southern Egypt and Sudan they would have flowed around and beyond the Tethys embayment to run directly on older, pre-Tertiary surfaces. The radar valleys in southwestern Egypt and northwestern Sudan discovered on SIR images represent the middle reaches of this drainage system.

The earlier Trans-Saharan Seaway that existed between the Tethys and the Atlantic in the Late Cretaceous, and which had closed by early Tertiary time (Kogbe, 1980), may have acted as a palimpsest guidance system for these new rivers as they sought the lowest ground of central North Africa. The trunk streams are well expressed in northwestern Sudan, from whence those trending to the southwest probably found their way into the Boélé-Chad Basins south of Faya. Drainage patterns, however, are confused by later tectonic and volcanic events in the area east of the Ennedi, between the domal uplifts of the Tibesti and Darfur regions. Some discharge into Chad may have been along the Mourdi Valley as previously suggested (McCauley et al., 1982), but more likely paths are the Marhdogoum-Derbeli gaps some 480 km east of Faya and the low regions south of the Ennedi (Figs. 1, 2, and 3).

Grove and Warren (1968) point out that boreholes in the vicinity of present Lake Chad show layers of sand alternating with thicker layers of clay, indicating deposition under fluvio-lacustrine conditions. A hippopotamus jaw, recovered from below 60 m, suggests that the deposits beneath the Paleo-Chad Sea (Mega-Chad) and its shrunken Holocene remnant are of probable Tertiary age.

No evidence is reported of regional ponding of the putative Tertiary drainages in the Chad Basin, as occurred when the Paleo-Chad Sea formed during the height of the last major North African pluvial about 10,000 years ago. At this time, Mega-Chad was about the size of the present Caspian Sea; a reasonably complete shoreline can be traced around it at an elevation of about 320 m. The waters of this great basin have risen as high as 380 to 400 m and the the Logone River, a tributary of the present lake, may have acted as a spillway to the Benue. Even today, waters from the shrunken remnant of Mega-Chad are reported to escape by way of a chain of small lakes that lead to the Mayo Kebbi River, a tributary of the Benue (Grove, 1970). The Mayo Kebbi is presently a small river occupying a large valley; it could represent the main mid-Tertiary outlet to the Atlantic of our suggested Trans-African drainage system (TADS).

The Bodélé depression now lies about 180 m below the present level of Lake Chad, and the 500-km-long Bahr el Ghazal that connects them now intermittently flows northeast. As described earlier, the drainages seen on both SIR and Landsat images around the flanks of the Tibesti and Darfur massifs are confused by multiple superposition patterns. Neither of these situations poses any major constraints on the mid-Tertiary drainage system proposed here because the Tibesti and Darfur, along with the intervening high ground of the ennedi, represent an arm of domal uplift related to the Central African Rift System of Browne and Fairhead (1983). The earliest lavas in the

Gebel Marra complex, which now forms the divide between the present Chad and Nile Basins, have been dated provisionally at 13.5 m.y. (Bermingham et al., 1983). The present-day topographic obstacles (domes, structural uplifts, and depressions) did not exist in mid-Tertiary time. The Bahr el Ghazal may represent the much-modified trace of one of the major trunk streams, or be part of the master stream of the Trans-African system that traversed the Chad Basin and flowed into the Atlantic by way of the Benue and the Niger (Fig. 3).

The Benue Trough, which is associated with the opening of the South Atlantic (Burke et al., 1971) and which split the West African and Congo Cratons, had closed by the Late Cretaceous. The Benue Trough has been interpreted by Adighije (1981) as an earlier, abortive attempt to open western Africa into an ocean similar to the later, more successful Red Sea Rift. Regardless of this failure, the trough controls the path of the Benue River, the largest tributary of the Niger River. By late Eocene time deltaic sediments had begun to spread westward down the Benue Valley toward the Atlantic and the present mouth of the Niger River, where they began to form a delta that ultimately grew three times larger than the Nile Delta. This trough, along with the other preconditioning elements described earlier, must have determined the courses of the lower reaches of a continental drainage system that extended some 4500 km from the crest line of the Red Sea Hills to the early Niger Delta (Fig. 3).

Other middle Tertiary branch streams that were originally part of this Trans-African drainage system may have been present in central and southern Sudan. Streams there might have flowed across or to the south of the Darfur area before uplift; the downstream parts of such drainages would have been controlled by the central African Rift System (particularly the Ngaoundere and the Abu Gabra Troughs in Cameroon and Chad). These areas are, however, beyond the scope of our present work.

The active life span of the Trans-African drainages described in this scenario was at least 20 million years (Table 1). The onset of middle Miocene doming and later intracontinental volcanism in North Africa began to disrupt the drainage system. Large segments would have remained active, but how long the drainages might have remained integrated all the way to the Atlantic is beyond speculation. At the end of the Miocene, an unusual set of circumstances (drying up of the Mediterranean) created the Eonile, a vigorous pirate stream in eastern Egypt. The headward (southward) incision of a deep Eonile Canyon (Said, 1982) brought the newly formed, north-flowing Eonile into direct conflict with the older, Atlantic-related Trans-African system. From the coastal cliffs of the Cairo area to Aswan, and possibly as far south as the second cataract of the present Nile, the Eonile beheaded the still-operational parts of the Trans-African drainages from their headwaters in the Red Sea Hills. This fatal blow left only the broad radar river valleys and the scattered "gravel spreads" elsewhere in the Eastern Sahara as testimony to the existence of a once-great transcontinental drainage system. Temporary rejuvenations occurred during the Quaternary pluvials, when episodic overbank flooding occurred on the terraces and small wadis (braided stream complexes and local ponds) formed in the floors of many of the old alluvial valleys. These ephemeral watercourses were utilized by successive groups of early humans until almost the dawn of the historical period, when climatic deterioration made the area virtually uninhabitable.

## REFERENCES


R. F. Peel, "The Gilf Kebir", part 4, in R. A. Bagnold, An expedition to the Gilf Kebir and Uweinat, 1939: Geographical Journal, v. 93, no. 4, pp. 295-307, 1939.

M. A. J. Williams, "Quaternary environments in northern Africa", in Williams, M.A.J. and Adamson, D.A. (eds.), A land between two Niles: Balkema, Rotterdam, pp. 13-22, 1982.

Rushdi Said, The geological evolution of the River Nile: Springer-Verlag, New York, 1981, 151 pp.

Rushdi Said, The geological evolution of the River Nile in Egypt: Zeitschrift für Geomorphologie, v. 26, no. 3, pp. 305-314, 1982.

J. F. McCauley, G. G. Schaber, C. S. Breed, M. J. Grolier, C. V. Haynes, B. Issawi, C. Elachi, and R. Blom, "Subsurface valleys and geoarchaeology of the Eastern Sahara revealed by Shuttle Radar": Science, v. 218, no. 4576, pp. 1004-1020, 1982.

S. E. Browne and J. D. Fairhead, "Gravity study of the Central African Rift System: a model of continental disruption, v. 1. The Ngaoundere and Abu Gabra Rifts": Tectonophysics, v. 94, pp. 187-203, 1983.

Bahay Issawi, "Ancient rivers of the eastern Egyptian desert": Episodes, v. 1983, no. 2, pp. 3-6, 1983.

P. M. Bermingham, J. D. Fairhead, and G. W. Stuart, "Gravity study of the Central African Rift System: a model of continental disruption, 2. The Darfur domal uplift and associated Cainozoic volcanism": Tectonophysics, v. 94, pp. 205-222, 1983.

Rushdi Said, "Proposed classification of the Quaternary of Egypt": Journal of African Earth Sciences, v. 1, no. 1, pp. 41-45, 1983.

Rafik Salem, "Evolution of Eocene-Miocene sedimentation patterns in parts of northern Egypt": American Association of Petroleum Geologists Bulletin, v. 60, no. 1, pp. 34-64, 1976.

C. A. Kogbe, "The Trans-Saharan Seaway during the Cretaceous", in M. J. Salem, and M. T. Busrewil, (eds.), The Geology of Libya, v. 1, Academic Press, 1980, pp. 91-95.

A. T. Grove and Andrew Warren, "Quaternary landforms and climate on the south side of the Sahara": Geographic Review, v. 134, pt. 2, pp. 194-208, 1968.

A. T. Grove, "Rise and fall of Lake Chad": Geographical Magazine, v. 42, no. 6, pp. 432-439, 1970.

Kevin Burke, T. F. Dessauvagie, and A. J. Whiteman, "Opening of the Gulf of Guinea and geological history of the Benue Depression and Niger Delta": Nature, v. 233, no. 37, pp. 51-55, 1971.

C. I. Adighije, "A gravity interpretation of the Benue Trough, Nigeria": Tectonophysics, v. 79, pp. 109-128, 1981.

J. F. McCauley, C. S. Breed, G. G. Schaber, W. P. McHugh, B. Issawi, C. V. Haynes, M. J. Grolier, and A. El Kilani, "Paleodrainages of the Eastern Sahara -- the Radar Rivers revisited (SIR-A/SIR-B implications for a mid-Tertiary trans-African drainage system)," IEEE Trans. GRS, v. GE-24, no. 4, pp. 624-648, 1986.

G. G. Schaber, J. F. McCauley, C. S. Breed, G. R. Olhoeft, "Shuttle Imaging Radar: physical controls on signal penetration and subsurface scattering in the Eastern Sahara," IEEE Trans. GRS, v. GE-24, no. 4, pp. 603-623, 1986.

F. W. B. Van Eysinga, Geological time table, 3rd Edition, Elsavier Scientific Publishing Co., Amsterdam, Netherlands, 1975.

Table 1. Geologic framework that affected development of Trans-African drainages. Relevant Pleistocene glacial events, which took place outside North Africa, shown in brackets. (Time scale after Van Eysinga, 1975)

CENOZOIC ERA

| PERIOD AND SUBPERIOD | EPOCH | AGE (m.y.: million years) | INFERRED CLIMATE | KEY GEOLOGIC EVENTS | ARCHAEOLOGY (See Table 1) | GEOMORPHIC SIGNIFICANCE |
|---|---|---|---|---|---|---|
| | Holocene | 0.005 | Onset of present hyperaridity | Desiccation of surface, loss of vegetation, eolian reworking of alluvial sediments | Neolithic | Almost total obscuration of fluvial imprint by active sand sheets and dunefields<br>Last pulses of fluvial activity (RR2 and RR3) |
| | | | Semiarid (Saharan pluvials) | Formation of Paleo-Chad Sea | | |
| | | 0.010 | | Integration of present Egyptian Nile with central African sources | | Beginning of modern Nile River |
| | | 0.020 | | | | Intermittent shedding of gravels from Red Sea wadis across filled alluvial valley of weak Nile River |
| | | 0.050 | Hyperarid | [Wisconsinan (Wurm) glaciation] | | Episodic calcification of fluvial deposits in Western Desert at 0.018, 0.50, .118, 0.300 m.y. |
| | Pleistocene | 0.250 | Semiarid (Abassian pluvial) | Deposition of Abbasia Formation | Paleolithic | |
| | | | | Deposition of Qena Formation | | Episodic runoff in incised and anastamosing channels (RR2 and RR3) |
| | | | Hyperarid | (Illinoian (Riss) glaciation) | | Intermittent eolian reworking of fluvial sediment into dune fields and sand sheets |
| | | | | Deposition of Idfu Formation | | Climatic deterioration. Final demise of now beheaded and tectonically dismembered Trans-African drainage system (RRI) |
| | | 1.5 | Hyperarid | [Kansan glaciation) | Pebble tools | |
| | | | Wet Tropical | | | |
| | | 2.0 | (Idfu pluvial) | | ---------- | |
| | | 2.5 | Onset of pro-progressive aridity | [Nebraskan glaciation) | | |
| | Pliocene | | | | | |
| | | 5.1 | | Deposition of 300-1000 m marine sediments in Nile Valley. Refilling of Mediterranean basin. Messinian event: drying up of Mediterranean; 3500-m drop in baselevel for active streams connected to Mediterranean | | Aggradation of Nile River Valley from Aswan to delta. Canyon 2500m deep, 700km long cut by Nile River through South Delta block to Aswan. Canyon cutting beheads consequent tributaries of Trans-African drainage in Red Sea Hills |
| | | 6.0 | | | | |
| | Miocene | 15.0 | Mostly humid(?) with some arid intervals | Domal uplift and volcanism in Hoggar, Tibesti, Darfur, Adamaoua areas | | Disruption of Trans-African drainage by creation of new divides between Nile Basin, Chad Basin, and Gulf of Guinea; streams become senile. Wadi Qena flows south, builds fans in depressions of Nile Trough. North-flowing drainages in Nile Trough begin southward extension |
| | | | | Mountains of South Delta block and other uplifts form elevated highlands along coast of northern Egypt and Libya | | Maximum development of Trans-African drainage (RRI) |
| | | 24.6 | | | | |

Table 1 (contd)

CENOZOIC ERA

| PERIOD AND SUBPERIOD | EPOCH | AGE (m.y.: million years) | INFERRED CLIMATE | KEY GEOLOGIC EVENTS | ARCHAEOLOGY (See Table 1) | GEOMORPHIC SIGNIFICANCE |
|---|---|---|---|---|---|---|
| | Oligocene | | Wet Tropical | Continental conditions prevail: Widespread deposition of fluvial coarse sands and gravels over Eocene limestones in northern Egypt. Episodic volcanism | | Initiation of Trans-African drainage pattern from Red Sea Hills southwestward down continental slope to Atlantic via Erdi and Chad Basins and Benue Trough |
| | | 38.0 | | Regression of Tethys Sea from North Africa, early doming, rifting of Afro-Arabian shield, and beginning of uplift of Red Sea Hills | | Southwestward continental slope develops across Northeast Africa. Streams consequent to Red Sea Hills begin to form Trans-African drainage net, emptying into Atlantic at paleo-Benue/Niger Delta |
| | Eocene | | | | | Widespread deposits of marine limetones in Northeast Africa (sediments of Limestone Plateau in Egypt, and equivalents in Libya) |
| | | 54.9 | | | | |
| | Paleocene | | | Tethys Sea Invades Northeast Africa | | |
| | | 65.0 | | | | |
| MESOZOIC ERA | | | | Closure of Benue Trough ends marine transgression in southern North Africa | | Widespread deposition of continental clastics of Nubia Fm. and equivalents in Northeast Africa |
| CRETACEOUS | Late | | | Trans-Saharan Seaway connects Tethys Sea with Atlantic through Benue Trough at Gulf of Guinea | | |

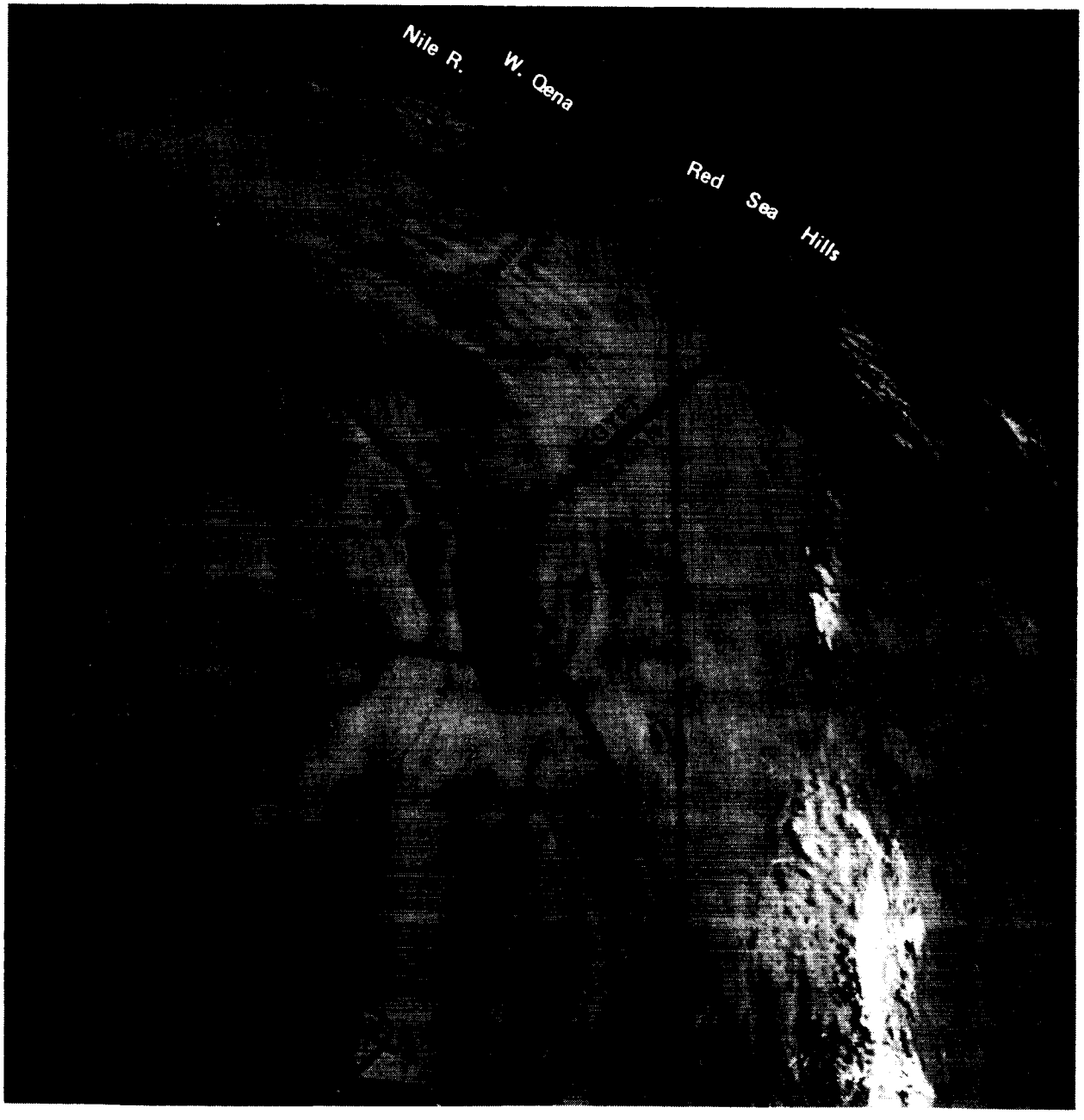


Figure 1. High altitude (Gemini XI) photograph shows the presently hyperarid Eastern Sahara west of the Nile River, and the Red Sea Hills, former headwaters of TADS, to the east. Piracy by the headward-incising Eonile cut off the headwaters of TADS, which once flowed across this now barren, sand-mantled region. SIR-A swath, on which TADS segments were first detected, indicated by dashed line.

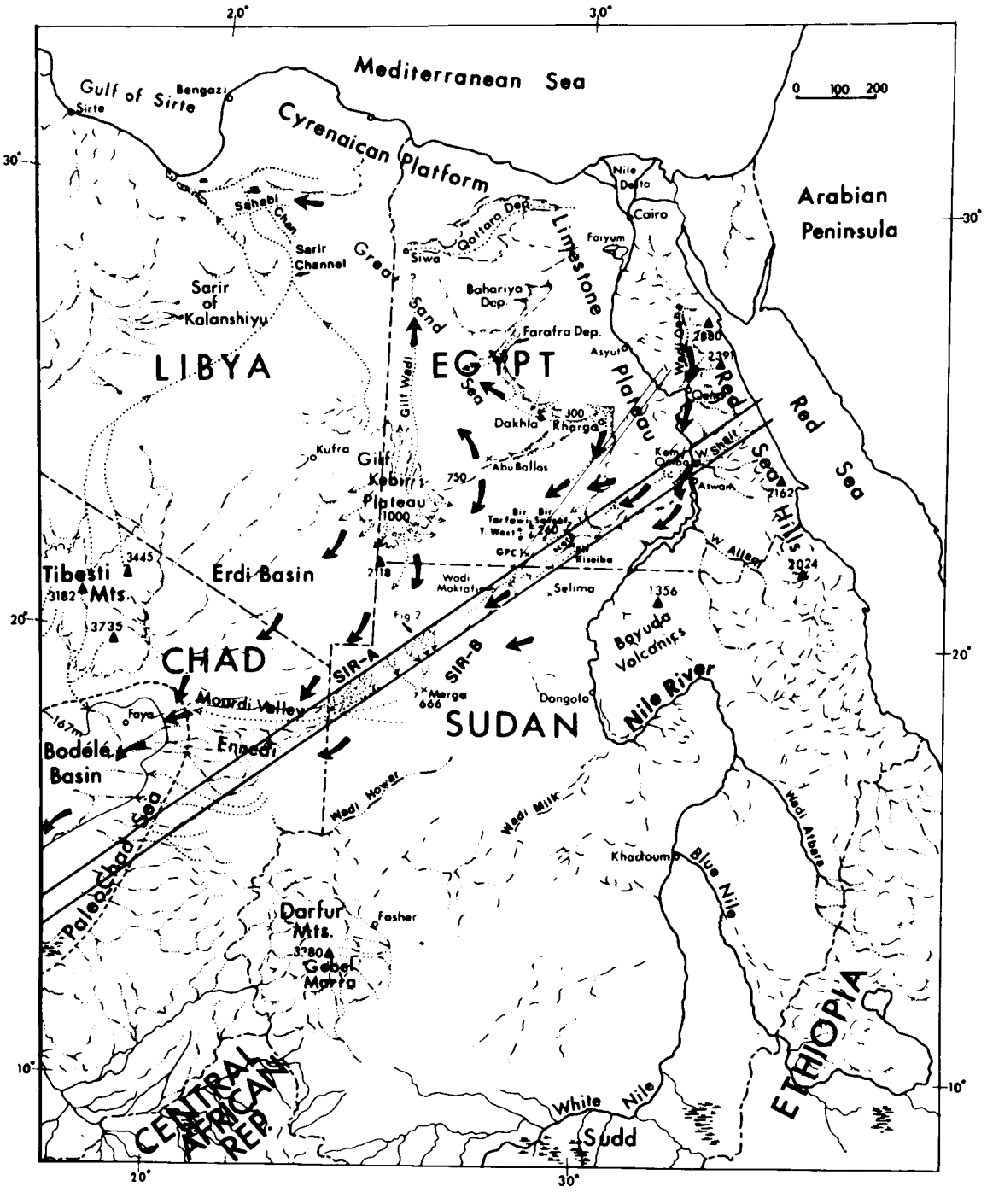


Figure 2. Map of Eastern Sahara, showing existing drainages with conventional symbols, and reconstructed paleodrainages with dotted lines. Paleodrainage north, south, and west of Kufra, Libya, from recent literature. Other reconstructions based on analysis of SIR-A, SIR-B and Landsat imagery, and field investigations. Large arrows show major drainage gradients inferred for mid-Tertiary time.

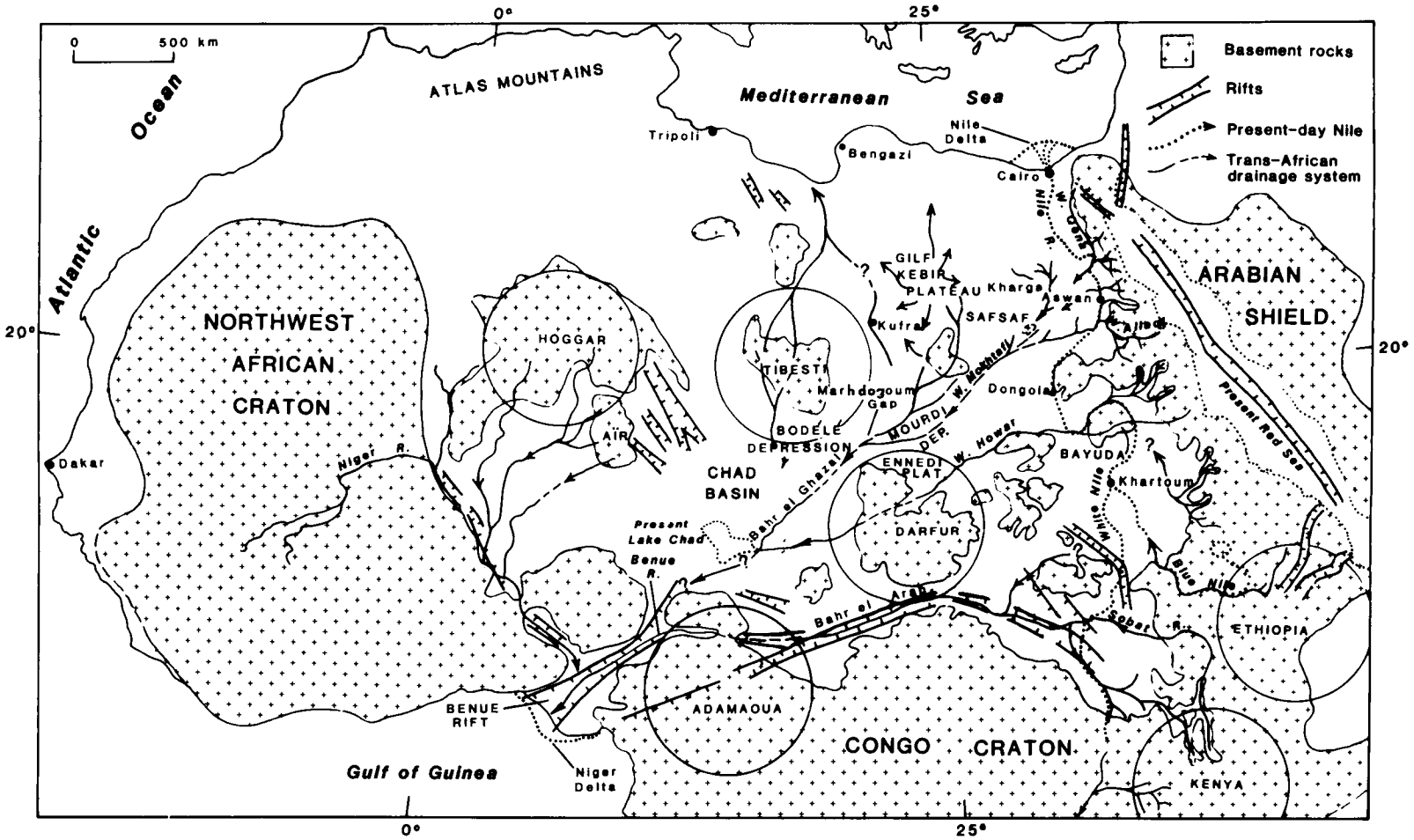


Figure 3. Major elements of proposed Trans-African Drainage System (TADS) as they may have existed at the time of its climax in the middle Tertiary. Circles indicate major centers of intracratonal doming and volcanism that disrupted TADS starting in middle to late Tertiary time, causing local ponding and drainage reversals. The present northeastward regional gradient in Egypt was probably not established until at least the late Miocene when the Nile Canyon was formed in response to drying up of the Mediterranean.

# GEOLOGICAL APPLICATIONS OF MULTIPOLARIZATION SAR DATA

Diane L. Evans
Jet Propulsion Laboratory, California Institute of Technology
Pasadena, California

Spaceborne Synthetic Aperture Radar (SAR) data acquired by Seasat and the Shuttle Imaging Radar (SIR-A/B) operating at L-band with HH polarization have been found to be useful in conjunction with other sensors for lithologic discrimination in arid environments with limited vegetation cover [1-3]. In order to assess the utility of more advanced sensors for geologic research and define the unique contributions each sensor makes, remote sensing data were collected over the Deadman Butte area of the Wind River Basin, Wyoming (Figure 1) as part of a cooperative study between the Jet Propulsion Laboratory Radar Sciences, Geology and Cartographic Applications groups, the Hawaii Institute of Geophysics, and the University of Wyoming. The Wind River Basin is an asymmetric sedimentary basin in central Wyoming created during the early Eocene Laramide orogeny. The stratigraphic section of the Deadman Butte study area, which was measured by Woodward [4] is made up of Paleozoic and Mesozoic marine shales, siltstones, limestones, and sandstones. Sensor systems included Landsat 4 Thematic Mapper (TM), Thermal Infrared Multispectral Scanner (TIMS) and the Multipolarization, L-band airborne SAR, a prototype for the next Shuttle Imaging Radar (SIR-C). Sensor parameters are given in Table 1.

Based on previous work by Kahle and Goetz [5], TIMS bands 1, 3 and 5 were processed with a decorrelation technique in order to suppress temperature differences and maximize emissivity differences related to crystalline structure in silicate minerals. All data were resampled to the TM pixel size (30m) and registered to the TM base. A rubber-sheet stretch of the data, based on a set of tiepoints, was used for the registration. The coregistered data are shown as Figure 2. In order to quantify the improvement in rock type discrimination that results from using the multisensor data over any individual data type, a Linear Discriminant Analysis was performed. The program used in this study is part of the UCLA Biomedical Data Processing Package [6] and is described by Blom and Daily [1]. Basically, areas of known rock types are selected as training areas, and means and standard deviations for each training area in each image are calculated. The program then determines which image is best for discriminating among the rock units by computing the discriminant function for each area and attempting to separate training areas into groups. Remaining images are then checked at the next step to find the next most useful for separating the training areas into groups, and so on. In this way, the multisensor images can be ranked in order of their utility for separating the units, and it is possible to determine which data set contributes to the discrimination between specific rock types.

Training areas were chosen for each of the major lithologic units outcropping in the Deadman Butte area, a dolomite member of the Phosphoria Formation, an unnamed red siltstone member of the Dinwoody Formation, the Red Peak Siltstone and Alcova Limestone members of the Chugwater Formation, the Redwater Shale Member of the Sundance Formation, and the Cloverly Sandstone,

Thermopolis Shale, Muddy Sandstone, Mowry Shale and Frontier Formation. The results of the Linear Discriminant Analysis are presented in Table 2. The increased capability to classify units using the multisensor data set over any individual sensor is shown graphically in Figure 3. Results show that classification accuracy increases with the addition of new channels up to 96% using 10 channels, with the three optimum channels being LVH, TIMS5 and TM5. The overall accuracy achieved using only the TM bands was 76%; using only TIMS, 73% and SAR alone, 62%. Thus, the multisensor data set provided at least 20% better classification accuracy than any of the individual sensors. However, it should be noted that this procedure only provides classification accuracies for the training areas themselves and may not represent the ability to classify entire rock units. The results can therefore only be used as one indicator of the optimum bandpasses. Another important factor is how well the training areas represent the various lithologies and can be used for classification, which is a topic of ongoing research.

## REFERENCES


[1] Blom, R. and M. Daily, Radar image processing for rock type discrimination, IEEE Trans. on Geoscience and Remote Sensing, Vol. GE-20, no. 3, 343-351, 1982.

[2] Evan, D. L., Use of coregistered visible, infrared and radar images for geologic mapping, Spaceborne Imaging Radar Symposium, Pasadena, JPL Pub. 83-11, 1983.

[3] Rebillard, P. and D. L. Evans, Analysis of coregistered Landsat, Seasat and SIR-A images of varied terrain types, Geophysical Research Letters, Vol. 10, no. 4, 277-280, 1983.

[4] T. C. Woodward, Geology of Deadman Butte area, Natrona County, Wyoming, Bull Amer. Assoc. Petroleum Geol., Vol. 41, pp. 212-262, 1957.

[5] A. B. Kahle, and A. F. H. Goetz, Mineralogic information from a new airborne thermal infrared multispectral scanner, Science Vol. 222, 24-27, 1983.

[6] W. J. Dixon, Ed., BMD Biomedical Computer Programs, Berkeley, California: University of California Press, 1970.

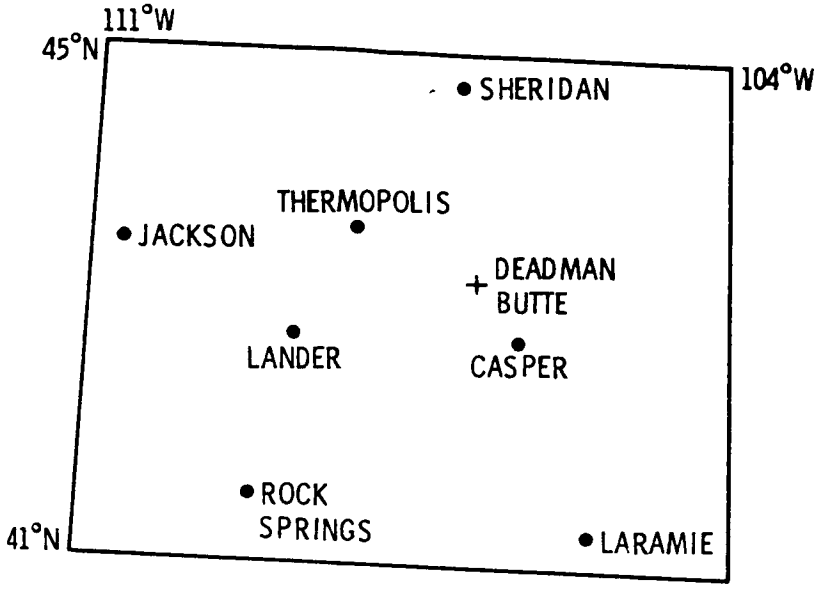


Figure 1. Location of Deadman Butte study area

Table 1. Imaging sensor systems

| Sensor | TM | TIMS | Quad-pol SAR |
|---|---|---|---|
| Platform | Landsat 4 & 5 | Aircraft | Aircraft |
| Altitude | 700 km | 10 km* | 10 km* |
| Swath width | 185 km | 4 km* | 6 km* |
| Wavelength | TM1: .45 - .52 μm | TIMS1: 8.1 - 8.5 μm | 24.6 cm |
| | TM2: .52 - .60 μm | | |
| | TM3: .63 - .69 μm | TIMS3: 8.9 - 9.3 μm | |
| | TM4: .76 - .90 μm | | |
| | TM5: 1.55 - 1.75 μm | TIMS5: 10.2 - 10.9 μm | |
| | TM7: 2.0 - 2.36 μm | | |
| Pixel size | 30 m (.45 - 2.36 μm) | 25 m* | 10 m* |

*Typical

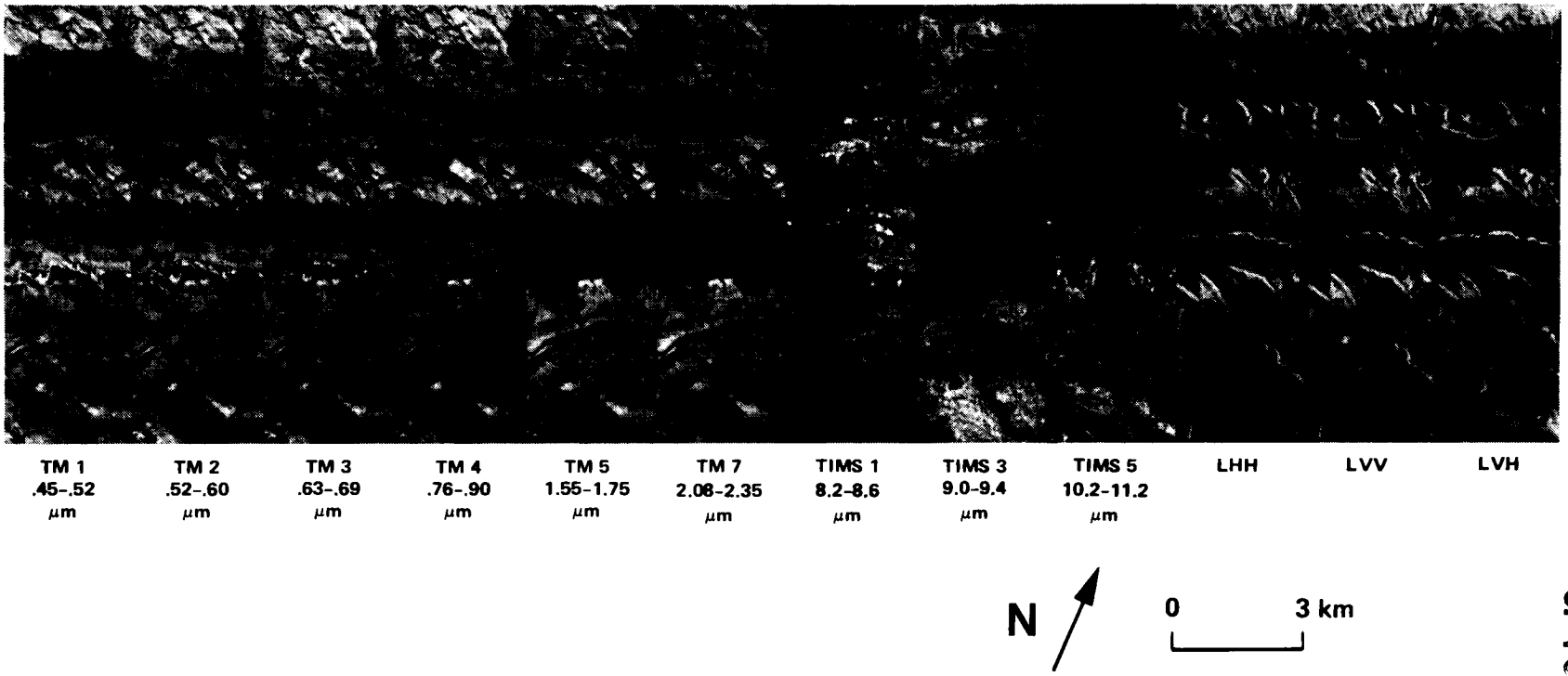


Figure 2. Multisensor data set of Deadman Butte study area

Table 2. Cumulative classification accuracy (%) ranked in order of decreasing usefulness

| | LVH | TIMS5 | TM5 | TM2 | LVV | TIMS3 | TM7 | TMS1 | TM4 | TM3 | TM1 | LHH |
|---|---|---|---|---|---|---|---|---|---|---|---|---|
| U. Frontier | 57 | 68 | 80 | 84 | 85 | 95 | 94 | 95 | 95 | 95 | 95 | 95 |
| L. Frontier | 43 | 46 | 60 | 62 | 81 | 85 | 89 | 89 | 91 | 92 | 92 | 92 |
| Mowry | 55 | 48 | 60 | 58 | 87 | 89 | 88 | 95 | 99 | 100 | 100 | 100 |
| Muddy | 75 | 75 | 100 | 100 | 100 | 100 | 100 | 100 | 100 | 100 | 100 | 100 |
| Thermopolis | 33 | 58 | 97 | 97 | 100 | 100 | 100 | 100 | 100 | 100 | 98 | 98 |
| Clovery | 37 | 55 | 84 | 89 | 90 | 93 | 95 | 97 | 98 | 98 | 100 | 98 |
| Sundance | 98 | 98 | 99 | 98 | 95 | 95 | 95 | 95 | 99 | 98 | 100 | 100 |
| Alcova | 16 | 81 | 90 | 96 | 96 | 98 | 98 | 100 | 100 | 100 | 94 | 95 |
| Chugwater | 11 | 42 | 48 | 86 | 89 | 90 | 91 | 93 | 92 | 92 | 89 | 89 |
| Dinwoody | 63 | 52 | 59 | 67 | 85 | 82 | 82 | 85 | 86 | 89 | 92 | 92 |
| Phosphoria | 25 | 79 | 79 | 85 | 86 | 89 | 89 | 90 | 87 | 89 | 100 | 100 |
| Average | 42 | 64 | 81 | 84 | 90 | 92 | 93 | 94 | 95 | 96 | 96 | 96 |

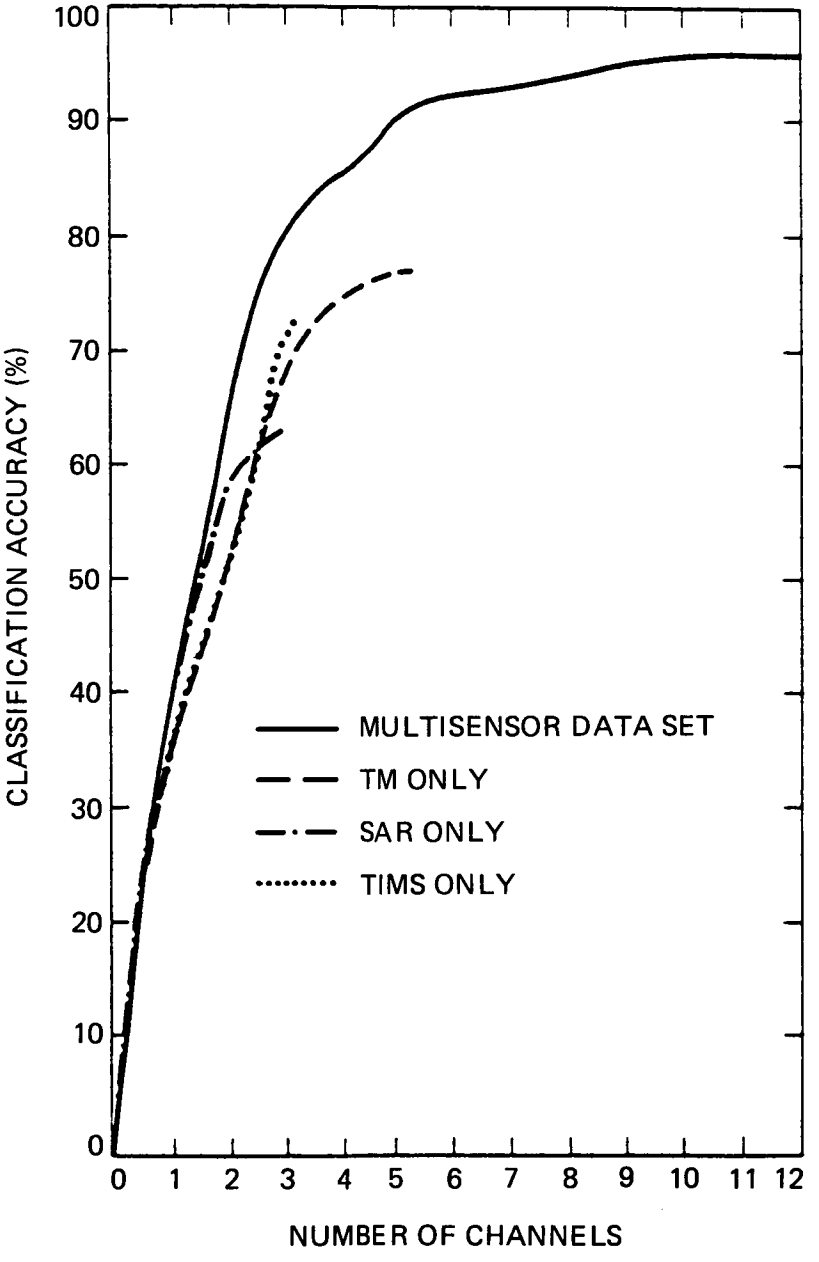


Figure 3. Improvement in classification accuracy using multisensor data set

# Future Projects

# SPACEBORNE IMAGING RADAR RESEARCH IN THE 90'S

Charles Elachi
Jet Propulsion Laboratory
California Institute of Technology
Pasadena, California

The imaging radar experiments on Seasat (1978) and on the space shuttle (SIR-A in 1981 and SIR-B in 1984) have led to a wide interest in the use of spaceborne imaging radars in Earth and planetary sciences. The radar sensors provide unique and complimentary information to what is acquired with visible and infrared imagers. This includes subsurface imaging in arid regions (1,2), all weather observation of ocean surface dynamic phenomena (3-5), structural mapping (6-8), soil moisture mapping (9), stereo imaging and resulting topographic mapping (10).

However, experiments up to now have exploited only a very limited range of the generic capability of radar sensors. With planned sensor developments in the late 80's and early 90's, a quantum jump will be made in our ability to fully exploit the potential of these sensors. These developments include (Figure 1): multiparameter research sensors such as SIR-C and X-SAR, long-term and global monitoring sensors such as ERS-1, JERS-1, EOS, Radarsat, GLORI and the spaceborne sounder, planetary mapping sensors such as the Magellan and Cassini/Titan mappers, topographic three-dimensinal imagers such as the scanning radar altimeter and three-dimensional rain mapping. These sensors and their associated research are briefly described in this paper.

## I. MULTIPARAMETER RESEARCH IMAGING RADAR. THE SIR PROJECT

An evolutionary ten-year program is ongoing at NASA's Jet Propulsion Laboratory to develop the scientific application and technological aspects of multiparameter imaging radars. The first two steps consisted of the SIR-A, which was a single-frequency proof of concept sensor, and the SIR-B, which was designed to acquire multiangle imagery. The SIR-A demonstrated the ability of spaceborne radars to acquire subsurface imagery in arid regions (Figure 2). The SIR-B provided for the first time stereo and three-dimensional imagery from space (Figure 3). For recent results acquired with SIR-B the reader is referred to references 10 and 11.

The next major step is the joint US/Germany/Italy SIR-C/X-SAR experiment which will allow the simultaneous acquisition of images at three frequencies (L, C and X) and at all polarization states (on the L and C channels). The multifrequency capability will allow the study of the surface spectral response and the classification of surface units based on the roughness and dielectric properties. In addition, it will allow the quantitative determination of the subsurface penetration which is a strong factor of the frequency.

The polarization capability will allow the synthesis of the surface images at each and every possible polarization state based on acquiring coherently the four fundamentals (HH, VV, HV, and VH) as shown in Figure 4 and discussed in detail in recent publications (12-14).

The SIR project activities also include major technological developments (distributed SAR, real-time ground data processing and calibration) which will form the basis for the EOS SAR.

## II. LONG-TERM AND GLOBAL OBSERVATIONS

The SIR experiment will be limited to short-period flights (1 week) until the EOS platform is put in orbit in the mid-90's. In the mean time, a number of imaging radar sensors are planned for launch on free flyers in the early 90's for long-term surface observation. These sensors will have limited parameter flexibility, but will play a major role in allowing the study of temporal behavior of surface phenomena such as sea ice, ocean waves and patterns, vegetation dynamics, forest clear cutting, etc... The European ERS-1 and Japanese ERS are approved projects that are planned for the early 90's with a lifetime of 2 to 3 years. However, because of their limited swath (100 km) and limited operation range (in view of a station) their monitoring capability will be localized. This led JPL scientists to the feasibility study of a Global Radar Imager (GLORI) which will allow global mapping every two days. This requires a sensor with dual 400-km swaths. Preliminary considerations correspond to a C-band sensor with a 100-m resolution and real-time processing on the EOS platform. Such a sensor will allow global and continuous monitoring of polar ice, large ocean phenomena (internal waves, eddies, weather fronts, current boundaries), soil moisture and vegetation cover.

Subsurface penetration is directly proportional to the observing radar wavelength. This led to the considerations of a low-frequency imaging SAR. Even though very low frequencies are desired, ionospheric efforts and frequency allocation considerations will limit the lower range to no less than about 400 MHz. This would extend the penetration depth in arid regions observed by SIR-A by a factor of 3. In addition, such a sensor would allow the sounding of the antarctic ice sheets down to a depth of many kilometers due to the extremely low loss of sheets of ice.

## III. PLANETARY OBSERVATIONS

The cloud penetration capability of radar sensors makes it necessary to use them to image the surfaces of Venus and Titan, which are continuously and completely cloud covered. The Magellan mission will put an S-band imaging SAR in orbit around Venus in 1990, which will provide images of at least 90% of the planet's surface at a resolution better than 250 meters. By the late 90's the Cassini spacecraft will be put in an orbit around Saturn and, through a series of flybys, the surface of Titan will be imaged and sounded with a dual-frequency (L-band and K-band) imaging radar sensor.

## IV. THREE-DIMENSIONAL IMAGING

The surface topography is the key data base that is necessary to fully interpret the imaging data acquired with multispectral (microwave, infrared and visible) sensors. When the topography is registered to the imaging data, the interpreter can use graphic techniques to observe the surface from a variety of perspective views (Figure 6), thus enhancing his interpretation capability.

High-resolution topography can be derived from stereoimagery (radar or visible/IR). However, this is practical only for regional coverage. The acquisition of a global digital data base at a reasonable cost and in a timely fashion requires the development of a direct technique which allows the direct measurement of the surface topography in a digital format. This can be done with a scanning radar altimeter (SRA) as shown in Figure 5.

The SRA uses a narrow beam antenna across the track with a surface footprint of 250 meters. This is possible with an 8-meter, 37-GHz antenna from an altitude of 250 km. Along the track, a synthetic-aperture technique is used to achieve the equivalent spatial resolution. This requires an antenna of only 0.3 meter. The beam is scanned back and forth across the track to cover a 150-km swath. In this configuration, two shuttle flights will be sufficient to acquire the global data sets. Height accuracy measurement of less than 3 meters is easily feasible.

The scanning radar altimeter concept can also be used for volumetric rain mapping. Figure 7 shows an example of rain profiles acquired with a down-looking airborne sensor (13). The rain intensity can be derived for each altitude level particularly if a dual-frequency sensor is used. By scanning back and forth, a three-dimensional "picture" of the rain region can be acquired.

## V. CONCLUSION

The above overview illustrates the wide range of experiments that are planned to fully capitalize on the capability of spaceborne radar sensors. It is important to note that in order to acquire a comprehensive information set about the surface, the radar data has to be used in conjunction with visible and infrared data. In this fashion the user will be able to determine the surface composition (from visible and infrared spectrometry), its thermal properties (from thermal infrared), its physical and electric properties (from multispectral imaging radar) and its morphology (from stereo imagers or scanning altimeters).

## REFERENCES


1. McCauley, J. et al. (1982), "Subsurface valleys and geoarcheology in the eastern Sahara revealed by shuttle radar," Science, vol. 218, p. 1004.

2. Elachi, C., L. Roth and G. Schaber (1984), "Spaceborne radar subsurface imaging in hyperarid regions," IEEE Trans. G&RS, vol. GE-22, p. 383. Note: The SIR-A and Landsat images in Fig. 2 were mistakenly interchanged.

3. Vesecky, J. and R. Stewart (1982), "The observation of ocean surface phenomena using imagery from Seasat SAR," JGR, vol. 87 (C3), p. 3397.

4. Elachi, C. (1980), "Spaceborne imaging radar: geologic and oceanographic applications," Science, vol. 209, p. 1073.

5. Elachi, C. (1978), "Radar imaging of the ocean surface," Boundary Layer Meteorology, vol. 13, p. 165.

6. Sabins Jr., F. F. (1983), "Geologic interpretation of space shuttle radar images of Indonesia," AAPG, vol. 67, p. 2076.

7. Ford, J. P. (1980), "Seasat orbital radar imagery for geologic mapping: Tennessee-Kentucky-Virginia," AAPG, vol. 66, p. 2064.

8. Sabins Jr., F. F., R. Blom and C. Elachi (1980), "Seasat radar image of the San Andreas Fault, California," AAPG, vol. 64, p. 614.

9. Carver, K., C. Elachi and F. Ulaby (1986), "Microwave Remote Sensing," IEEE Proc., vol. 73, p. 970.

10. See Science Issue of June 20, 1986, vol. 232.

11. Cimino, J. B., C. Elachi and M. Settle (1986), "SIR-B - The second shuttle imaging radar experiment," IEEE Trans. G&RS, vol. GE-24, p. 445.

12. Evans, D., T. Farr, J. P. Ford, T. Thompson, C. Werner (1986), "Multipolarization radar images for geologic mapping and vegetation discrimination," IEEE Trans. G&RS, vol. GE-24, p. 246.

13. Van Zyl, J., H. Zebker and C. Elachi, "Theory of imaging radar polarimetry through wave synthesis," submitted to Radio Science, 1986.

14. Zebker, H., J. van Zyl and D. Held, "Imaging radar polarimetry from wave synthesis," submitted to Journal for Geophysical Research, 1986.

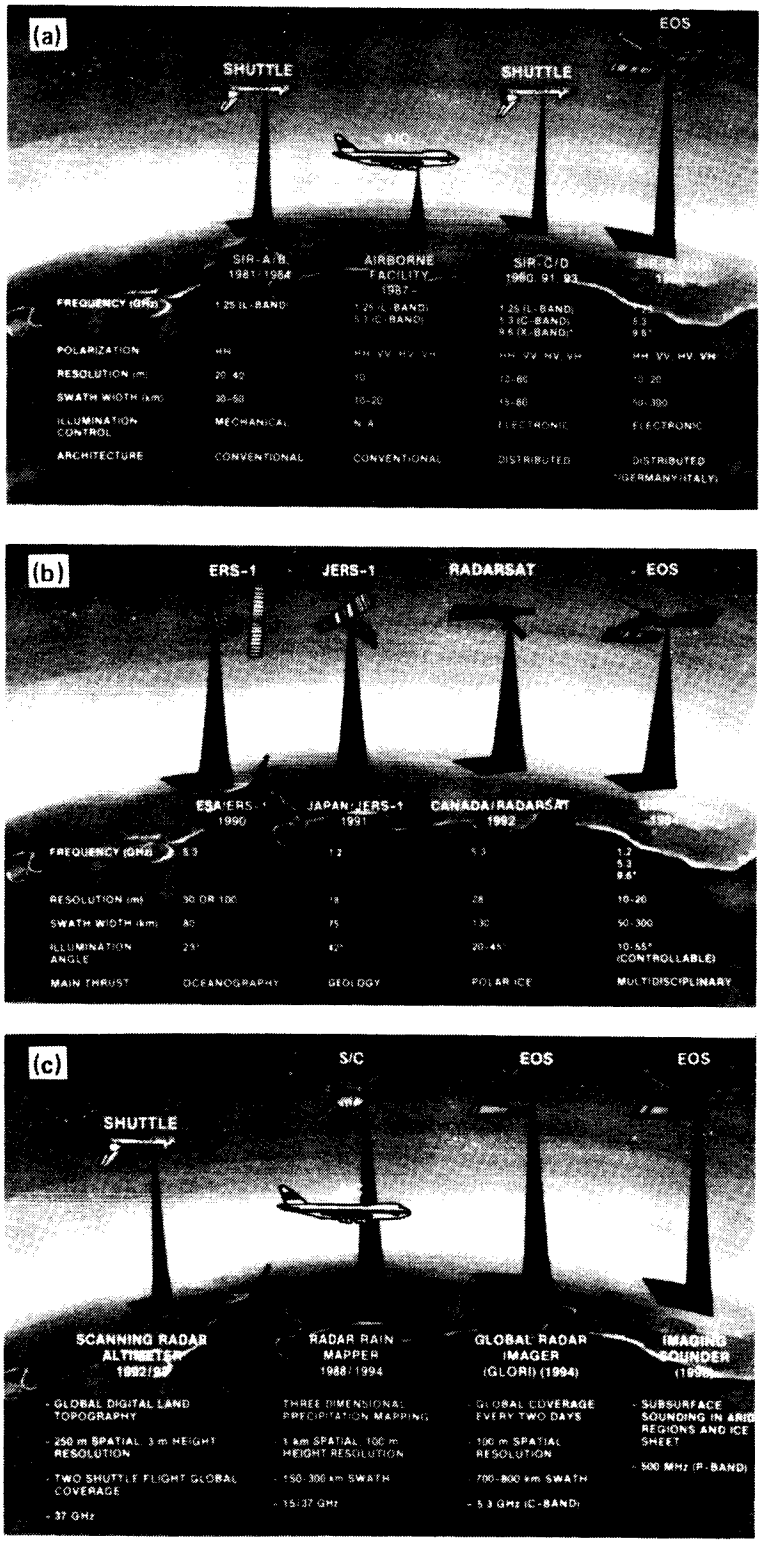


Figure 1. Spaceborne imaging radar sensors of the 80's and 90's: a) Completed and ongoing elements of the NASA SIR core project; b) International free flying sensors; c) non-conventional spaceborne imaging radar sensors being studied.

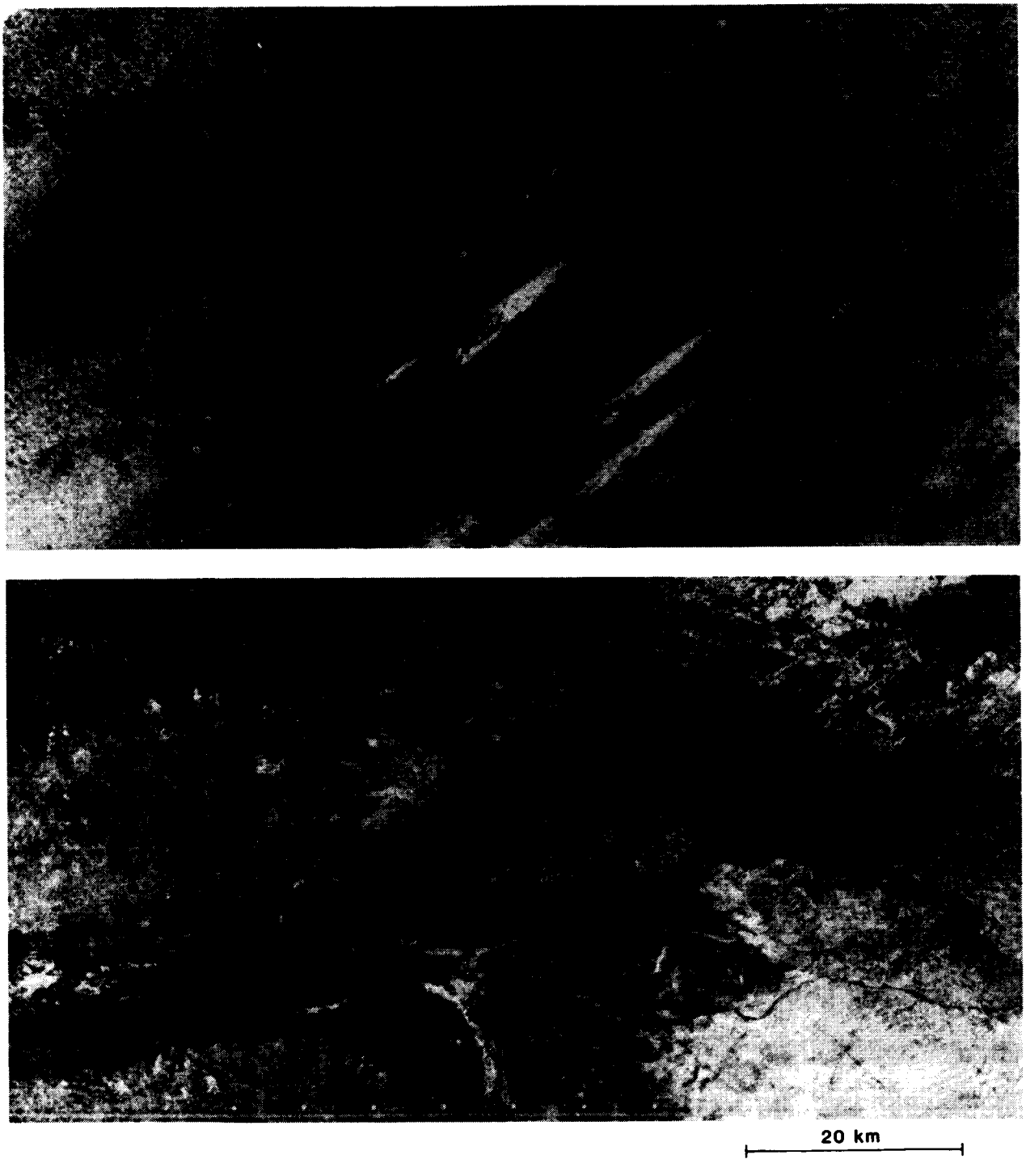


Figure 2. SIR-A and Landsat images of the same desert area in southwestern Egypt. The SIR-A image (bottom) clearly shows the morphology of dry river channels buried a few meters under a layer of dry sand.

(a)

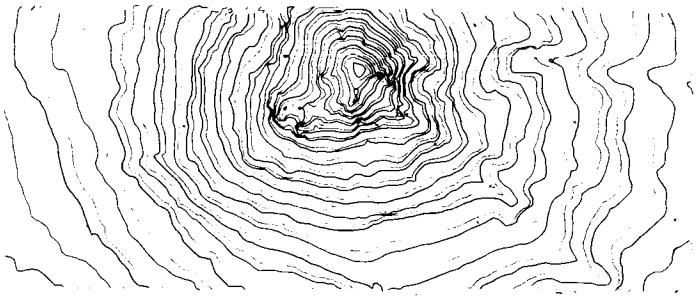

(b)

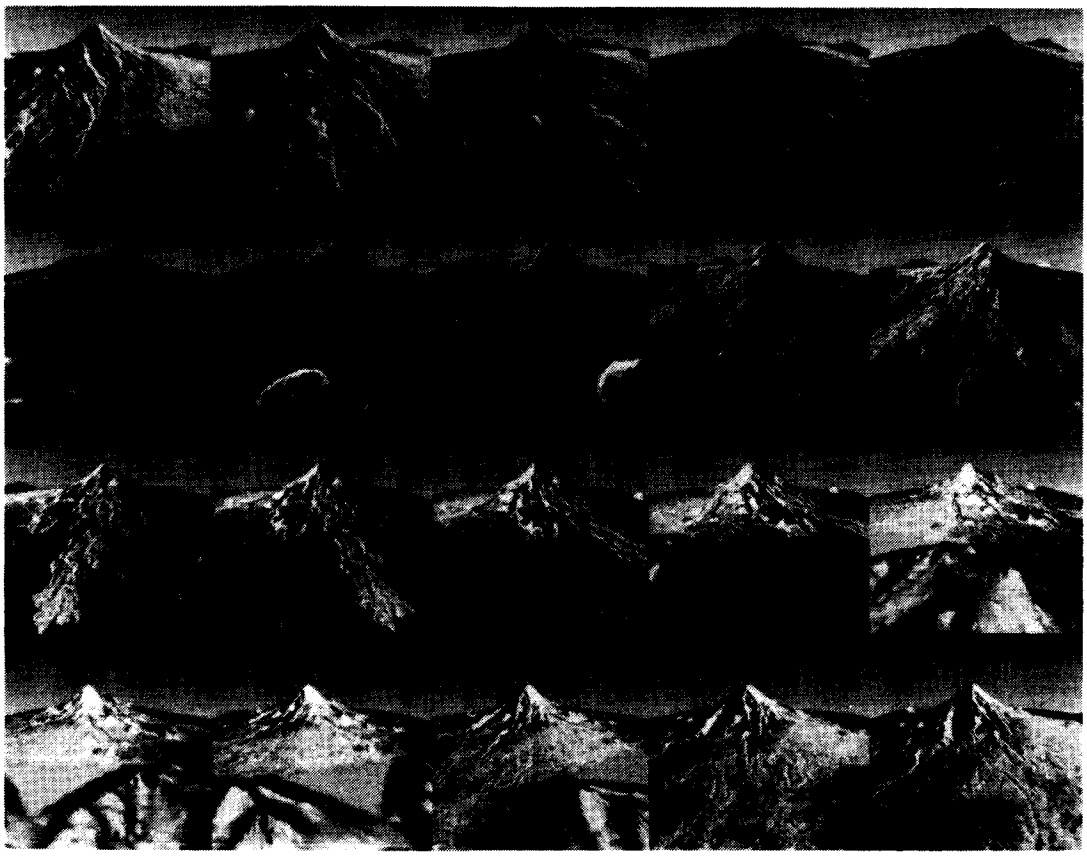

Figure 3. Stereo images acquired by SIR-B were used to generate (a) topographic contours and (b) perspective views of Mt. Shasta, California.

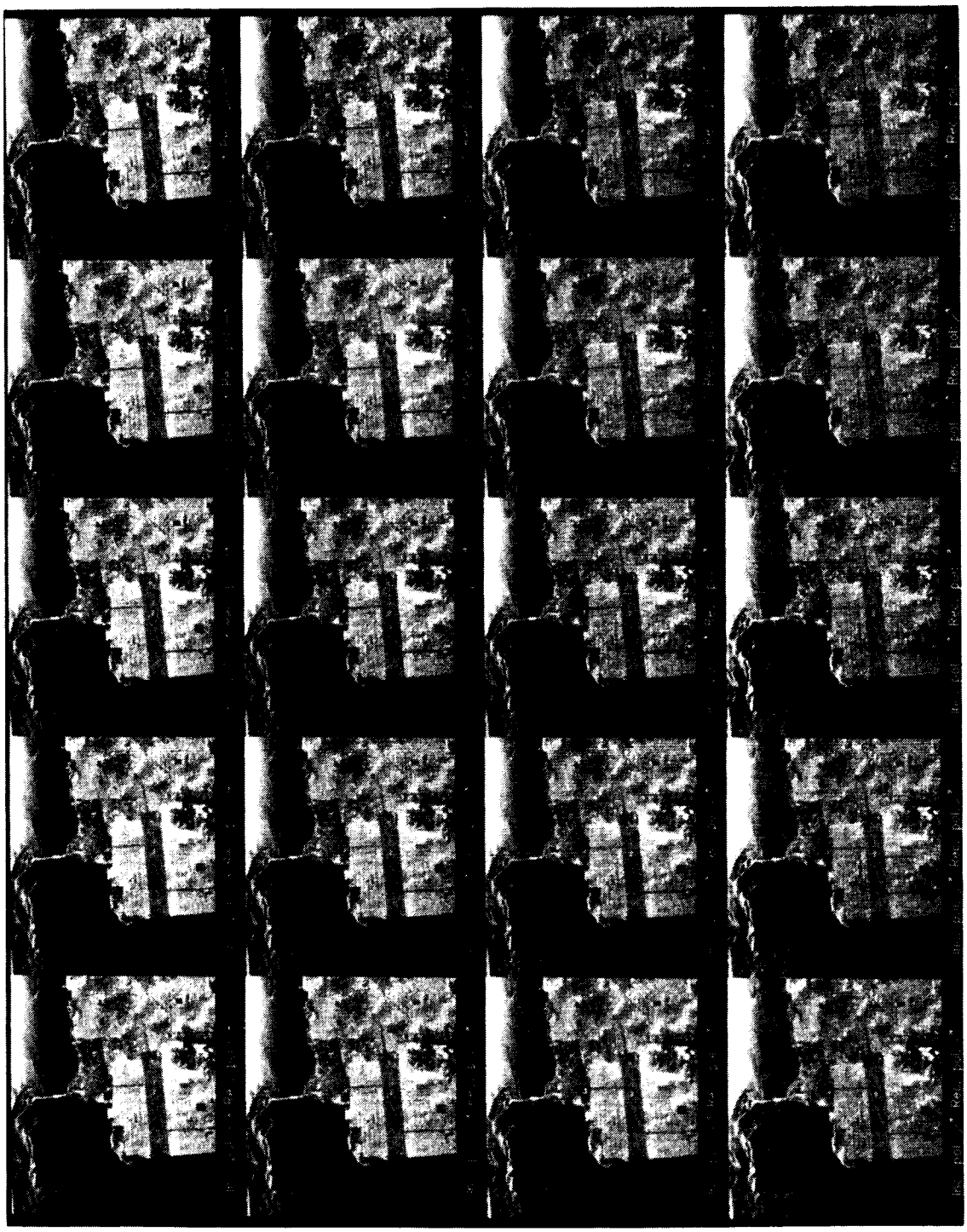

Figure 4. Synthesized polarization diversity images of San Francisco Bay generated from the four basic coherent images at HH, VV, VH, and HV polarization acquired with the JPL L-band airborne radar.

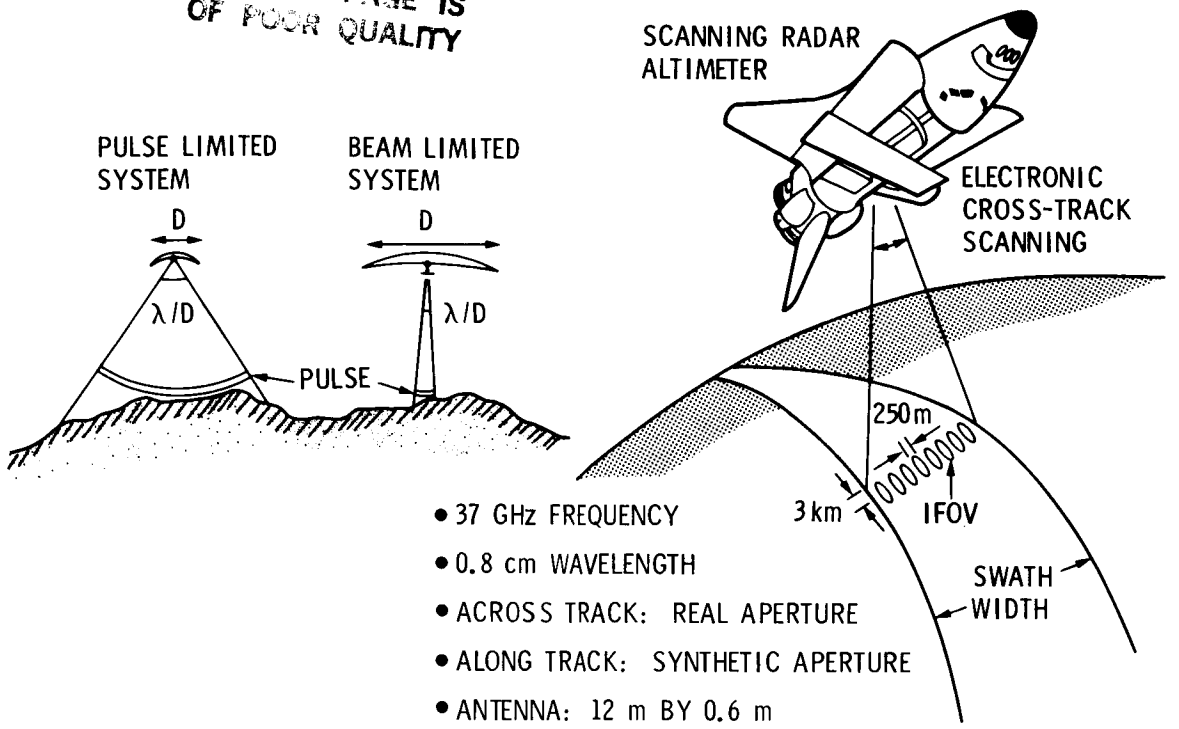


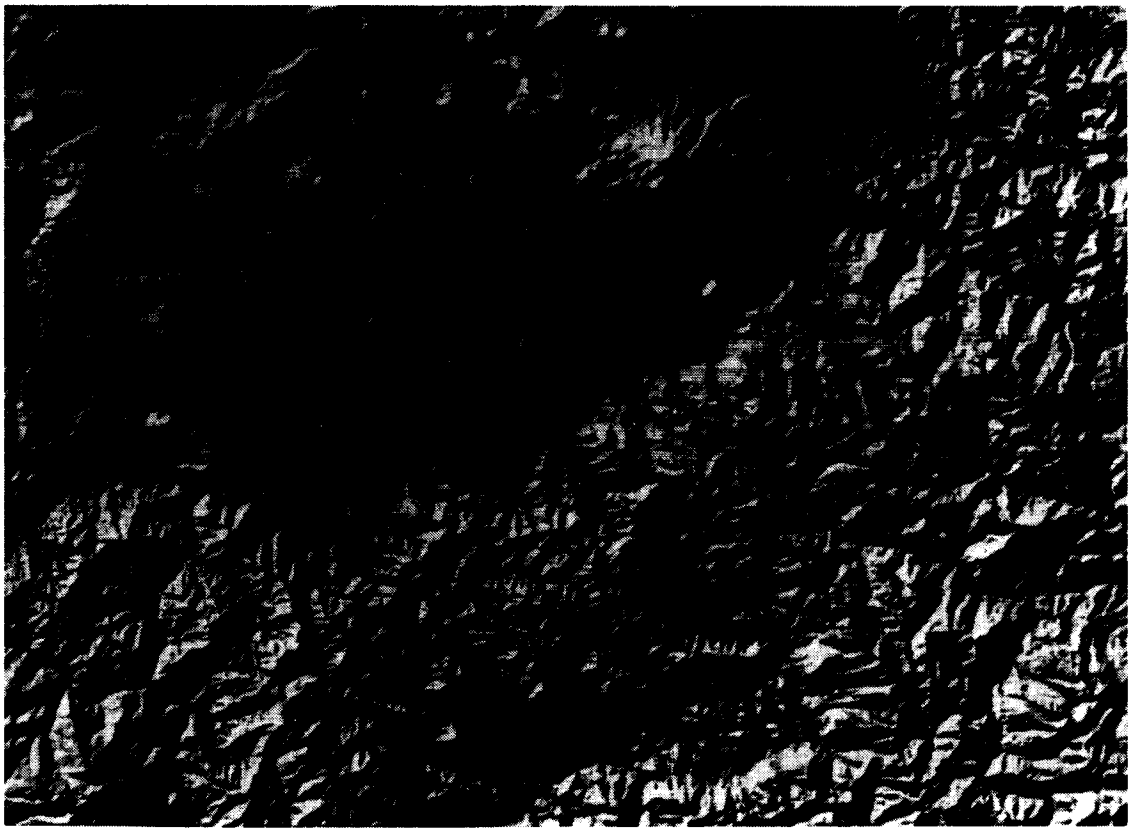

Figure 5. Concept of a scanning imaging altimeter for global topographic mapping and a shaded relief map of Mt. Shasta generated from a simulation of the data that will be provided by such a sensor.

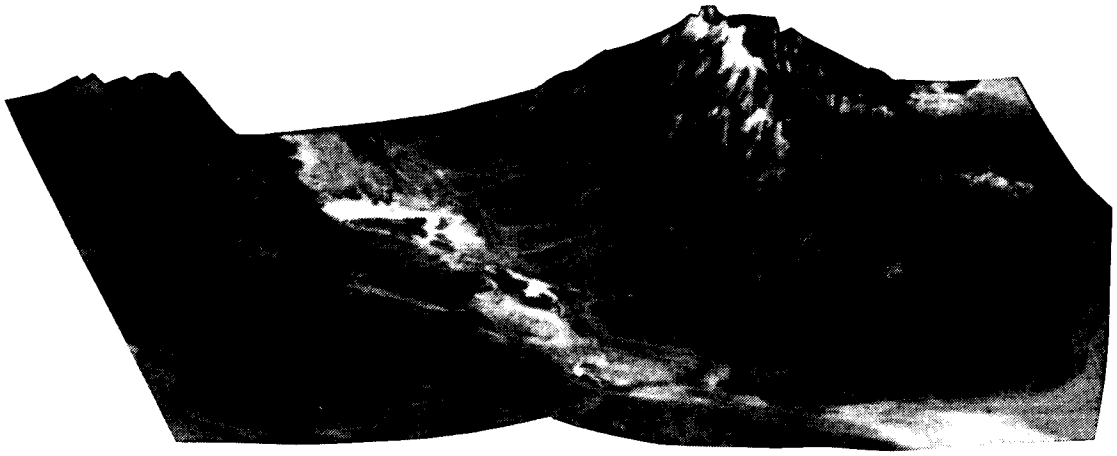

DEATH VALLEY FROM NORTHEAST - TM BAND 1

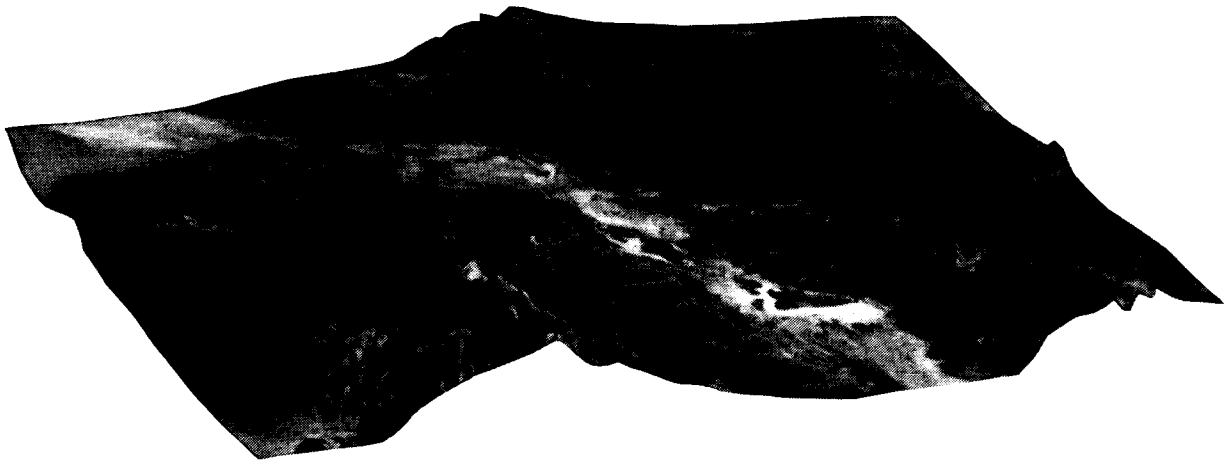

DEATH VALLEY FROM SOUTHEAST - TM BAND 1

Figure 6. Perspective views of Death Valley, California, generated from thematic mapper data coregistered on a digital surface topography base.

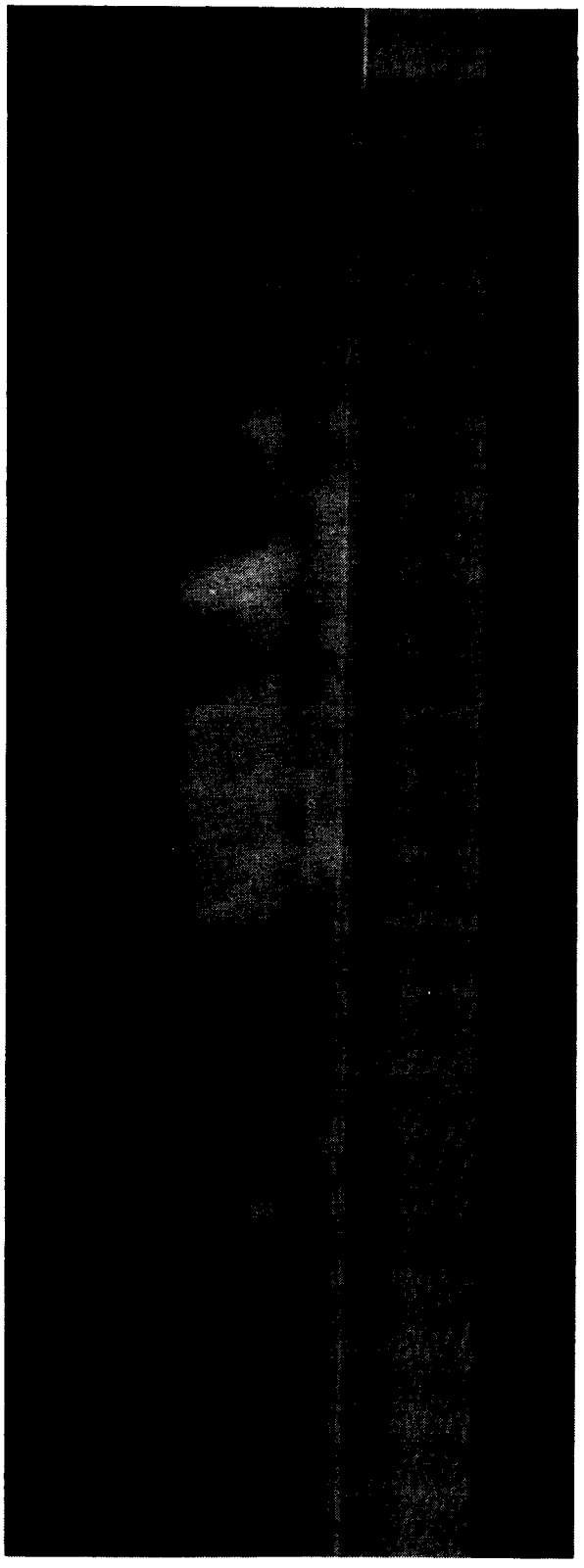

Figure 7. Concept of a scanning radar rain mapper and example of airborne radar data showing rain images in one vertical plane.

# VENUS RADAR MAPPER (VRM): MULTIMODE RADAR SYSTEM DESIGN

William T. K. Johnson
Jet Propulsion Laboratory
California Institute of Technology
Pasadena, California, U.S.A.

Alvin T. Edgerton
Hughes Aircraft Company
Space & Communications Group
El Segundo, California, U.S.A.

## I. INTRODUCTION

The surface of Venus has remained a relative mystery because of the very dense atmosphere that is opaque to visible radiation and, thus, normal photographic techniques used to explore the other terrestrial objects in the solar system are useless. The atmosphere is, however, almost transparent to radar waves and images of the surface have been produced via earth-based and orbital radars. The technique of obtaining radar images of a surface is variously called side looking radar, imaging radar, or synthetic aperture radar (SAR). The radar requires a moving platform in which the antenna is side looking. High resolution is obtained in the cross-track or range direction by conventional radar pulse encoding. In the along-track or azimuth direction, the resolution would normally be the real antenna beam width, but for the SAR case, a much longer antenna (or much sharper beam) is obtained by moving past a surface target as shown in Figure 1, and then combining the echoes from many pulses, by using the doppler data, to obtain the images.

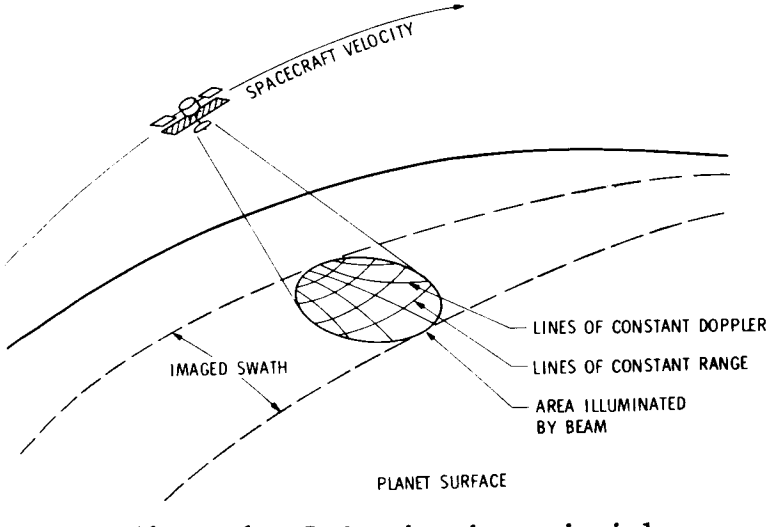


Figure 1. Radar imaging principle

The subject of this paper is the radar design of the Venus Radar Mapper (VRM) which is a United States National Aeronautics and Space Administration (NASA) planetary mission to be launched in 1988, that will acquire global radar imagery and altimetry data of the surface of Venus. The project is managed for NASA by the Jet Propulsion Laboratory (JPL) in Pasadena, California.

## II. SCIENCE RATIONALE

Venus is the planet most like the Earth in the solar system. Great interest has been shown in it by both the U.S. and U.S.S.R.[1] In addition to Earth-based radar studies from the NASA Goldstone Deep Space Station, the U.S. has sent two missions, Pioneer Venus Orbiter and Pioneer Venus Multiprobe; and three fly-by missions, Mariners 2, 5, and 10, while the U.S.S.R. has sent several probes, orbiters, and landers: Veneras 4 to 16 and Vegas 1 and 2. The results of the surface imaging studies are summarized in Figure 2, along with the expected performance of the SAR portion of the VRM radar, while Figure 3 shows in more detail the VRM-SAR performance.

The science objectives of the VRM mission are: to improve the knowledge of the tectonics and geologic history of Venus by analysis of the surface morphology and the process that controls it; to improve the knowledge of the geophysics of Venus, principally its density distribution and dynamics; and to improve the knowledge of the small scale surface physics. To meet these objectives, the requirements on the radar system are: to produce contiguous images of at least 70% of the planetary surface with a radar resolution better than 300m; to produce surface brightness temperature measurements of the imaged areas at a temperature resolution better than 2°K; and to produce topographic and scattering characteristics maps with a height resolution better than 30m.

## III. MISSION CONSTRAINTS

A combination of factors led to the major mission constraints listed in Table 1[2] [3] [4] [5]. The elliptical orbit and small antenna (compared to Earth orbiting SAR's) are the most demanding constraints from a radar system design view. The requirement on the design was to meet all science objectives within the mission constraints. The design had to make very efficient use of each of the limited resources, especially data rate. The mission must also complete all its objectives in one Venusian year or 243 days.

Table 1. Mission constraints

| | |
|---|---|
| 1. | Elliptical orbit with period 3.1 to 3.7 hr. |
| 2. | Periapsis altitude 250 to 300 km |
| 3. | Voyager antenna 3.7 m (shared with telecommunications) |
| 4. | Data record rate 806 kbps |
| 5. | Data volume per orbit 1700 Mbits |
| 6. | Data rate to earth: 270 kbps |
| 7. | No real-time or near real-time commanding |
| 8. | Low-cost mission operations |
| 9. | Use existing digital processor |

The absence of real-time command capability and desire for a simple radar dictates the use of navigation capability to set the radar data collection parameters. The radar is commanded by the spacecraft from repetitive sequences stored in the command memory. These sequences are calculated from navigation predictions and uploaded to the spacecraft three times a week.

| | 1978 Pioneer | 1983 Venera 15/16 | 1988 VRM |
|---|---|---|---|
| Periapsis altitude (km) | 200 | 1000 | 250 |
| Apoapsis altitude (km) | 67000 | 65000 | 7800 |
| Period (hr) | 24 | 24 | 3.2 |
| Shift in track at equator (km) | 157 | 157 | 20.9 |
| Attitude control method | Spin | Gas | Momentum wheels |
| SAR antenna (m) | | 6 x 1.4 parabolic | 3.7 Dish |
| Altimeter antenna (m) | 0.38 | 1 parabolic | 0.08 x 0.8 Horn |
| Polarization | Linear | Linear | HH |
| Transmitter type | Solid state | TWT | Solid state |
| Peak power (W) | 20 | 80 | 350 |
| SAR bandwidth ($MH_z$) | 0.25 | 0.65 | 2.26 |
| Radar frequency ($GH_z$, cm) | 1, 75, 17 | 3, 75, 8 | 2, 38, 12 |
| Swath width (km) | Variable | ~120 | 20 - 25 |
| SAR data rate to S/C (kbps) | Low | ~70 | 750 |
| Operating altitude (km) | 200-4000 | 1000 - 2000 | 250 - 3500 |
| Record capacity (bits) | - | $\sim 10^8$ | $2 \times 10^9$ |
| Range resolution (m) | 23,000 - 70,000 | 1000 - 2000 | 120 - 300 |
| Azimuth resolution (m) | | 1000 - 3000 | 120 |
| Looks | Many | 4 - 10 | 4 - 25 |
| Coverage (%) | 92 | 25 | 95 |
| Incidence angle (deg) | 0 - 5 | 7 - 17 | 15 - 45 |

Figure 2. Comparison of Venus radar missions

| Altitude (km) | Latitude (deg) | Incidence angle (deg) | Range res (m) | Azimuth res (m) | Looks No. |
|---|---|---|---|---|---|
| 250 | +10 | 46 | 120 | 120 | 5 |
| 400 | +23, -3 | 42 | 125 | 120 | 6 |
| 600 | +46, -26 | 36 | 135 | 120 | 7 |
| 1000 | +62, -42 | 28 | 170 | 120 | 8 |
| 1750 | +83, -63 | 19 | 250 | 120 | 9 |
| 2100 | +90, -70 | 17 | 260 | 120 | 10 |

Figure 3. SAR performance

The sharing of the rigidly mounted high-gain antenna (HGA) means frequent turns of the spacecraft for mapping and communications with Earth, along with star sighting for navigation. This sequence is repeated each 186 minutes, as shown in Figure 4.

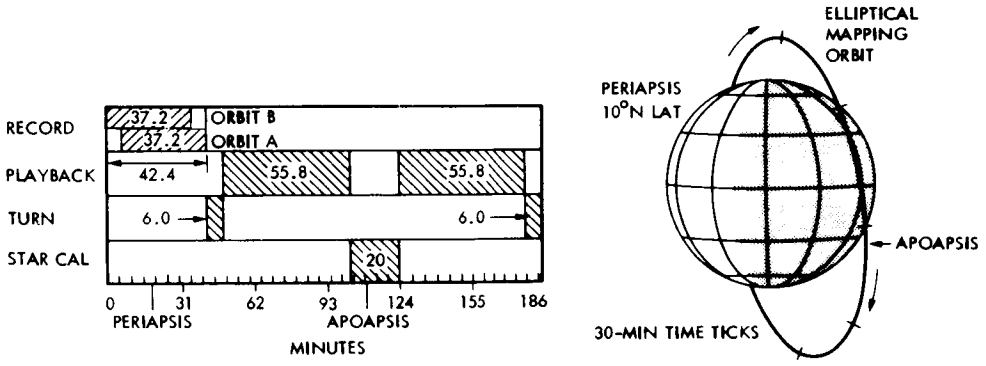


Figure 4. Mapping timeline and orbit geometry

Because a great deal of redundant data is acquired near the poles, alternate passes are biased north (orbit A) or south (orbit B). The spacecraft accomplishes the turns with the required high accuracy through a three-axis stabilized gyro system. Even with all the turning, very little consumable liquid propellant is used which would limit the mission life.

The spacecraft including high-gain antenna, is an assembly of many parts from previous planetary missions, mainly Galileo and Voyager, while the radar is new, designed and built by Hughes Aircraft Corporation of El Segundo, California, under contract to JPL.

# IV. SYSTEM DESIGN

The inherent high data rate of the SAR system must be reduced to satisfy the fixed data rate constraint imposed by the flight hardware. As shown in Figure 5, the radar employs a "burst mode" data collection scheme. The burst mode is a time domain data reduction method in which the transmitter is turned off periodically. The duration of the burst (i.e., the "on" time of the transmitter) determines the resolution, and the ratio of the burst period to the full operation duration determines the number of looks. This figure also shows the methods used to reduce the high instantaneous data rate. The echo is quantized initially to eight bits in two channels (inphase and quadrature) at the radar bandwidth of 2.26 MHz. This data is then passed through the Block Adaptive Quantizer (BAQ), discussed later, which reduces the data by a factor of four. The data is then buffered by the burst-on factor and sent at a constant rate to the spacecraft, which records the data. Later in the orbit, the recorded data is played back at a slower rate for transmission to Earth.

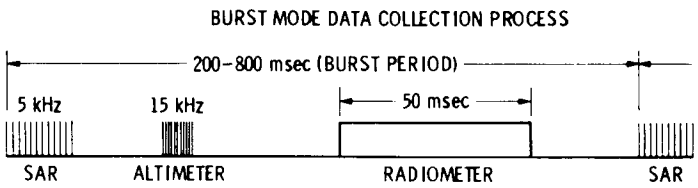


INSTANTANEOUS DATA RATE (BITS / SAMPLE x CHANNELS x SAMPLE RATE)

$8 \times 2 \times 2.26 \times 10^6 = 36.2 \times 10^6$ BITS/SEC

USE BLOCK ADAPTIVE QUANTIZER (INSTANTANEOUS DATA RATE x BAQ FACTOR)

$36.2 \times 10^6 \times \frac{2}{8} = 9.05 \times 10^6$ BITS/SEC

BUFFER INTERPULSE AND BURST (REDUCED DATA RATE x BURST DUTY FACTOR)

$9.05 \times 10^6 \times 0.088 = 0.806 \times 10^6$ BITS/SEC

WITH 37.2 min RECORD AND 112 min PLAYBACK (AVERAGE RATE TO RECORDERS x RECORD TIME/ PLAYBACK TIME)

$0.806 \times 10^6 \times \frac{37.2}{112} = 0.268 \times 10^6$ BITS/SEC

Figure 5. Burst mode process and data rate calculation

The above reduction in data rate had to be accomplished without significant loss of image quality. SAR image quality can be described by five parameters: looks, spatial resolution, amplitude resolution, signal to noise ratio (SNR), and incidence angle. These parameters are not independent and a balance must be achieved to satisfy all these requirements within the mission constraints.

## A. Looks

The "looks" in a SAR system are needed to reduce the coherent, or speckle, noise associated with images derived from coherently-illuminated sources. The looks are independent observations and are generally produced by frequency-domain filtering which reduces the azimuth resolution by a factor equal to the number of looks. For VRM SAR the looks are taken by using each burst of SAR data for a single look.

B. Spatial Resolution

The range (across-track) and azimuth (along-track) resolutions for a SAR are individually selectable, and both are independent of range to the target. The range resolution is determined by the transmitted bandwidth. The azimuth resolution is independent of radar bandwidth and is determined by the length of the "synthetic aperture" created while moving past a target.

C. Amplitude Resolution

The amplitude resolution of a SAR system is the ability to produce an output image with amplitude proportional to the radar backscatter coefficient of the surface. The system must have sufficient accuracy and dynamic range to satisfy rather stringent science requirements. A large dynamic range is associated with a large number of bits per sample, but since the data rate is of critical importance here, a new method was employed to achieve large dynamic range while using fewer bits, the "Block Adaptive Quantizer" (BAQ). This approach yields a larger dynamic range by first quantizing to a large (8) number of bits, and then selecting the most significant bits (2) for recording. The "significant bits" are determined through a block "threshold detector" which preserves a portion of the amplitude information in the original signal. The threshold information is combined with the selected bits in the ground processor to reconstruct the original data as accurately as possible. Figure 6 shows this process for low and high signals. One negative aspect of the BAQ and burst mode is the need for a memory in the radar of sufficient size to contain all the bits from one complete burst so that a constant rate of data is sent to the spacecraft recorders.

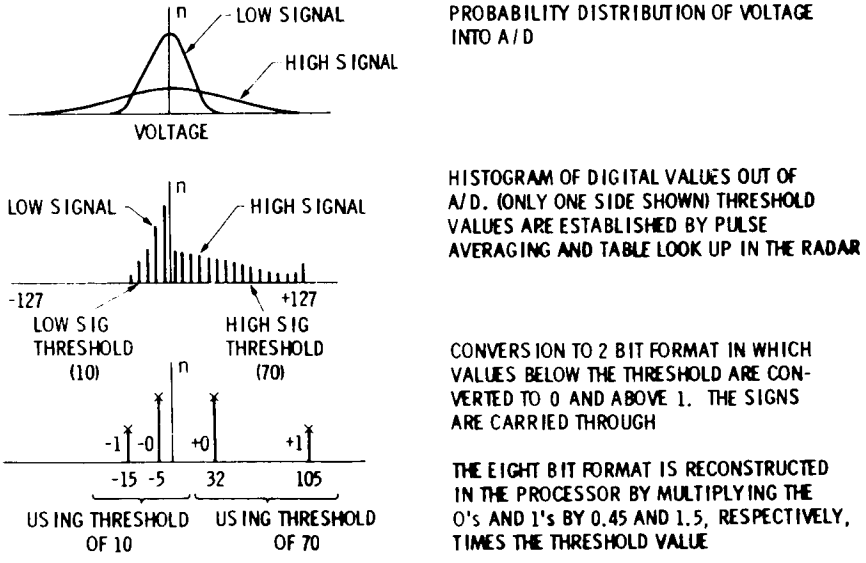


Figure 6. Block adaptive quantizer operation

D. Signal to Noise Ratio

The thermal signal to noise ratio (SNR) for the system was chosen to be 8 dB based upon several simulation studies of images at various SNR's and quantization levels using real SAR data. For a 2-bit quantization level and more than four looks, higher values of thermal SNR were difficult to discern and lower values degraded the images. The system SNR which includes the sum of all noise contributors such as thermal noise, ambiguities, saturation and quantization noise, noise associated with the processor, and link error noise effects is about 5 dB in the output image.

## V. RADAR SYSTEM

The radar system is comprised of the radar flight equipment, the radar data processing subsystem, and those elements in the Spacecraft Flight System, the Deep Space Network, and the JPL Mission Operations System that are involved in uplink command and control and downlink transmitting and recording of the radar data stream. The radar flight equipment consists of the sensor subsystem and the altimeter antenna subsystem. Figure 7 illustrates the spacecraft system and the radar system.

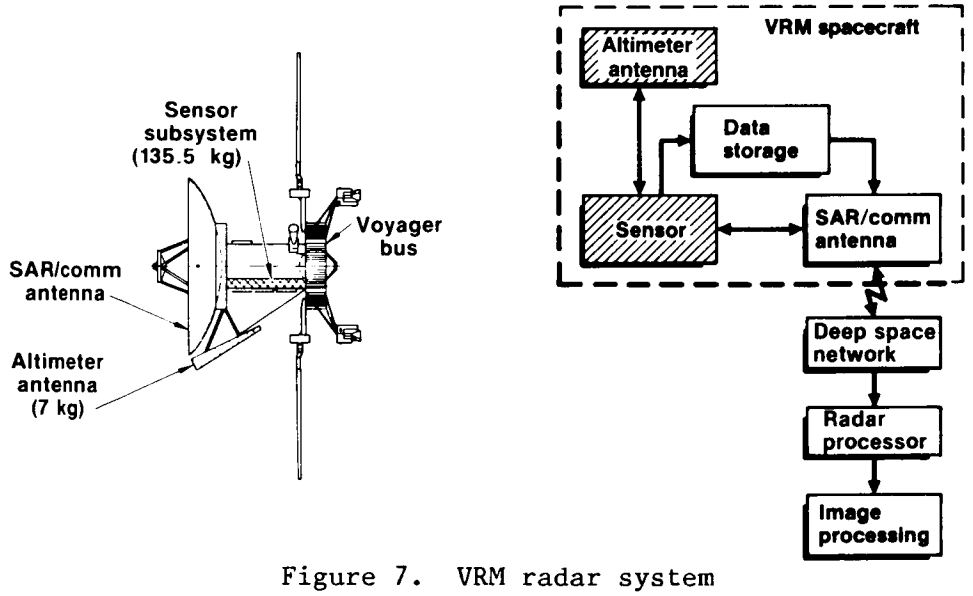


Figure 7. VRM radar system

The VRM spacecraft, a modified Voyager bus, transports the sensor subsystem and antennas along an interplanetary trajectory. It then inserts itself into a 3.2-hour, nearly polar, elliptical orbit around Venus, with a 250 km periapsis altitude at 10 deg north latitude. Mapping commands, generated on the ground, are relayed to the sensor subsystem by the spacecraft command and data subsystem. The sensor subsystem operates in a mapping mode up to an altitude of 2200 km (degraded operation to 3500 km) sending radar data containing SAR, altimeter, and passive radiometer data to the spacecraft tape recorders for storage. During the remainder of the orbit (near apoapsis), the spacecraft reorients itself toward Earth, and the radar data and engineering telemetry are transmitted to the Deep Space Network (DSN) via the same 3.7-meter parabolic high-gain antenna (HGA) used for mapping.

Preliminary ground processing removes overhead data added by the spacecraft, performs initial decoding, and provides the radar processor the radar data generated by the sensor subsystem along with ancillary data. The radar data are subsequently processed into image data records. The altimeter and radiometer data products are generated by the Multimission Image Processing Laboratory at JPL which also mosaics the image data records from each mapping pass into large maps.

## A. Radar Flight Equipment

The sensor subsystem implementation blends many electronic domains including dc power conversion, microwave pulsed power, low noise microwave amplification, RF and video amplification, analog-to-digital conversion, coding, and digital data formatting, and employs many digital logic families including ECL, Schottky, low power Schottky, and CMOS. The sensor subsystem mounts to the spacecraft in one mechanical assembly. Subsystem electrical interfaces with the spacecraft include power, command, telemetry, radar transmission, RF digital reception, and the radar data stream.

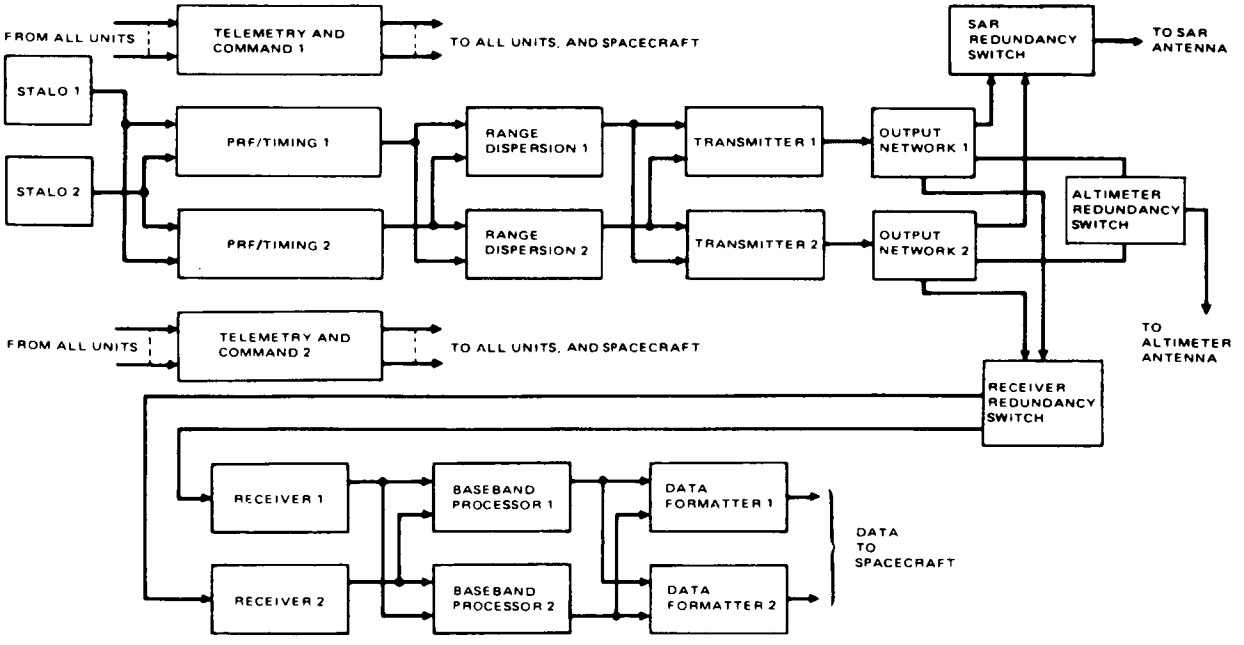


Figure 8. Sensor subsystem

The sensor subsystem is partitioned into the units shown in the Figure 8 functional diagram. Each unit has clearly defined elements grouped on the basis of similarity of function, electronic discipline, packaging efficiency, redundancy cross-strapping, and power consumption. The sensor subsystem is comprised of redundant, cross-strapped units which are separately testable. All circuit replacement is accomplished at the unit level. The unit functions are shown in Table 2.

Table 2. Unit functions

| | |
|---|---|
| PRF and timing | Generate stable timing and clocks |
| Range dispersion | Generate coded S-band signal |
| Transmitter | Amplify S-band signal |
| Output network | Connect transmitter/antenna/receiver; monitor forward/reverse power |
| Receiver | Amplify low level echos and planet emission; provide first downconversion and gain control |
| Baseband processor | Provide downconversion and digitization to 8 bits |
| Data formatter | BAQ, buffer high-rate radar data and create radar data stream |
| Telemetry and command | Accept and execute spacecraft commands, time; process radar engineering telemetry |

Units are packaged in one or more modules. A unit is defined to be nonredundant; thus two units of each function are flown in the sensor subsystem. Should a unit be removed from the sensor subsystem, the testing can continue using the remaining unit. An exception is the output network unit, which contains single antenna and receiver redundancy select switches. Subsystem test cannot proceed on a backup path if an output network module is removed. Figure 9 shows the sensor subsystem layout. The sensor subsystem mass is 137kg and draws 220 watts (average) during mapping. Sensor dimensions are 1.35m by 85cm by 33cm.

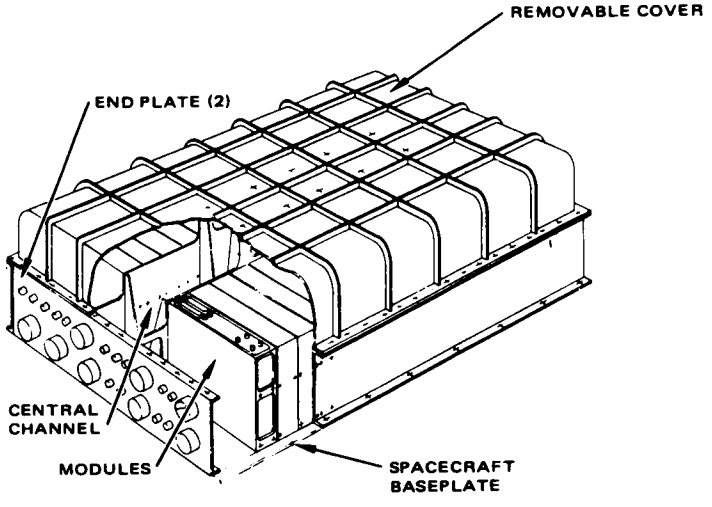


Figure 9. Sensor subsystem conceptual external view

The Stable Local Oscillator (STALO) is the heart of the subsystem. It is the source of all clocks and timing pulses used by the subsystem and serves as the input to the frequency synthesizer that produces the S-band carrier. The stability of the STALO is specified such that the entire system is coherent over a real aperture period. All clocks and timing signals are derived from the STALO by the PRF/Timing unit and distributed to the appropriate units.

The STALO frequency (72.27 MHz) is multiplied by 33 in the range dispersion unit, where a biphase code modulates the S-band carrier. The encoded S-band signal (2385 MHz) is gated into the transmitter, where it is amplified to a 350 watt peak power S-band pulse. The pulse is 26.5 μsec long and consists of a 60:1 code, each chip being .442 μsec. It is the chip time (bandwidth) that determines the radar range resolution.

There are two transmitter output ports, one to the altimeter antenna, the other to the HGA. When imaging, the output network connects the transmitter output to the HGA during the high-power transmit time and steers the target echo power captured by that antenna to the receiver. During the altimeter function, the output network connects the transmitter altimeter port to the altimeter antenna and directs the echo energy to the receiver.

The receiver, which has a high power switch to protect it from leakage during the transmit time, amplifies the S-band echo power and provides, by commandable gain control, the radar sensitivity. The echo information is then downconverted to IF and amplified further. A second downconverter in the baseband processor generates in-phase and quadrature signals, which are digitized after differentially accounting for the dc restore level. The resultant digital words are sent to the data formatter unit which rate buffers the data.

After combining the SAR imaging data with altimetry data, time tags, and format headers, the data formatter provides the data stream, which is clocked across the spacecraft interface in two parallel streams at a 403.2 Kbps rate each.

Within the telemetry and command unit, spacecraft commands are distributed by the command element and engineering data are digitized, buffered, and sent to the spacecraft by the telemetry element.

The sensor also collects radiometer samples every burst cycle, to obtain passive radiometric measurements of the planet's surface brightness temperature. PRF/Timing logic creates a radiometer sample gate and reset/dump signal, and adjusts the commandable receiver gain during the radiometer integration period. Within the receiver, a separate integrate-hold-dump circuit is provided for the radiometer samples.

Radiometer and calibration measurement samples are interleaved, with one or the other taken every burst. Calibration is normally accomplished by a radiometer measurement of the receiver protect switch. Occasionally, cold sky observations may be taken. Radiometric measurement data are digitized by a 12-bit A/D converter and sent to the data formatter, where they are included with the radar burst header.

## VI.- DEVELOPMENT STATUS

Development models of the sensor and altimeter antenna subsystem are in test at this writing and construction of the flight model sensor subsystem is in process. These items will be completed and delivered to spacecraft integration in May 1986.

## VII. CONCLUSIONS

The Venus Radar Mapper mission presents challenging radar design requirements which have been satisfied through the use of an existing Voyager antenna for the SAR function and newly developed sensor and altimeter antenna subsystems. The sensor uses a block adaptive quantizer to maximize science data return with minimum transmission of radar data back to earth.

## ACKNOWLEDGMENTS

The Venus Radar Mapper mission is funded by the Jet Propulsion Laboratory, Pasadena, California, under funding by the United States National Aeronautics and Space Administration, Washington, D.C. The sensor subsystem and altimeter antenna subsystem are developed by Hughes Aircraft Company, El Segundo, California, under contract to Jet Propulsion Laboratory.

## REFERENCES

[1] D. M. Hunten, L. Colin, T. M. Donahue, and V. I. Moroz, VENUS, Tucson, Arizona, The University of Arizona Press, 1983.

[2] J. H. Kwok and S. S. Dallas, "Mission and Trajectory Design for a Venus Radar Mapper Mission," AIAA 21st Aerospace Sciences Meeting, Reno, Nevada, 10-13 January 1983.

[3] W. T. K. Johnson, "The Venus Radar Mapper: Radar System Design for Highly Elliptical Orbits," Int. Geosciences and Remote Sensing Symposium, Strasbourg, France, 1984.

[4] E. Cutting, J. H. Kowk, and S. H. Mohan, "The Venus Radar Mapper (VRM) Mission," AIAA 22nd Aerospace Science Meeting, Reno, Nevada, 9-12 January 1984.

[5] S. S. Dallas, "The Venus Radar Mapper Mission," XXXVth IAF Congress, Lausanne, Switzerland, 7-13 October 1984.

# SPACEBORNE IMAGING RADAR PROJECT

Neil Herman
Jet Propulsion Laboratory, California Institute of Technology
Pasadena, California

In June of 1985 the Project Initiation Agreement was signed by the Jet Propulsion Laboratory and the NASA Office of Space Science and Applications for the Spaceborne Imaging Radar Project (SIR). The thrust of the Project is to continue the evolution of synthetic aperture radar (SAR) science and technology developed during SEASAT, SIR-A and SIR-B missions to meet the needs of the Earth Observing System (EOS) in the mid 1990's. As originally formulated, the Project plans were for a reflight of the SIR-B in 1987, the development of a new SAR, SIR-C, for missions in mid 1989 and early 1990, and the upgrade of SIR-C to EOS configuration with a qualification flight aboard the shuttle in the 1993 time frame (SIR-D). However, the loss of the shuttle Challenger has delayed the first manifest for SIR to early 1990. This delay prompted the decision to drop SIR-B reflight plans and move ahead with SIR-C to more effectively utilize this first mission opportunity.

The implementation plan calls for combined SIR-C/XSAR mission on the Space Shuttle, presently scheduled for January 1990, and again in July 1990. The SIR-C, developed by NASA/JPL, will consist of L and C-band SARs. The XSAR operating at X-band will be developed by the Federal Republic of Germany (BMFT/DFVLR) in collaboration with Italy (CNR/PSN). Integration of the three SAR units and interfacing with the appropriate shuttle support teams are the responsibility of JPL. Separate, but coordinated, Announcements of Opportunity and Science Team Selection are planned for SIR-C and XSAR. There will be joint Science Team planning and mission operations. The schedule of SIR-C/XSAR activities is presented in Figure 1.

The SIR-C configuration is illustrated in Figure 2. The 12 x 4.1 meter antenna is a distributed, active element array for L- and C-band. There are 18 L-band panels each containing 14 transmit/receive (T/R) units and 18 C-band panels each containing 28 T/R units. The XSAR antenna is a waveguide array with vertical polarization. The baseline performance requirements are well documented in the SIR-C Science Working Group and EOS SAR Panel Reports. A summary of major design drivers common to SIR-C and EOS are:

- Bandwidth - 10 or 20 MHZ
- Polarization - H, V, HV, VH (any combination)
- Incidence angle - 15 to 60 degrees (selectable)
- Min. swath - greater than 15 km
- Wide swath - greater than 150 km (scan mode)
- Calibration - $\pm$ 3 dB absolute
  - $\pm$ 1 dB relative
- Recording - 5 channels at 45 Mbps

The major SIR challenges derive from the requirement for development of a SIR-C design which can be utilized on EOS. Some of the more significant comparisons between SIR-C and EOS needs follow:

| | | SIR-C | EOS |
|---|---|---|---|
| o | Performance altitude | 250 km | 500 - 800 km |
| o | Reliability | 2 weeks | 2 - 15 years |
| o | Processing | 500 hrs/45Mbps in 1 year | 45Mbps continuous with keep up |
| o | Mission operations and data distribution | Labor intense | Automated and user interactive |

To meet the higher altitude performance demands of EOS, the distributed antenna will be expanded from 12 to 20 meters. Figure 3 is illustrative of the SIR-C and EOS performance with comparisons to that of SEASAT, SIR-A and SIR-B.

The distributed element antenna design is ideally structured to gracefully degrade with multiple element failures. This fact coupled with redundancy in all other SIR-C subsystems provides the reliability base needed for EOS. The following are examples of design fault tolerance:

| | | |
|---|---|---|
| o | Random T/R unit failures of 10% | - 1dB gain loss and 2 dB in peak sidelobes |
| o | 1, 2, or 3 panel failures | - 0.5 dB, 1.02 dB, 1.58 dB one way loss |
| o | Failure of RF feed, charging power supply, receiver | - loss of one polarization |
| o | Failure of controller, stahlo, calibration unit, exciter | - block redundant, loss of time to switchover |
| o | No single component failure causes loss of both L&C SAR | |
| o | EOS provides modular replacement/ repair in two year intervals | |

The Advanced Digital SAR Processor (ADSP) developed under sponsorship from the NASA Office of Aeronautics and Space Technology (OAST) will complete engineering model performance tests in the summer of 1986. This processor can handle the 45 Mbps data in real-time. It will also be possible to simultaneously process H, V, VH, and HV channels to maintain uniform processing parameters and simplify registration to support polarization utilization investigations. There are numerous special products that must be handled off line, for example: precision calibration, geocoding, terrain

correction, polarization synthesis, etc. While this is satisfactory for SIR-C, EOS needs more time efficient output of special products. It is anticipated that EOS will also need an onboard expert system to aid in the massive data management problems. The use of an onboard processor has a high potential for satisfying this need. The continuation of a strong research and advance development program by NASA OAST and Information Systems Offices is urgently needed to support these developments in preparation for EOS.

The SIR-C instrument control center concept is presented in Figure 4. The basic elements of this system were developed in SIR-B and, as noted, require only subsets to be further modified for SIR-C. This approach using segmented, micro-computer based software elements can be readily updated for EOS. It is envisioned that these elements will be consolidated into one automated planning center for instrument control. Expansion of the control center to provide capability for user interaction, both in data acquisition and data distribution, is critical to EOS. A proposal is in development to add a telescience experiment to SIR-C. The concept is shown in Figure 5. Besides the real real-time control and data access capabilities of the telescience station, the real-time interaction through the data catalog and image processor would provide direction to the special products generation process.

The SIR Project provides significant advancements needed for effective and efficient EOS SAR application. In summary, these are:

- Opportunities for scientific investigations with multiple frequencies, polarizations, and incidence angles.
- A core instrument upgradable for EOS use.
- Operational real-time processing.
- Evolvable instrument control technology.

Important steps in the SAR evolution to EOS remain dependent on supporting research and technology sponsorship. In summary, these are:

- Development of techniques to incorporate special products into the real time processing cycle.
- Development of onboard processing technologies for use in end-to-end data management.
- Development of telescience techniques for user mission optimization and effective data acquisition.

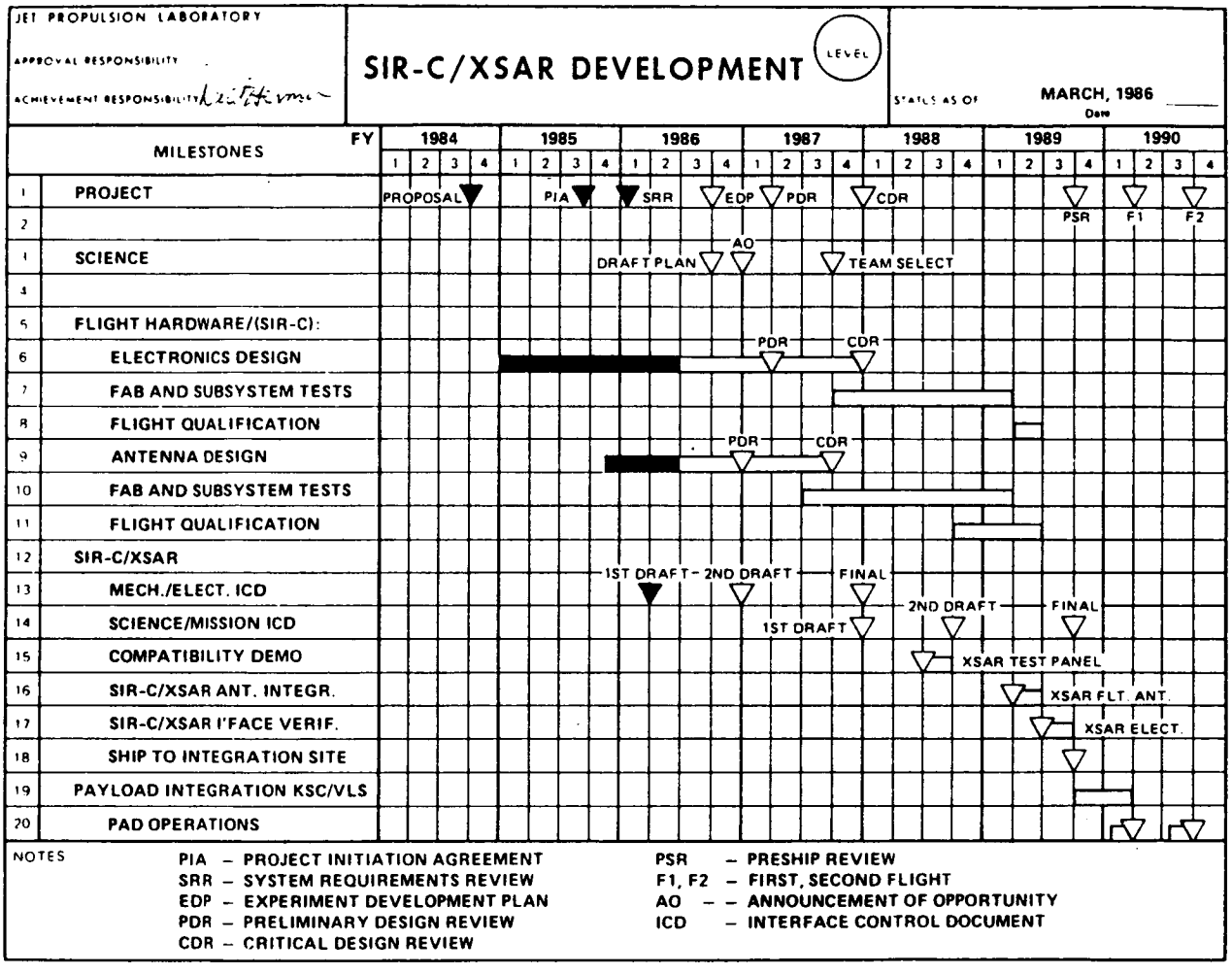


Figure 1. SIR-C/XSAR Development

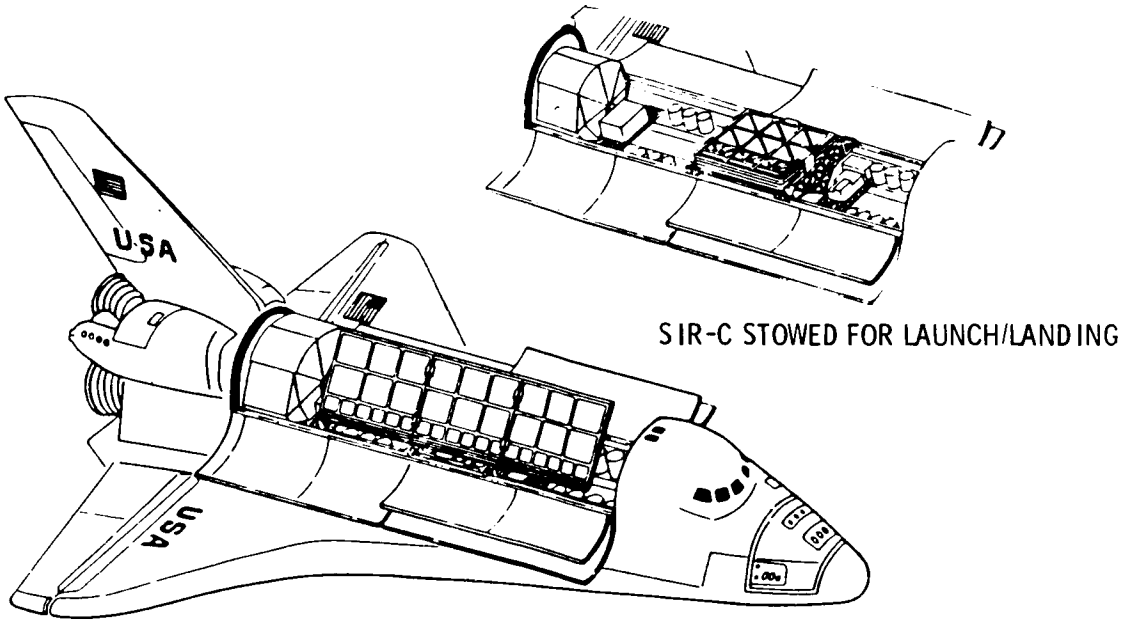


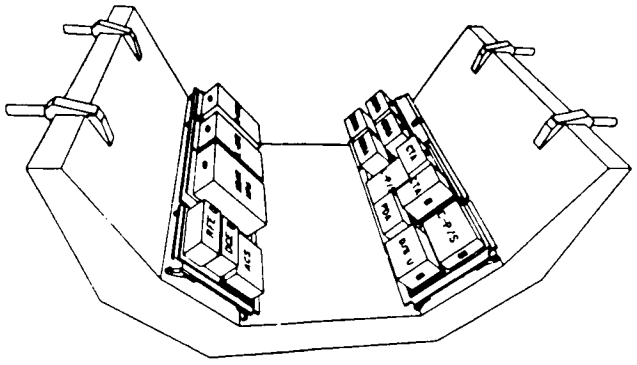

**SIR-C/X SAR PALLET LAYOUT**

Figure 2. SIR-C Configuration

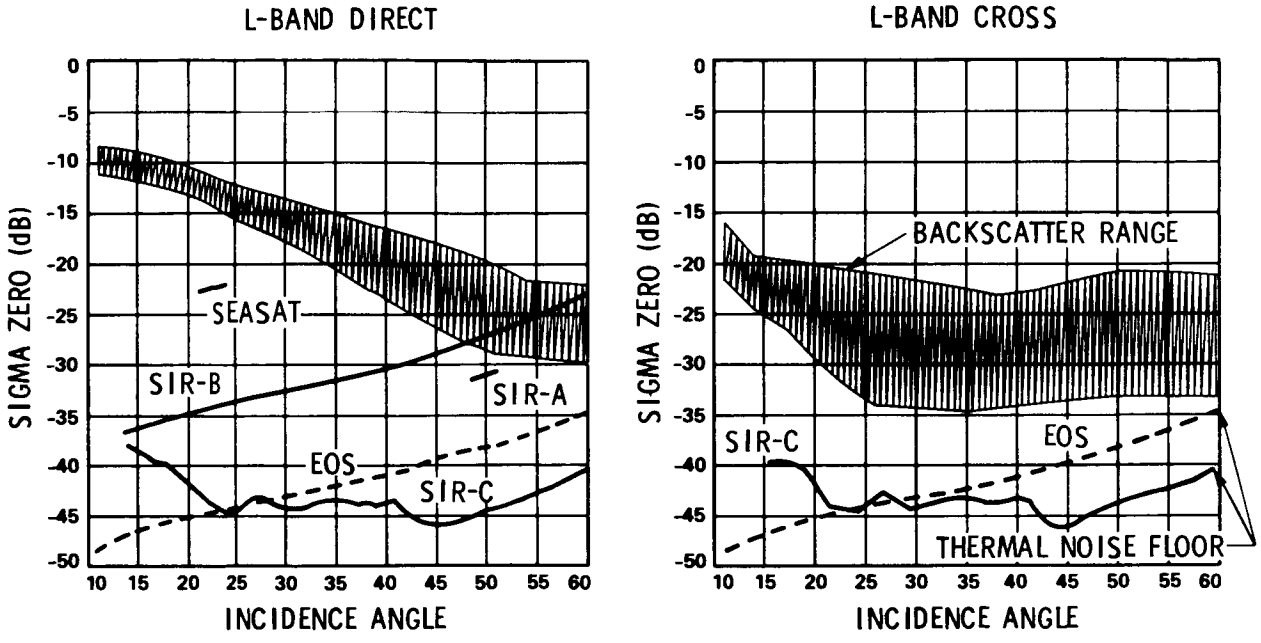


Figure 3. SIR-C Sensitivity, Geologic Targets

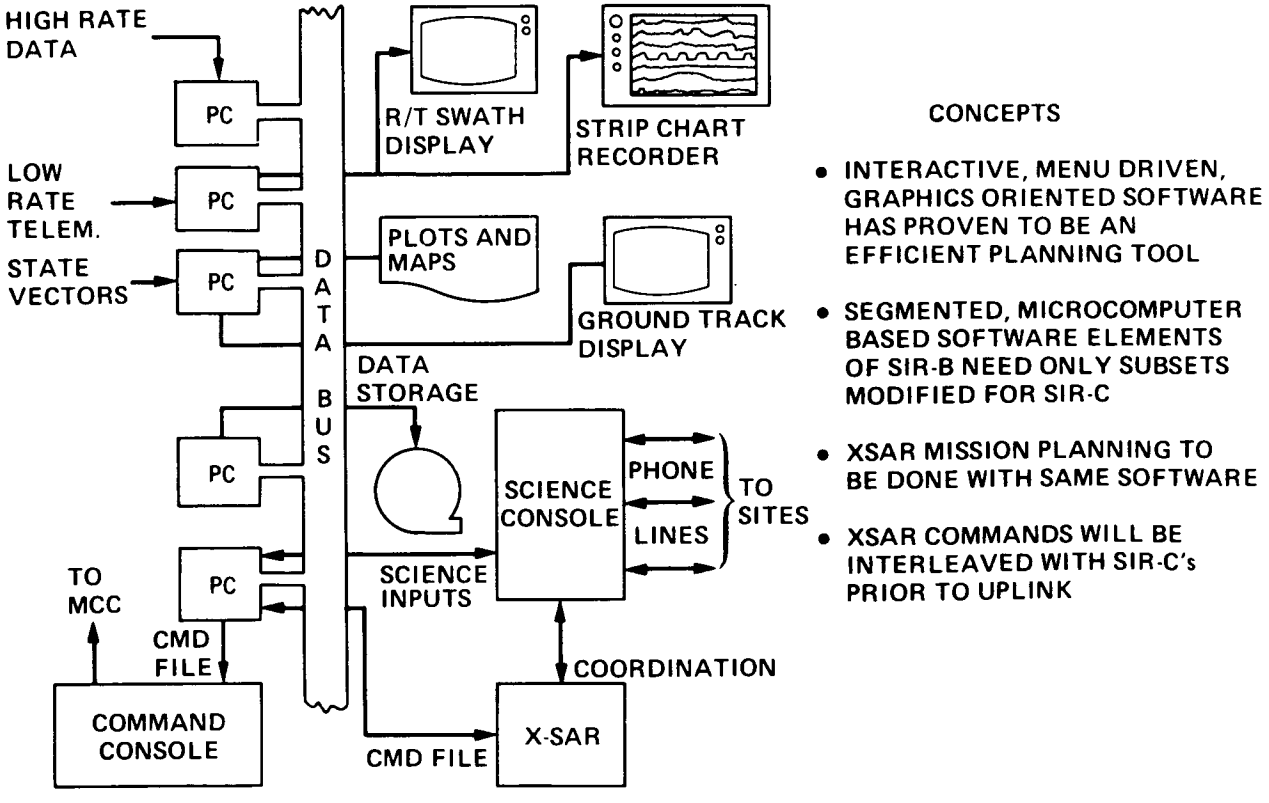


Figure 4. SIR-C Instrument Control Center

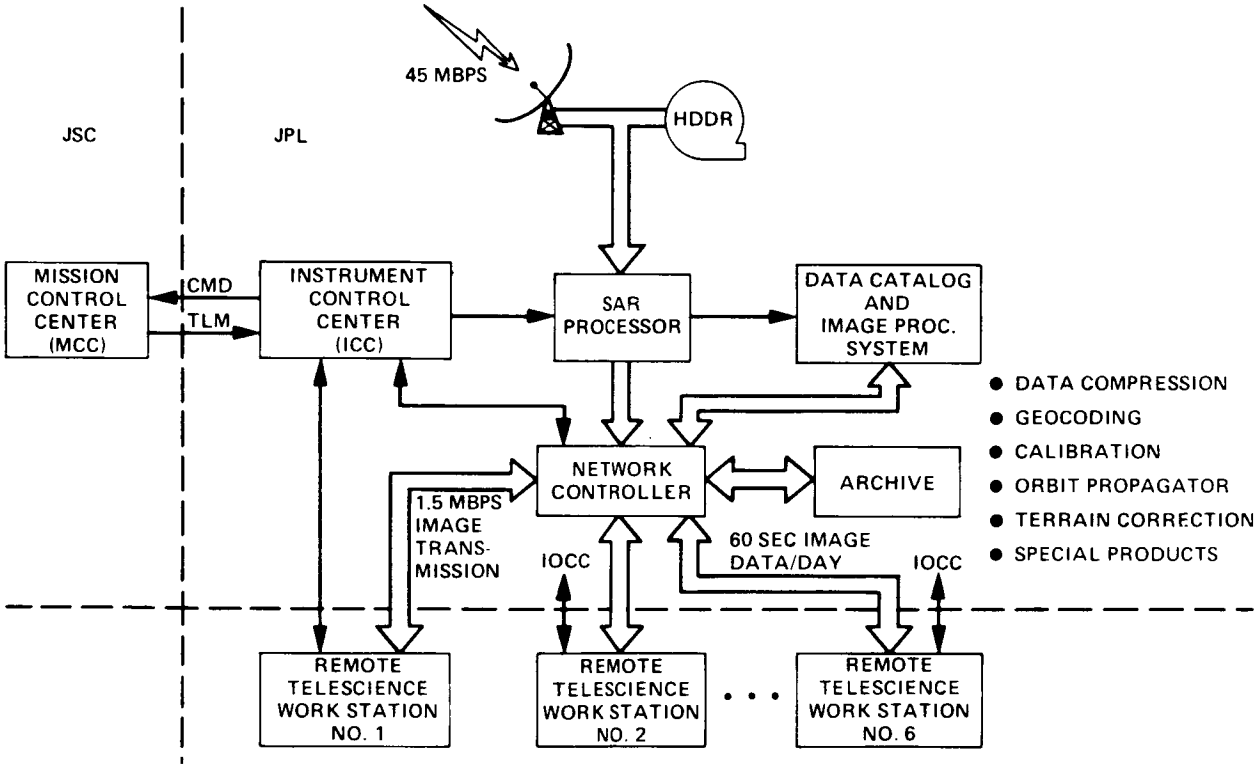


Figure 5. SIR-C Telescience Testbed Concept

# AN ALTERNATIVE MULTI-MODE SAR FOR RADARSAT

R. K. Raney
RADARSAT Project Office
Ontario, Canada

## I. INTRODUCTION

The RADARSAT project was asked by the Canadian government in the spring of 1986 to design for reduced costs and increased radar performance as compared to the well-known baseline design (Ref. 1). Both the Project Office and Canadian industry (lead by SPAR Aerospace of Montreal) have undertaken to meet this request, with a proposal to Cabinet to be submitted in the fall of 1986.

Innovation in partnerships, funding and business plans, and in SAR configuration will be required to achieve a programme with full government approval.

This paper outlines one alternative SAR concept which is under consideration for a revised RADARSAT configuration. The radar system described uses two frequencies (C&L band) over four possible modes: near range swath; far range swath; wide swath; and high resolution. Good sensitivity, resolution, and coverage are obtained with modest power and data rates. The antenna systems are relatively simple. Indeed, no break-through technological developments are needed. The design allows several mode combinations for simultaneous data collection or performance enhancement. The principal parameters are described in Table 1. A nominal mean altitude of 700 km is assumed.

## II. SYSTEM HIGHLIGHTS

A two-frequency SAR system is proposed, having a high resolution mode and a wide swath mode. Like polarization is required, either HH or VV being acceptable. The frequencies suggested are C&L. Two nominal incidence angles of 21° and 49° are offered. These and related design features deserve some comment (Ref. 2). Derived specifications assume system losses of 5 dB, antenna losses of 4 dB (one way), and a noise figure of 2 dB.

### A. Incidence Angles

From a careful review of the user requirements for incidence angle, it is clear that two incidence angle regions are needed, steep and shallow. Unfortunately, it is not possible to satisfy users by a single compromise with an intermediate angle, for such a choice leaves virtually everyone unsatisfied. Indeed, the users have gone on record as prefering two incidence angles as the dominant specification, with other parameters such as swath width to be sacrificed if need be (Ref. 3, Table 5). The current design attempts to be responsive to this requirement.

B. Frequency

The requirements favour C-band, with L-band desired as a parallel or back-up channel. The possibility of X-band, although appealing from the standpoint of air-borne data experience, does not seem feasible within the current state of the art. Recent work suggests that a frequency lower than L-band might be desirable, such as about 50 cm (in P band). The baseline alternative presented here is at C & L band. If two frequencies are available, they should be capable of simultaneous operation over the same swath coverage.

C. Wide Swath Mode

Wide swaths are more easily obtained at near range than at far range. Pressing swath width usually implies relatively more energy received from azimuth and/or range ambiguities. These two facts suggest that a wide swath mode be implemented at near range, and with somewhat relaxed range ambiguity restraints and sensitivity requirements.

Use of antenna rapid beam switching to synthesize wide swaths (Ref. 4) requires a comparable reduction in resolution. By use of one antenna pattern, and by accepting the possibility of larger range ambiguities, a rather wide swath can be achieved with no implied loss of resolution and with a rather simple antenna design.

D. Resolution

Most users have been influenced by positive experiences with SEASAT and the SIR series of radars. As a result, "everyone" wants about 25m x 25m x 4 look data. For many applications, however, a lower resolution (coupled with wide swath) is desirable. There is some demand for higher resolution data (with adequate looks), even though the swaths may have to be reduced to achieve it.

E. Image Quality

There is a uniform chorus of demand for image quality in a space SAR to be at least as good as that of SEASAT. This impacts all aspects of system design, including specifically sensitivity, resolution, and coverage. The example design described here attempts to respect reasonable allowances in this area. The system should incorporate calibration references and standards.

F. Mode Selection

Any pair of normal swath modes should be available, such as Near Swath (C) and Near Swath (L). To accommodate simultaneous (near and far swath) modes, the PRF should be chosen to be identical for both swath windows, and transmissions for L & C must be synchronized and simultaneous. Any two high resolution modes can be operated together, including two at the same frequency. Four high resolution channels are available using both C & L band, and using all four receivers, assuming conventional redundancy in SAR implementation.

## III. HIGH RESOLUTION MODE

In order to achieve substantial improvement in resolution from a space radar constrained either by ambiguity considerations or data rate, some sacrifice in other performance parameters is mandatory. Swath width, system sensitivity, and along track image size are usually given up to achieve high resolution. A novel high resolution mode is proposed herein that minimizes both performance compromises and system complexity.

The logic of the design is approached as follows. High resolution may be achieved with an un-steered antenna using its full aperture if azimuth looks are exchanged for full azimuth resolution. Image quality can be maintained if looks are taken in range rather than in azimuth. High range resolution and range looks together normally imply very large range bandwidth, which if implemented in the usual way would result in a severe loss of SNR, and added restraints on the radar receiver, processor, and data handling.

In the conceptual design suggested here, a full range de-ramp scheme is used to realize the range resolution desired at relatively small cost in system bandwidths and complexity. This method (Ref. 5) depends on a very long linear FM pulse to be generated and transmitted, then used again as the demodulator reference against data from a range gated segment of the return signal. Only a relatively small bandwidth is required of the system after demodulation.

The results of a conceptual design analysis incorporating the deramp approach to high resolution are presented in Table 1. Since the design proposed is unusual, some aspects are elaborated here.

The full de-ramp approach requires additional performance of signal generation, transmission, demodulation, and timing control. For the design baselined here, a pulse 283 microseconds long of approximately 85 MHz bandwidth and linear FM rate of 0.3 MHz/microsec must be generated and transmitted. The same average power and PRF as in the normal modes can be used. On receive, a replica is used in demodulation leading to a required video bandwidth of 15 MHz, the same as that already built into the SAR for the conventional near range swath mode. Range gating of the received signal and timing of the demodulator replica to extract a narrow range swath from the far range window (approximately half of which is accessible in this mode) is done by an on-board computer. PRF is controlled as in the normal imaging mode. A continuous strip map is available 10 km wide with resolution better than 8m x 8m and 3 looks. The SNR is good, losing only 3.8 dB relative to the standard far swath image of this design. The bandwidth of the signal to be A/D converted and downlinked is 15 MHz, with a time duration of 233 microseconds. At 4 bits per sample for each of the in-phase and quadrature components, the average data rate is about 25 MBPS, including oversampling factors.

A second channel of high resolution data derived from the same transmission can also be received, digitized, and down-linked. This can be used to extend the effective high resolution swath width to 20 km, or to obtain simultaneous high resolution C & L band data. To receive two channels of one frequency simultaneously of course requires appropriate signal access in the receiver to those signals before the de-ramp demodulators.

If both the receive channels and the redundant receive channels are used, four reception paths are available. These can be used, two per wavelength, to bring the total high resolution swath width imaged to 40 km. The data rate (4 x 25 MBPS) is satisfactory. Adequate short-term storage registers must be provided after the A/D conversion to handle the required merge of four channels into one data stream.

The sensitivity of the radar to phase noise and platform motion increases with better resolution and with longer wavelengths. Likewise, processing complexity increases as wavelength/(resolution)$^2$. Finally, image content with respect to many user requirements is somewhat richer at C-band than at L-band. For these reasons, if only one channel of high resolution were implemented, C-band should be favoured over the longer wavelength. In the design proposed here, high resolution is available at small additional cost in both channels.

## III. CONCLUSIONS

The baseline RADARSAT SAR uses eight (or more) beam positions for a single frequency (C-band) single resolution (30m x 30m x 4 look) 500 watt mean power system. The example conceptual design described in this brief note as an alternative is a two-beam position dual-frequency dual-resolution system with mean power of 360 watts. This radar as described is more responsive to many user requirements, and should be less expensive to realize in full spacecraft implementation. During 1986 RADARSAT will be restructuring its program using these and related ideas together with partnership arrangements to achieve a programme worthy of full government approval.

## REFERENCES

(1) N. G. S. Freeman and L. McNutt, Ocean & Ice Measurements from Canada's RADARSAT, Marine Technology Journal, Special Issue on Satellite Remote Sensing, June, 1986.

(2) R. K. Raney, Advanced Space Platform Radar (a Draft Specification), RADARSAT Project Office, August, 1985.

(3) RADARSAT Mission Requirements Document, Report 82-71, RADARSAT Project Office, Ottawa, Ontario.

(4) Kiyo Tomiyasu, Conceptual Performance of a Satellite Borne Wide Swath Synthetic Aperture Radar, IEEE Transactions on Geoscience and Remote Sensing, Vol. GE-19, No. 2, April, 1981.

(5) W. J. Caputi, Jr., Stretch; A Time-Transformation Technique, IEEE Transactions on Aerospace and Electronic Systems, Vol. AES-7, No. 2, March, 1971.

Table 1. Requirements on space SAR

| | Near swath (C) | Near swath (L) | Far swath (C) | Far swath (L) | Wide (C) | Wide (L) | Hi res (C) | Hi res (L) |
|---|---|---|---|---|---|---|---|---|
| Given specifications | | | | | | | | |
| AZ Resolution (m) | 30 | 30 | 30 | 30 | 30 | 30 | 8 | 8 |
| looks | 4 | 4 | 4 | 4 | 4 | 4 | 1 | 1 |
| R Resolution (m) | 30 (21°) | 30 (21°) | 30 (49°) | 30 (49°) | 30 (21°) | 30 21°) | 8 (49°) | 8 (49°) |
| looks | 1 | 1 | 1 | 1 | 1 | 1 | 3 | 3 |
| Swath width (km) | 112 | 112 | 106 | 106 | 190 | 190 | 10(+10) | 10(+10) |
| Incidence (near, far) | (17°, 26°) | (17°, 26°) | (46°, 51°) | (46°, 51°) | (16°, 31°) | (16°, 31°) | --- | --- |
| nominal | 21° | 21° | 49° | 49° | (26°) | (26°) | 49° | 49° |
| Noise Eq $\sigma_0$ (dB) | -26 | -25 | -28 | -27 | -20 | -19 | -24 | -22 |
| Azimuth ambiguities (dB) | < -22 | < -22 | < -22 | < -22 | < -22 | < -22 | < -22 | < -22 |
| Range ambiguities | < -30 | < -30 | < -20 | < -20 | < -18 | < -18 | < -24 | < -24 |
| Derived specifications | | | | | | | | |
| Average power (W) | 300 | 60 | 300 | 60 | 300 | 60 | 300 | 60 |
| Average data (MB/S) rate (4I, 4Q) | 48 | 48 | 48 | 48 | 96 | 96 | 25(+25) | 25(+25) |
| Antenna length (m) | 15 | 15 | 15 | 15 | 15 | 15 | 15 | 15 |
| Bandwidth of RCVR (MHz) | 15 | 15 | 7.5 | 7.5 | 15 | 15 | 15 | 15 |
| Nominal PRF (Hz) | 1300 | 1300 | 1300 | 1300 | 1300 | 1300 | 1300 | 1300 |

# PRESENT STATUS OF JAPANESE ERS-1 PROJECT

Yasufumi Ishiwada
Earth Resources Satellite Data Analysis Center (ERSDAC)

Yoshiaki Nemoto
Technology Research Association of Resources Remote Sensing System (RRSS)

## I. INTRODUCTION

Earth Resources Satellite 1 (ERS-1) will be launched in the FY 1990 with the H-1 rocket from Tanegashima Space Center. ERS-1 will seek to firmly establish remote sensing technologies from space by using synthetic aperture radar and optical sensors, as well as primarily exploring for non-renewable resources and also monitoring for land use, agriculture, forestry, fishery, conservation of environment, prevention of disasters, and surveillance of coastal regions. ERS-1 is a joint project in which the main responsibility for the development of the mission equipment is assumed by the Agency of Industrial Science and Technology, MITI, and the Technology Research Association of Resources Remote Sensing System, while that for the satellite itself and launching rocket is assumed by the Science and Technology Agency (STA) and the National Space Development Agency (NASDA). In relation to this project, users have maintained a close working relationship with the manufacturers after submitting their requirements in 1984 on the specifications of the mission equipments.

## II. OUTLINE OF ERS-1

Table 1 shows the orbit parameters of ERS-1. The mission equipments which will be fitted on ERS-1 are Synthetic Aperture Radar (SAR), Optical Sensors (OPS), Mission Data Recorder (MDR), and Mission Data Transmitter (MDT).

The salient characteristics of ERS-1 are as follows:

(1) Both the Synthetic Aperture Radar and the Optical Sensors are mounted on the same satellite.

(2) The Optical Sensors have two wave ranges: a visible and near infrared region and a shortwave infrared region.

(3) The Optical Sensors have a capability of stereoscopic imaging.

Table 2 shows the parameters of SAR. It has L-band and H-H polarization, its off-nadir angle is 35 degrees, its spatial resolution is 18m x 18m approximately, and its swath width is about 75 km.

Table 3 shows the provisional parameters of the Optical Sensors.

Figure 1 shows the development schedule for ERS-1. The project started in 1984, and now we are in the process of the basic design. In FY 1990 (around February 1991, to be more specific), we are planning to launch it from Tanegashima Space Center. Figure 2 shows a configuration of ERS-1 in orbit.

## III. USER'S REQUIREMENTS FOR SAR

### A. Off-Nadir Angle

In order to investigate the mutual relationship among the roughness of earth surface, image distortions, and the incident angle to earth surface, we developed SAR simulation software. We examined 3 test areas as representatives of flat, intermediate, and rugged topography with this simulation software, and users came to the conclusion that for ERS-1's SAR system, the desirable off-nadir angle will be between 40 and 50 degrees, and larger than 45 degrees if possible.

We performed a feasibility study about the off-nadir angle of over 40 degrees, and it turned out that we will not be able to secure an adequate S/N as well as S/A with over 40 degrees off-nadir angle because of restrictions of hardware, so we decided to adopt an off-nadir angle of 35 degrees.

### B. Frequency Band

With regard to the selection of frequency band, users wanted L-band for the reason of its greater penetration and greater effectiveness for geomorphological analysis. Also, given the conditions related to electrical power, it was easier to realize SAR with L-band. Thus, there was no problem in deciding to select L-band.

### C. Polarization

With regard to polarization, only one mode is permitted, and an overwhelming majority wanted H-H polarization which is effective in observation of physiography and which was also used by Seasat SAR and SIR-A.

### D. Spatial Resolution

On the question of spatial resolution, many users expressed a strong desire for a spatial resolution of about 20m because that would enable us to discriminate detailed physiographic features, which, in turn, would bring about a wide range of possibilities for data utilization. When the manufacturers examined the feasibilities, it became clear that it is possible to realize a spatial resolution of approximately 18m, so the decision was made for this figure.

## IV. SUBJECTS TO BE DETERMINED

The subjects that we are examining at the present time include:

- How to operate the mission equipments.
- How to select the areas to be observed.
- How many and where to set data receiving stations.

Table 1. ERS-1 orbit (preliminary)

| Item | Descriptions |
|---|---|
| Orbit | Sun synchronous |
| Altitude | 568 km |
| Inclination | 97.7° |
| Recurrent period | 44 days |
| Local time of descending node | 10:30±30 min. |

Table 2. Characteristics of SAR (preliminary)

| Item | Characteristics |
|---|---|
| Frequency | L-band |
| Polarization | H-H |
| Spatial resolution | 18m x 18m (approximately) |
| Swath width | 75 km (approximately) |
| Off nadir angle | 35° |
| Quantization | 3 bit |
| Antenna size | 2.2m x 12m (electrical dimension) |
| Transmitter power (peak) | 1.1 kW |
| Noise equivalent $\sigma_0$ | $\leq$ - 20.5 dB |
| S/A | $\geq$ 14 dB |

Table 3. Characteristics of OPS (preliminary)

| Item | OPS (VNIR) | OPS (SWIR) |
|---|---|---|
| Wave length | 4 bands | 4 bands |
| IFOV | 18m (approximately) | 18m (approximately) |
| Swath width | 75 km (approximately) | 75 km (approximately) |
| Stereoscopic imaging | Base height ratio 0.3 | - |

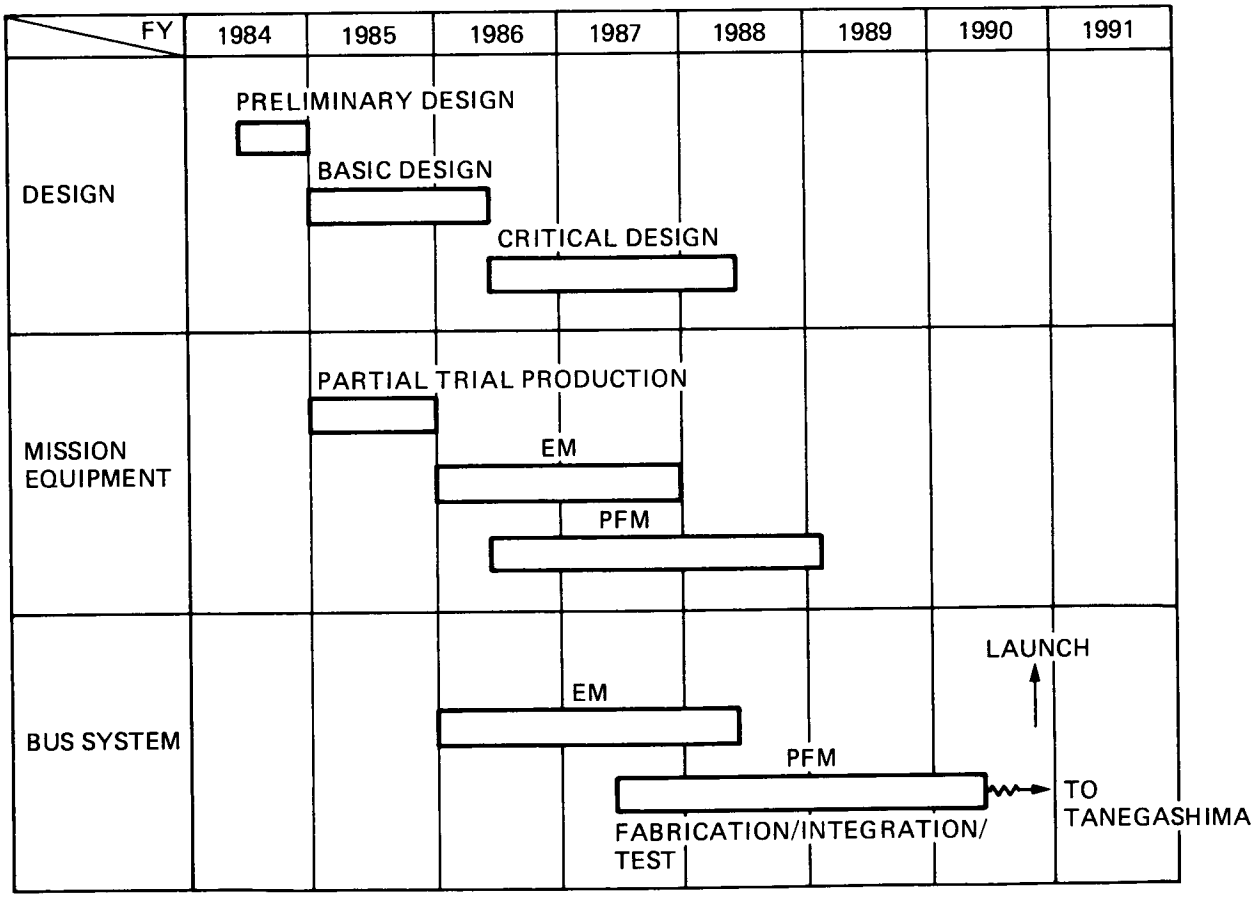


Figure 1. Development schedule of ERS-1

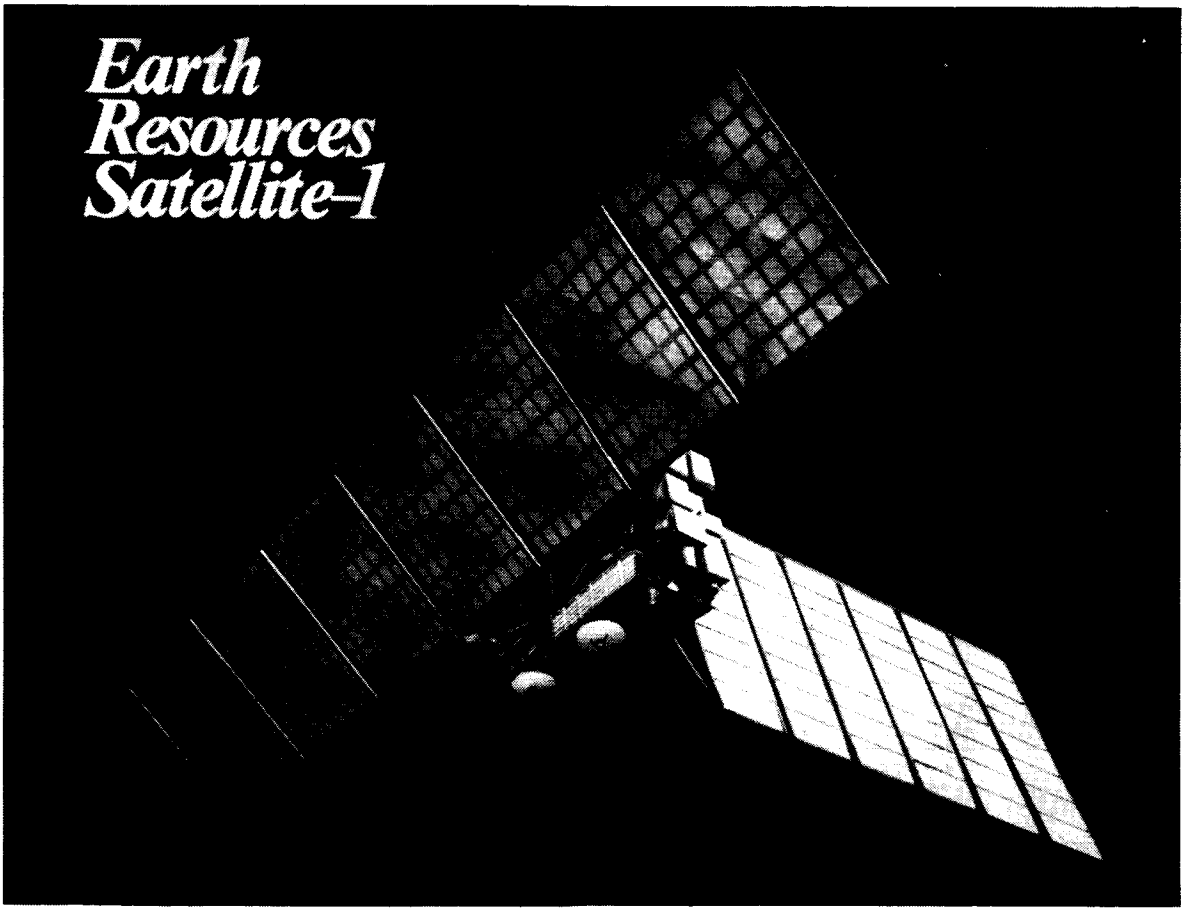


Figure 2. ERS-1 in orbit configuration (preliminary)

# A SCANNING RADAR ALTIMETER FOR MAPPING CONTINENTAL TOPOGRAPHY

T. H. Dixon
Jet Propulsion Laboratory, California Institute of Technology
Pasadena, California

Topographic information constitutes a fundamental data set for the earth sciences. For example, temperature, rainfall, rain runoff, evaporation rate and soil moisture are often critical parameters in botany, hydrology and other ecosystem sciences, and can exhibit a strong dependence on elevation, local slope and slope aspect. In the geological and geophysical sciences, topography combined with gravitational information provides an important constraint on the structure and rheologic properties of the crust and lithosphere. Detailed topography data can also be used to map offsets associated with faulting and to reveal the effects of tectonic deformation. In the polar regions, elevation data form a crucial but as yet largely unavailable resource for studying ice sheet mass balance and ice flow dynamics. The vast Antarctic ice sheet is the largest fresh water reservoir on earth and is an important influence on ocean circulation and global climate. However, our knowledge of its stability is so limited that we cannot even specify whether the Antarctic ice sheet is growing or shrinking. It is clear that there is need for high quality global topography data. A summary of potential applications with their resolution requirements is shown in Figure 1.

Global continental topography is poorly and unevenly known at all but the coarsest resolution (Figure 2). Topographic data of moderate to high resolution is generally available for small, local areas in the form of topographic maps, consisting of hand or machine drawn contours around unevenly distributed spot height measurements. Unfortunately, for many areas coverage is limited, inaccurate or nonexistent. Mountain belts, deserts, tropical rain forests and polar areas, critical sites for a variety of earth science research, suffer from topographic coverage that is highly inadequate, reflecting difficulties in physical access.

Even if topographic maps exist, they may be generated in such a way as to preclude many types of studies. The distribution of horizontal and vertical control points across a map sheet may be quite uneven, resulting in variable accuracy within the map. Even maps which are internally consistent (precise) cannot be assembled to generate good regional coverage. Lack of uniformity for the individual map datum (reference level) compromises the integrity of world topographic data. For example, the United Nations lists 18 separate reference ellipsoids in the world's countries. This lack of standardization effectively limits the scope of any regional or global study where topography is an important parameter.

Regional or global studies require the manipulation of large data sets. These studies benefit greatly from the availability of digital data. Unfortunately this form of topographic data is extremely limited in terms of world-wide coverage. High resolution (1:250,000 or better) digital topography exists only for the U.S., Australia, and Western Europe (Figure 2). The best global coverage has only 18 km resolution. Moreover, digital elevation data



C-2

are usually generated by digitizing contour maps, and hence suffer from the same problems that afflict the original data set, particularly in terms of long wavelength (long spatial scale) integrity.

It is clear that there is a great need for high resolution global topographic data, preferably in a digital, machine-readable format. Such data can only be acquired in a cost effective manner by space-borne techniques.

Several technological approaches now exist for space-based acquisition of topographic data. The most promising of these is a narrow beam, scanning synthetic aperture radar altimeter. This system is capable of generating moderate to high resolution (250-500 m horizontal and 2-5 m vertical) global topographic data. It can be deployed on the space shuttle, promising a relatively low cost experiment. GPS tracking of the shuttle would be required to ensure accurate recovery of the elevation data. Global coverage can be achieved with two or three shuttle flights if at least one flight has a polar orbit.

Conventional wide-beam ("pulse limited") altimeters are not well suited for mapping the high relief continental areas (Figure 3). Reflections from cross-track topography can be confused with the nadir echo, rendering such data difficult if not impossible to interpret. Topographic mapping of the continents with radar altimetry therefore requires small radar footprints to achieve adequate feature resolution. This implies the use of large antennas (large D in Figure 3), high frequencies, or some combination of both characteristics. The proposed system is sketched in Figure 3. The antenna consists of a long rail with an array of individual antenna elements. Scanning of the beam from side to side is achieved by electronic beam steering of the phased array. Swath widths up to 100 km are envisioned. The rail is long in the cross-track direction ensuring a narrow radar footprint in this dimension. Such an antenna, while having good cross-track resolution, has large footprints in the along-track dimension. However, doppler information in the reflected pulse can be used to distinguish the precise along-track position of a particular part of the reflected echo, synthesizing the effect of a large antenna in this dimension. Such synthetic aperture techniques have been widely employed in the more difficult problem of radar imaging. Extension of these techniques to an altimeter is straightforward.

The high effective resolution achieved by this approach satisfies a wide range of scientific requirements, and promises to provide an important global data set.

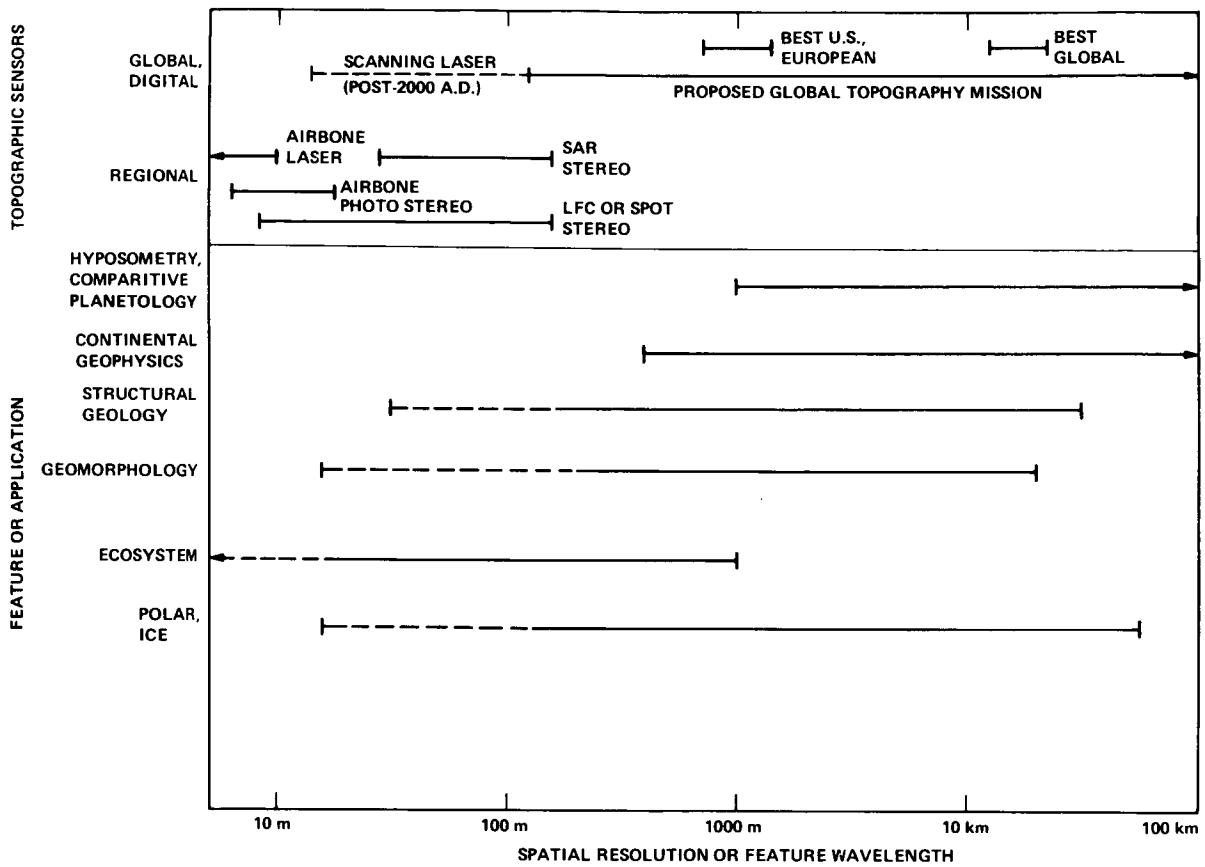


Figure 1. Potential applications of topographic data as a function of feature size (bottom), and various topographic techniques versus their respective resolution (top).

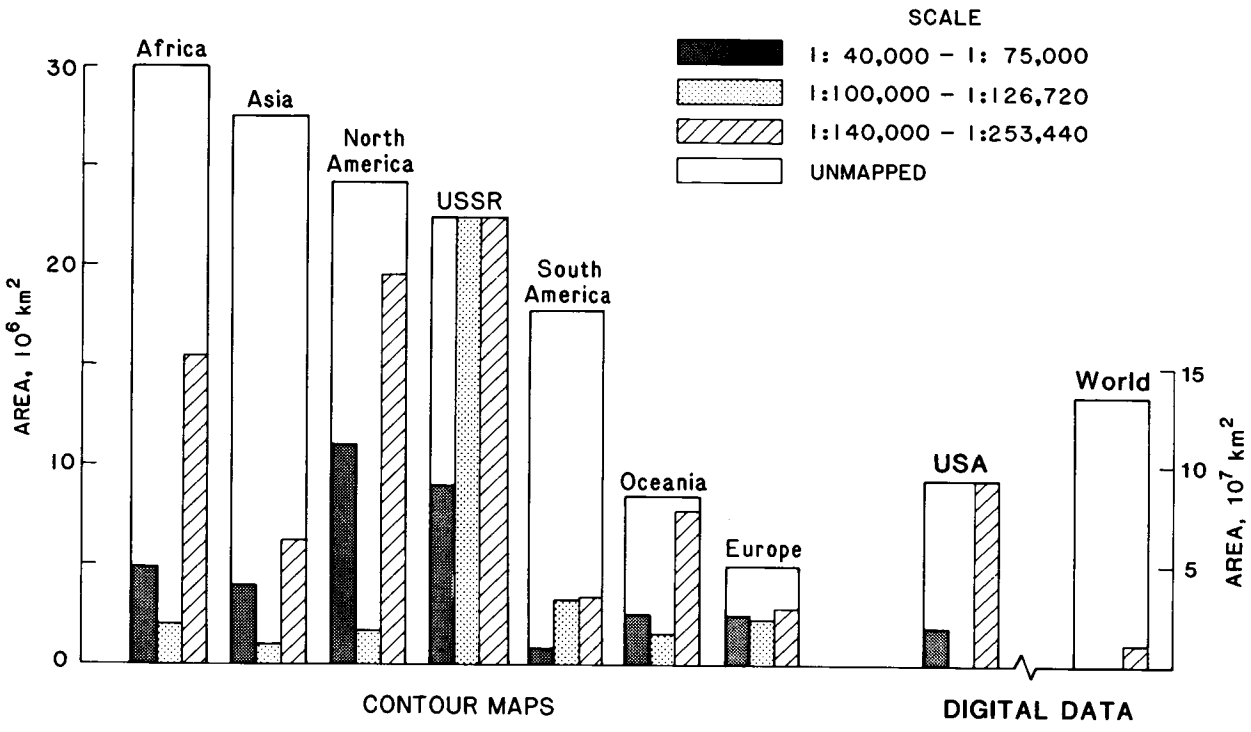


Figure 2. Availability of world-wide topographic data. Only Europe, the USSR, and North America are adequately covered by high-resolution (better than 1:100,000) topographic contour maps. No continent is adequately covered by digital topographic data.

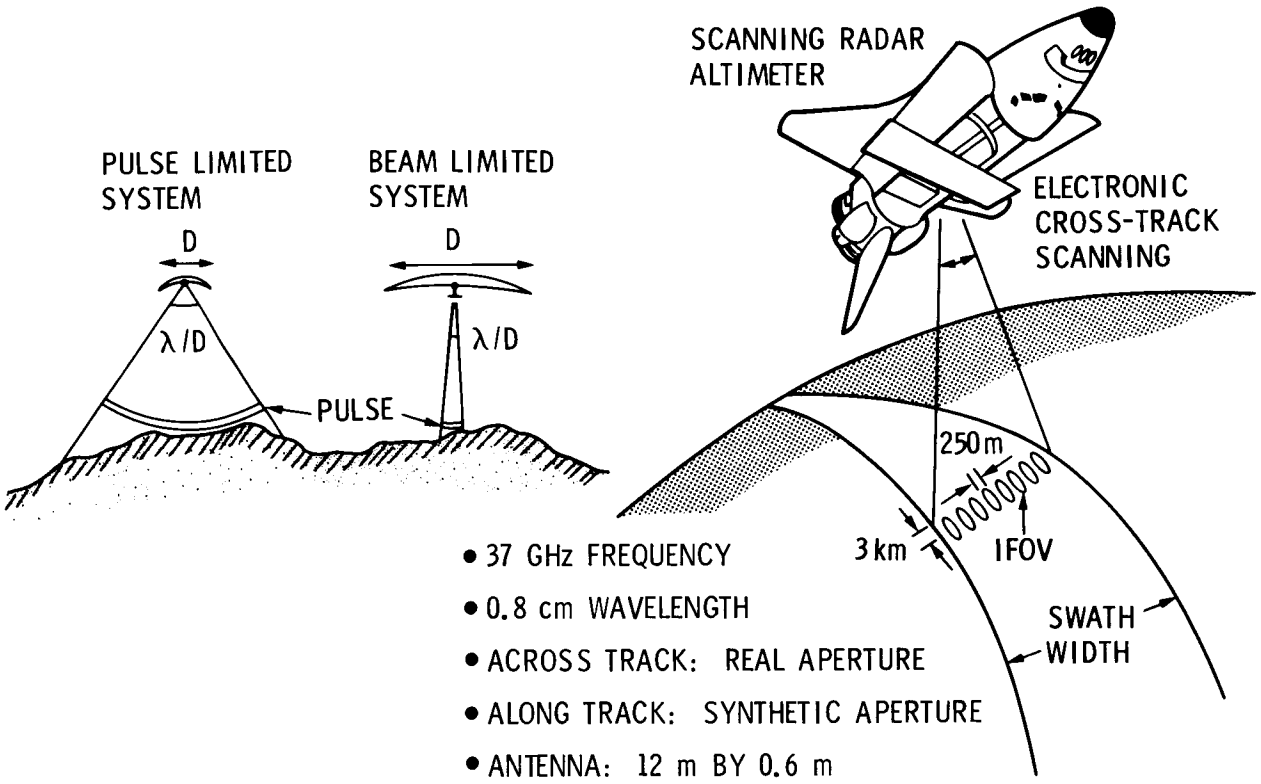


Figure 3. A possible system design to obtain high-resolution continental topographic data. Conventional radar altimeters (pulse limited systems) produce a wide footprint, unsuitable for altimetric measurement in high-relief continental terrain. However, the combination of a large antenna and high frequency would enable narrow-beam, small-footprint altimetry suitable for continental mapping. A proposed hybrid system would operate at relatively high frequency (37 GHz) and would utilize an antenna large in one dimension, giving cross-track resolution at 250 m. Synthetic aperture techniques allow recovery of along-track resolution of similar dimensions, even though the instantaneous field of view (IFOV) would be of order 3 km. Electronic scanning of individual antenna elements would generate the required swath width.

Ocean and Ice Research

# HYDRODYNAMICS OF INTERNAL SOLITONS AND A COMPARISON OF SIR-A AND SIR-B DATA WITH OCEAN MEASUREMENTS

J. R. Apel, R. F. Gasparovic and D. R. Thompson
The Johns Hopkins University
Applied Physics Laboratory
Laurel, Maryland

## ABSTRACT

Large internal solitary waves have been observed by Shuttle SIR-A and SIR-B at locations in the Andaman Sea and the New York Bight. Satellite imagery and oceanographic measurements are used in conjunction with hydrodynamic interaction and electromagnetic scattering models to estimate the expected SAR image intensity modulations associated with the internal waves. There is reasonable agreement between the predicted and observed internal wave signatures.

## I. ANDAMAN SEA SOLITONS

The Andaman Sea is located along the eastern side of the Indian Ocean between the Malay Peninsula and the Andaman and Nicobar Islands. It is a maritime regime containing internal solitary waves of extraordinary amplitude, wavelength and speed that exhibit signatures via surface roughness variations that are visible to the eye, to cameras, to scanning imagers, and to imaging radars. Internal solitary waves, or solitons, are generally waves of depression, more or less isolated from their fellows, that propagate over great distances with very little change in shape. Several satellite images have revealed that the Andaman Sea is rich in such excitations. The joint US-USSR space mission, Apollo-Soyuz, returned color photographs that showed narrow stripes of rough water in the sun glint region. These were interpreted by Apel (1979) as surface signatures of large internal waves, presumably produced by semidiurnal tidal flow over underwater topography; the inferred group speeds were approximately 2.5 m/s, as derived from their interpacket separation. In addition, examinations of visible wavelength imagery from the scanner on the Defense Meteorological Satellite Program (DMSP) spacecraft revealed similar surface signatures on several dates. Synthetic aperture radar images from the Shuttle Imaging Radar-A (SIR-A) on November 11, 1981, also contain several internal wave packets in the vicinity of the Andaman and Nicobar Islands (Cimino et al., 1982; Ford et al., 1983; Apel et al., 1986).

Figure 1 is a section of the SIR-A radar image of that date, having dimensions of 51.2 by 51.2 km, with the white marks along the lower border being 1-s time tics (or a distance of 7.14 km). North is along the direction shown, at an angle of approximately 38° from the lower edge. It is a high resolution (40-m), geographically corrected representation of the surface wave roughness variations and has been selected for further analysis because of the qualities that the internal waves possess. The objectives of the analysis are: (a) to use the historical density data in conjunction with the known nonlinear properties of internal solitons to estimate the amplitudes, currents, strain

rates, and propagation speeds from the SIR-A image; (b) to estimate wind speed and direction from the image; and (c) to apply theories of radar backscatter modulation to the deduced hydrodynamic and wind properties, in order to calculate the radar signatures. The signatures will then be compared with image intensity modulations.

The internal solitons are revealed mostly by dark (smooth) regions, with the associated rough regions not clearly visible, probably due to the large, 43° earth-incidence angle of the synthetic aperture radar. The approximately semicircular dark region near right center is thought to be an area of rainfall toward which the local winds are blowing, as revealed by subtle wind row streaks overlying portions of the waves; the wind direction is nearly from the west. The wind speed is estimated to be about 3 to 4 m/s, based on the general level of backscatter and the visibility of the waves, but the error in this estimate is easily ±100 percent.

The hydrodynamic properties are estimated from the image and from the historical density data by the application of a "modulated cnoidal wave" model of the solitary waves (Apel and Gonzales, 1983). In the Korteweg-deVries equation describing such solitons, a Mode-1 solitary wave train can be written as the product of an eigen function, W(z), giving the relative amplitude variation with depth, z, and a horizontal amplitude function, A(s,t), describing propagation along a horizontal arc, s(x,y), in the x,y plane. Thus, we write for the amplitude, η,

$$\eta(x,y,z,t) = W(z)\, A(x,y,t)\,. \tag{1}$$

The equations obeyed by the separation functions W and A are

$$\frac{d^2W}{dz^2} + k_t^2 \left[\frac{N^2(z)}{\omega^2} - 1\right] W = 0\,,$$

$$W(0) = W(-H) = 0\,, \tag{2}$$

(where the ocean bottom is at the depth -H), and the K-dV equation,

$$\frac{\partial A}{\partial t} + c_0 \left(\frac{\partial A}{\partial s} + \gamma \frac{\partial^3 A}{\partial s^3} + \alpha A \frac{\partial A}{\partial s}\right) = 0\,. \tag{3}$$

Here, $\omega = \omega(k_\ell)$ is the dispersion equation relating wave angular frequency, ω, to linear wave number, $k_\ell$; the quantities, N, γ, and α are environmental parameters termed the Brunt-Väisälä (or buoyancy) frequency, the dispersion coefficient, and the nonlinear coefficient, respectively. These may all be calculated from a knowledge of the variation of density with depth.

A useful approximate solution to the K-dV equation describing a bounded wave packet may be written as a modulated cnoidal function, wherein a propagating envelope function, $\eta_0(s-ct)$, moving at speed, c, is assumed to multiply the periodic cnoid, just as a modulated cosine may be used to describe a propagating linear wave packet. In this fashion, the varying amplitudes and degrees of nonlinearity existing within a group of waves such as those in Fig. 1 may be modeled without invoking the full apparatus of inverse scattering theory in the analysis. Algebraic relationships exist between the stretched wavelength, $\lambda_s$, and $k_\ell$, m, $\eta_0$, and c, and can be used to estimate the amplitude and speed if the other quantities can be evaluated. These relationships are

$$\lambda_s = \left(\frac{2\pi}{k_t}\right) \cdot \frac{K(m)}{\pi/2} = \lambda_\infty \frac{K(m)}{\pi/2} , \tag{4}$$

$$m = \frac{\alpha\eta_0}{\frac{1}{2}\gamma k_t^2} = \frac{\alpha\eta_0}{c - c_0} , \tag{5}$$

$$\begin{aligned} c &\approx c_0 \left(1 - \tfrac{1}{2}\gamma k_t^2 + \frac{\alpha\eta_0}{3}\right) \\ &\approx c_t + c_0 \frac{\alpha\eta_0}{3} . \end{aligned} \tag{6}$$

In Eq. 4, $\lambda_\infty = 2\pi/k_\ell$ is the small-amplitude, linear wavelength and K(m) is the complete elliptic integral of the first kind, which for m=0 reduces to $\pi/2$, while for $m \to 1$, $K(m) \to \infty$. In Eq. 6, the speed c is given in terms of the long-wavelength speed $c_0$ for which $k_\ell \approx 0$. The speed of a solitary wave is increased by the nonlinear amplitude-dependent term in Eq. 6; thus, larger solitons travel faster than smaller ones, all else being equal.

Using these quantities, the modulated cnoidal wave solution can be written as

$$\begin{aligned} \eta(x,y,z,t) &= -W(z)\eta_0(s - ct) \\ &\times cn_m^2 \left[\tfrac{1}{2}(\mathbf{k}_t \cdot \mathbf{s} - \omega t + \Phi)\right] . \end{aligned} \tag{7}$$

To apply Eqs. 4 to 7 to the case at hand, the image of Fig. 1 is used to evaluate (a) $\lambda_\infty$ from the wavelength at the rear of the wave packet, and (b) the stretched wavelength, $\lambda_s$, from the spacings of the other waves throughout the packet. The ratio $\lambda_s/\lambda_\infty$ is used to calculate the values of K(m) and m from Eq. 4; from Eq. 5 one then derives $\eta_0$.

Having obtained the wave amplitudes, the known hydrodynamics of the waves may be used to obtain the currents, u and w, and the horizontal strain rate, $\partial u/\partial s$, as well as the other desired properties.

In order to evaluate the equations numerically, functional forms of W(z) and its derivative are required; these are obtained via numerical solutions to Eq. 2. This in turn requires a vertical profile of $N^2(z)$ in terms of water density, $\rho$:

$$N^2(z) = -\frac{g}{\rho}\cdot\frac{d\rho}{dz} \quad . \tag{8}$$

A temperature profile was obtained from Osborne et al. for the Andaman Sea (Osborne and Burch, 1980) and used in this calculation.

Figure 2 illustrates the estimated surface current and surface strain rates versus distance, s - ct, throughout approximately 40 km of the packet. The peak currents are about 1.1 m/s, the strain rates are 1.3 x $10^{-3}$ $s^{-1}$ and peak amplitudes (not shown) are approximately 60 m - reasonable values in light of the measurements made in the Andaman to date (Osborne and Burch, 1980).

Figure 3 shows a comparison between the measured intensity modulation along the cut through the SIR-A image of Fig. 1 and the predicted modulation from our wave-current interaction model. One can see that the predicted modulation depth agrees fairly well with that measured from the synthetic aperture radar image. The intensity minima occur at nearly the same position and the spatial behavior of the predicted and measured curves is in reasonable agreement, although the theory underestimates the observations by about a factor of two.

## II. NEW YORK BIGHT

During Orbit 91 (11 October 1984) of the SIR-B mission on the shuttle Challenger, a synthetic aperture radar image of oceanic internal waves was obtained simultaneously with ship and current-meter measurements of the waves. These observations were part of the second phase of the Synthetic Aperture Radar Signature Experiment (SARSEX), a major experiment sponsored by the Office of Naval Research to investigate the basic hydrodynamic and electromagnetic phenomena responsible for internal wave signatures in SAR images and to test theories for predicting such signatures. The SIR-B image taken at 05:03:08 EDT (Fig. 4) shows several packets of tidally generated internal waves, low to moderate wind fronts, and the location of the research vessel Cape. The geographical area extends from about 100 km south of Long Island to immediately northeast of the Hudson Canyon, near 40°N, 72°15'W, a region that had been studied by Apel and coworkers (Apel et al., 1975a,b) during observational programs on internal waves on the continental shelf.

In situ measurements were made of horizontal water velocity components from current meters at depths of 15 and 67 m, water column temperature and density profiles, 200-kHz downward-looking echo sounder internal wave profiles, surface wave height spectra, and wind speed. The major properties of the internal wave field can be estimated when these measurements are used in conjunction with the type of internal wave model used above, with certain modifications. From the in situ measurements and a solution of the internal

wave equation, we find that $\eta_0 \simeq 9$ m, L $\simeq$ 250 m, and c $\simeq$ 0.4 m/s. At the surface, the estimated maximum induced current is $u_0 \simeq 0.15$ m/s, and the maximum surface current gradient, or strain rate, is approximately 0.004 $s^{-1}$ (Gasparovic et al., 1986).

A more extensive observational program of some nonlinear internal waves was carried out four weeks earlier during Phase I of SARSEX. This effort was structured to quantify the dominant processes contributing to the SAR signatures of internal waves: (i) the internal wave hydrodynamics, especially the surface current strain rates; (ii) modifications to the surface wave spectrum induced by the currents; (iii) the radar backscatter from the modulated surface waves; and (iv) the formation of SAR images from the backscatter modulations (Gasparovic et al., 1985).

A theory describing the perturbation of the surface wave height spectrum by the internal wave surface currents has been used to calculate the expected backscatter modulations associated with the internal waves (Hughes, 1978). This theory assumes that the energy input from the wind acts to restore the surface wave height spectrum S(k, x , t), which is perturbed by the presence of the internal wave currents u(x,t), to its equilibrium value $S_0(k)$. In particular, it is assumed that the fractional change in the wave action spectrum

$$N(\mathbf{k}, \mathbf{x}, t) = \rho \frac{\omega}{k} S(\mathbf{k}, \mathbf{x}, t) \tag{9}$$

(where $\rho$ is the water density) is proportional to the departure of the spectrum from its equilibrium value $N_0(k)$. Mathematically, this implies

$$\begin{aligned} \frac{1}{N}\frac{dN}{dt} &= \frac{1}{N}\left(\frac{\partial N}{\partial t} + \dot{\mathbf{x}} \cdot \nabla_x N + \dot{\mathbf{k}} \cdot \nabla_k N\right) \\ &= -\frac{\beta(\mathbf{k})}{N_0}(N - N_0) \end{aligned} \tag{10}$$

where

$$\dot{x}_i = \frac{\partial \omega}{\partial k_i} + u_i \tag{11}$$

and

$$\dot{k}_i = -k_j \frac{\partial u_j}{\partial x_i} \tag{12}$$

In these equations, the indices i, j = 1, 2 denote horizontal coordinates, and repeated indices are summed. The function $\beta(k)$ - the so-called wave relaxation rate - determines the effectiveness of both wind and dissipation in restoring equilibrium (Hughes, 1978). There is at present considerable uncertainty about its exact functional form, although there is general agreement that it increases with wave number and wind speed. We made the calculations that follow by using Hughes' expression for $\beta(k)$ which is consistent with field observations.

To relate the internal wave-induced change in surface wave spectrum to the SAR image intensity modulation, we make use of the fact that ocean backscatter at the SIR-B radar wavelength $\lambda_0$ = 23.5 cm and incidence angle $\theta$ is dominated by Bragg scattering (Thompson and Gasparovic, 1986; Thompson, 1986). In this limit, the normalized radar cross section $\sigma$ is proportional to the surface wave spectrum of the Bragg waves, that is, those waves traveling in the radar "look" direction with a wavelength $\lambda_B = \lambda_0/2(\sin\theta)$. The fractional change in cross section from its mean value $\sigma_0$ is given by

$$\frac{\Delta\sigma}{\sigma_0} = \frac{N(\mathbf{k}_B, x, t) - N_0(\mathbf{k}_B)}{N_0(\mathbf{k}_B)} \tag{13}$$

where $k_B$ is the Bragg wave number. When the internal wave features propagate in the radar look direction as in Fig. 4, the SAR image intensity variations are essentially equivalent to the cross-sectional variations given by Eq. 13.

Image intensity variations for some of the features of the internal waves in Fig. 4 are shown in Fig. 5, which was taken through the wave group along the vertical line A-A'; it shows nine distinct waves in the packet with peak-to-peak intensity variations ranging from 2 to 12 dB. The average spacing between waves in this packet is approximately 380 m. There is another group of waves near the center of the image along the vertical line B-B' and the four waves at the front of this packet have peak-to-peak intensity variations of 3 to 10 dB.

We have made predictions of the SAR image intensity modulations for these internal waves using the above theory, with internal wave and surface parameters obtained from the in situ observations. Maximum internal wave surface strain rates of 0.002 to 0.005 $s^{-1}$ were assumed, consistent with intrapacket variations encountered during the Phase I observations. The large-scale brightness variations in Fig. 4 are indicative of the presence of wind speeds greater than the value 1 m/s recorded at the ship location which is in a dark region of the image. For the wave packet along A-A', we assumed a wind speed of 2 m/s along line B-B'; the actual wind speed is presumed to lie between these two values. With a wind speed of 2 m/s, the calculated peak-to-peak SAR image intensity modulations range from 2 to 7 dB for maximum surface strain rates of 0.002 and 0.005 $s^{-1}$, respectively. These calculated modulations agree with the observations along lines A-A' and B-B' to within 3 to 5 dB, or within a factor of 2 to 3. This result is consistent with initial findings for the Phase I SAR aircraft L-band images, for which more extensive comparisons between theory and observations are possible.

ACKNOWLEDGEMENTS

The authors appreciate the SIR-A and SIR-B data support by the Jet Propulsion Laboratory. This work was supported by U.S. Naval Sea Systems Command under Contract N00024-56-C-5301.

REFERENCES

J. R. Apel, H. M. Byrne, J. R. Proni, and R. L. Charnell, J. Geophys. Res. 80, 865 (1975).

J. R. Apel, J. R. Proni, H. M. Byrne, and R. L. Sellers, Geophys. Res. Lett. 2, 128 (1975).

J. R. Apel, "Observations of Internal Wave Surface Signatures in ASTP Photographs," Apollo-Soyuz Test Project II, F. El-Baz and D. M. Warner, eds. NASA SP-412 (1979).

J. R. Apel and F. I. Gonzalez, J. Geophys. Res. 88, 4459 (1983).

J. R. Apel, D. R. Thompson, D. G. Tilley, and P. Van Dyke, "Hydrodynamics and Radar Signatures of Internal Solitons in the Andaman Sea," Johns Hopkins APL Technical Diget, 6, 330 (1986).

J. B. Cimino and C. Elachi, "Shuttle Imaging Radar-A (SIR-A) Experiment," NASA/JPL 82-77, pp. 5-53 (1982).

J. P. Ford, J. B. Cimino, and C. Elachi, "Space Shuttle Columbia Views the World with Imaging Radar: The SIR-A Experiment," NASA/JPL 82-95, pp. 144-145 (1983).

R. F. Gasparovic, J. R. Apel, D. R. Thompson, and J. S. Tochko, "A Comparison of SIR-B Synthetic Aperture Radar Data with Ocean Internal Wave Measurements," Science, 232, 1529 (1986).

B. A. Hughes, J. Geophys. Res. 83, 455 (1978).

A. R. Osborne and T. L. Burch, "Internal Solitons in the Andaman Sea," Science 208, 451 (1980).

SARSEX Experiment Team, "SARSEX Interim Report" (Report STD-R-1200, Johns Hopkins University Applied Physics Laboratory, Laurel, MD, May 1985).

D. R. Thompson and R. F. Gasparovic, Nature (London) 320, 345 (1986).

D. R. Thompson, "Intensity Modulations in Synthetic Aperture Radar Images of Ocean Surface Currents and the Wave/Current Interaction Process," Johns Hopkins APL Technical Digest, 6, 346 (1986).

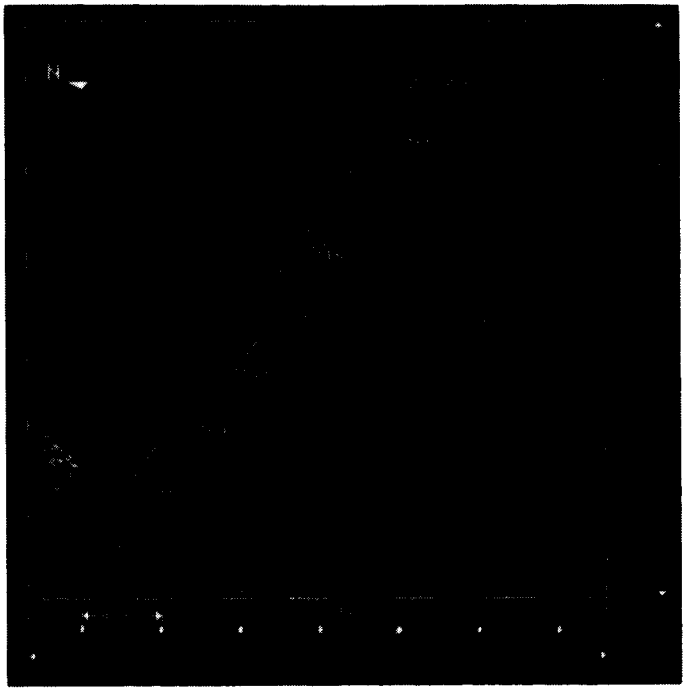

Figure 1. L-band radar image from SIR-A taken November 11, 1981, near the Andaman Islands, showing a packet of 6-kilometer-long solitons and what is thought to be a rain squall. Dimensions are 51.2 by 51.2 kilometers.

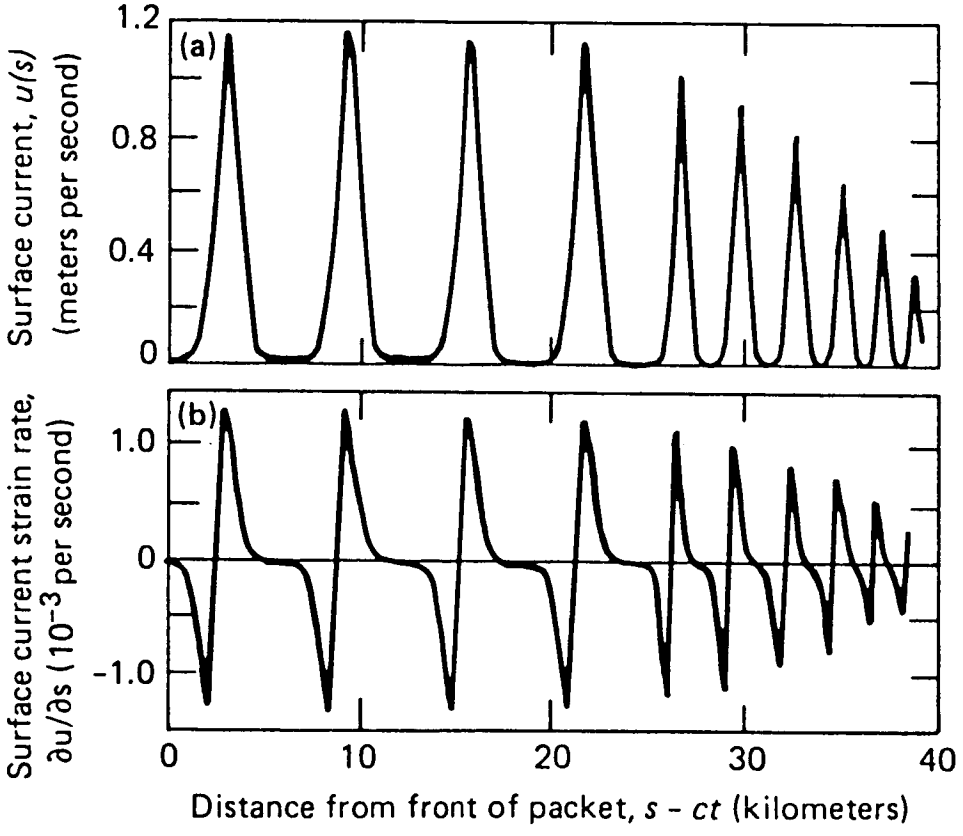


Figure 2. (a) Calculated horizontal surface currents and (b) surface strain rates for cnoidal wave packet. The front of the packet is at left.

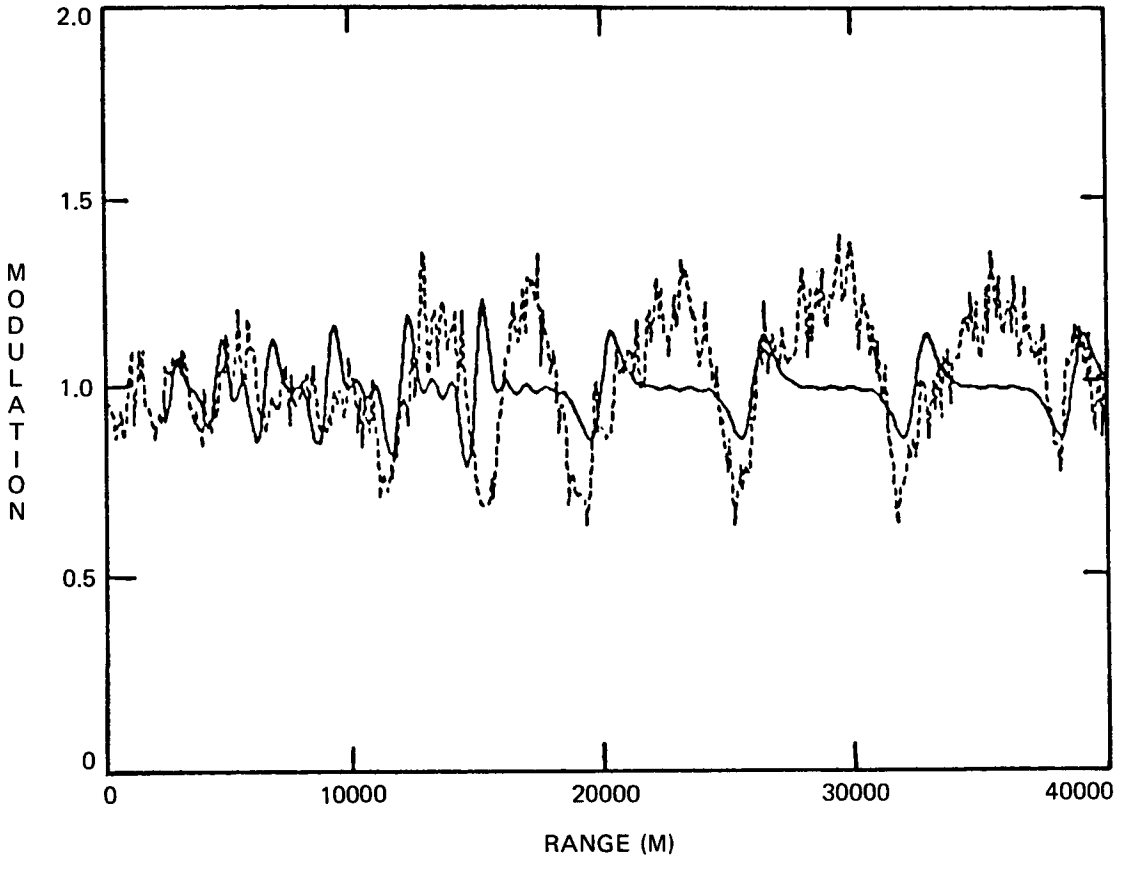


Figure 3. Comparison of observed (dashed curve) and calculated (solid curve) radar backscatter power modulation from rectangle of Fig. 1. The phase of the calculated modulation is reproduced quite well, but the amplitudes are generally underestimated by factors of 2 or more. The overall agreement is considered reasonable.

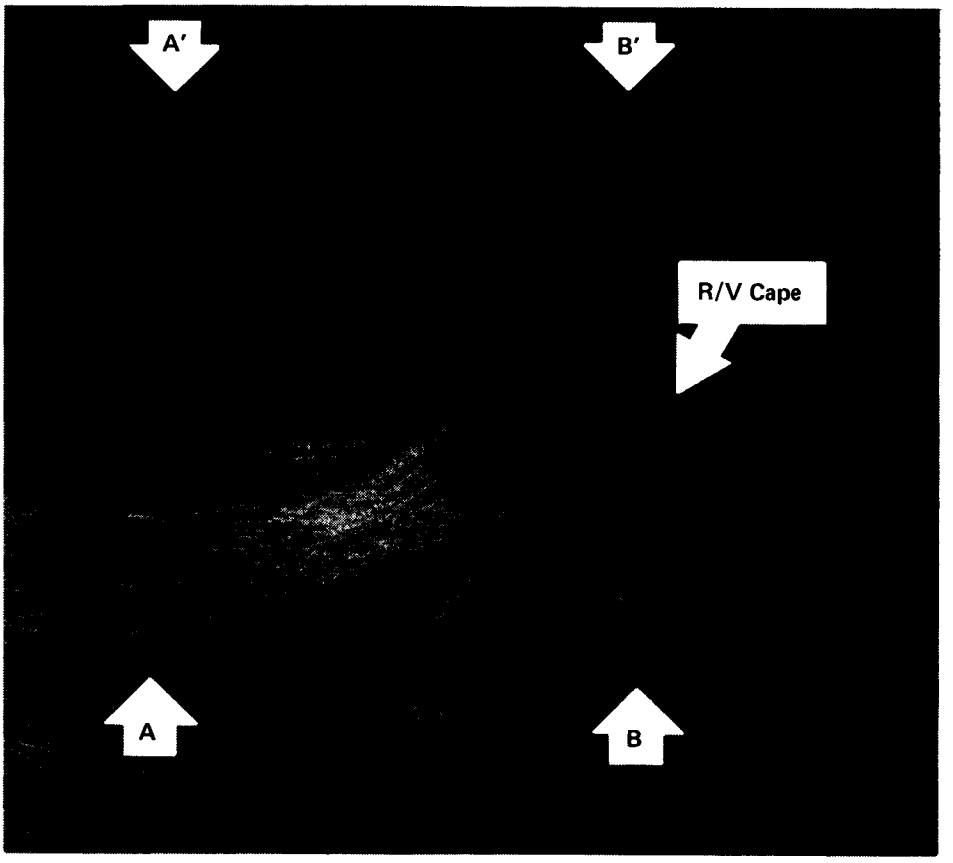


Figure 4. SAR image of oceanic internal wave features from orbit 96 of the SIR-B mission. The bright linear features crossing lines A-A' and B-B' are due to increased surface wave roughness within the internal wave packets, which are propagating toward the top of the image (313° true heading). A surface wind of 1 $m^{s-1}$, blowing toward 190° true heading, was recorded at the ship position. The radar incidence angle at the center of the image is 20°.

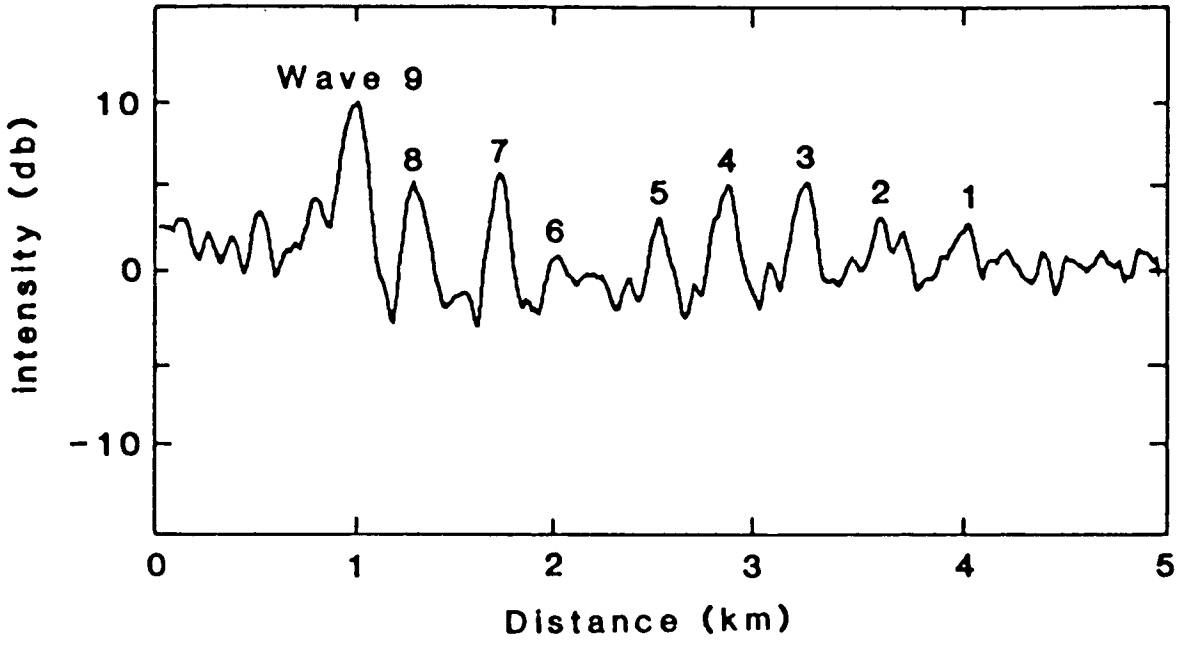


Figure 5. SAR image intensity traces through Fig. 4 along line A-A'. Trace has been averaged over 625 m in the azimuth direction and then smoothed 62.5 m in the range direction.

# OCEAN WAVES NEAR HURRICANE JOSEPHINE FROM SIR-B

Benjamin Holt
Jet Propulsion Laboratory, California Institute of Technology
Pasadena, California

F. I. Gonzalez
Pacific Marine Environmental Laboratory
National Oceanic and Atmospheric Administration
Seattle, Washington

Radar images of ocean surface waves near hurricane Josephine were acquired with the Shuttle Imaging Radar-B (SIR-B) system on October 12, 1984. Analyses of the directional ocean wave spectra derived from the imagery have been performed along most of the 600 km image track. These data reveal the presence of at least two dominant wave systems which undergo significant spatial variations in wavelength and direction.

Both satellite and airborne imaging radar systems, with their ability to penetrate clouds and produce high resolution data, have been used to study surface wave fields generated by hurricanes, the most complex condition for wave generation studies due to the rapidly changing and curving wind fields (The SWAMP Group, 1985; Elachi et al., 1977; McLeish and Ross, 1983; Gonzalez et al., 1982). These studies confirmed that the surface waves with the longest wavelength were generated near the area of maximum winds, the right rear quadrant, of the moving hurricanes. The rare opportunities to obtain synoptic observations of the wavenumber vector field near hurricanes such as provided by imaging radars are particularly valuable and can also be used, for example, as test cases for intercomparison studies for wave prediction models (The SWAMP Group, 1985).

Imaging radar data were acquired near hurricane Josephine from 16:31 to 16:33 GMT on October 12, 1984 (orbit 117). The resultant radar swath lay ahead and to the east of the hurricane at an approximate 45° angle to the storm track, with the closest approach at about 16:31:40 GMT at a point located about 90 km northeast of the hurricane center (Figure 1). The SIR-B data was obtained during the period of maximum hurricane intensity when the peak wind values were 90 knots.

The radar imagery revealed the presence of at least two dominant wave systems. The dominant wave system was detectable along the entire radar swath propagating north and northeast away from the storm track with a fan-shaped directional distribution. Secondary wave systems were detected which appear to be roughly aligned in the direction of the local cyclonic wind and propagating northwest and west in the upper portion of the radar track. These waves decrease in wavelength from north to south, disappear altogether at a point nearest the hurricane center, and then reappear in the southernmost portion of the radar imagery propagating east. This lack of signal in a portion of the imagery does not appear to be related to either azimuth-falloff or to limitations imposed by the finite resolution of SIR-B; rather, it may accurately reflect the chaotic nature of the winds and waves and the lack of a fully developed sea in the region nearest the hurricane.

Further analysis will include developing kinematic and dynamic models to study the wave characteristics. The kinematic model will determine the source regions for the evolving waves based on accurate measurements of wavelength, wave direction, timing, and hurricane position. The dynamic model will incorporate waveheight and observed gradients in wavelength and direction plus energy considerations to study waveheight as a function of time, radial spreading, and dissipation.

## REFERENCES


Elachi, C., T. W. Thompson, and D. King, "Ocean wave patterns under Hurricane Gloria: Observation with an airborne synthetic-aperture radar," Science, Vol. 198, 609-610, 1977.

Gonzalez, F. I., T. W. Thompson, W. E. Brown, Jr., and D. E. Weissman, "Seasat wind and wave observations of northeast Pacific Hurricane Iva, August 13, 1978," J. Geophys. Res., Vol. 87, No. C5, 3431-3438, 1982.

Holt, B., and F. I. Gonzalez, "SIR-B observations of dominant ocean waves near hurricane Josephine," J. Geophys. Res., 1986, in press.

McLeish, W., and D. B. Ross, "Imaging radar observations of directional properties of ocean waves," J. Geophys. Res., Vol. 88, No. C7, 4407-4419, 1983.

The SWAMP Group, Ocean Wave Modeling, Plenum, New York, 262 pp., 1985.

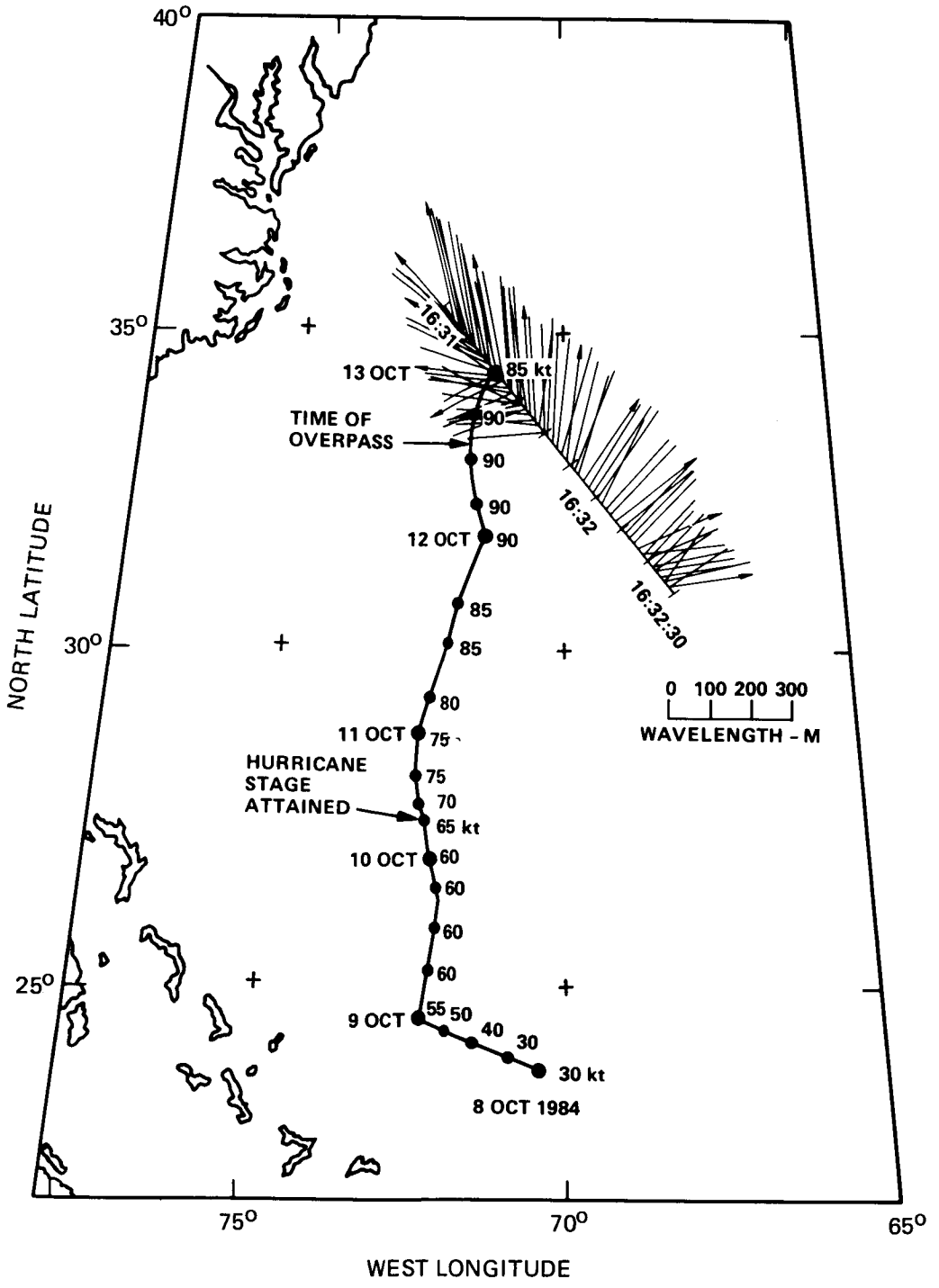


Figure 1. Map of partial track of hurricane Josephine (October 8-13, 1984) with maximum wind speeds in knots indicated for the storm center at 6-h intervals, track of SIR-B radar imagery (October 12, 1984) with times of acquisition indicated. Wavelength and direction of dominant wave systems are displayed along radar track. Arrows indicate general propagation direction of neighboring waves.

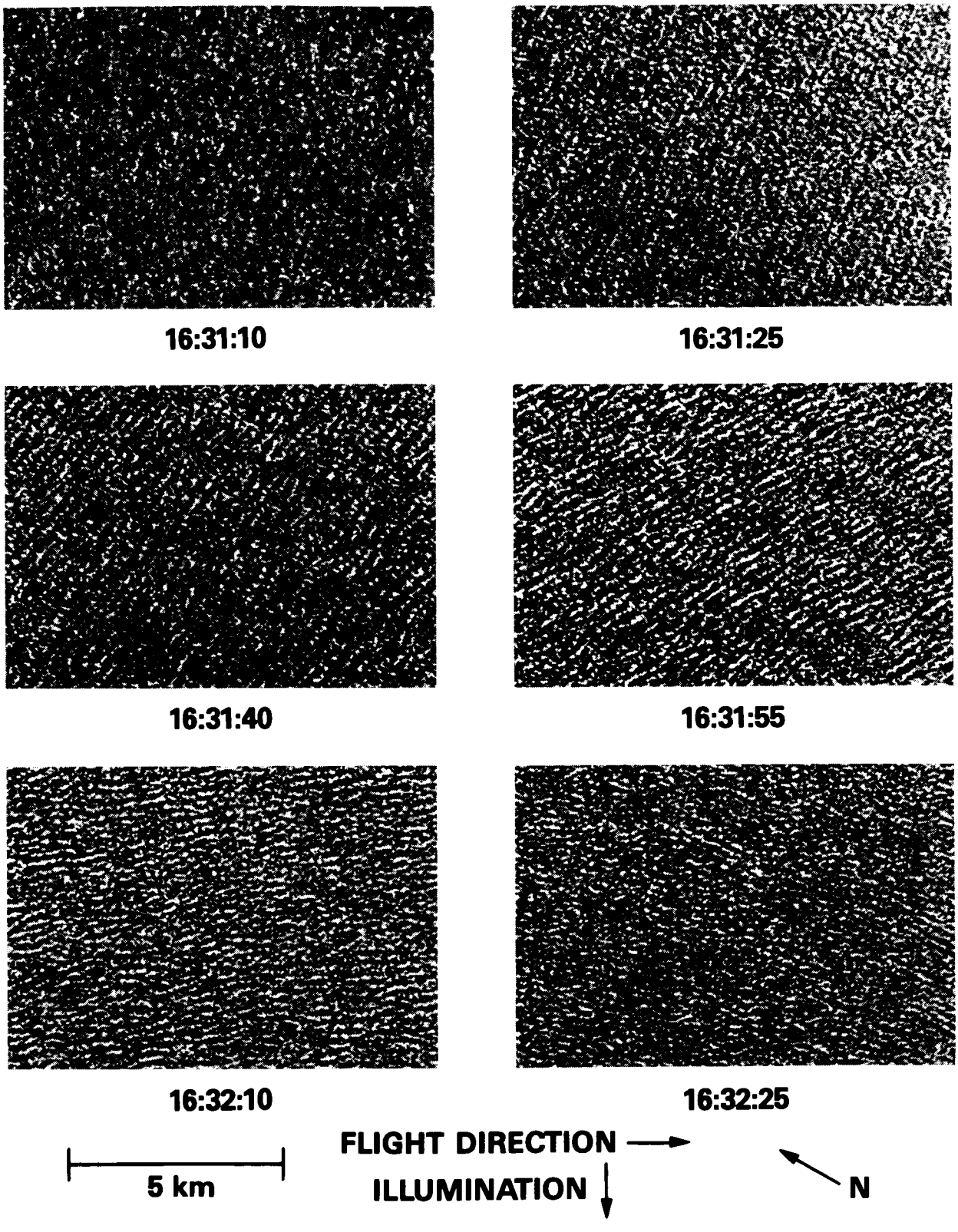


Figure 2. Enlargements of SIR-B radar imagery of surface waves near hurricane Josephine (Data take 117.4). Each image covers an area 7 x 10 km in size and is centered in the radar swath at the time (GMT) indicated.

# OPERATIONAL WAVE FORECASTING WITH SPACEBORNE SAR: PROSPECTS AND PITFALLS

R. C. Beal
Applied Physics Laboratory
The Johns Hopkins University
Laurel, Maryland

## I. INTRODUCTION

In April 1965, now more than 20 years ago, a small number of radio scientists and oceanographers congregated at the Woods Hole Oceanographic Institute to consider how the new tools of remote sensing might enhance our understanding of the global ocean environment. Among the techniques considered were radar altimetry, radar scatterometry, and synthetic aperture radar. Of course, at that time, good data sets were scarce, and many of the recommendations were by necessity somewhat speculative in nature. Nevertheless, the complement of active microwave instruments that was identified was very similar to the suite later flown on SEASAT in 1978.

Of particular interest to the topic of ocean wave forecasting is the following quotation from Gifford Ewing, the conference editor. With respect to the value of SAR in monitoring the global wave spectrum, he said:

> "What is needed is the directional energy spectrum of the waves on a two dimensional surface, and for this, the vantage point offered by a satellite is ideal .... It is within the capability of present day radar technology to give a complete description of the sea surface."

That statement was made over 21 years ago. Since then, we have had SEASAT, SIR-A, and SIR-B, all containing high resolution synthetic aperture radars, and all collecting varying "descriptions of the sea surface." The descriptions, however, are only more or less complete, and we are just recently beginning to accumulate the evidence necessary to assess the true value of SAR for obtaining useful estimates of the global directional energy spectrum.

## II. THE PROBLEM OF WAVE PREDICTION

Ocean wave prediction over global scales has been a fond hope of oceanographers for several decades. Significant progress was made during and soon after World War II, particularly when the concept of a "wave spectrum" was advanced to describe the statistical properties of the wave field. The idea of an "equilibrium spectrum" gained support from both theoretical and experimental perspectives in the late 1950's, and has served as a framework for departure even up to the present. Moreover, theories of wave growth are now well developed in terms of the source wind field properties, such as fetch and duration, and to some extent even in terms of the "background" wave field. And yet, in the perspective of the global wave prediction problem, there are still several fundamental unanswered questions. These questions center on both the models and on the means for verifying them. For example:

- How often must we measure the wave field in order to predict it?

- Does the background wave field modify wave growth? Are its directional characteristics important?

- Is the directional wave spectrum a sufficiently complete descriptor? How important are wave groups, which may give rise to non-Gaussian statistics?

- How good are the models? How efficiently can they assimilate the data?

- How well can we remotely measure the wave field? How well can we measure it from orbital altitude?

- Can we learn any new physics from the measurements?

- What is the optimum strategy for global wave monitoring? Is it practical? Is its implementation likely to improve wave forecasting?

We do not yet know the answers to these questions, but we are beginning to accumulate a data base which is offering some major contributions toward the solutions.

## III. THE SIR-B EXTREME WAVES EXPERIMENT OFF CHILE

From October 8 to 12, 1984, as part of the SIR-B experiment, simultaneous and coincident measurements of the ocean wave directional energy spectrum were made in a NASA P-3 aircraft flying off the southwest coast of Chile. Sea states during the experiment ranged from 1.5 m to 4.5 m, and included fresh seas, decaying swells, and both unimodal and bimodal wave fields. The two primary aircraft instruments were the Surface Contour Radar (SCR; Walsh, 1985) and the Radar Ocean Wave Spectrometer (ROWS; Jackson, 1985), each of which was independently capable of measuring the directional energy spectrum.

Figure 1 illustrates the geometry of the Chile experiment, and Table 1 summarizes the various means of estimating (or predicting) properties of the wave field. The SIR-B was operated through a variety of off-nadir incidence angles, from 40° to 18°. Independent spectral estimates also were made with the airborne optical laser (AOL) and the "AAFE" altimeter, a nadir-looking altimeter yielding estimates of significant wave height. In addition to the aircraft and spacecraft estimates, the U.S. Navy's Global Spectral Ocean Wave Model (GSOWM), which only recently began operating in the Southern Hemisphere, yielded separate estimates of the directional wave spectrum.

## IV. EXPERIMENTAL RESULTS

Although a complete set of spectral comparisons is available for each of the last four days of the experiment, only one set will be shown here, that of October 11, 1984. Preliminary comparisons are also reported in Beal et al, 1986a, and more complete comparisons of the entire data set will be forthcoming.

Figure 2 shows the four-way comparison of wave number spectra for each of the aforementioned methods. The spectra from the SCR, ROWS, and GSOWM are all displayed in relative spectral energy density units of $m^4$. The SAR spectrum is displayed in a similar format simply by assuming that the image Fourier transform, after appropriate spectral smoothing and correcting for a stationary point source response function, Beal et al, 1983; 1986b, is closely related to the ocean wave slope spectrum. With this assumption, the displayed spectrum is simply the slope spectrum times $1/k^2$, where k = wavenumber.

All the spectral estimates are similar in their gross features, with both the ROWS and SAR exhibiting 180° ambiguity. There are, however, slight differences, particularly in the high wavenumber tails of the spectrum, which are not yet satisfactorily resolved. Nevertheless, all instruments agree well in wavenumber and direction, as well as in spectral and angular width of the dominant system. On the other hand, the GSOWM estimate appears rotated clockwise by nearly 30°. This angular bias of GSOWM persists throughout the entire data set, and clearly shows the potential value of actual wave measurements as an update and correction for global models.

On other days, the agreement is not always so impressive. In particular, azimuth traveling waves in low sea states (i.e., wave systems having large dominant wavenumber) are severely attenuated and sometimes obliterated. This azimuth wavenumber distortion results from the Doppler nature of the SAR, and is a particular problem for high altitude (>300 km) orbiting platforms. For this reason, it now appears that global spectral estimates may best be obtained from a low altitude satellite employing both a SAR and a ROWS. Such a design has been described at a recent symposium on "Measuring Ocean Waves from Space," held at the Applied Physics Laboratory. A more complete description of the concept, dubbed "Spectrasat," can be found in the Symposium Proceedings, to appear in the first half of 1987.

## SUMMARY

Measurements collected in the SIR-B Extreme Waves Experiment confirm the ability of SAR to yield useful estimates of wave directional energy spectra over global scales, at least for shuttle altitudes. However, azimuth fall-off effects tend to become severe for wavelengths shorter than about 100 m in most sea states. Moreover, the azimuth fall-off problem becomes increasingly severe as the platform altitude increases beyond 300 km. The most viable solution to the global wave measurements problem may be a low altitude spacecraft containing a combination of both the SAR and the ROWS. Such a combination could have a synergy which would yield global spectral estimates superior to those of either instrument singly employed.

## ACKNOWLEDGMENTS

This work is a portion of the SIR-B Extreme Waves Team effort. Members of the team are: F. M. Monaldo, D. G. Tilley, D. E. Irvine, E. J. Walsh, F. C. Jackson, D. W. Hancock III, D. E. Hines, R. N. Swift, F. I. Gonzalez, D. R. Lyzenga, and L. F. Zambresky. Many others also contributed. This work was supported by NASA and the Office of Naval Research.

## REFERENCES

Beal, R. C., F. M. Monaldo, D. G. Tilley, D. E. Irvine, E. J. Walsh, F. C. Jackson, D. W. Hancock III, D. E. Hines, R. N. Swift, F. I. Gonzalez, D. R. Lyzenga, and L. F. Zambresky, "A Comparison of SIR-B Directional Ocean Wave Spectra with Aircraft Scanning Radar Spectra and Global Spectral Ocean Wave Model Predictions," Science (in press), 1986a.

Beal, R. C., F. M. Monaldo, and D. G. Tilley, "Large and Small Scale Spatial Evolution of Digitally Processed Ocean Wave Spectra from the SEASAT Synthetic Aperture Radar," J. Geophys. Res., 88, 1761-1778, 1983.

Beal, R. C., T. W. Gerling, D. E. Irvine, F. M. Monaldo, and D. G. Tilley, "Spatial Variations of Ocean Wave Directional Spectra from the SEASAT Synthetic Aperture Radar," J. Geophys. Res., Vol. 91, No. C2, 2433-2449, February 15, 1986.

Jackson, F. C., W. T. Walton, and C. Y. Peng, "A Comparison of In Situ and Airborne Radar Observations of Ocean Wave Directionality," J. Geophys. Res., 90, 1005-1918, 1985.

Walsh, E. J., D. W. Hancock III, D. E. Hines, R. N. Swift, and J. F. Scott, "Directional Wave Spectra Measured with the Surface Contour Radar," J. Phys. Oceanogr., 15, 566-592, 1985.

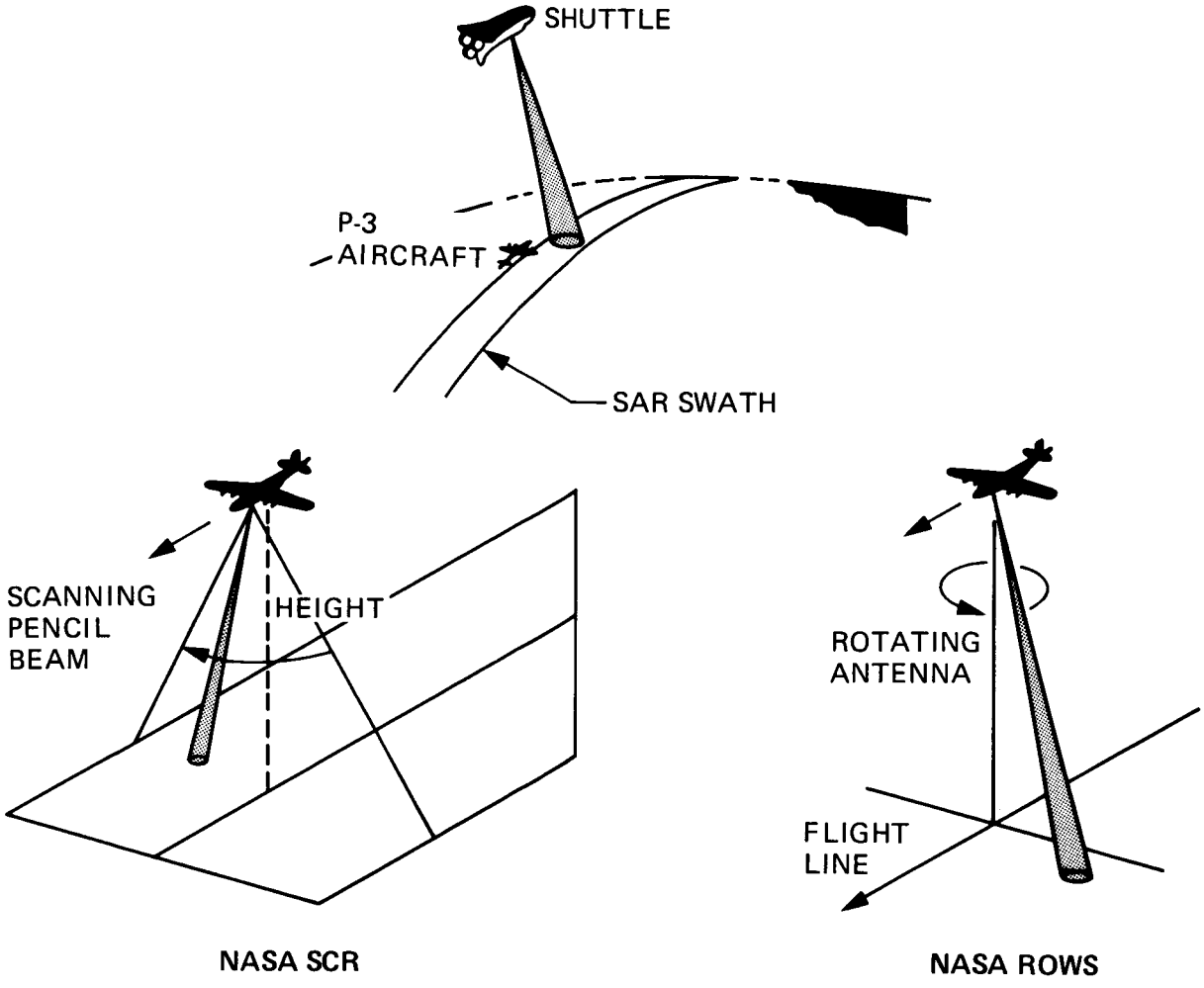


Figure 1. SIR-B Chile experiment

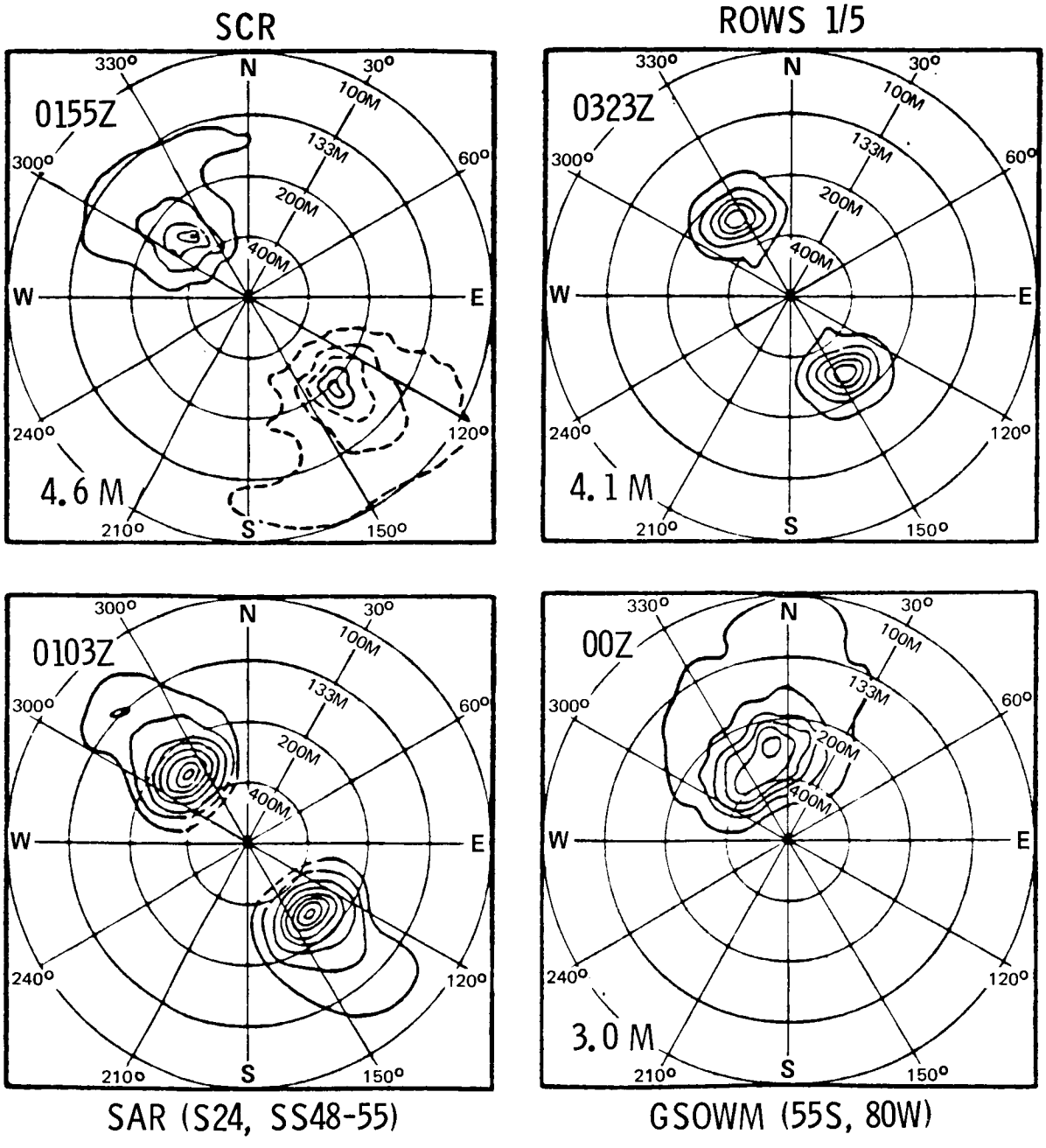


Figure 2. SIR-B spectral comparisons, Chilean coast, October 11, 1984; data take 91.50 (flight #4)

Table 1. Chile data set summary

| Date | SIR-B | Wave estimates | | | | | |
|---|---|---|---|---|---|---|---|
| | | NASA P-3 aircraft | | | | | GSOWM |
| | | FLT # | SCR | ROWS | AOL | AAFE | |
| 8 Oct | 40° | 1 | X | X | √ | √ | √ |
| 9 Oct | 35° | 2 | √ | √ | √ | √ | √ |
| 10 Oct | 30° | 3 | √ | √ | X | (√) | √ |
| 11 Oct | 25° | 4 | √ | √ | √ | √ | √ |
| 12 Oct | 18° | 5 | √ | √ | √ | √ | √ |

Data quality: √good (√) marginal X absent

# IMAGING RADAR CONTRIBUTIONS TO A MAJOR AIR-SEA-ICE INTERACTION STUDY IN THE GREENLAND SEA

Robert A. Shuchman*
Radar Science Laboratory
Environmental Research Institute of Michigan
Ann Arbor, Michigan

The Marginal Ice Zone (MIZ) is the region of the outermost extent of the polar ice field. The MIZ is the critical region in which polar air masses, ice and water masses interact with the temperate ocean and climate systems. The processes that take place there profoundly influence hemispheric climate and have a significant effect on petroleum/mineral exploration and production, naval operations, and commercial fishing. To gain an understanding of these processes sufficient to permit modeling and prediction, a research strategy was developed for summer and winter measurement programs (Wadhams et al., 1981), and a series of field experiments were planned and executed (Johannessen et al., 1983). One such experiment was conducted in the Fram Strait region of the Greenland Sea in the summer of 1983 and 1984. The purpose of the program in the Fram Strait was to study the mesoscale physical processes by which ice, ocean, and atmosphere interact in the MIZ in summer (Johannessen and Horn, 1984).

In this program synthetic aperture radar (SAR) was used as both a real-time reconnaissance tool as well as a scientific instrument. Due to extensive and persistant cloud cover over the MIZ, SAR data obtained from aircraft was the only means to provide weather independent data in real-time to the ice-strengthened ships conducting sea truth in the area. Figure 1 summarizes the coordination of the remote sensing activities during the 83 and 84 experiments. A field coordination center was maintained on the ice-strengthened ship R/V POLARSTERN that served as a center for all remote sensing ocean- and sea-ice-truth activities. A land coordination station, located at Tromso, Norway, interpreted aircraft and satellite data, and transmitted this information to the field center. The ship utilized the satellite information when available along with SAR provided data, voice communication from the various aircraft, directly received satellite data, and helicopter reconnaissance flights to direct the local remote sensing activities (helicopter, ship based, and surface).

The SAR data set collected on 5 July during the MIZEX program serves as an example of the remote sensing analyses possible. Mosaicked L-band (23-cm wavelength) imagery from that day is shown in Figure 2. The high reflectivity of the ice in the MIZ relative to that of open water is responsible for the excellent ice edge and floe definition seen in this imagery. Likewise, the structure in the three eddies visible in this image is well defined due to the high reflectivity of small, 50-500 m rough, broken floes entrained in the eddy currents. In the field, being able to locate eddies in real-time SAR output allowed research ships to be directed to active sites.

*Co-Chairman MIZEX Remote Sensing Group. This research was supported by ONR Contracts N00014-81-C-0295 and N00014083-C-0404. The ONR technical monitor is Mr. Charles Luther.

By collecting imagery over several days, it has been possible to monitor the evolution and motion of these eddy features, as well as the motion of floes throughout the MIZ ice field (Shuchman and Burns, 1985).

Manual interpretations done on the mosaics, such as the one for 5 July shown in Figure 2, are based on features observed in both the X-band (3-cm wavelength) and L-band data. These channels provide complementary information. The X-band gives better ice/water contrast and therefore good floe definition, whereas the L-band provided more detail on features within floes and, under some conditions, ocean wave features. In the case of the 5 July data, the melt water front and the ocean slicks that may be associated with internal waves are observed in the L-band but not in the X-band imagery.

The manual interpretation was carried out in three parts. The first was to identify unique features; eddies, large floes, polynyas, and internal waves. The second step was to segment ice-covered regions into areas with the same signatures; that is, the same perceived overall tone and texture. In general, each area or class appears to be associated with a different combination of ice concentration and floe size distribution. Step three was to then quantify the ice concentration and median floe size associated with each class. Using a machine-assisted manual analysis approach, representative subareas for each class were selected from the mosaic and located on the image strips. Floe boundaries for all floes within each subarea were then digitized using a DIGI-PAD 5 digitizer interfaced to a Z-100 micro-computer. Once in digital format, the data were manipulated to obtain area, perimeter, and diameter of each floe and total ice concentration of the subarea. The same approach has been applied to the multi-temporal SAR images to obtain maps of the ice field motion.

Values of ice concentration and floe size obtained in this way appear in the interpretation key (see Figure 2). The accuracy of this procedure was determined with data from 30 June 1984 where it was applied to both SAR imagery and coincident, near-simultaneous aerial photography also obtained by the CV-580. Discrepancy between SAR-derived and aerial photo concentration estimates was at most 5 percent for concentrations ranging from 30 percent to 80 percent. Correspondence between floe size was also evaluated and found to be within 5 percent on average.

In summary, by virtue of the SAR's imaging capabilities, such as all-weather imaging, relatively high resolution, and large dynamic range of backscatter from SAR ice and open ocean, information on the important MIZ parameters can be derived from the SAR data. Information on ice edge location and location of ice-edge eddies, for example, can be obtained directly from examination of the imagery as can detection of ocean fronts and internal waves. With machine-assisted manual image analysis, estimates of ice concentration, floe size distributions, and ice field motion can also be derived. Full digital analysis, however, is required to obtain gravity wave spectral information and backscatter statistics for ice type discrimination and automated ice concentration algorithms.

## REFERENCES

Johannessen, O. M., W. D. Hibler III, P. Wadhams, W. J. Campbell, K. Hasselmann, I. Dyer, and M. Dunbar, MIZEX, A program for mesoscale air-ocean-ice interaction experiments in Arctic marginal ice zones, II. A science plan for a summer marginal ice zone experiment in the Fram Strait/ Greenland Sea (MIZEX Bulletin II), U.S. Army Cold Regions Research and Engineering Laboratory, CRREL Special Report 83-12, 1983.

Johannessen, O. M., and D. Horn (Ed.), MIZEX 84, Summer experiment PI preliminary reports (MIZEX Bulletin V), U.S. Army Cold Regions Research and Engineering Laboratory, CRREL Special Report 84-29, 1984.

Shuchman, R. A. and B. A. Burns, Remote sensing of the marginal ice zone during MIZEX 83 and 84, Proceedings of the Arctic Oceanography Conference and Workshop, NORDA, Hattiesburg, MS, June 1985, U.S. Dept. of the Navy, 178-189, 1985.

Wadhams, P., S. Martin, O. M. Johannessen, W. D. Hibler III, and W. J. Campbell (Ed.), MIZEX: A program for mesoscale air-ice-ocean interaction experiments in arctic marginal ice zones, I. Research strategy (MIZEX Bulletin II), U.S. Army Cold Regions Research and Engineering Laboratory, CRREL Special Report 81-19, June 1981.

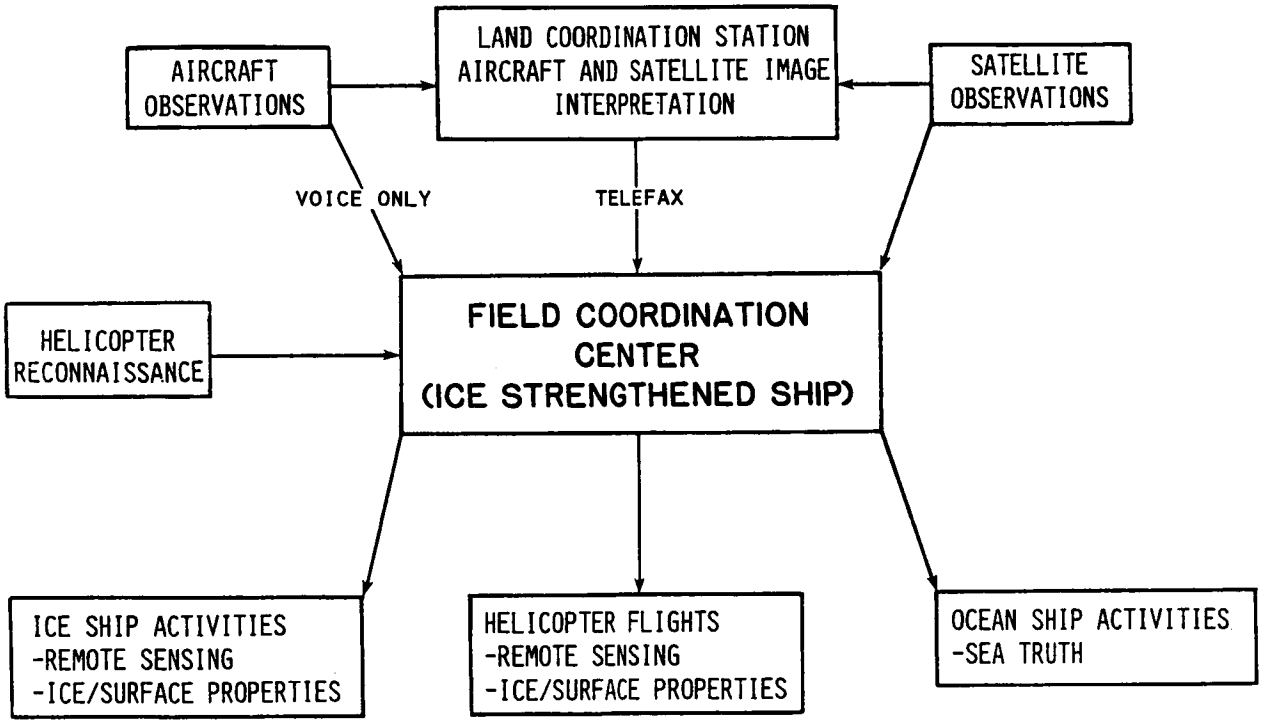


Figure 1. Approach utilized to coordinate the MIZEX 83 and 84 remote sensing activities

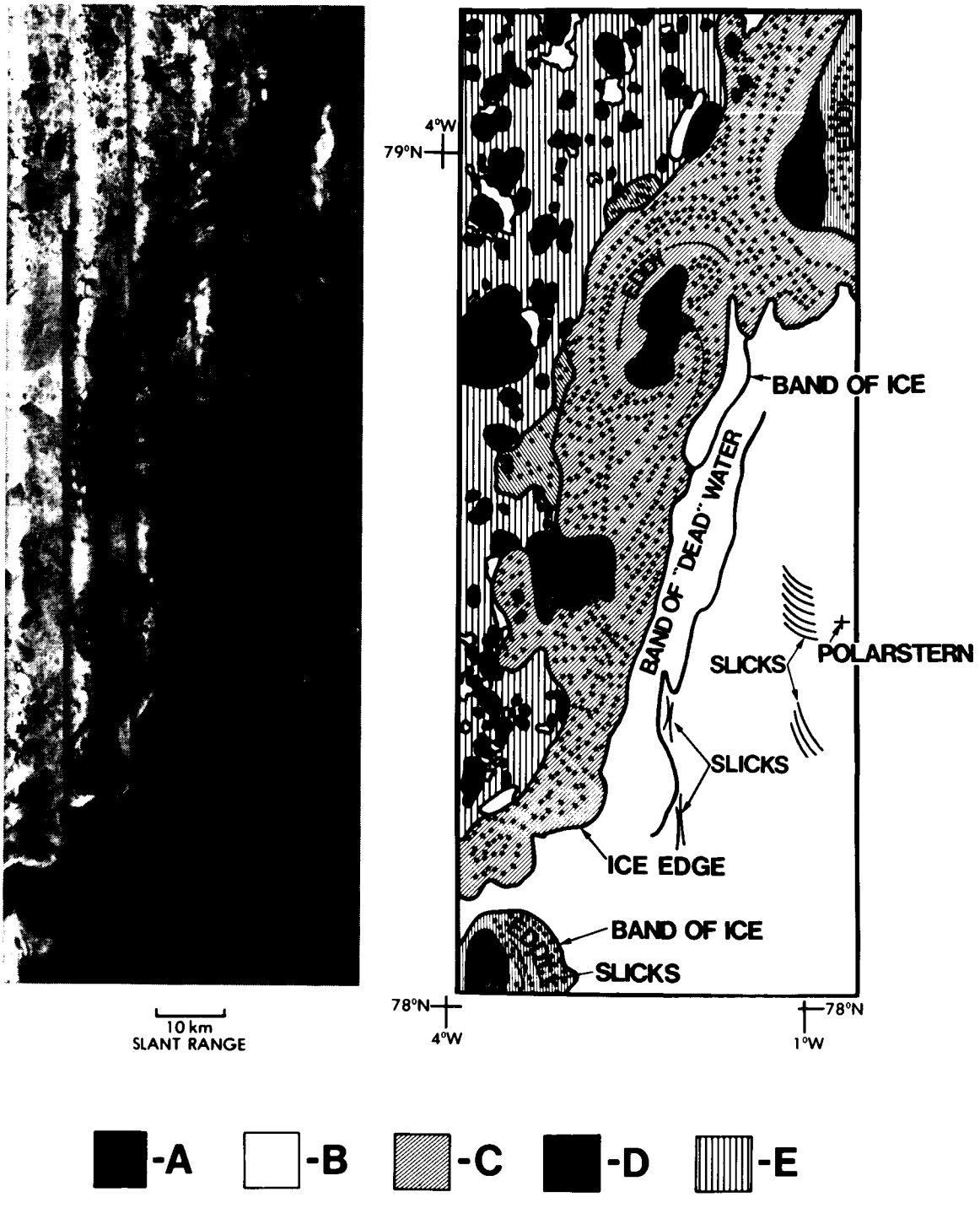


Figure 2. L-band (1.2 GHz) mosaic collected by the ERIM/CCRS X-C-L-band SAR system on 5 July 1984 (1400-1700 GMT). The large eddy is clearly visible on the 3m x 3m resolution data, as are large individual floes (labeled 'A' on the interpretation) and polynyas and ice-free ocean areas (labeled 'B'). The interpretation also indicates areas of varying ice concentration, the range of floe sizes, and the median size: 30%, 1-50m, 12m, for 'C'; 80%, 1-1500m, 150m for 'D'; and 80%, 10m-6km, 1km for 'E', respectively.

N87-17151

# OBSERVING THE POLAR OCEANS WITH SPACEBORNE RADAR

Drew Rothrock
Applied Physics Laboratory, University of Washington
Seattle, Washington

In this brief presentation, I would like to explore the application of spaceborne imaging radar data to polar oceanography and sea ice. Several problems come to mind which are presently ripe with ideas and models, but are in need of new data--SAR data--for any progress to be made. These are the study of the ice mass balance, the ice momentum balance, and the circulation of the Arctic Ocean. We will describe these problems and the data which is applicable to them and can be extracted from SAR imagery. Finally, we will discuss some uses of these data to explore mesoscale processes which affect the oceans and ice cover.

The ice cover undergoes advances and retreats on a range of time scales, but predominantly over the annual cycle. To understand the balance which determines ice extent, we must observe where ice is produced and where it melts. To do this at the most simple level--to describe the balance of ice covered area, we need to observe ice velocity and ice concentration. To describe the mass balance requires additional observations of ice thickness, which are presently beyond the direct reach of remote sensing, but can be estimated from continuous observations of the field of ice motion (Thorndike et al, 1975).

Consider recent studies of ice balance. Walsh et al (1985, Figure 14) analyze model output and find a strong net sink of ice mass in the northern Greenland Sea. Moritz (personal communication) analyzes buoy motions and concentrations from ice charts and finds the northern Greenland Sea to be a weak source of ice area. These results are not incompatible; the ice grown in the region is thin whereas the ice melted there is presumably older thick ice advected down from the Arctic Ocean. The point is that the first result is based on model output rather than direct observations of ice thickness, concentration or motion, and the second result is based on a very modest data set. Much stronger results on this description of the ice mass balance will be derived with kinematic data from SAR and with concentration data from SAR and passive microwave.

Another problem susceptible to SAR data is the circulation of the Arctic Ocean. We have the potential to observe the surface velocity of this ocean (that is, the motion of its ice cover) better than any other, and to prescribe its surface buoyancy flux by virtue of ice motion, ice concentration and air temperature observations. The thermohaline structure of the ocean is determined by advected Atlantic Water, and by the formation of dense waters at the surface in the Greenland and Iceland Seas and over the Siberian continental shelves (e.g., Aagaard et al, 1985). Good SAR observations of ice velocity and ice deformation would add enormously to our ability to simulate this circulation and compare results to oceanographic observations from buoy-mounted thermistor and conductivity chains, and from SOFAR floats.

A third appetizing problem is that of ice momentum balance, approximated most simply as a balance between air stress and water stress U = A*G + C, where U is ice velocity, A is a matrix involving ratios of wind and water drag coefficients, G is the geostrophic wind, and C is the current at the base of the ocean mixed layer. An investigation using surface pressure and ice velocity data from buoys showed that through this relationship, the wind explained about 70% of the variance of the ice motion (Thorndike and Colony, 1982). Spaceborne SAR would allow the study of this relationship in the seasonal ice zones where buoys cannot survive and where ice stress may add a term to the momentum equation. Ice stress depends on ice deformation which can be measured by SAR, but not by the coarse buoy network.

To apply SAR data to these problems, we must develop a suitable sampling strategy for use of data from ERS-1 and subsequent satellite radars. The requirement is to settle on an area over which to average deformation and concentration, and then verify how these averages vary spatially. Can we interpolate these mean quantities between SAR ground swaths several hundred kilometers apart?

An observational program based on SAR images will require automated algorithms for extracting geophysical data. What variables can be extracted, and to what extent are the necessary algorithms in hand? The most promising variables appear to me to be ice velocity and deformation, ice concentration, and floe size and lead size and spacing statistics. The latter group concerning the fragmentation of the ice cover has as yet received little effort towards automation, but techniques for extracting these data are available, and automating them should not be difficult. Floe and lead geometrics are of interest more to operations than to the issues of mass and heat balance being focussed on here.

Ice drift and deformation, on the other hand, are central to the problems outlined above, and are ideally suited to measurement from SAR imagery, whose high resolution makes it possible to follow a dense set of ice features--each grid intersection in Figure 1. (See Curlander et al, 1985, and Fily and Rothrock, 1985.) Such dense data allow a far more useful and reproducible estimate of mean deformation than just three or four data points from imagery or from buoys. This data extraction problem is clearly defined, is receiving attention at several institutions, and will yield, it appears, to further development before ERS-1 is launched. Ice motion measurement is facilitated by two facts: feature recognition depends on relative not absolute brightness, and the accuracy of deformation estimates can be estimated by applying the technique to (non-deforming) land.

Ice concentration (areal fraction of ice coverage) has been estimated from SAR imagery by several investigators, with techniques that tend to be operator dependent (e.g., Shuchman, this volume). The problem is more difficult than motion measurement because both absolute backscatter and field corroboration are crucial to identifying ice types correctly from imagery. Concentrations of several types of ice--multiyear ice, first year ice, grease ice, and open water--have been estimated from SIR-B imagery by supervised classification by Holt and Carsey (personal communication). Comparisons with SMMR concentration estimates have been within one percent for some scenes, and within five to ten percent for others.

These types of observations can unravel some of the puzzles about processes which occur on scales of one to one hundred kilometers. For instance, the detailed measurements in Figure 1 suggest replacing the traditional continuum velocity assumption with a model consisting of a set of random cracks with velocity discontinuities along those cracks (Thorndike, 1981). They can also allow us to pin down the relation between mean deformation of a large area and the production of new open water where ice grows rapidly and salt flux to the ocean is intense. (Fily and Rothrock, 1985).

SAR is an excellent tool for observing ice covered oceans. To realize its promise, we must develop firm sampling requirements and strategies, and automated algorithms for extracting ice kinematics, ice concentrations, and floe and lead statistics. Challenging problems await this new data.

## REFERENCES


Aagaard, K., J. H. Swift, and E. C. Carmack, 1985. Thermohaline circulation in the arctic mediterranean seas. J. Geophys. Res., 90, No. C3, 4833-4846.

Curlander, J. C., B. Holt, and K. Hussey, 1985. Determination of sea ice motion using digital SAR imagery. IEEE J. of Oceanic Engineering, Vol. OE-10, No. 4, 358-367.

Fily, M. and D. A. Rothrock, 1985. Extracting sea ice data from satellite SAR imagery. Int'l Geoscience and Remote Sensing Symp., 7-9 October, 1985, Amherst, Mass.

Thorndike, A. S., 1981. Kinematics of sea ice. NATO Advanced Study Institute, Maratea, Italy, September, 1981. The Geophysics of Sea Ice, N. Untersteiner, Ed., in press, Plenum Publ. Co.

Thorndike, A. S., and R. Colony, 1982. Sea ice motion in response to geostrophic winds. J. Geophys. Res., 87, No. C7, 5845-5852.

Thorndike, A. S., D. A. Rothrock, G. A. Maykut, and R. Colony, 1975. The thickness distribution of sea ice. J. Geophys. Res., 80, No. 33, 4501-4513.

Walsh, J. E., W. D. Hibler, and B. Ross, 1985. Numerical simulation of northern hemisphere sea ice variability, 1951-1980. J. Geophys. Res., 90, No. C3, 4847-4865.

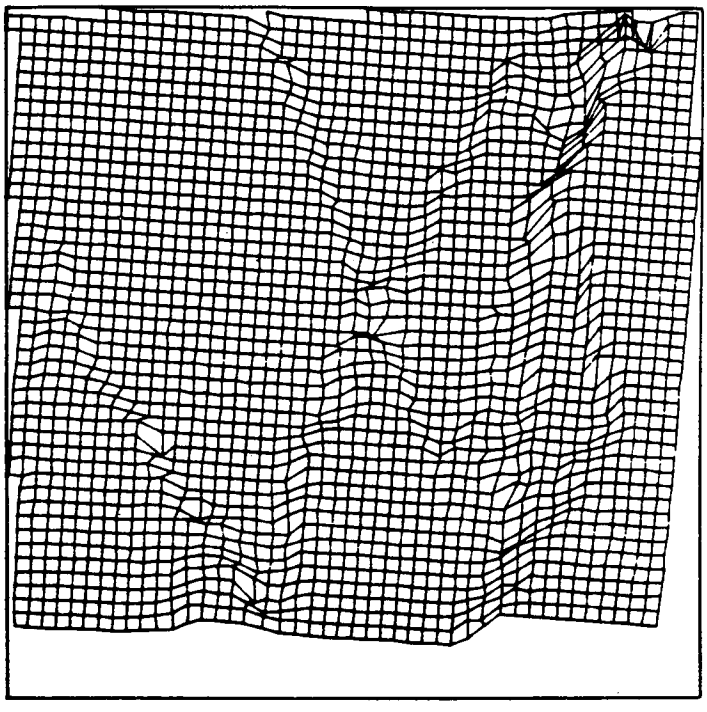

Figure 1. The deformation of a grid embedded in the ice. The grid was undeformed three days earlier. The displacement of each grid vertex was tracked automatically by cross-correlating small sections of two sequential SEASAT SAR scenes, first at highly degraded resolution, but iterating through scenes with increasing resolution (Fily and Rothrock, 1985). No role was played by an operator. The figure is 100 km on each side. Note the large rigid floes separated by narrow zones of intense deformation. The figure is 100 km on each side.

# Sensor and Processing Technology

N87-17152

# FEATURES AND TECHNOLOGIES OF ERS-1 (ESA) AND X-SAR ANTENNAS

H. Schüssler and R. Wagner
Dornier System GmbH
Friedrichshafen, Germany

## ABSTRACT

The paper describes features and technologies of planar waveguide array antennas developed for spaceborne microwave sensors. Such antennas are made from carbon fibre reinforced plastic (CFRP) employing special manufacturing and metallisation techniques to achieve satisfactory electrical properties.

Mechanical design enables deployable antenna structures necessary for satellite applications (e.g. ESA ERS-1). The slotted waveguide concept provides high aperture efficiency, good beamshaping capabilities, and low losses. These CFRP waveguide antennas feature low mass, high accuracy and stiffness, and can be operated within wide temperature ranges.

## I. BACKGROUND AND CONCEPTUAL APPROACH

In view of mutual cooperative interests in the field of SAR antenna development, the German and Swedish space administrations agreed to sponsor a common antenna technology programme in 1980. Overall technical responsibility was given to Dornier System, whereas Ericsson was responsible for all electrical aspects. This programme has proven the feasibility of CFRP technology for space-borne antennas. This technology is currently being applied to two SAR missions for different carrier frequencies, but having a number of mechanical parameters in common:

- The synthetic aperture radar, to be flown on the first ESA remote sensing satellite ERS-1, has a 10 m x 1 m deployable array for C-band operation, and

- X-SAR, conceived for cooperative missions together with SIR-C, employs a 12 m x 0.5 m planar array for the 9.6 GHz frequency band.

ERS-1 mission requirements, visible during the course of the technology programme, suggested an antenna concept as outlined in Table 1: Planar array, subdivided into appropriate mechanical and electrical subpanels, employing slotted waveguides made from carbon fibre reinforced plastic. The panels are supported by a lightweight deployable truss structure having a minimum number of bars. CFRP technology is applied wherever reasonable, particularly for all parts of significant dimensions. This concept provides lightweight deployable structures with good planarity maintained under severe environmental conditions.

Table 1. Conceptual approach

| Requirement | Solution |
|---|---|
| Large deployable structure, one long dimension > 10 m | Planar array, stiff-mounted centre panel with wings comprising 2 or more outer panels |
| High stiffness, high alignment accuracy, locking function | Deployable supporting truss structure with thin tabular bars |
| Low mass, thermally stable | Carbon fibre reinforced plastic (CFRP) |
| High aperture efficiency, low losses, beam-shaping requirements | Slotted waveguide array with coupling guides and waveguide distribution network |

## II. WAVEGUIDE TECHNOLOGY

The CFRP material offers considerable performance advantages when compared to aluminium: The specific stiffness to mass ratio of suitably designed CFRP is about three times that of aluminium, which leads to structures of markedly lighter weight. The coefficient of thermal expansion of CFRP is 1/25 that of aluminium. Even though a CFRP construction is likely to experience higher thermal differentials in a changing environment due to its lower thermal capacity and conductivity, an order of magnitude advantage still remains. The electrical conductivity of CFRP is unfortunately far from adequate. Thus coating processes with highly conductive materials have been developed.

Waveguide metallisation, especially of the internal walls, required extensive experimental work. Of the numerous metallisation processes available, the indirect technique has provided superior adhesion. Here mandrels are metallised prior to CFRP lay-up. A special surface treatment is applied to the metal which assures excellent adhesion of the metal layer to the cured CFRP. This process can be applied to straight mandrels, which can be extracted and reused after CFRP manufacturing. It can also be applied to sacrificial mandrels for more complex components. These mandrels are made from aluminium, and chemically decomposed after each use. Metallisation after final machining and slot cutting is accomplished by silver paint with a stable binder. This indirect metallisation technique has been space qualified for temperatures ranging from -70 to +115 degrees centigrade.

## III. ANTENNA DESIGN

As illustrated in Fig. 1, the antenna consists of horizontal radiating waveguides having longitudinal slots on the broad side. A subarray is fed by a vertical coupling waveguide. Radiating and coupling waveguides

are operated in resonant mode. This requires careful design with respect to VSWR, sidelobes, and bandwidth, but avoids beam squinting during emission and reception of the chirped radar pulse. Bandwidth limitations of the resonant guides, and the need for a suitable mechanical subdivision for folding, led to 1 m long subarrays for the ERS-1 antenna. Each pair of subarrays is combined into one mechanical panel. This can be seen in Fig. 2, which depicts the mechanical configuration of the deployable antenna and shows panels together with the supporting truss structure. The waveguide distribution network on the rear side of the panels has been omitted.

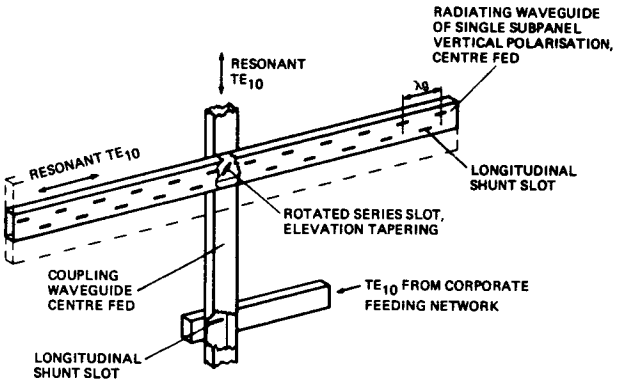


Figure 1. Electrical concept

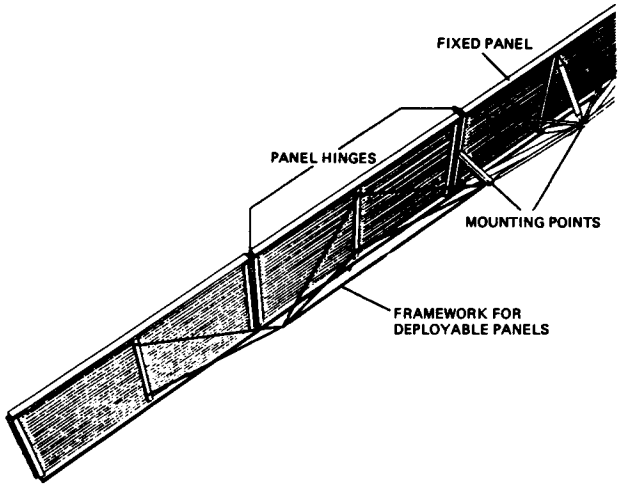


Figure 2. Mechanical configuration

## IV. SAR ANTENNA FOR ERS-1 (ESA)

The ERS-1 SAR antenna is currently in full production, after completion of all essential design activities. Among these, a 2-panel (4 m x 1 m) functional model was manufactured and tested. A series of deployment tests under simulated zero-g conditions was carried out with this model. Measured out-of-plane distortions were within $\pm$0.4 mm peak and $\pm$0.1 mm average. The complete 10 m engineering model for ERS-1 will be assembled this summer. Stowed dimensions of this C-band antenna are about 2 m x 1 m x 0.6 m, and its mass is around 68 kg.

## V. X-SAR ANTENNA

X-SAR, a joint project together with SIR-C, is currently in the definition and specification phase. The foldable CFRP slotted waveguide array, to be operated at 9.6 GHz, will be attached to the 12 m long SIR-C antenna support structure. This project will result in the first multi-frequency SAR facility for microwave remote sensing from space. It will illuminate the earth at incidence angles ranging from 15 to 60 degrees.

General features of the X-SAR antenna are included in Fig. 3. This also depicts the ideal antenna elevation diagram, and the computed side-looking geometry for incidence angles around 57 degrees. The useful swath for this specific scenario is between 338 and 384 km from the shuttle ground-track. There are two ambiguous regions, including one around the nadir point. Theoretically the (strong) nadir return could be avoided by suitable timing of the radar (i.e. through selection of appropriate pulse repetition frequency and echo window). However, there are too many uncertainties in the required timing during real flight conditions. As a preventive counter-measure, elevation sidelobes at angles between 30 and 55 degrees off the antenna boresight will be further suppressed.

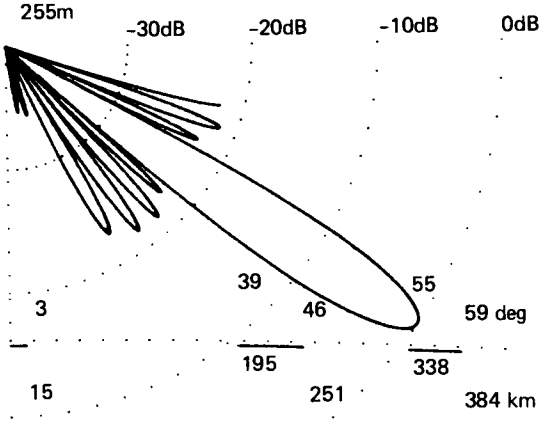


- 9600 ± 10 MHz frequency band
- 12 m long VV polarised antenna
- Elevation sidelobe suppression
- Antenna will be mounted onto SIR-C antenna frame
- Peak power is 3 kW
- Planarity shall be better than ± 1 mm

Figure 3. X-SAR antenna features

## ACKNOWLEDGMENTS

The CFRP antenna technology programme was sponsored by the German Ministry of Research and Technology, and by the Swedish Space Corporation. The ERS-1 programme is financed by the European Space Agency. X-SAR is being designed on behalf of the German Ministry of Research and Technology, and coordinated by the Deutsche Forschungs- und Versuchsanstalt für Luft- und Raumfahrt (DFVLR).

## BIBLIOGRAPHY

Ingvarson, P., Wagner R., "Synthetic Aperture Radar Antenna from CFRP." Proc. of the 1982 Int. Geoscience and Remote Sensing Symp. (IGARSS '82), Munich, June 1982, pp. 4.1-4.6.

Wagner, R., "Technology for the ERS-1 Antenna," Proc. of a Workshop on Mechanical Technology for Antennas, Noordwijk, The Netherlands, June 1984 (ESA SP-225), pp. 59-66.

Wagner, R., "Carbon Fibre Waveguide Metallisation." Proc. of the 5th Int. Conf. on Composite Materials (ICCM-V), San Diego, California, July/August 1985, pp. 419-432.

# OFF-LINE PROCESSING OF ERS-1 SYNTHETIC APERTURE RADAR DATA WITH HIGH PRECISION AND HIGH THROUGHPUT

J. Gredel, W. Markwitz, W. Noack, and G. Schreier
Deutsche Forschungs- und Versuchsanstalt für Luft- und Raumfahrt
Federal Republic of Germany

## I. INTRODUCTION

The first European remote sensing satellite ERS-1 will be launched by the European Space Agency (ESA) in 1989. The expected lifetime is two to three years. The spacecraft sensors will primarily support ocean investigations and to a limited extent also land applications. Prime sensor is the Active Microwave Instrumentation (AMI) operating in C-Band either as Synthetic Aperture Radar (SAR) or as Wave-Scatterometer and simultaneously as Wind-Scatterometer.

In its SAR mode the AMI will cover a 100 km wide swath with a 23° incidence angle at midswath. The satellite orbit will be sun-synchronous, with a nominal altitude of 777 km. The ground repeat pattern will be 3-days during the initial stages, but will be changed up to twice a year to give variable repeat patterns of up to 30 days.
ERS-1 will perform 5256 orbital revolutions per year. Assuming an average of 8 minutes SAR acquisition time per orbit - corresponding to 32 scenes (100 km x 100 km) - a total of 168,000 scenes per year will be acquired. The raw data wil be transmitted in real time with 105 Mbps via an X-Band link to a worldwide network of acquisition stations where all data will be reported on High Density Digital Tapes (HDDT). A significant amount of this data volume will be received with European ground stations.

In Europe there will be two distinct types of processing for ERS-1 SAR data, Fast Delivery Processing and Precision Processing.
Fast Delivery Processing will be carried out at the ground stations and up to three Fast Delivery products per pass will be delivered to end users via satellite within three hours after data acquisition.
Precision Processing will be carried out in delayed time and products will not be generated until several days or weeks after data acquisition. However, a wide range of products will be generated by several Processing and Archiving Facilities (PAF) in a joint effort coordinated by ESA.

The German Remote Sensing Data Center (Deutsches Fernerkundungsdatenzentrum DFD) will develop and operate one of these facilities. DFD has been implemented by DFVLR to promote and support the utilization of remote sensing data in the Federal Republic of Germany (FRG). The related activities include the acquisition, processing and evaluation of such data for scientific, public and commercial users.
Since many years DFD is involved in processing of SAR data including data from the SEASAT L-Band SAR, the Canadian airborne X/C/L-Band SAR and the Shuttle Imaging Radar SIR-B. For SEASAT several hundred scenes acquired over Europe were processed under ESA contract with a processor that was developed by the Canadian firm MDA [Bennett, 1981] under a joint contract from the Canadian Center for Remote Sensing and DFVLR.

Based on this experience the German Remote Sensing Data Center is presently performing a phase-B study regarding the development of a SAR processor for ERS-1. The conceptual design of this processing facility is briefly outlined in the following chapters.

## II. SYSTEM DESCRIPTION AND PRODUCT DEFINITION

The SAR Processing and Archiving Facility is functionally divided into several subsystems executing processing tasks and performing monitor and control functions as outlined in Figure 1. The major processing tasks are Preprocessing, Geocoding and Data Management.

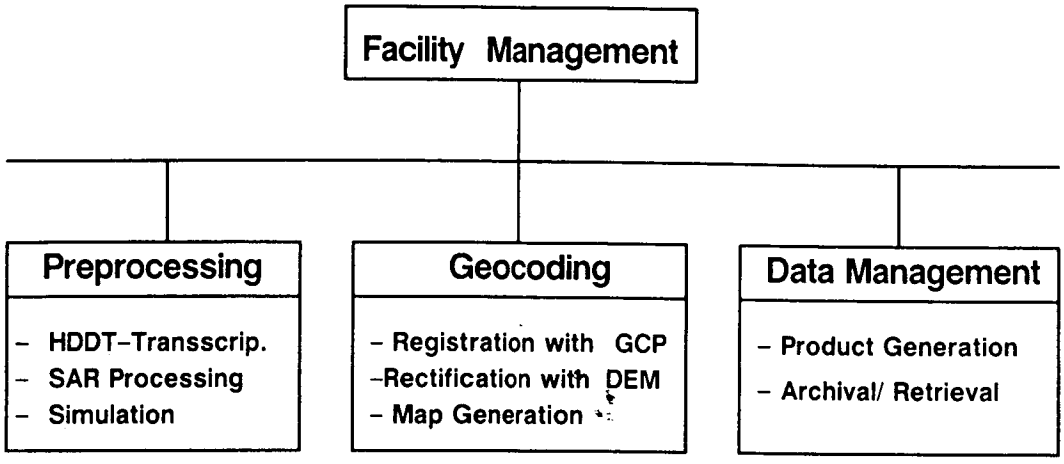


Figure 1. The SAR data processing chain

The Preprocessing task comprises several functions such as the transcription of HDDT's, the SAR processing and the simulation of raw SAR data. The major of these tasks is the SAR processing. Depending on the selected processing parameters, image data sets with different characteristics will be generated and passed to the other subsystems for further processing and handling. The Preprocessing subsystem in itself is complex enough to require operations control support using an expert system. Accordingly the subsystem is called Intelligent SAR Processor ISAR.

The Geocoding task accepts the earth located preprocessed data sets as input and performs geometric manipulations. The major subtasks are the optional rectification of SAR data with Ground Control Points (GCP) and/or Digital Elevation Models (DEM) - and the subsequent resampling to a geocoded grid in different map projections.

The Data Management task finally comprises product generation and all related archival and retrieval functions. The Product Generation step converts the annotated data sets which are generated during Preprocessing and Geocoding into physical products that can either be archived or distributed to the user who has requested it. Products are either digital products such as Computer Compatible Tapes (CCT) or different kinds of optical disks or photographic images on film or paper in various formats.

The above described processing subsystems for Preprocessing, Geocoding and Data Management form the SAR Data Processing Chain. This chain represents a distributed processing system with the subsystems executing their tasks in parallel, often in a pipeline configuration. All subsystems are attached to a high performance Local Area Network (LAN) which enables

- the exchange of large data sets among the different subsystems and
- the operations control of the integrated system.

The data flow through the system and the operations and quality control is performed by software tools for data and facility management which are implemented on workstations that have access to all subsystems via the LAN. These functions might again be supported by an expert system.

A variety of SAR Products will be derived with the SAR Data Processing Chain. Starting with Raw Spacecraft Telemetry Data (level 0), recorded on HDDT, plus orbit and attitude data, the ISAR transcription task generates Annotated Raw Data Sets (level 1), which can be extracted on request. The subsequent SAR processing task generates a variety of Bulk Products while the Geocoding task finally generates Geocoded Products from Bulk Products.
Bulk Products (level 1.5) are digital images which are earth located. The image data sets consist of pixel arrays ordered in range and azimuth, representing a segment of the ground swath. The radiometric information is as accurate as possible. The earth location is derived from a precise orbit and the best attainable attitude information. Geometric manipulations are restricted to an optional slant range to ground range conversion.
Geocoded Products comprise Corrected Products, Precision Products and Map Products. Corrected Products (level 2A) are derived from Bulk Products in ground range. Such products are of use for scenes taken over the open ocean, coastal areas and flat terrain. Depending on the area, none to many GCP's are used for the rectification resulting in quite different absolute and relative geometric accuracies. Several map projections such as UTM, stereographic and others can be selected. Precision Products (level 2B) and Map Products (level 2C) are both derived from Bulk Products in slant range. Such products will be generated for areas with moderate to strong variations of terrain elevation. The rectification makes use of Digital Elevation Models to avoid severe geometric distortions and shall achieve absolute and relative geometric accuracies in the order of the pixel sizes (30 m for ERS-1). However, the accuracy finally achieved depends very much on the accuracy of the DEM used. While a precision product would be derived from a single scene, a map product could originate from several scenes applying mosaicking techniques. The Map Product in a proposed scale of 1:200,000 can directly be compared with existing topographic or thematic maps.

## III. THE PREPROCESSING SYSTEM

According to the system description given in chapter 2 Preprocessing is the first step in the production procedure of SAR imagery. The term Preprocessing designates the task that converts raw data sets plus auxiliary information to annotated raw data sets and to digital image data sets. The ERS-1 satellite will carry the first SAR sensor which is designed to work operationally for several years. This is the most significant difference to

all spaceborne SAR systems flown up to now. From that it is clear that existing Preprocessing systems like GSAR [Bennett, 1981] with an average throughput figure of one product per day will not be adequate to process a reasonable amount of data. Therefore a high throughput capability represents a hard requirement for the processor. Because the output product of the Preprocessor can be used as an input to the Geocoding system this latter task can best be performed if the Preprocessor products are of best possible quality. Therefore both requirements - high precision and high throughput - are very important to the Preprocessor.

The term high precision will be applied in a many layered way. First of all it shall be a requirement which is closely related to product quality. In this context pixel location accuracy in cross-track and along-track direction shall be a key issue. These parameters are effected essentially by the accuracy of the earth model, the state vector of the satellite and the attitude measurements.
It is required to achieve a location accuracy of 20 m in cross-track and 150 m in along-track for all level 1.5 products (acquired over slow varying terrain slope). In the case of ERS-1 the GEM-6 earth model [Klinkrad, 1985] will be the standard model which is characterized by the earth oblateness coefficient and the semimajor axes. The state vector gives all necessary information about the position of the satellite in all three axes as well as the velocity vector. The Mission Management and Control Center of ESA delivers the predicted orbit with an accuracy of 36 m, 51 m and 1300 m (radial, cross-track, along-track). The restituted orbit values are 25 m, 25 m, and 100 m. However, one product offered by the German PAF will be a refined state vector using primarily laser tracking data which have an accuracy of less than 1 meter in the position and less than 10 cm/s in the velocity and it will be available a few weeks after acquisition. Therefore it is one of the main differences between the Fast Delivery Processor and the Off-line Processing Facility that high precision orbit data are used which are not available shortly after data acquisition.
The refinement of the satellite attitude measurements in its three axis, roll, pitch and yaw as well as the related acceleration figures will be done by a cross-correlation of a replica of the theoretical antenna pattern positioned according to the attitude data with several ensembles of the real azimuth spectral data. This operation can be done randomly and repeatedly across the swath and along the whole 100 km in azimuth supported by the fact that the data are accessible in both image directions without delay and that the host will be a very fast machine with a floating point performance of 2 megaflops.
Another topic of accuracy will be the calibration of the range chirp and the compensation of the antenna gain. High precision will also be applied to the calculation of all parameters relevant to the latter items. Moreover each complex sample will be represented with 32 bits throughout the processing.
In order to give the user a full flexibility for his choice of product, a whole family of intermediate products (level 1.5) will be available which comprise the Fast Delivery Product, Bulk Products in slant- or ground-range and even products with complex pixel representation preserving phase information.
The system is designed to achieve a throughput in the order of 6000 products per year. This requirement has several consequences in terms of hardware and software design which will be described in the next chapters. The software related aspects will be given comprehensively in a separate paper [Noack, 1986].

The requirements high precision and high throughput have been the main driving factors for the hardware selection. It has already been mentioned that the processor shall be capable of processing 6000 products per year. Assuming standard operation times this results in a processing time of 1/2 hour per level-1.5-product. Moreover the system shall be flexible to be adapted to other spaceborne sensors like the German XSAR.

There has been chosen a distributed, parallel architecture arranged as a lattice whose nodes are single purpose CPUs and the branches represent computer-computer links. Figure 2 gives an overview of the ISAR hardware configuration.

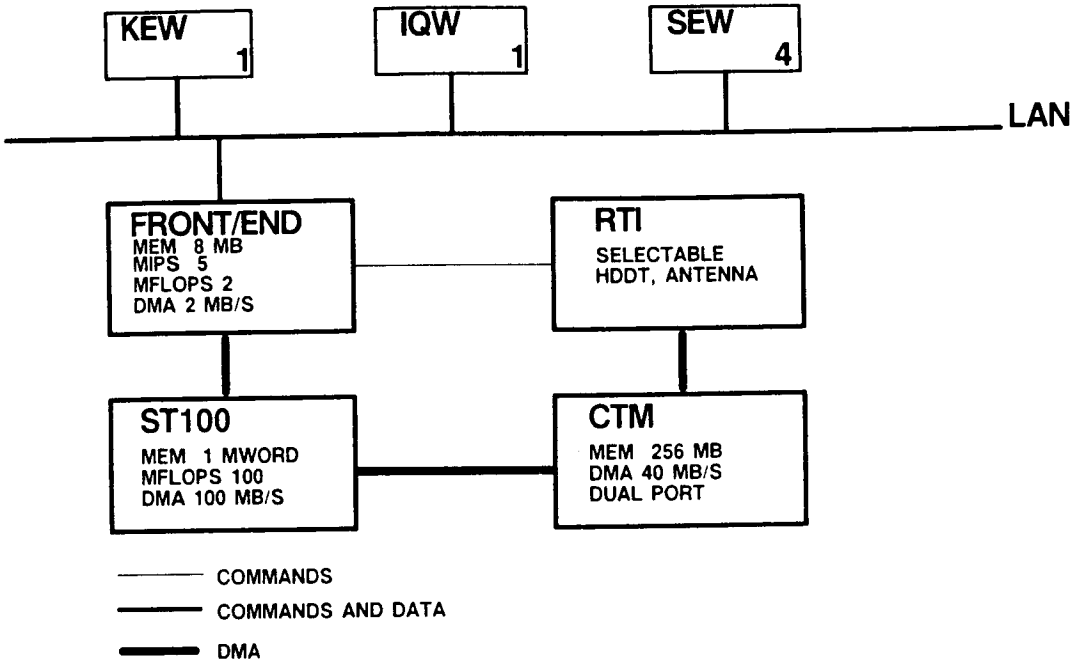


Figure 2. ISAR hardware configuration

The particular subsystems are the Knowledge Engineering Workstation (KEW), the Image Quality Analysis Workstation (IQW), the Software Engineering Workstation (SEW), the Front/End Hostcomputer (FEH), the ST-100 Arrayprocessor (ST-100), the Corner Turn Memory (CTM) and the Real Time Input Facility (RTI).

The Local Area Network connects all systems with interactive tasks like software development, process configuration, image quality analysis etc. with the high throughput computers FEM, ST-100 or RTI. As a special device the CTM will be used as a data buffer between HDDT, the regular input medium to the processing system, and the ST-100 Arrayprocessor. It will be loaded directly from HDDT with a full reproduce speed of 105 Mbit/sec. From this point the SAR data are accessible randomly in range and azimuth with a DMA speed of 40 Mbyte/sec.

The data flow (see Figure 3) is organized as follows: First of all the Data Management System sends a processing request to the KEW. There the order will be worked out to a full scene configuration. After the HDDT has

been mounted and automatically positioned the data transfer will take place for a full ERS-1 scene in about 15 seconds. Now the ST-100 can start the required correlation task up to the final processing level. At the end the data are stored on a disk of the Front/End Computer ready for being transferred to the Image Quality Workstation or to the Data Management Computer.

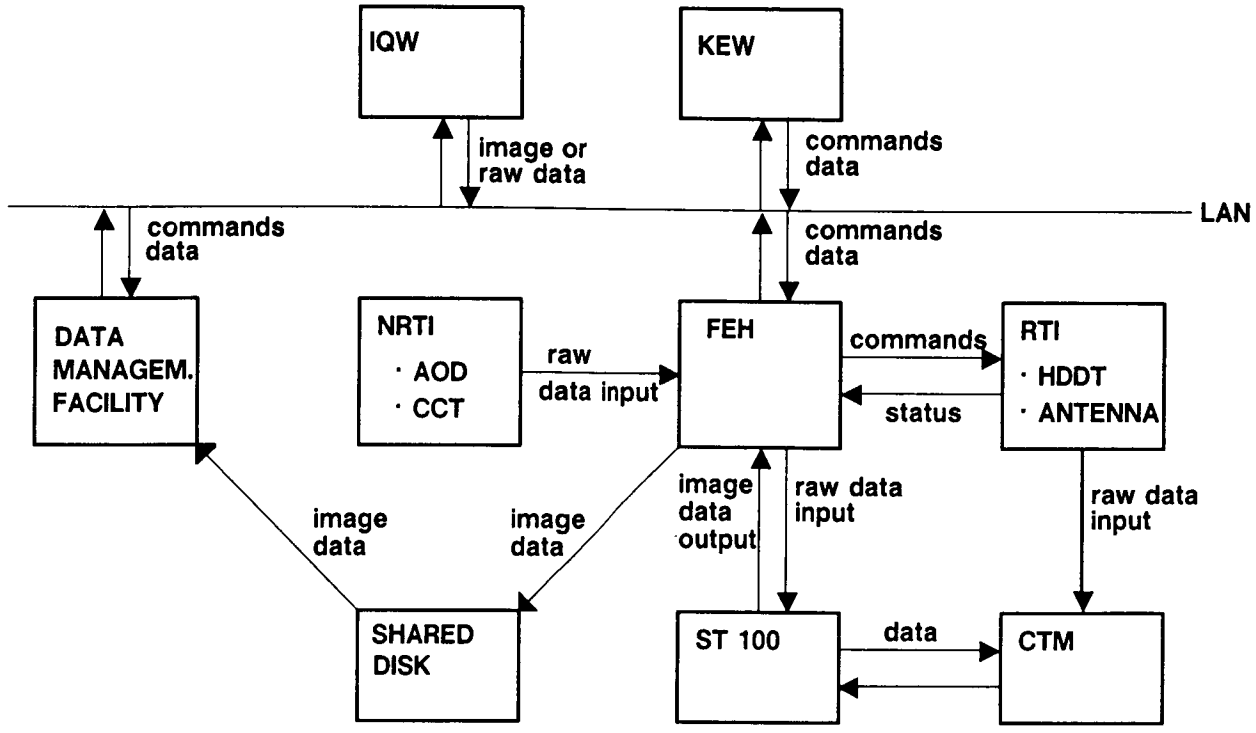


Figure 3. ISAR data flow

Basically SAR imaging and processing is a two-dimensional operation whose coordinate axes are designated across track and along track respectively. The Range-Doppler-Algorithm uses a separate matched filter operation implemented in the Fourier frequency domain and turns out very advantageously in terms of quality and speed. It is a very well known and documented procedure and has therefore been chosen as the standard processing algorithm for ISAR.

The term Range-Doppler designates the timely ordered subsequence of processing steps of which the most important are

- Range Compression,
- Azimuth Compression and
- Interpolation

The penalty for breaking up the two-dimensional nature of the imaging process into two one-dimensional procedures comprises in two additional processing steps which take care for earth rotation and for effects due to varying across track distance to a target during integration time.

There is a requirement that the software shall be implemented in a high-level language. Additionally there shall be an integrated software development system covering all phases of the software lifecycle. An analysis of all development systems on the market showed a large variety of products all of which had some deficiencies. From that point of view ADA has been chosen as implementation language, because it includes its own development environment.

All central parts of the software system will be managed by the expert system running on the KEW which controls the whole production process by

- receiving production orders from the PAF,
- configuring the production process,
- supervising the correlation sequence and
- supporting the operator in all decision processes.

Up to that point all processing is related to products of level 1.5. The generation of all higher level SAR products of the German PAF will be described in the subsequent chapter.

## IV. THE GEOCODING WORKSTATIONS

The term Geocoding describes the task, which accepts digital SAR image data sets from the Preprocessing System and generates geometrically corrected and precisely located Geocoded Products in different map projections. The high accuracy shall be achieved using precise orbit/attitude data, Ground Control Points and Digital Elevation Models. The achieved accuracy shall be within the range of the pixel size. The throughput design goal for the Geocoding System is to produce an average of 8 Geocoded Products per day or 2000 products per year.
The precision Geocoding of SAR images is a task which requires both an image display system for the interactive subtasks such as registration and quality control and a high performance processor for the rectification tasks which are required for the rotation and resampling of large data matrices with high throughput. The hardware to be selected shall be compatible with other systems presently used at the German Remote Sensing Data Center.

The DFD has started to implement a network of UNIX-workstations, all interfaced to a Local Area Network, with some of these workstations performing image processing tasks. The UNIX-workstation concept was chosen deliberately to become as far as possible independent of the selected hardware configuration for future software developments. In addition to that, such workstations are cheap compared to minicomputers and the use of several identical workstations increases the throughput capability and the operational reliability.
Present plans are to implement three workstations for the SAR Geocoding task. Though the final decision for the manufacturer has not been made, a state of the art workstation SUN-3/160 from SUN Microsystems, Inc. is being used as model configuration (see Figure 4).

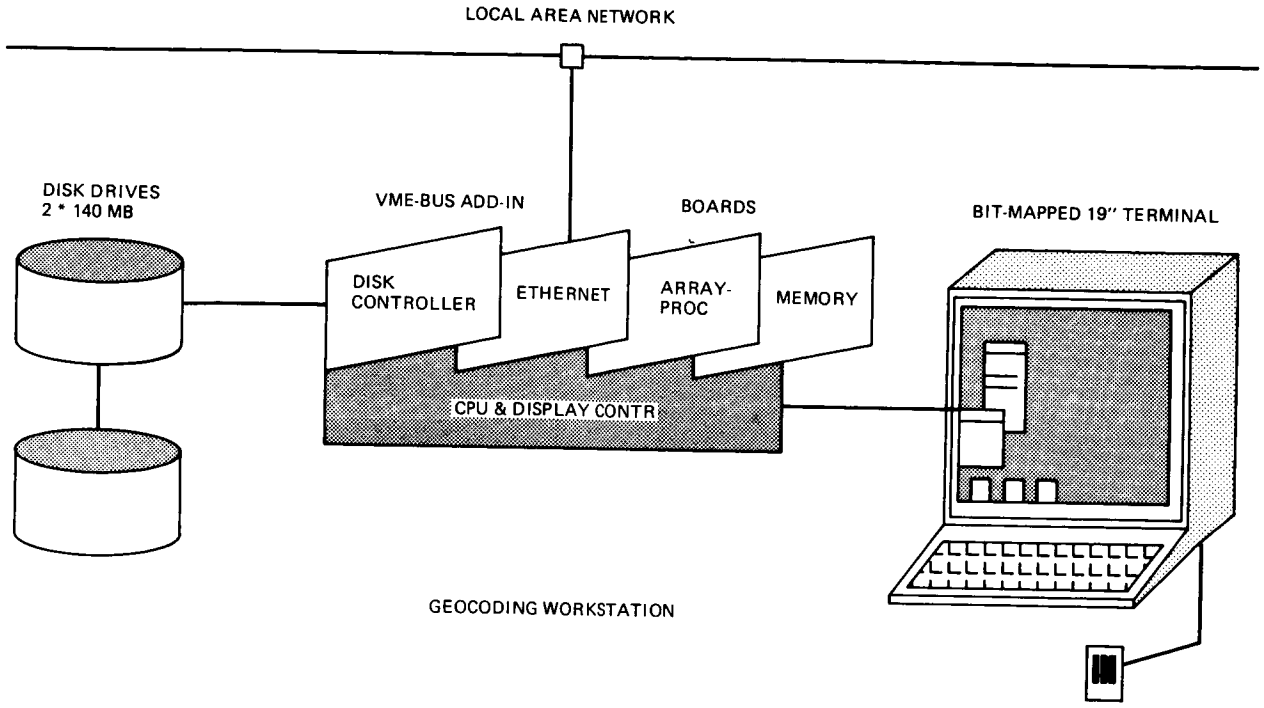


Figure 4. Workstation for Geocoding of ERS-1 SAR data

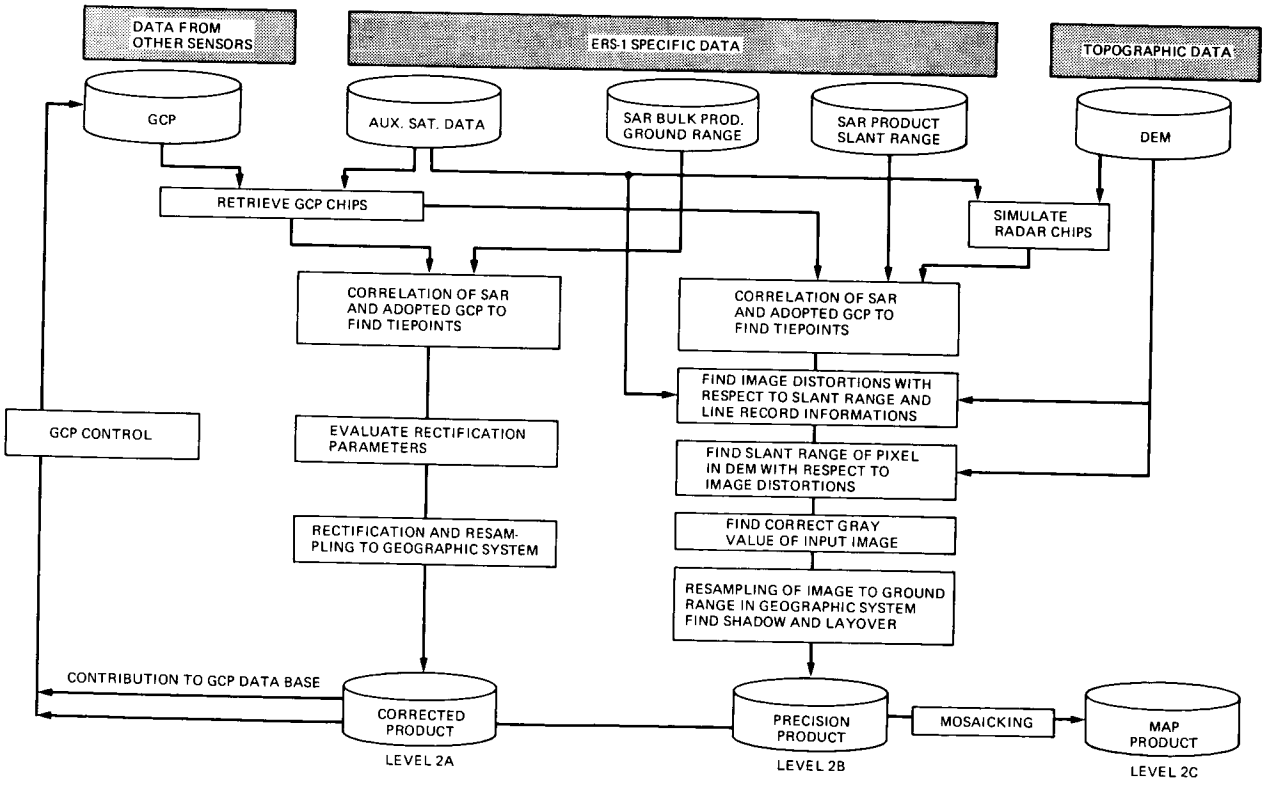


Figure 5. Data flow and processing steps for the generation of Geocoded products

The Geocoding algorithms will be part of the UPSTAIRS image processing software. UPSTAIRS - installed in 1985 at the German Remote Sensing Data Center - is designed to fulfill the requirements of remote sensing users and is open to incorporate future developments due to its modular structure and programming interface. Figure 5 depicts a flowchart for the generation of Geocoded products.

Coming from five data bases, two main data streams can be distinguished. The first describes the generation of a Corrected Product, using only geographic coordinate information from the satellite auxiliary data and, if required and available, Ground Control Points. When the GCPs are detected in the radar image by automatic algorithms, standard rectification and resampling procedures will generate the Corrected Product.

The second data stream uses GCPs to compute the internal distortions of the SAR image especially in azimuth with respect to slant range distance. Coming from exact located DEM points, the slant range is computed involving the distortions found above and thus giving a reference to a point in the slant range input image. Therefore pixel coordinates will be found even in regions of typical radar distortions. Notice that the process of generating Corrected and Precision products will enhance the GCP library, thus contributing "boot-strapping" information for following radar images. Map Products will be generated by mosaicking methods from the Precision Product.

To meet the requirements of the Geocoding System, approaches and algorithms are modified for restituting the radar geometric distortions and producing level precision and map products. (More detailed information can be found in Domik, 1984; Ehlers, 1983; and Maier, 1985.)

To cope with the huge amount of GCP and DEM data, a GCP library and a DEM data base will be installed, both able to accept data from different sources and in different formats. The design of these data bases fulfills the requirements of SAR data Geocoding, but will also serve as a data pool for mapping applications using data of other satellites.

The GCP data base will consist of small image chips containing features such as water boundaries, road crossings and other outstanding points on the earth surface, which can be found in satellite images. The effort to fill the data base with suitable Ground Control Point chips will be supported by automatic pattern recognition algorithms, which could be used to extract features from Landsat MSS/TM and SPOT images. In addition to that, the GCP data base can also be filled with chips from SAR images processed earlier and topographic map information. A special problem will arise from the fundamental difference between optical satellite data and radar images. Therefore algorithms are now under investigation, to increase the correlation between image chips of different sources.
The implementation of a GCP data base will be a dynamic process, which will start before ERS-1 is in orbit. The data needs maintenance and update and efforts will be done to cover all regions of interest with Ground Control Point chips.

The second necessary information, to rectify radar images and to restitute radar specific distortions like layover, foreshortening and shadow, is the digital elevation data of the terrain, which will be stored in a DEM

data base. The storage of DEM data needs no sophisticated data format design, if a regular grid of values is used and the location is referenced with geographical coordinates. For example, the area of the Federal Republic of Germany is covered by approx. 500 megabytes of 16-bit elevation data using a grid of 30 m x 30 m. Transformation and resampling to other geographic coordinate systems can be performed with standard map and image transformation algorithms.
The severe problem is the availability of DEM data in the required accuracy. Even for countries covered with small scale maps, digital elevation information is available only for selected regions. Huge data sets of terrain information of the Federal Republic of Germany will be compiled for governmental planning purposes until 1987. Besides, few data are existent for Middle Europe. All of them come with different format and accuracy and need thorough compilation before they can contribute to a DEM data base.

However, the use of DEM data to be derived from the new generation of satellites such as SPOT is being investigated as a serious alternative.

## V. THE DATA MANAGEMENT FACILITIES

The results of Preprocessing and Geocoding are annotated SAR data sets in digital form, primarily image data at different processing levels. At this stage the Precision Processing task is completed. However, further processing steps are required to finally provide products to users in a coordinated way. The major tasks are Digital Product Generation, Image Recording and Archival and Retrieval. These tasks will be performed by a central facility which will operate all necessary peripheral devices.

Digital Product Generation comprises two processing steps that transfer the annotated and processed SAR data sets to an archival medium for subsequent storage in the digital archive for at least 10 years and that copies such data sets on media suited for distribution to users.
For both tasks it is planned to make use of the evolving Optical Disk Storage Technology. Since the requirements for the archival product and for the user product are quite different it makes sense to distinguish

- Archival Optical Disk (AOD) and
- User Optical Disk (UOD).

The Archival Optical Disk shall hold many complete data sets storing in the order of 1 to 10 Gbytes of data with preferences for higher storage capacities. The AOD may be a WORM device, which shall have nearly error free access guaranteed for at least 10 years.
The User Optical Disk shall hold a minimum of one complete data set, since this concept shall also be used for the distribution of other remote sensing data sets, such as LANDSAT Thematic Mapper data. The required storage capacity per UOD is in the order of 300 Mbytes of data.

Image Recording is the task that produces master transparencies for the image archive. This is generally performed in two consecutive steps by generating latent images using special film recorders interfaced to data processing systems and subsequent development processing in a photo laboratory.
It is assumed that an existing image recorder will be used to record the

various SAR image products on 240 mm black and white roll film. The recorder is presently used on a routine basis in a batch operating mode requiring manual operator interaction for each single image being generated. The standard interface is via CCT in a specific data format. To cope with the image recording requirements of the ERS-1 era, it is necessary to enhance the recording capabilities to enable automatic operation.

Archival and Retrieval covers the remaining data handling tasks including implementation and maintenance of data archives, implementation and maintenance of catalogues, order handling for ESA and national users, distribution and dissemination of products and user service.
Cataloguing and order handling shall be performed with computer assistance using a relational data base management software system.

## REFERENCES AND BIBLIOGRAPHY


1. Bennett, J. R., Cumming, I. G., "A Digital Processor for the Production of SEASAT Synthetic Aperture Radar Imagery," ESA-SP-154, December 1979

2. Bennett, J. R., Cumming, I. G. et al, "Features of a Generalized Digital Synthetic Aperture Radar Processor," Proc. of the 15th Int. Symp. on Remote Sensing of the Environment, Ann Arbor, May 1981

3. Curlander, J. C., "Utilization of Spaceborne SAR Data for Mapping," IEEE Transactions on Geoscience and Remote Sensing, Vol. GE-22, No. 2, 1984

4. Curlander, J. C., Pang, S. N., "Geometric Registration and Rectification of Spaceborne SAR Imagery," IGARSS, München, 1982

5. Derenyi, E. E., Szabo, L., "Cartographic Accuracy of Synthetic Aperture Radar Imagery," Proceedings of the 6th Canadian Symposium on Remote Sensing, 1980

6. DFVLR, "Performance Prediction of an Enhanced SAR Processor in View of ERS-1," ESA Study Contract Report No. 5127/83/GP-I(SC), Oberpfaffenhofen, May 1984

7. Domik, G., Raggam, J., Leberl, F., "Rectification of Radar Images Using Stereo-derived Height Models and Simulation," XV International Congress of Photogrammetry and Remote Sensing, Rio de Janeiro, 1984

8. Dowideit, G., "Eine Blockausgleichung für Aufzeichnungen des Seitwärts-Radar (SLAR)," Bildmessung und Luftbildwesen, H. 1, 1977

9. Ehlers, M., "Entzerrung von SEASAT-Radar auf Landsat-MSS mit Hilfe digitaler Bild-Korrelation," Bildmessung und Luftbildwesen, Bd. 50, H. 6, S. 210-213, 1983

10. Guertin, F. E., Shaw, E., "Definition and Potential of Geocoded Satellite Imagery Products," Proceedings of the 7th Canadian Symp. on Rem. Sens., 1981

11. Hiller, E. R., "Map-matching technique for synthetic aperture radar images," SPIE Vol. 186, Digital Processing of Aerial Images, pp. 115-122, 1979

12. Klinkrad, H., "Algorithms for Orbit Prediction and for the Determination of Related Static and Dynamic Altitude and Ground Trace Quantities," ESA ER-RP-ESA-SY-0001

13. Leberl, F., "Satellitenradargrammetrie," München, 1978

14. Maier, E. H., Nüesch, D. R., "Registration of Spaceborne SAR-Data to large scale topographic Maps," ERIM, Ann Arbor, 1985

15. Noack, W., "Designing a Knowledge Based SAR Processor," submitted for publication at ISPRS 1986

16. Raggam, J., Triebnig, G., Buchroithner, M. F., Domik, G., Leberl, F. W., "Radargrammetric Aspects of SAR Data Evaluation," from Proc. Workshop on Thematic Applications of SAR Data, Frascati, Italy 9-11 Sept., 1985 (ESA SP-257), pp. 57-64

17. Wong, F., Orth, R., Friedmann, D. E., "The use of Digital Terrain Model in the Rectification of Satellite-Borne Imagery," Proceedings of the 15th Int. Symp. on Remote Sensing of Environment, Ann Arbor, MI, S. 653-662, 1981

# RADARSAT HIGH THROUGHPUT SAR PROCESSOR DEVELOPMENT

P. George
MacDonald Dettwiler & Associates
Richmond, British Columbia, Canada

## I. INTRODUCTION

MacDonald Dettwiler & Associates has been involved with the Canadian Radarsat (RSAT) project for a number of years. This included Phase A definition studies and for the past two years, Phase B ground station design and processor prototyping efforts. This paper describes the current baseline design for the SAR processing facility (SARDPF), its requirements and functional decomposition. This forms the context for then discussing the prototype SAR processor and extensions necessary to meet current ground station processing requirements.

## II. GROUND PROCESSING FACILITY

The SARDPF is to be built in two phases. The first phase would have complete functionality but reduced throughout. This phase would be completed in time for the launch of ERS-1 and would be required to process and distribute imagery from an anticipated five minutes of SAR data per day. The second phase would upgrade the facility to accommodate the substantially greater RSAT processing load based on receiving 160 minutes of SAR data per day.

The facility is required to produce a variety of products for ERS-1 and RSAT including:

- raw data CCTS;
- full resolution single look imagery both detected and complex;
- high (25m) and low (50m) resolution multilook imagery in sensor coordinates; and
- high resolution precision (digital terrain model corrected) imagery in various map projections.

Turnaround varies from three hours to two weeks with fast turnaround low resolution imagery being the dominant product. These products are digitally transmitted to the Ice Information Centre for analysis on the MacDonald Dettwiler Ice Data Integration and Analysis System (IDIAS).

SAR data acquisition takes place remotely from the processing facility. Currently two data acquisition facilities (DAF's) are baselined: one at Ottawa (Gatineau) Ontario, and another at Fairbanks, Alaska. Acquired data is relayed to the SARDPF via communication satellite (ANIK).

Figure 1 shows a block diagram of the Ottawa DAF and the SARDPF. RSAT or ERS-1 DATA is received and buffered on HDDT. After the pass, the HDDT is rewound and replayed into the communication link at 1/4 of the real time rate. At the SARDP, the data is received and simultaneously recorded and processed (RSAT only). SAR processor output is buffered onto HDDT for subsequent precision correction and geocoding (MacDonald Dettwiler's Geocoded Image Correction System) and simultaneously fed to a subsampler to form a low resolution product.

Fast turnaround products are delivered to users via a digital transmission network. The remaining products (CCTs/film products) are delivered by post or courier.

## III. PROTOTYPE PROCESSOR

The RSAT prototype processor was built using a VAX 750 host and a Motorola TASP 2080 array processor. All processing takes place within the TASP with no intermediate storage to disk. The TASP is a commercially available array processor that has a number of features that make it useful for SAR processing including:

- 40 bit complex word format (16 bits real, 16 bits imaginary, 8 bits common exponent);
- large internal memory (up to 64 M complex words);
- high speed I/O channel (15 Mbs); and
- single instruction multiple data architecture (up to 8 AUs).

The primary objectives of the prototyping effort were:

- to implement a significant subset of range-doppler SAR algorithm sufficient to demonstrate that the TASP was a suitable processing vehicle; and
- to refine timing estimates used in the design and sizing of the SARDPF Radarsat processor.

The range doppler algorithm was chosen because: it can accommodate both L- and C-band processing; it is well understood and successfully implemented (MacDonald Dettwiler SEASAT and GSAR processors). The algorithm was, however, adapted to continuous strip processing from scene processing. As a result several interesting implementation problems had to be addressed including:

- memory limitations and infeasibility of disk storage;
- continuous doppler centroid evaluation;
- potential processing block discontinuities due to centroid updates; and

- continuous processing parameter updates.

Input and output for the prototype was limited to that provided by high-speed 6250 bpi tape drives. Thus the TASP I/O channel was not exercised at rates anticipated in the SARDPR. This lack of testing was considered low risk and not cost effective for the prototyping stage.

Figure 2 shows the algorithm's implementation and partition of activities between host and AP. Multiple 'concurrent' processes on the VAX provide:

- operator command processing;
- CCT input and checking;
- FM rate estimation;
- Doppler centroid estimation;
- control parameter generation;
- host/AP data interchange;
- CCT output; and
- data logging.

Concurrent processes running on the TASP provide:

- input data assembly;
- data processing (both range and azimuth);
- centroid data extraction; and
- output data assembly.

Results to date indicate that image quality goals have been achieved and with optimization of TASP code (both application and executive) throughput goals are achievable.

## IV. RADARSAT PROCESSOR

The SARDPF RADARSAT processor must be able to process data at 1/4 real time rates to meet requirements for short turnaround (3 hour) products as well as zero backlog processing (160 minutes received and processed per day).

Figure 3 shows the functional block diagram of such a processor based on multiple TASPs. The input subsystem performs input data unpacking and checking. Range compression is performed by the first bank of processors (AP1 to APN). The processed range lines are broken into M azimuth subswaths

and azimuth processed to imagery by the second bank of M processors. The bus arbitrator allows any processor of the first bank to transfer data to any processor of the second. The output subsystem buffers subswath imagery until blocks of complete range lines are ready for output. It also provides the host with intermediately processed data for doppler centroid evaluation.

## V. SUMMARY

MacDonald Dettwiler has successfully undertaken work in the design and construction of a prototype high speed, continuous strip SAR processor of low development risk. The results of this effort are being included in the design of the Canadian ERS-1 and Radarsat SAR processing facility.

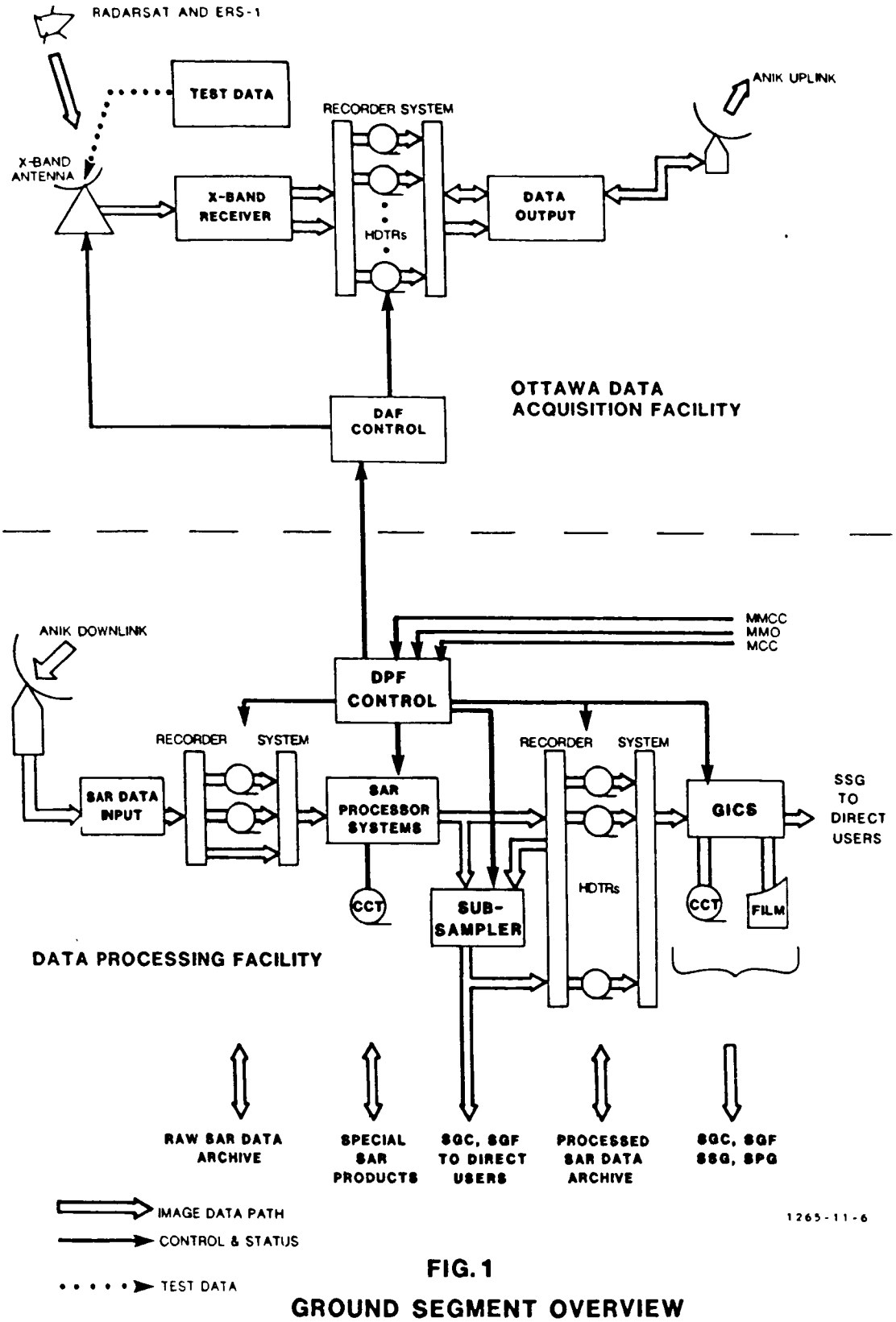


**FIG. 1**

**GROUND SEGMENT OVERVIEW**

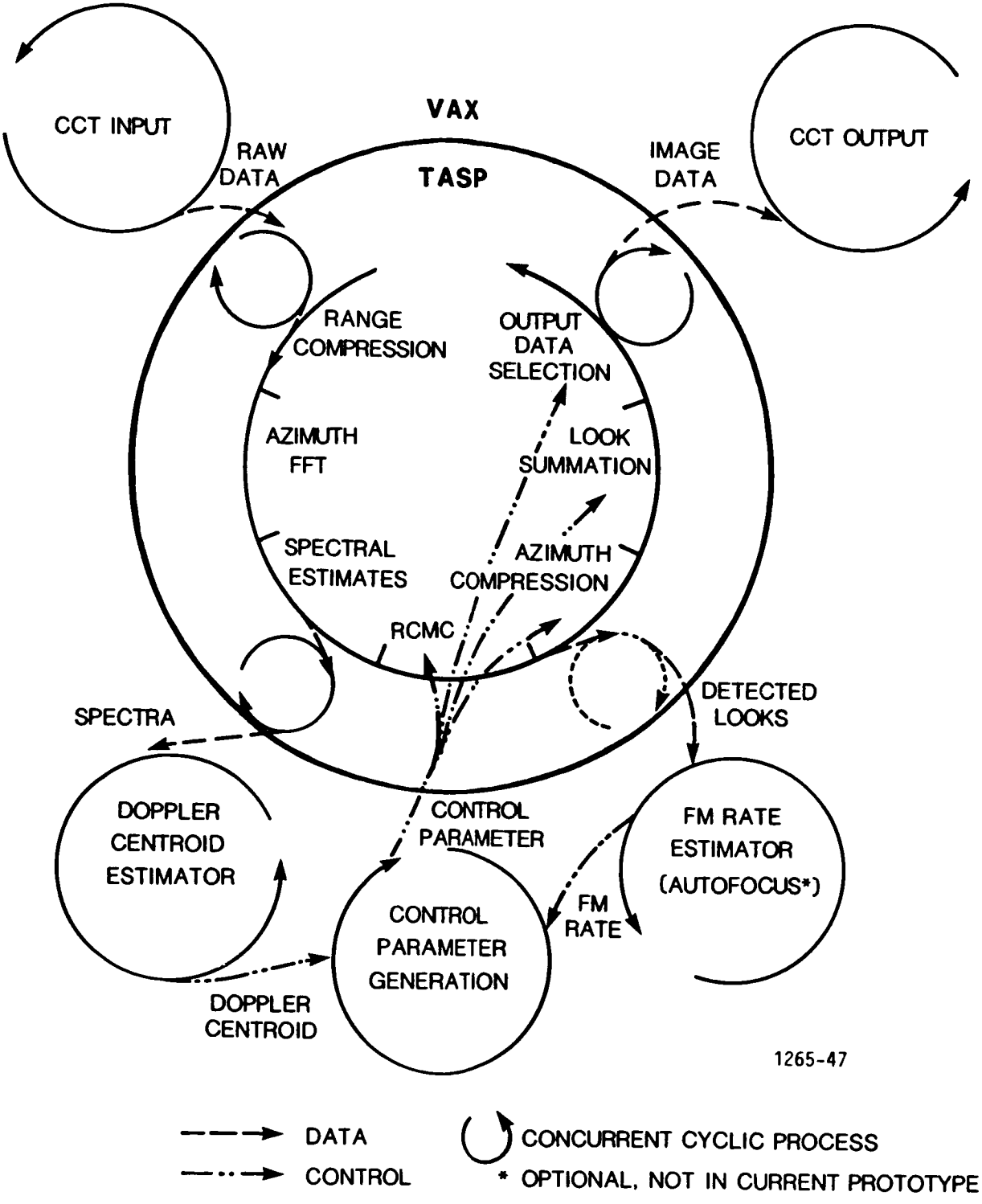


**FIG. 2**

**RADARSAT PROTOTYPE PROCESSOR: ALGORITHM IMPLEMENTATION**

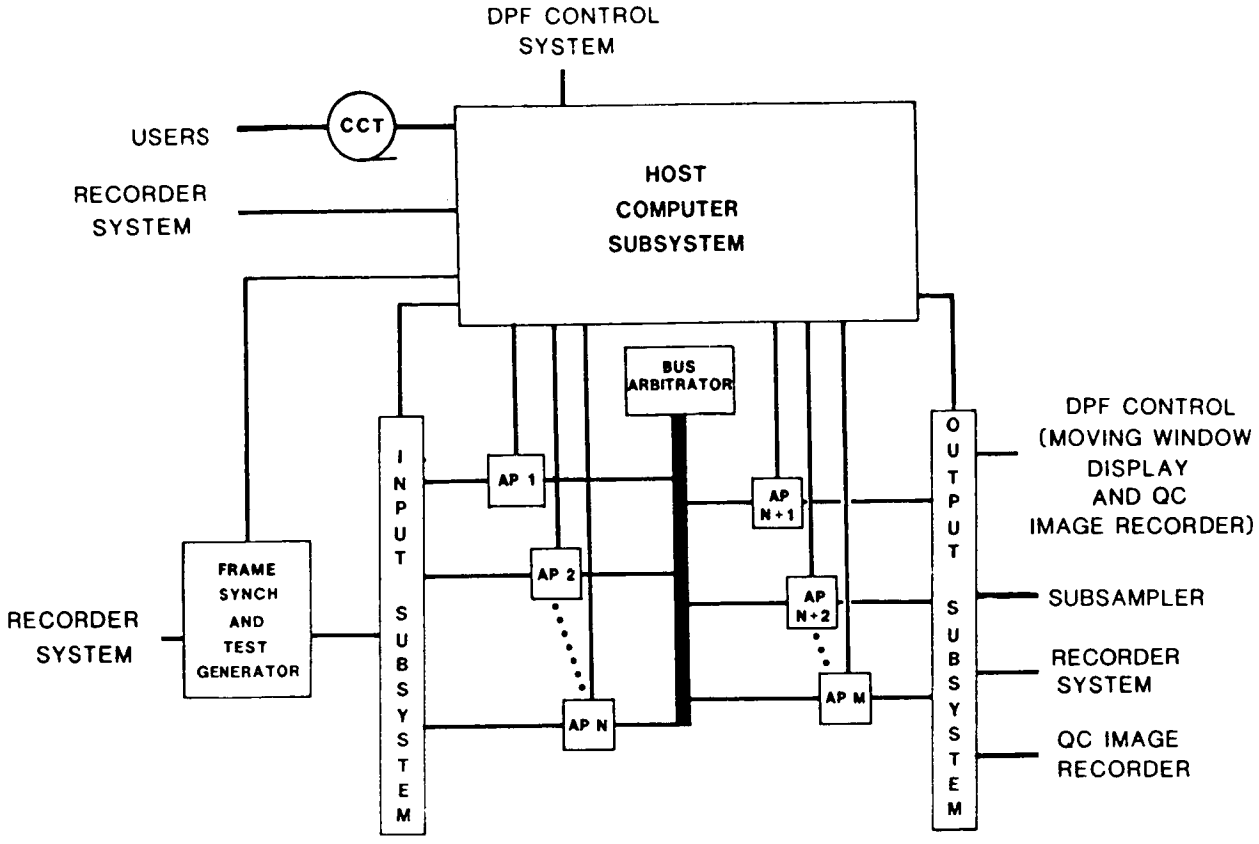


**FIG. 3**

**RADARSAT SAR PROCESSOR**

1265-1-5

# THE SIR-C GROUND DATA SYSTEM: DIGITAL PROCESSOR, DATA PRODUCTS, INFORMATION FLOW

John C. Curlander
Jet Propulsion Laboratory, California Institute of Technology
Pasadena, California

The SIR-C instrument will collect both C-Band and L-Band data with each frequency band consisting of direct (HH or VV) and cross-polarized (HV or VH) data. Considering all possible combinations as many as eight different data channels will be available for any given target area. This data will be digitized and formatted on-board for direct downlink via the Tracking and Data Relay Satellite System (TDRSS), or it will be buffered through on-board high density digital recorders for storage or transmission when TDRSS is available. The data is received by the TDRSS ground station at White Sands and is nominally relayed via DOMSAT to the high data rate recording facility at GSFC (Figure 1). The tapes are then shipped to JPL for processing into imagery and eventual distribution to the SIR-C investigators.

## I. IMAGE PROCESSING

All SIR-C raw data is to be processed digitally by the Advanced Digital SAR Processor (ADSP). This processor, designed and built by JPL, can perform SAR image correlation at real-time or near real-time throughput rates. The system configuration for SIR-C is shown in Figure 2. It centers around the ADSP which consists of four racks of VSLI circuit boards controlled by a VAX 11/785. The system also features a SIR-C custom input interface, two high density digital recorders for the input and output data, a scrolling display with a video cassette recorder (VCR) and a laser beam recorder (LBR) for quick-look image products.

The input interface contains the logic necessary to decode the sub-commutated header data in real-time, reformat the block floating point coded data into integer bytes, and perform data quality analyses such as BER checks, radar parameter change detection, or data drop-out detection. The decoded header data is transferred to the VAX controller for initialization of the autofocus and clutterlock algorithms. In addition, this data is used for determination of range line and reference function sizes as well as estimation of the geometric and radiometric correction parameters (e.g., antenna pattern, incidence angle, azimuth skew, slant range, etc.).

The correlation algorithm is essentially two one-dimensional matched filtering operations performed in the frequency domain (Figure 3). The reference functions are determined from the characteristics of the transmitted pulse for the range reference and from the Doppler characteristics of the echo data for the azimuth reference.

The ADSP can perform up to $6 \cdot 10^9$ complex operations per second. It is designed to process SAR raw data into imagery in strips rather than on a frame-by-frame basis as in SIR-B. It also has the capability to dynamically update the azimuth reference function during the processing to compensate for variations in the earth rotation rate or the shuttle attitude. However, the

ADSP has limited capability for updating the radiometric and geometric correction parameters. This may require, depending on the stability of the shuttle during a data take and the application of a specific data set, special processing to maintain the fidelity of the output product. For this purpose a special purpose processor (SPP) has been added to perform postprocessing operations on the image products. This system will interface with the ADSP output and will include an array processor, mass storage, a video display and a frame-type film recorder. Its primary function is to meet the special processing requirements of the SIR-C investigators on selected segments of image data.

## II. DATA PRODUCTS

The SIR-C raw data set will consist of digitized echo data of two frequencies with each frequency containing one to four different polarizations. Contained in the raw data header are the radar parameters and shuttle parameters required for the processing. In addition, high precision postflight attitude and trajectory files will be available 2 to 3 months after the mission.

In the processor timeline, a period for data validation and sensor performance evaluation of approximately 1 month will be allotted. Following this period data will be processed in a quick-look mode to assess the quality and specific coverage of the data set. As a minimum for the survey processing, one image set (up to 4 channels) will be produced for each of the planned 50 investigator sites. This output will be recorded on HDDT and video cassettes (or film strips) of this imagery will be distributed to investigators over their test sites. The survey processing will not involve any special corrections for shuttle instability, or registration of multiple polarizations or frequencies and will require approximately 2 months. All imagery will consist of detected (real), 4-look pixels.

The third phase of the processing, requiring approximately 9 months per flight, will produce image products as per the primary investigation for each data take. The SIR-C processor is capable of allowing options such as: (1) complex data, 16-bit floating point; (2) single-look, double-look or 4-look data; (3) real data, 8-bit or 16-bit integer; (4) range compressed only data; (5) radiometrically uncompensated data; and (6) slant range deskewed data. However, discussions are on-going in an attempt to define a single image standard. The real-time output will be recorded on HDDT and film strips via the laser beam recorder. These film strips will be annotated with time and location each 10 seconds ($\approx$ 75 km) and an ancillary data record generated for each data take containing the full set of shuttle, processor and radar parameters including updates of time varying parameters each 10 seconds. The ancillary data record will be stored in the SPP and written to CCT for distribution to the investigators. This processor will interface to both the HDDR and the ADSP and serve an additional function as the SAR data catalog. In parallel with refinement of the standard image products as described above, this processor will produce a limited amount of special products as required by the investigators. For example, within this category are: (1) geocoded images (i.e., rotated to north and resampled to specified map projection); (2) radiometrically calibrated products in geophysical units (i.e., backscatter coefficient); (3) imagery corrected for foreshortening due to terrain

variations; and (4) pure phase imagery, phase difference between any two polarizations, or magnitude ratios between polarizations or frequencies. Depending on the amount of special processing, it is expected that this phase of the processing will last from 9 to 12 months, being completed approximately 15 months following the second mission.

## III. DATA DISTRIBUTION

As previously described, the special purpose processor will also act as a data base management system for the SIR-C, and to a limited extent, the entire terrestrial SAR catalog. It will contain all of the fundamental and derived parameters for the SIR-C data set. This catalog will contain maps illustrating the SIR-C coverage as well as the capability to cross-reference target location with any of the SIR-C parameters to determine the extent of a particular type of coverage. In addition, coverage maps from SEASAT, SIR-A, and SIR-B will be available with algorithms to determine the extent of multisensor/multimission coverage.

This catalog will be accessible by modem to remote users for determination of processing status, coverage of a target area, or to communicate to the processing team a special processing or distribution request. It is also desired, depending on technological development, to provide the capability for on-line access of low resolution image data to remote users. This will depend primarily on the expected development of mass optical disk storage and high data rate modems and communication links.

The primary means of product distribution will be via mail in one or more of the following forms. The initial product will be a quick-look video cassette (or optical disk if practical) or film strip of the investigator's test area. This will be provided approximately 3 months postflight primarily for survey purposes. Associated with this will be a limited ancillary data set with periodic time and location updates. Note that the high precision ephemeris and attitude data will not be available in this time frame, therefore, the radiometric and geometric fidelity of the survey products may not meet final product requirements.

Based on the investigators' evaluation of the survey products and a priority schedule determined by the science team, production and distribution of the final products will begin 3 months postflight and will last for a period of approximately 1 year for each flight. This system will be designed to optimally meet the special needs of the investigators by having the capability to generate a variety of image products. The large volume of data associated with full resolution SAR imagery precludes electronic transfer of this imagery in the SIR-C time frame. However, the processor development plan will include - as a minimum - access to the SIR-C ancillary data set and potentially remote access to low resolution or compressed SIR-C imagery.

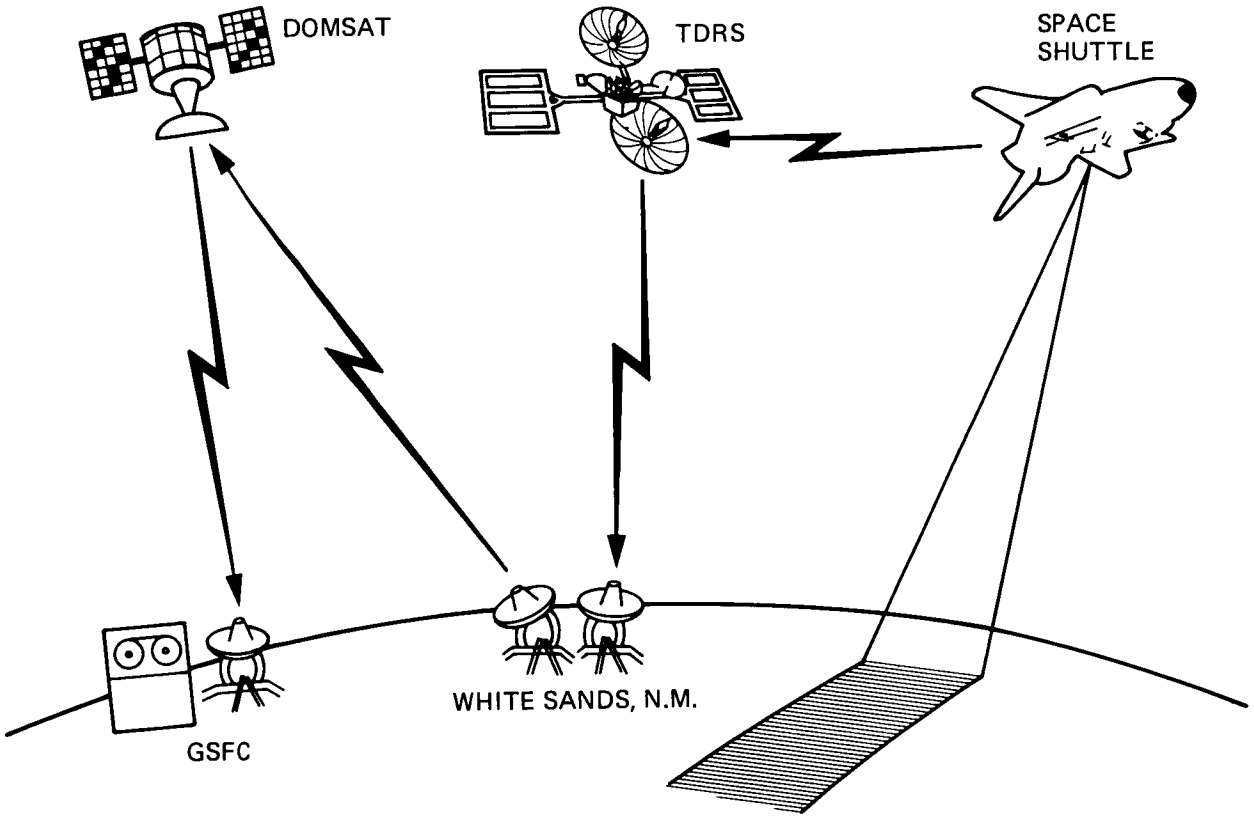


Figure 1. SIR-C data flow

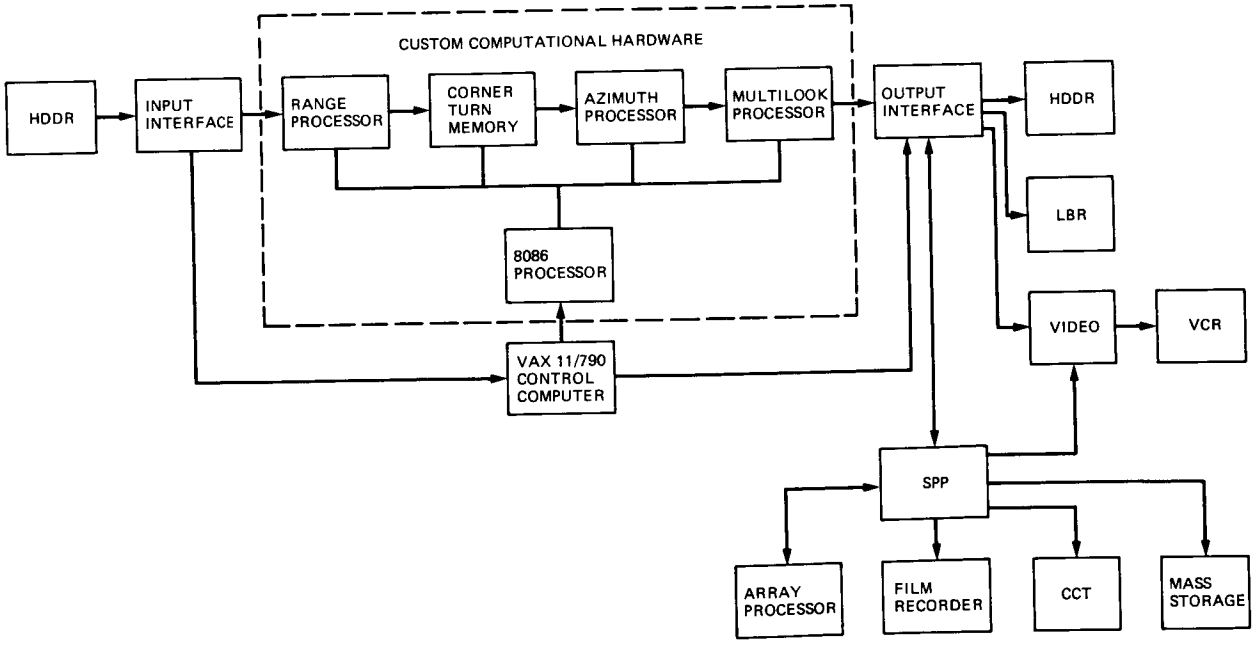


Figure 2. SIR-C processing system block diagram

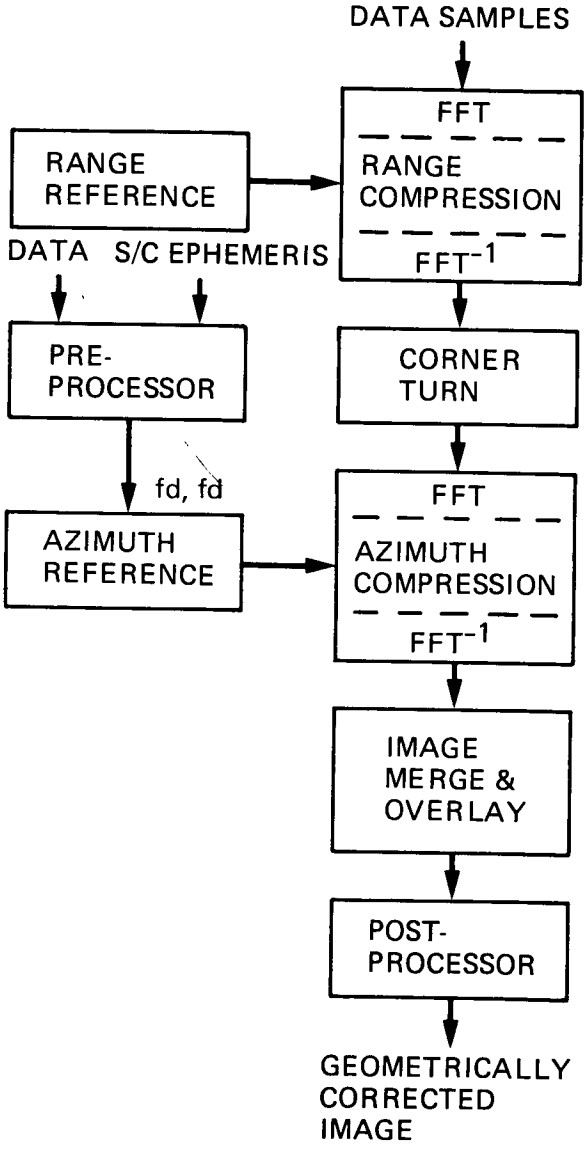


Figure 3. Functional block diagram of SAR processing algorithm

# AN OPTIMUM SAR PROCESSOR

Dr. Carter M. Glass
Goodyear Aerospace Corporation
Arizona

## I. INTRODUCTION

Recent experience has shown that synthetic aperture radar (SAR) processing costs can be prohibitively large when conventional computers and/or array processors are used. Special-purpose signal processors are unattractive because it is generally not cost effective to develop such devices for a single application. The problem is to find an architecture which is both optimized for SAR processing yet flexible enough to be used for a variety of systems and modes. This paper describes a flexible SAR processor which has been built, tested and shown to be a cost-effective solution to the problem.

## II. ARCHITECTURAL APPROACH

SAR image formation requires a sequence of independent steps performed on complex data vectors. The optimum way to implement the sequence is as a pipeline interconnection of processing elements (PEs), each of which works on a vector and then passes it on (see Figure 1). As some PEs may be faster than others, it is often necessary to "fan out" the pipeline into parallel paths at various points.

The monumental task of scheduling data through many simultaneously active PEs is avoided by asynchronicity, achieved through double buffering the PEs (see Figure 2).

Each PE could be a general-purpose computer or array processor, and although this minimizes the need to develop new hardware, it can lead to excess equipment in proportion to the computational rate achieved. The optimum PE should implement only those functions needed at its stage in the pipeline. Because the processing operations are ultimately arithmetic, it might seem that a central processing unit (CPU) would be a good choice as a universal PE. The problem is that decomposing the functions to such a low level results in excessive numbers of buffers and data paths. A better approach is to escalate the functional complexity to the highest level which neither restricts flexibility nor results in redundant capabilities. For example, all SAR algorithms can be implemented with only seven high-speed functions:

1. Fast Fourier Transform - used for range and azimuth matched filtering
2. In-Plane Filter - filter samples along a data vector
3. Cross-Plane Filter - filters across data vectors
4. Reference Function Generator - stores and/or creates reference functions and applies them to the data

5. Corner-Turn Memory - allows data to be written by columns and read by rows, and vice versa

6. Automatic Focus - removes residual phase errors

7. Detector/Log Encoder - converts output samples to logarithmically encoded image pixels.

## III. IMPLEMENTATION

If interconnecting the PEs required wiring backplanes and designing interfaces, the development of an optimum processor would be too expensive. This problem is solved by the implementation of Figure 3, which shows the processor as a wheel, with a matrix crossbar switch at the hub, the PEs as spokes, and a control and initialization bus at the rim.

The structure of Figure 3 implements the features of an optimum processor as follows:

1. Modularity - the processor is scaled to a specific requirement by "plugging in" only the precise combination of PEs needed.

2. Reconfigurability - the machine is reconfigured by reprogramming the crossbar switch, either before processing (to establish a base configuration) or during processing (to time multiplex PEs).

3. Control - The PEs are initialized and controlled by a combination of (a) instructions from the control microcomputer via the control bus and (b) operation codes and data tags contained in vector header words.

4. Test and Fault Isolation - the control computer can test each PE independently by inserting test patterns and comparing the results with prestored responses.

5. Graceful Degradation - spare PEs can be provided so that if an active PE fails, the spare can be switched in without loss in processing time. Even when spares are unavailable, it is often feasible to shift the load of a failed PE to another unit by time multiplexing, thus leaving the processor functionally operational but at a reduced throughput rate.

## IV. CONCLUSION

The nature of SAR processing dictates a pipeline parallel interconnection of PEs. While any number of bus structures and PE types can be envisioned, the scheme above has already been developed and shown to be successful.

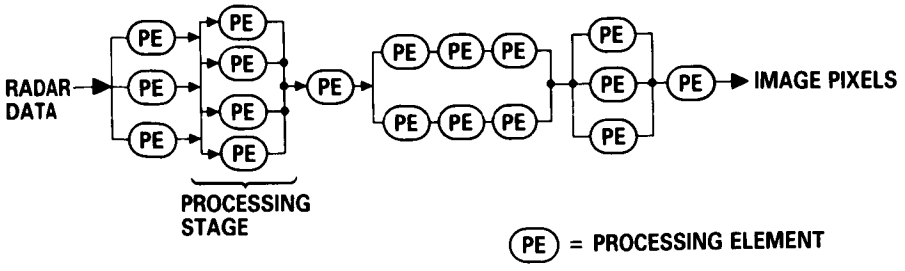


Figure 1. The optimum SAR processor is a pipeline/parallel interconnection of processing elements.

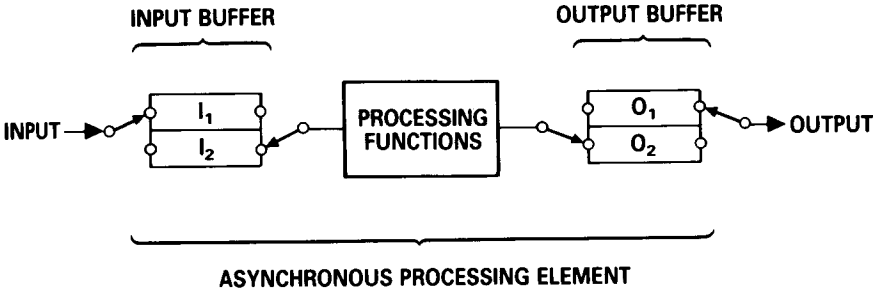


Figure 2. Asynchronicity requires PEs with input and output double buffers.

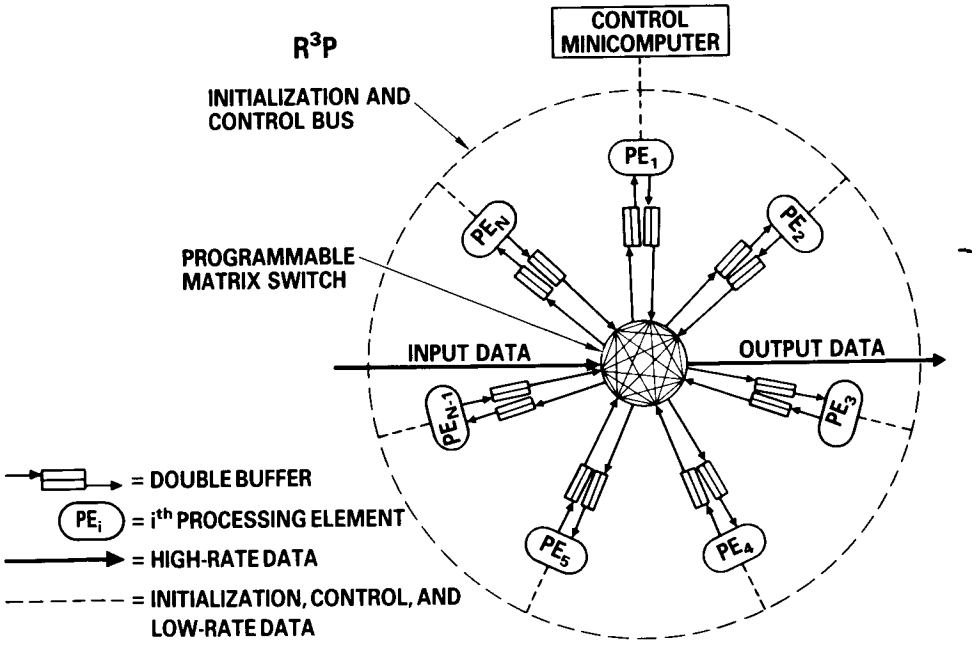


Figure 3. Processing elements and a crossbar switch are used to implement the optimum SAR processor.

# Ecosystems and Hydrology Research Techniques

# ANALYSIS OF MULTIPLE INCIDENCE ANGLE SIR-B DATA FOR DETERMINING FOREST STAND CHARACTERISTICS

R. M. Hoffer, D. F. Lozano-Garcia, D. D. Gillespie, and P. W. Mueller
Department of Forestry and Natural Resources, Purdue University
West Lafayette, Indiana

M. J. Ruzek
Jet Propulsion Laboratory, California Institute of Technology
Pasadena, California

## I. INTRODUCTION

For the first time in the U. S. space program, digital synthetic aperture radar (SAR) data were obtained from different incidence angles during Space Shuttle Mission 41-G. Shuttle Imaging Radar-B (SIR-B) data were obtained at incidence angles of 58°, 45°, and 28°, on October 9, 10, and 11, 1984, respectively, for a predominantly forested study area in northern Florida. Cloud-free Landsat Thematic Mapper (T.M.) data were obtained over the same area on October 12. The SIR-B data were processed and then digitally registered to the Landsat T.M. data by scientists at the Jet Propulsion Laboratory. This is the only known digitally registered SIR-B and T.M. data set for which the data were obtained nearly simultaneously.

## II. OBJECTIVES

1. Determine the potential for utilizing L-band, HH-polarized Shuttle Imaging Radar (SIR-B) data, obtained at incidence angles of 58°, 45°, and 28° to:
   - discriminate and identify forest and other cover types;
   - define differences in density, volume, and biomass in commercial stands of southern yellow pine.

2. Define effective methodologies to quantitatively process and analyze synthetic aperture radar data.

3. Assess changes in forest cover between 1978 and 1984 through the utilization of digitally registered Seasat and SIR-B data.

## III. CHARACTERISTICS OF THE TEST SITE

The test site is an area of approximately 1000 sq. km. in northern Florida, approximately 65 km west of Jacksonville. The area has relatively flat terrain and sandy soils. Most of the area is forested, primarily with plantations of slash pine (Pinus elliottii). In addition, there are numerous cypress and creek swamps throughout the area which are predominantly pondcypress (Taxodium distichum var nutans), tupelo (Nyssa spp.), and scattered slash pine (P. elliottii).

Cover type maps and detailed forest stand inventory data were provided by the U.S.D.A. Forest Service and the three forest products companies operating in the area (Champion International, Owens-Illinois, and Southern Resin). Additionally, at the time of the SIR-B mission, various types of quantitative and qualitative data were obtained, including vegetation and soil moisture samples, temperature and relative humidity measurements, ground and aerial photographs, and stand descriptions.

## IV. DATA ANALYSIS AND RESULTS

A data base of more than 1500 forest stands has been developed, although this entire data set could not be used in some of the analyses due to differences in the type and detail of data obtained by each forest product company and the Forest Service. Therefore, statistical analyses were conducted individually on the data base from each company. Significant correlations (0.99 confidence level) were found between many of the forest stand parameters, such as cords/acre and age, trees/acre and age, cords/acre and site index, basal area/acre and cords/acre, and height and age.

Seventy-one stands of slash pine of known characteristics were located in the SIR-B data set, and the relationships between radar backscatter and various stand parameters were determined. Mean radar return was found to be statistically correlated (at the 0.99 confidence level) with age and also with cords/acre for all three SIR-B incidence angle data sets (Table 1). Figure 1 illustrates the relationship between the 58° SIR-B backscatter and age of the forest stands.

Total above-ground wood biomass in tons/acre was calculated for the Owens-Illinois data using a model for slash pine based on D.B.H. (diameter at breast height) and tree height. As indicated in Table 1, statistically significant correlations were found between biomass (in tons/acre) and the 45° and also the 28° incidence angle SIR-B data ($r = 0.60^{**}$ and $r = 0.51^{*}$, respectively), even though this sample contained only a small number of stands.

Analysis of this 58°, 45°, and 28° multiple incidence-angle data set has shown that the incidence angle significantly influences the capability to separate forest cover types. In the 28° incidence angle data set, deciduous swamplands have relatively high radar backscatter while pine planations have only a moderate backscatter, but on the 58° incidence angle data set there are no definable differences, either qualitatively or quantitatively, between these major forest cover types. The very high return observed for the dense cypress and the cypress-tupelo swampland areas on the 28°, and to a lesser degree the 45° data, is believed to be due to the specular reflectance of the radar signal from the standing water in the swamp in combination with the tree trunks, thereby creating a complex corner-reflector effect. The importance of incidence angle on the SIR-B data is dramatically shown in Figure 2.

To determine the most effective procedure for filtering SIR-B data, three different types of low-pass filters (square mean, square median, and separable recursive median) of varying window widths were applied to the data. A separable recursive median filter with a window size of 1 X 5 pixels provided the optimum reduction of speckle effects, based on qualitative evaluations. This filter also enabled somewhat higher computer classification performances to be obtained, as compared to the results using the data generated by the other filters.

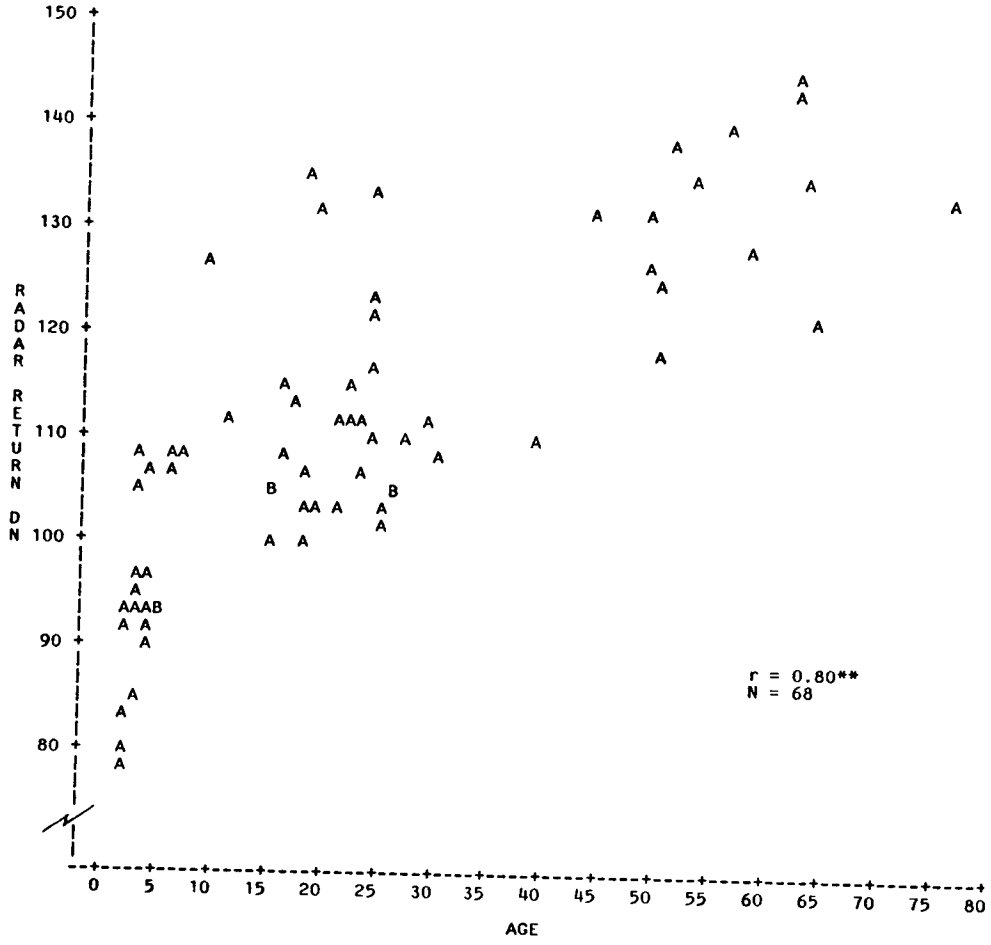


Figure 1. Plot of SIR-B radar backscatter versus age of slash pine. (N = 68 stands; r = 0.80**).

Table 1. Correlation coefficients indicating the relationship between various stand parameters and mean radar return for the stand. A low pass Separable Recursive Median Filter having a 1x5 pixel window has been applied to each of the SIR-B data sets.

| Stand parameter | No. stands | SIR-B data set | | |
|---|---|---|---|---|
| | | 28° | 45° | 58° |
| Age | 71 | 0.73** | 0.69** | 0.81** |
| Cords/acre | 52 | 0.58** | 0.67** | 0.52** |
| Trees/acre | 52 | 0.21 | 0.32 | 0.34 |
| Biomass (tons/acre) | 17 | 0.51* | 0.60** | 0.41 |

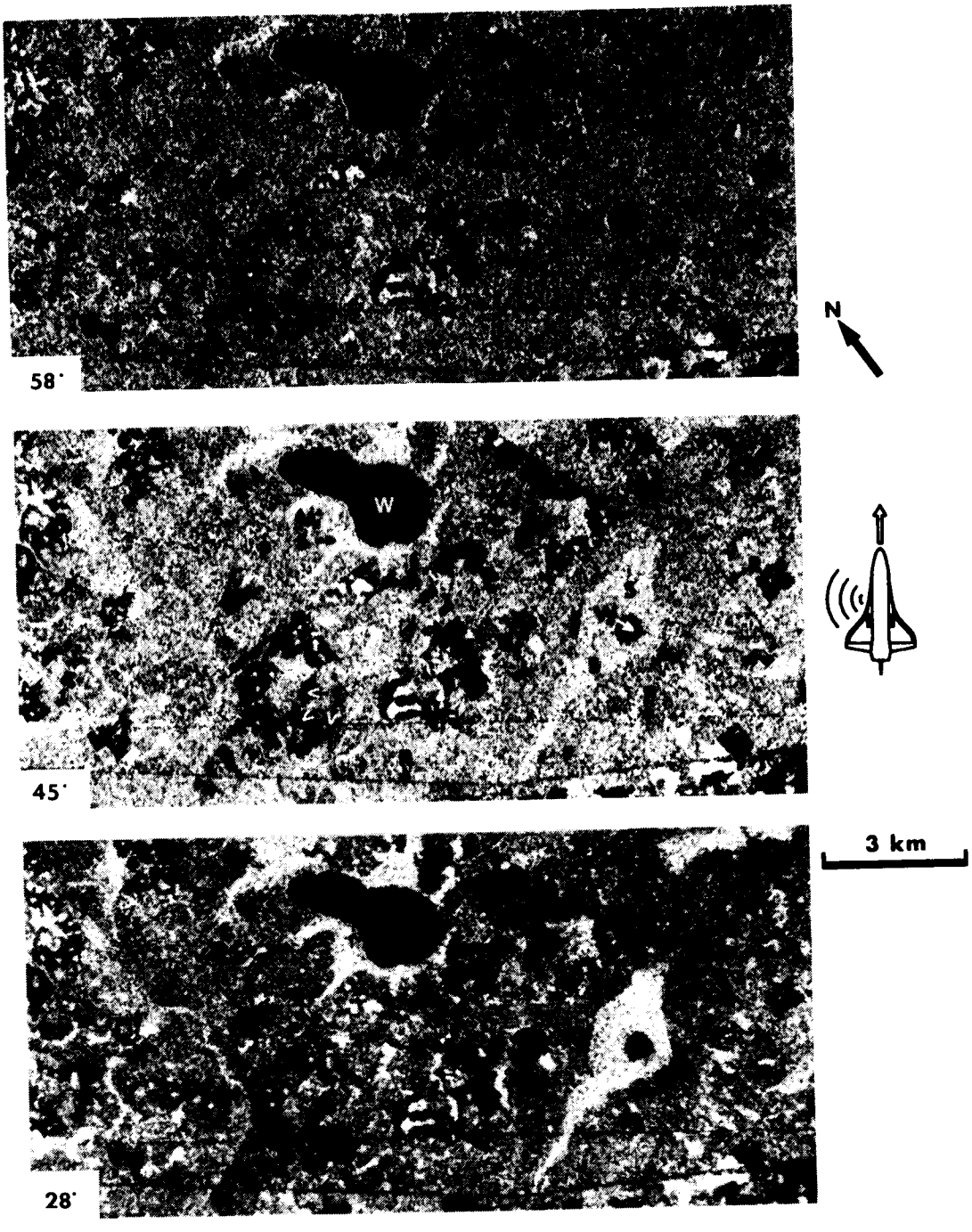


Figure 2. Multiple incidence-angle SIR-B data of the Florida test site. The light-toned areas of deciduous swampland forest are very distinct on the 28° image (bottom), but cannot be differentiated from the surrounding slash pine on the 58° image (top). The center image was obtained at an incidence angle of 45°. W = Water; F = Slash Pine Forest; S = Deciduous Swampland; C = Clearcut; R = Road; and P = Powerline.

Computer classifications were obtained for both the multiple incidence angle SIR-B data and the Landsat T.M. data, using a Gaussian Maximum Likelihood (GML) per-point and also a contextual (SECHO) algorithm. The results were evaluated using 122 test fields containing a total of 8,648 pixels. As shown in Table 2, slash pine forest, deciduous swampland, and other (soil, pasture, water) classes could be classified with reasonably good accuracy using only the multiple incidence angle SIR-B data. Classifications involving old slash pine (>40 yrs.), medium slash pine (6-40 yrs.), young slash pine (<6 years), clearcut, soil, pasture, water, and deciduous swampland produced less accurate results (as would be expected). The overall classification accuracy based on these detailed classes was 70.7% for the per-point GML algorithm and 73.8% for the contextual SECHO algorithm. The Landsat TM multispectral scanner data resulted in higher classification performances for both the generalized and detailed classifications than could be obtained using only the three incidence angles of L-band HH polarized SIR-B data.

Analysis of the digitally registered 1978 Seasat data and 1984 28° SIR-B data showed that areas of deforestation and reforestation could be effectively defined. Although additional work is needed to determine the time period between clearcutting and sufficient forest regrowth to preclude such change detection assessment, it would appear that synthetic aperture radar data could be a very effective tool for monitoring the rate of deforestation in tropical regions of the world, especially since such areas are often cloud covered.

In summary, it is very clear that incidence angle controls, to a very large extent, the characteristics of the data and the type of information that can be obtained from L-Band HH-polarized satellite SAR data. Results of work with aircraft data indicate that the additional frequencies and polarizations that will be available on future satellite platforms will make SAR data an important source of forest resource management information.

Table 2. Results of computer classifications of the unfiltered and filtered SIR-B multiple incidence-angle data for the Gaussian Maximum Likelihood per point and the contextual SECHO classification algorithms. These results are based on 122 test areas containing a total of 8,648 pixels.

GML (per-point) classification algorithm

| SIR-B data set (type of low pass filter applied) | Cover type | | | Overall performance |
|---|---|---|---|---|
| | Slash pine | Deciduous swampland | Other | |
| Unfiltered | 87.6 | 79.9 | 71.6 | 79.7 |
| 3 x 3 mean | 94.0 | 90.4 | 65.2 | 85.2 |
| 3 x 3 median | 92.5 | 89.9 | 65.4 | 84.6 |
| 1 x 3 sep. recur. med. | 92.4 | 89.2 | 65.0 | 84.1 |
| 1 x 5 sep. recur. med. | 95.5 | 92.4 | 63.8 | 86.2 |

Contextual SECHO classification algorithm

| SIR-B data set (type of low pass filter applied) | Cover type | | | Overall performance |
|---|---|---|---|---|
| | Slash pine | Deciduous swampland | Other | |
| Unfiltered | 94.2 | 92.8 | 70.4 | 87.3 |
| 3 x 3 mean | 96.9 | 92.7 | 67.3 | 87.0 |
| 3 x 3 median | 94.7 | 93.1 | 60.8 | 84.8 |
| 1 x 3 sep. recur. med. | 96.4 | 92.8 | 63.4 | 85.8 |
| 1 x 5 sep. recur. med. | 97.6 | 93.2 | 68.6 | 87.8 |

# MULTIPLE INCIDENCE ANGLE SIR-B EXPERIMENT OVER ARGENTINA

JoBea Cimino, Daren Casey, and Stephen Wall
Jet Propulsion Laboratory
California Institute of Technology
Pasadena, California

Aldo Brandani
Consejo Nacional de Investigaciones Cientificas y Técnicas
and Centro de Geologia de Costas
Mar del Plata, Argentina

Gitta Domik and Franz Leberl
VEXCEL Corporation
Boulder, Colorado

## I. INTRODUCTION

The Shuttle Imaging Radar (SIR-B), the second synthetic aperture radar (SAR) to fly aboard a shuttle, was launched on October 5, 1984. One of the primary goals of the SIR-B experiment was to use multiple incidence angle radar images to distinguish different terrain types through the use of their characteristic backscatter curves. This goal was accomplished in several locations including the Chubut Province of southern Argentina. Four descending image acquisitions were collected providing a multiple incidence angle image set. The data were first used to assess stereo-radargrammetric techniques (Leberl, et al., 1986a). A digital elevation model was produced using the optimum pair of multiple incidence angle images. This model was then used to determine the local incidence angle of each picture element to generate curves of relative brightness vs. incidence angle (Cimino, et al., 1986). Secondary image products were also generated using the multi-angle data (Domik, et al., 1986).

## II. OBSERVATIONS

### A. Acquired Data

The images examined in this study were acquired on consecutive days of the SIR-B mission with incidence angles from vertical of 33.0°, 44.7°, 53.7° and 59.4° (Figure 1 and Table 1). The center latitude and longitude of the site are 43°20'S and 71° 27'W, respectively, near a peak named Cordón la Grasa. The images were collected at about 6 p.m. local time between October 8 and 11, 1984. The width of the area of coincident coverage ranges from about 12 to 15 km.

### B. Description of the Study Area

The majority of the study area imaged by SIR-B is within a sharp boundary controlled by a strong east-west rainfall gradient which divides the Andes ecosystems from the Patagonian desert. The ecotone includes plant species from the Andean forests and from the Patagonian steppe (Figure 1b). The study area encompasses the Valle Rio Frio and the terrain just east and

west of it. Cordón la Grasa, one of the series of ranges forming the Andes Pre-Cordillera, dominates the western portion of the image. A pure Nothofagus pumilio, or lenga, forest is found at higher elevations and along water courses. Below the lenga to the Valle Rio Frio, there is a complex unit formed by both pure Nothofagus antarctica, or ñire, forest between 1000 m and 1050 m elevation, and ñire mixed with maiten (Maytenus boaria), laura (Schinus patagonicus) and several species of Berberis below 1000 m. Locally, the ratio of ñire, maiten, laura and berberis varies depending on slope, exposure, and available moisture. The ecosystems are described in detail by Cimino, et al., 1986.

## III. ANALYSIS OF THE IMAGERY

### A. Radargrammetric Analysis

The multiple incidence angle data set permits one to study the capabilities and limitations of radargrammetric mapping in a manner previously not possible due to a lack of available data. Figure 2(a) is a sketch of the imaging configurations. The largest intersection angle for stereoscopic analysis was 23 degrees (Table 2). This stereo model may present a different quality of stereo-viewing than one using data with smaller intersection angles. Generally one can expect the best visual stereo-matching when the intersection angles are at a minimum. Unfortunately, however, this would lead to poor vertical exaggeration of the stereo-model.

The radargrammetric measurements and computations were performed on a computer-controlled photogrammetric analytical stereo-plotter. The analysis procedure consists of several steps:

- Ground control points are identified on existing topographic maps and in each of the 6 pairs of overlapping radar images;
- On the computer-controlled stereo instrument, 18 different stereo models were set-up and measurements of coordinates were taken;
- A digital contour map was created from the most accurate of the radar stereo models;
- A reference digital elevation matrix was obtained using the maps of the study area; and
- The radar- and map-derived digital elevation data were compared.

Figure 2(b) illustrates graphically the results of the comparison in terms of the change in accuracy as a function of stereo-intersection angle. The results at a 5° intersection are nearly as predicted; at 23° the experimental data are poorer than those expected. Figure 2(b) is based on the Cordón la Grasa data set and on results from another SIR-B multiple angle data set of Mt. Shasta (Leberl et al., 1986b).

It is evident that height values are less accurate than theoretical prediction based on range resolution. This difference becomes more distinct as stereo-intersection angles increase. Limitations in accuracy at large intersection angles may be due to

- effects of "specular point migration" and migration of edges due to differences in illumination;

- changes in backscatter due to differences in incidence angles;
- variations in radar azimuth angle and resulting edge migration;
- effects of noise.

B. Generation of Color Composite Image

To assess visually the value of a multiincidence angle image set over that of a single image for vegetation classification, a color composite was generated using three of the four SIR-B images. Registered, geometrically corrected digital images (Domik, et al., 1986) from three of the four acquisitions of the Cordón la Grasa area were used to produce the color composite by assigning each image a color. The 33.0° incidence angle image was assigned to a blue color, the 44.7° image to a green and the 59.4° image to red. The composite (see Cimino, et al., 1986) clearly delineates the forest units which may be discriminated when the multiple incidence angle data sets are combined.

C. Generation of Relative Brightness Curves

Although SIR-B was designed as a calibrated system, images in the resulting data set resist quantitative interpretation because of an unexpected breakdown in the insulation of the cabling connecting the transmitter/receiver unit to the antenna during the flight. The effect of the breakdown was to modulate the effective antenna gain; the frequency spectrum of this modulation is unknown. However, short term variations in azimuth are strongly damped by the correlation process, which effectively averages returned echoes over a 2-second interval. Such averaging insures that comparisons of data separated by 15 km or less are legitimate.

Day-to-day variations in transmitted power are compensated by the use of ratios--that is, all multiple-angle data are presented in terms of brightness relative to a reference forest unit.

For selected forest units, several areas uniform in image brightness were chosen for analysis (Figure 3a). The digital values or data numbers (DN) of the pixels in each box were averaged to remove speckle. The averages were corrected for all known receiver and processing gain variations and plotted as a function of local incidence angle using topographic information generated by Leberl, et al., 1986a. The curves for each vegetation type were then ratioed to the low ñire forest curve (unit 8). Error bars are the root-sum-square of the speckle noise and the overall relative calibration error (SIR-B Science Plan). In general, the overall relative calibration error dominates.

## IV. RESULTS AND DISCUSSION

The resulting curves of relative brightness vs incidence angle (Figure 3b) describe in a more quantitative fashion the results displayed in the color composite. The lenga forest has a significantly stronger response at the smaller incidence angles than the surrounding ñire forest. At 59°, the curves of the lenga and the ñire forests on the west side of Cordón la Grasa

converge. The lenga in the Andes also has a much stronger response than the nire but a slightly weaker response than the lenga on Cordón la Grasa.

The ñire forests on the east and west sides of Cordón la Grasa have very similar responses at the three smallest incidence angles. The regenerated ñire (unit 3) has a slightly lower response than the other ñire forests. At the largest incidence angle, however, the ñire on the west side of Cordón la Grasa have a much stronger response than the low ñire forests (unit 8) on the east side. The wind damaged ñire (unit 7) has a response similar to the low ñire. The grazed mallines have a much lower response at all three larger incidence angles than the forests, however at the smallest incidence angle, their responses are similar to the regenerated ñire. The bare rocks and snow at the peak of Cordón la Grasa have the weakest response at all incidence angles.

At the smallest incidence angle the lenga forest has the strongest backscattered return. The relative openness of the canopy suggests that a significant amount of radiation is reaching the surface. The extreme brightness may be due to a high density of trees and branches littering the ground below the canopy. For the horizontally polarized radar these horizontal branches are likely to be very good scatterers. At higher incidence angles the incident radar beam must penetrate increasingly greater amounts of canopy before breaking through to the understory, until at the highest incidence angle little radiation reaches the surface and the lenga backscatter is reduced to that of the ñire. The branching structures of the lenga and ñire tree canopies are very similar, and in situations where most of the radiation is either scattered or absorbed within the upper levels of the canopies, such as at 59°, it is reasonable to assume these two forests look the same to the radar.

The ñire forests have a wide variety of structures depending on the elevation, exposure to the sun and wind and the stage of regeneration if burning has occurred. The shrub-like ñire (unit 8) is a weaker scatterer than the tree-like ñire at the largest incidence angle. A possible explanation for this relatively low backscatter is that the canopy is so dense that it scatters like a smooth surface. At other incidence angles the two types of ñire have essentially the same brightness.

The results of this work indicate that (1) various forest species and various structures of a single species may be discriminated using multiple incidence angle radar imagery and (2) it is essential to consider the variation in backscatter due to a variable incidence angle when analyzing and comparing data collected at varying frequencies and polarizations.

## ACKNOWLEDGEMENTS

The work described in this paper was carried out under contract with the National Aeronautics and Space Administration at the Jet Propulsion Laboratory, California Institute of Technology.

## REFERENCES


Cimino, J., A. Brandani, D. Casey, J. Rabassa, and S. Wall, 1986, "III. Multiple Incidence Angle SIR-B Data over Argentina: Mapping of Vegetation Units," IEEE, July issue.

Domik, G., F. Leberl and J. B. Cimino, 1986, II. Multiple Incidence Angle SIR-B Experiment Over Argentina: Generation of Secondary Image Products, IEEE, July issue.

Leberl, F., G. Domik, J. Raggams, J. Cimino, M. Kobrick, 1986a, I. Multiple Incidence Angle SIR-B Experiment Over Argentina: Stereo-Radargrammetric Analysis, IEEE, July issue.

Leberl, F., J. Raggam, G. Domik, M. Kobrick, 1986b, "Radar Stereo Mapping Techniques and Application to SIR-B Images at Mt. Shasta, IEEE, July issue.

SIR-B Science Plan, 1984, JPL Publication 82-78, Pasadena, CA.


Table 1. Multiple incidence angle SIR-B data set

| Data take | Center incidence angle | Date (1984) | On GMT | Duration (min) | Azimuth look direction |
|---|---|---|---|---|---|
| 56.4 | 33.0° | Oct. 8 | 282/22:31:0 | 4 | N42E |
| 72.4 | 44.7° | Oct. 9 | 283/22:14:0 | 2 | N40E |
| 88.4 | 53.7° | Oct. 10 | 284/21:57:0 | 2 | N40E |
| 104.4 | 59.4° | Oct. 11 | 285/21:39:0 | 4 | N39E |

Table 2. Intersection angles

| Case | Data takes | Look angles | Intersection angles |
|---|---|---|---|
| I | 104/88 | 56°/51° | 5° |
| II | 88/72 | 51°/43° | 8° |
| III | 72/56 | 43°/33° | 10° |
| IV | 104/72 | 56°/43° | 13° |
| V | 88/56 | 51°/33° | 18° |
| VI | 104/56 | 56°/33° | 23° |

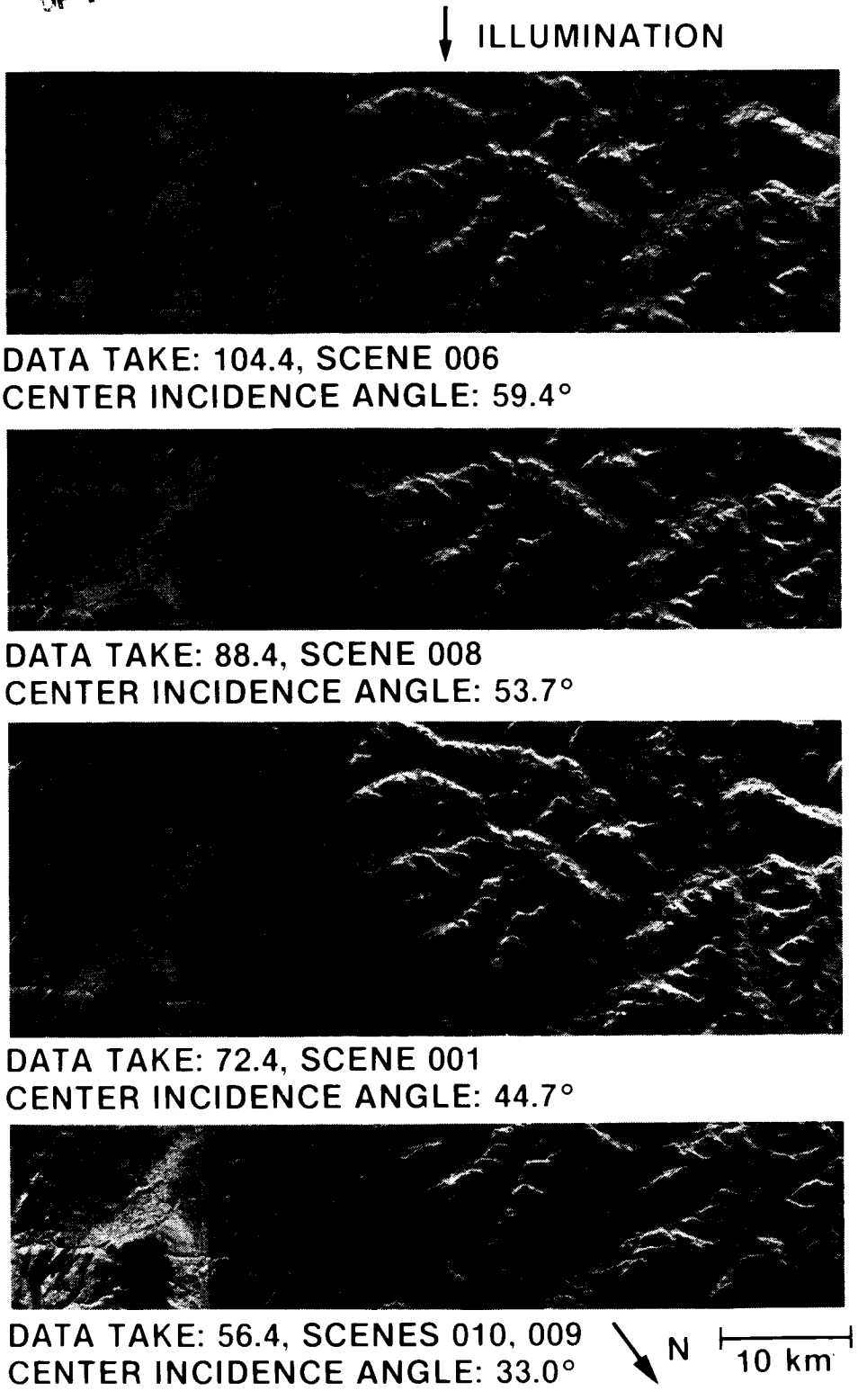


Figure 1a. The four multiple incidence angle images of the Cordón la Grasa region.

# SIR-B/ARGENTINA
# MAP OF ECO-GEOMORPHOLOGIC UNITS

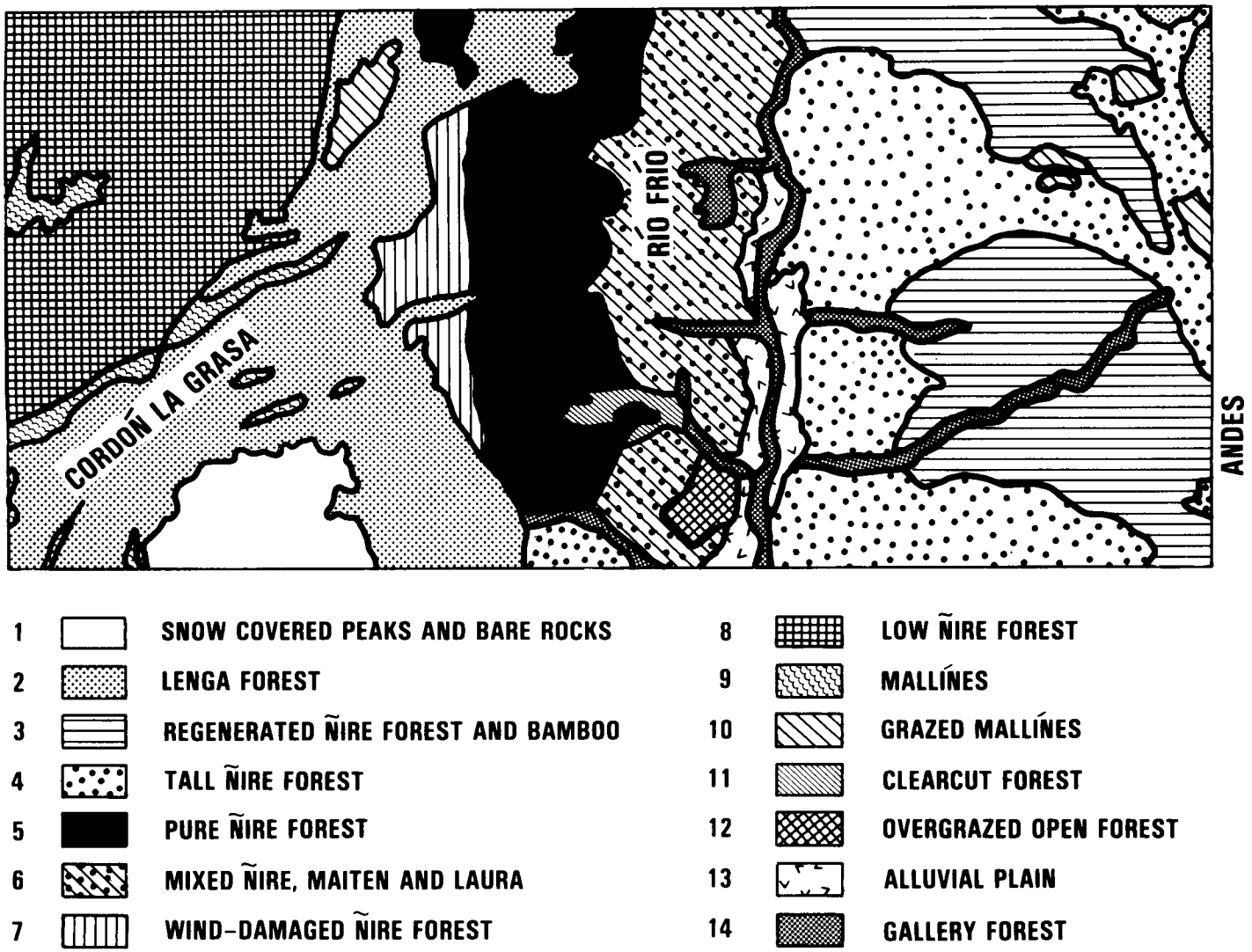


Figure 1b. Vegetation map of the Cordón la Grasa region.

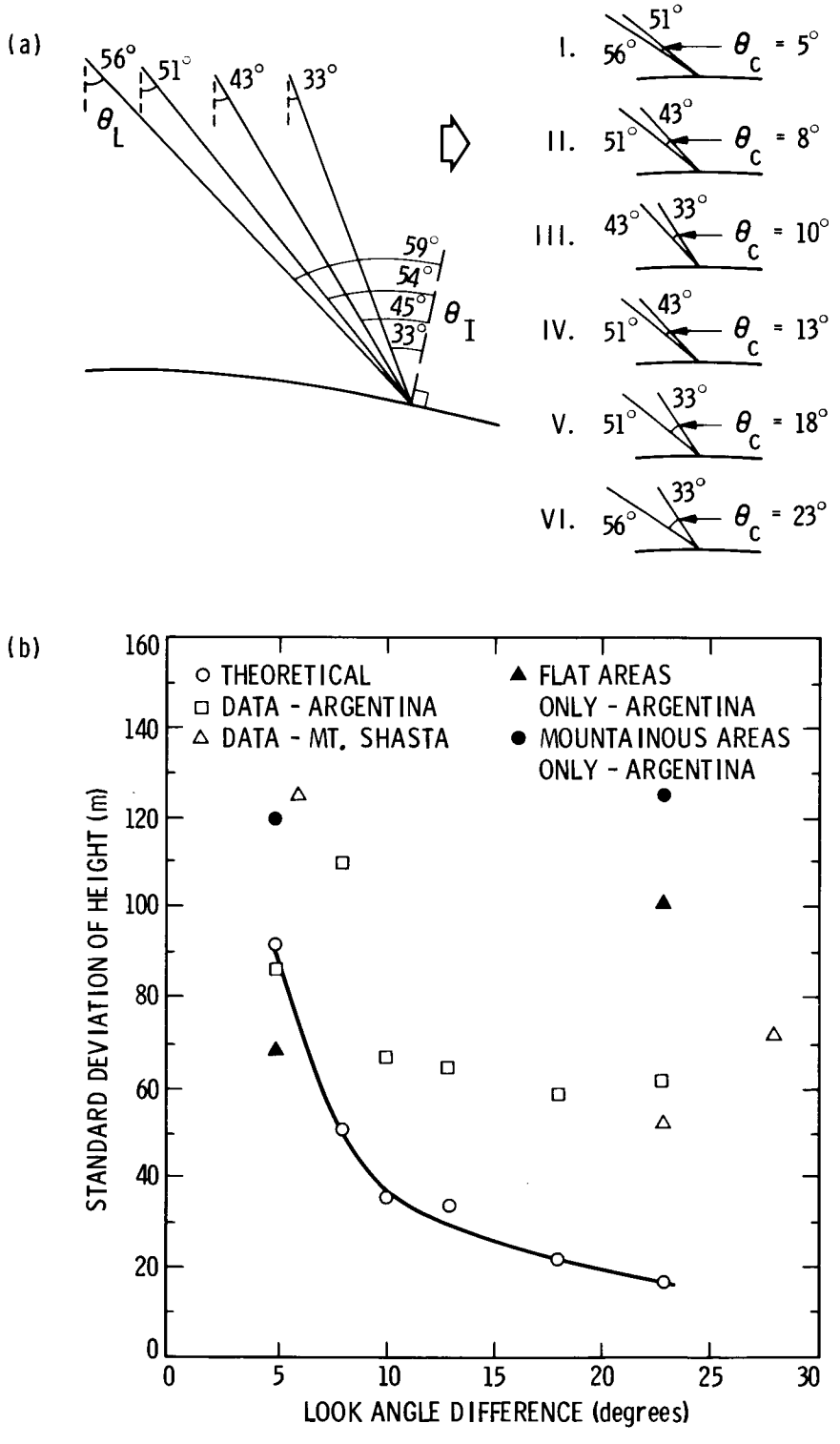


Figure 2. (a) Look angle geometry of 6 stereo models formed by the 4 images of Figure 1a; (b) Height accuracy versus stereo intersection angles, both as predicted and obtained experimentally.

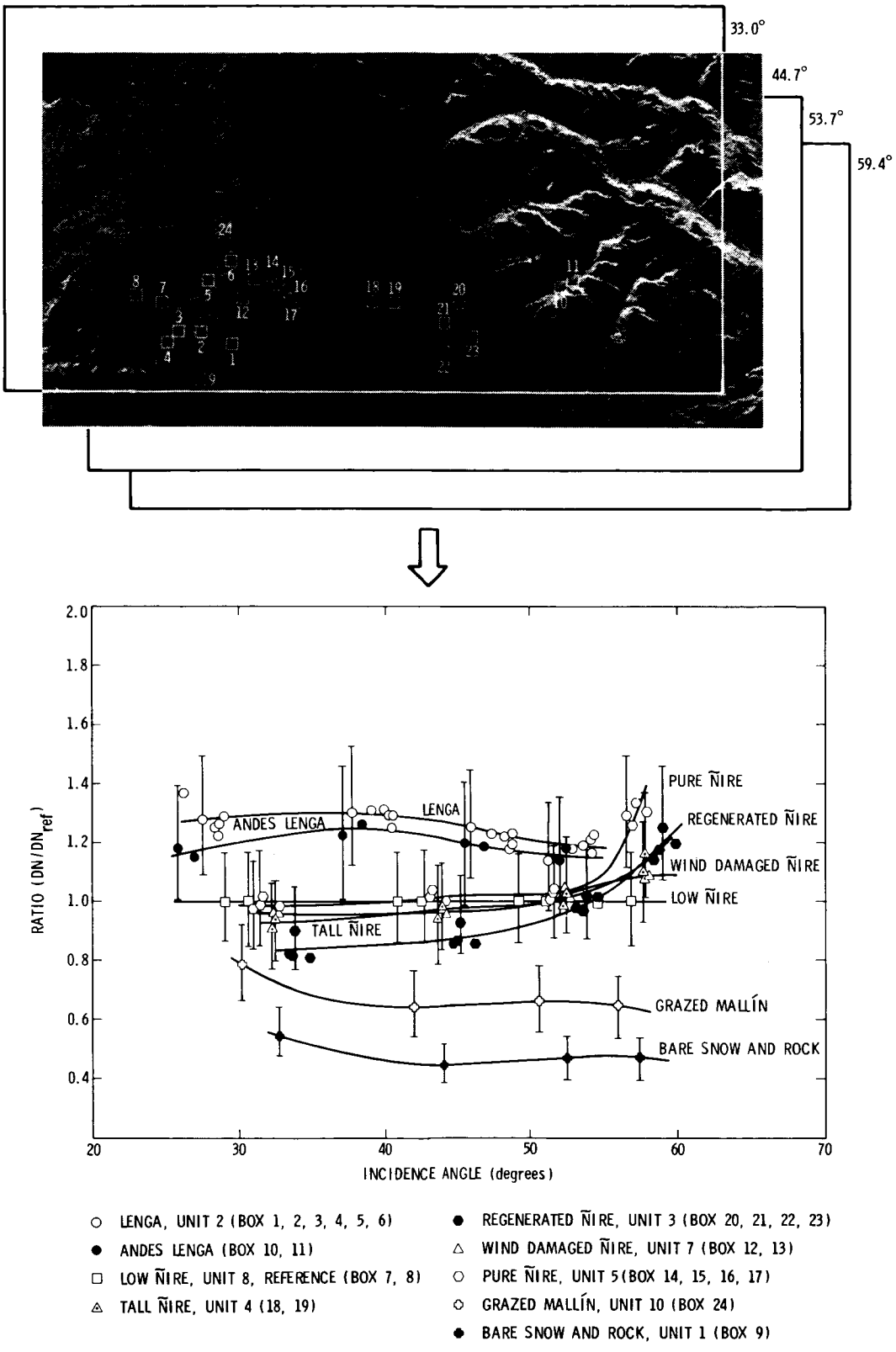


Figure 3. (a) SIR-B image showing location of areas used to generate relative brightness curves; (b) Relative brightness as a function of local incidence angle.



C-3

N87-17158

# IMAGING RADAR POLARIMETRY FROM WAVE SYNTHESIS

Howard A. Zebker, Jacob J. Van Zyl, and Daniel N. Held
Jet Propulsion Laboratory, California Institute of Technology
Pasadena, California

## I. INTRODUCTION

An imaging radar polarimeter measures the radar backscatter intensity and relative phase as a function of both the transmitted and received wave polarization states. We measure directly the amplitude and phase of all elements of the scattering matrix for each individual pixel in a radar image, and subsequent data processing combines these elements to synthesize any desired combination of transmit and receive antenna polarizations. Different scattering models predict different functional dependences of intensity on polarization--observation of this dependence for actual targets permits identification of the dominant scattering mechanisms contributing to the measured backscatter. For example, we find that Bragg scattering closely approximates the observed scattering from the ocean. Urban areas can be modeled as two-bounce dielectric corner reflectors.

Radar remote sensing provides information about the geometric and electric structure of an object. A conventional imaging radar measures a single value of reflectivity for many thousands of points in a scene for a single polarization, whereas observation with an imaging radar polarimeter can completely determine the dependence of reflectivity on polarization for each point in the scene. The radar polarization signature of an object permits stronger inferences of the physical scattering process than single-polarization measurements through identification and characterization of the dominant scattering mechanism, thus the solution for geometric shape and dielectric constant of an object is less ambiguous. The techniques required to generate arbitrary radar polarization through reconfiguration of system hardware have been known for some time, at least since Hagfors' (1967) lunar observations. This subject has recently been reviewed in some detail by Giuli (1986). A severe limitation of this approach is that the hardware must be modified for each observation, making it infeasible to measure the complete polarization signature of many points in a scene. Here we report a new approach to measurement of the complete polarization signature of an image implemented with an airborne synthetic aperture radar system: we utilize signals recorded on one data pass from orthogonal linearly-polarized antennas which we combine in the data processor to synthesize any desired combination of transmit and receive polarizations. This technique allows us to measure the complex, multichannel reflectivity of a scene on a single aircraft pass and later reprocess the data to provide multiple image maps, each representing the backscattered energy from the scene measured with a different combination of observational transmit and receive polarizations. The resulting polarization signature measurements indicate optimum polarizations for observations of certain classes of objects, and give insight into the identification of dominant scattering mechanisms for each kind of object. Knowledge of the scattering mechanism is helpful in providing an accurate description of the object of interest.

## II. POLARIZATION OF THE TRANSMITTING AND RECEIVING ANTENNAS

We can denote the polarization state of the transmitting antenna by a complex 2-vector $C_t$ such that

$$C_t = \begin{matrix} C_{t,x} \\ C_{t,y} \end{matrix} \tag{1}$$

Where $C_{t,x}$ is the phasor representation of the transmitted, complex (amplitude and phase) wave amplitude in the x direction, and $C_{t,y}$ represents the complex wave amplitude in the y direction when a unit voltage signal is applied to the antenna terminals. The wave amplitudes in equation (1) are related to the Stokes parameters $s_i$ of the antenna by

$$\begin{aligned} s_0 &= |C_{t,x}|^2 + |C_{t,y}|^2 \\ s_1 &= |C_{t,x}|^2 - |C_{t,y}|^2 \\ s_2 &= |C_{t,x}|\ |C_{t,y}| \cos w \\ s_3 &= |C_{t,x}|\ |C_{t,y}| \sin w \end{aligned} \tag{2}$$

where w is the phase difference between $C_{t,x}$ and $C_{t,y}$. We list some of the more commonly used radar polarizations and their expression in terms of the above quantities in Table 1.

Simarily, we can describe the polarization of the receiving antenna by another 2-vector $C_r$, where $C_{r,x}$ represents the response of the antenna to a unit field aligned with the x direction and $C_{r,y}$ represents the response to a unit field aligned with y.

## III. POLARIZATION CHARACTERISTICS OF THE SCATTERERS

We model the scattering behavior of an object as a two-by-two scattering matrix S with complex elements (see, for example, van de Hulst, 1980), that is, each element describes the relative magnitude and phase of the incident and scattered waves in the coordinate system described above, hence the matrix S includes the transformation from transmitted wave to received wave directions. In the most general case, element is a function of the angles of incidence and scattering, and the scattering matrix has the form

$$S = \begin{matrix} S_{xx}(r_i,d_i;r_s,d_s) & S_{xy}(r_i,d_i;r_s,d_s) \\ S_{yx}(r_i,d_i;r_s,d_s) & S_{yy}(r_i,d_i;r_s,d_s) \end{matrix} \tag{3}$$

with the elements of S defined as in the following example: The quantity $S_{xy}(r_i,d_i;r_s,d_s)$ represents the complex ratio

$$\frac{E_{s,x}(r_s,d_s)}{E_{i,y}(r_i,d_i)} \tag{4}$$

where $E_{i,y}$ is the y-component of the incident wave, for incidence direction $(r_i d_i)$, and $E_{s,x}$ is the x-component of scattered wave amplitude in the direction $(r_s, d_s)$. The other elements of S are defined correspondingly, and several representative S-matrices for various scattering models are given in Table 2. Using the above definitions of $C_t$, $C_r$ and S, we model the voltage V measured at the terminals of an antenna $C_r$ in response to a wave initially generated by the antenna $C_t$, and subsequently scattered by an object characterized by S by

$$V = C_r^T \, S \, C_t \tag{5}$$

where the superscript T denotes the matrix transpose operation. Expanding the matrix multiplication (5), we have

$$V = C_{r,x} \, S_{xx} \, C_{t,x} + C_{r,x} \, S_{xy} \, C_{t,y} + C_{r,y} \, S_{yx} \, C_{t,x} + C_{r,y} \, S_{yy} \, C_{t,y} \tag{6}$$

The resulting received power P is then given by

$$P = V \, V^* \tag{7}$$

where the * denotes complex conjugation.

Note that using horizontally-polarized antennas ($C_t$ = (1 0), $C_r$ = (1 0)) for both transmit and receive functions permits inference of $S_{xx}$ directly from our measurement V, as only the first term of (6) contributes. The remaining combinations of horizontal and vertical transmit and receive antennas yield each of the other elements $S_{xy}$, $S_{yx}$, and $S_{yy}$.

Knowledge of all elements of S then allows us to calculate the measured scattering behavior of an object in response to synthesized, arbitrary transmit and receive polarizations. For example, from the actual measured voltages $S_{ij}$, the polarization vectors of the desired antenna polarizations, and equation (10), we can express the voltage we would have measured with RCP ($C_t$ = $(1/2^{1/2}$ (1 i)) transmit and LCP ($C_r$ = $(1/2)^{1/2}$(i 1)) receiving antennas as

$$\begin{aligned} V &= C_r^T(\text{LCP antenna}) \; S \; C_t \; (\text{RCP antenna}) \\ &= (1/2)^{1/2} \quad (i \;\; 1) \begin{matrix} S_{xx} & S_{xy} \\ S_{yx} & S_{yy} \end{matrix} (1/2)^{1/2} \begin{matrix} 1 \\ i \end{matrix} \\ &= (1/2) \quad (i \;\; 1) \begin{matrix} S_{xx} + iS_{xy} \\ S_{yx} + iS_{yy} \end{matrix} \\ &= (1/2) \quad (iS_{xx} - S_{xy} + S_{yx} + iS_{yy}) \end{aligned} \tag{8}$$

In this manner, we can determine the measured voltage, and hence the power corresponding to any arbitrary combination of transmit and receive polarizations utilizing only horizontally and vertically polarized antennas, if we employ equations of the form (6).

It is instructive at this point to consider a simple example of target backscatter behavior as a function of polarization in order to understand the basic operation of the polarimeter. The scattering matrix S that describes a unit-area isotropically scattering sphere is (van de Hulst, 1980)

$$S = \begin{matrix} 1 & 0 \\ 0 & 1 \end{matrix} \qquad (9)$$

The backscatter coefficient is unity for both of the diagonal elements of the scattering matrix, and zero for the off-diagonal elements. With this scattering matrix, equation (6) simplifies to

$$V = C_{r,x}\, C_{t,x} + C_{r,y}\, C_{t,y} \qquad (10)$$

We note that if the transmit polarization is horizontal ($C_t$ = (1 0)) and the receive polarization is vertical ($C_r$ = (0 1)), the response of the polarimeter will be zero. If RCP is chosen for transmit and LCP for receive ($C_t = (1/2)^{1/2}$ (1 i), $C_r = (1/2)^{1/2}$ (i 1)), however, the power received is maximized and equal to 1. Same-sense circular polarization for transmit and receive (RCP-RCP ro LCP-LCP) again yields zero power.

In summary, if our airborne hardware permits direct measurement of each element of S, through use of both horizontal and vertical antennas for transmit and receive, then these elements can be combined in the data processor to produce images representing any desired polarization state. Our imaging radar polarimeter thus consists of i) a conventional imaging radar with linear, orthogonally-polarized horizontal and vertical antennas, and ii) a data processor that can be used to synthesize the complete polarization signatures for each point in a scene.

## IV. POLARIZATION SIGNATURES

Imaging radar polarimeter observation of an object with scattering matrix S yields a measured voltage V, and power P, as given by equations (6) and (7) above. Since this quantity depends on the polarization states $C_t$ and $C_r$ of the transmitting and receiving antennas, respectively, we can define the polarization signature of S as the variation of P as a function of the polarizations of the antennas. The most general representation allows arbitrary values for each of the transmitting and receiving polarizations.

We illustrate some typical polarization signatures by first calculating scattering matrices corresponding to several scattering models, and then displaying the signatures resulting from application of equations (6) and (7) to each model. The first is an isotropically-scattering sphere (see equation (9) above), the second is a Bragg model, and the third is a dihedral corner reflector made of a dielectric material that is applicable to modeling urban areas. We note that the Bragg model predicts higher reflectivity for vertically-polarized waves than for horizontally-polarized waves, while the dihedral model predicts the reverse.

Examination of the plots in Figure 1 corresponding to the isotropic sphere shows that for co-polarized imaging, linear polarization provides the greatest return, and that the signal strength is independent of linear polarization angle. This independence of linear polarization direction is a consequence of the lack of a preferred orientation for spheres. For the cross-polarization spectrum, signals are greatest for the circular polarizations and smallest for linear polarizations. The Bragg model is somewhat different in nature from the isotropic sphere models in that an enhancement for vertical polarization over horizontal polarization is evident in the co-polarized spectrum. Also, the co-polarized minimum occurs not at LCP and RCP but slightly towards linear polarization for each. This behavior is due to $|S_{yy}|$ exhibiting greater magnitude than $|S_{xx}|$. A dielectric dihedral corner reflector model exhibits a very different polarization signature from the previous two models. The co-polarized spectrum possesses two minima at linear polarizations offset by $\pm 45°$ from the x and y directions, and the cross-polarized spectrum possesses maxima at these locations.

We note that use of an imaging polarimeter to observe the full polarization signature of an object, coupled with interpretation in terms of simple scattering mechanisms such as those illustrated here, allows us to develop a scattering model that is consistent with the measured polarization properties of the object, even if we cannot exclude all other possible models. While we have clearly not considered all possible scattering models, it follows from the above that if the polarization signature of a real object could be unambiguously identified as resembling any one of the models depicted here, the dominant scattering mechanism may be described and analyzed with some confidence.

In Figure 2 we present polarimeter images in synthesized polarization combinations, and also present some complete polarization signatures of sub-areas of these images. The data shown here were processed by synthesizing a set of linear, co-polarized antennas and applying them to data collected over San Francisco, California. This figure consists of twenty images; the upper left image corresponds to horizontal transmit, horizontal receive polarization. Scanning from left to right and from top to bottom, the angle of the electric field vector is advanced 2.5° per image and the amplitude of the result is displayed. The lower right image thus corresponds to linear polarization oriented 47.5° from horizontal. We note that the urban area, for example, exhibits great variation in brightness as the polarization changes, while the Golden Gate Park area changes little. As we note in the discussion of the polarization signatures below, we can predict the variation of the urban area quite well using a two-bounce corner reflector model, while we interpret the relative constancy of the park as indicative of a higher degree of multiple scatter than is apparent elsewhere in the image.

Measurement of the brightness of any sub-area of an image as the polarization is varied yields the observed polarization signature of that region. The complete polarization signatures for each of three sub-areas are shown in Figure 3. The observed signature of the ocean closely resembles the Bragg signature of Figure 1b, thus it is likely that some Bragg-like mechanism is responsible for backscatter from the ocean. The urban polarization signature is similar in appearance to the dihedral model (Figure 1c), with the addition of a "pedestal" to the overall signature. The park signature

exhibits a still greater pedestal than does the urban signature. We ascribe this additive term to an unpolarized component in the observed backscatter, thus the signal from an urban area can be modeled as including a polarized, dihedral-type return plus an unpolarized component.

We have shown that it is possible to measure the complete scattering matrix of an object using data acquired on a single aircraft pass, and can combine the signals later in the data processor to generate radar images corresponding to any desired combination of transmit and receive polarization. Various scattering models predict different dependence on polarization state of received power from an object. Our imaging polarimeter permits determination of this dependence, which we call the polarization signature, of each point in a radar image. Comparison of the theoretical predictions and observational data yield identification of possible scattering mechanisms for each area of interest. We have found that backscatter from the ocean is highly polarized and well-modeled by Bragg scattering, while scattering from trees in a city park possesses a considerable unpolarized component. Urban regions exhibit the characteristics expected from dihedral corner reflectors and their polarization signatures are quite different from the one-bounce Bragg model.

## REFERENCES


Giuli, D., Polarization Diversity in Radars, Proc. of the IEEE 74, 245-269, 1986.

Hagfors, T., A Study of the Depolarization of Lunar Radar Echoes, Radio Science 2,445-465, 1967.

Van de Hulst, H., Light Scattering by Small Particles, Dover Publications, New York, 1981.


Table 1. Some common radar polarizations

| Polarization | Vector C | Complex polarization p | Stokes vector |
|---|---|---|---|
| Linear horizontal | (1 0) | 0 | (1,1,0,0) |
| Linear vertical | (0 1) | B | (1,-1,0,0) |
| Right-hand circular (RCP) $(1/2)^{1/2}$ | (1 i) | i | (1,0,0,-1) |
| Left-hand circular (LCP) $(1/2)^{1/2}$ | (i 1) | -i | (1,0,0,1) |

Table 2. Representative S - matrices

| Model | S-matrix | Notes |
|---|---|---|
| Isotropic sphere | $\begin{matrix} a & 0 \\ 0 & a \end{matrix}$ | a real, a > 0 |
| Bragg | $\begin{matrix} a & 0 \\ 0 & b \end{matrix}$ | a,b real<br>a >0, b >0<br>b > a |
| Real-dielectric dihedral corner reflector | $\begin{matrix} -a & 0 \\ 0 & b \end{matrix}$ | a,b real<br>a > 0, b >0 |

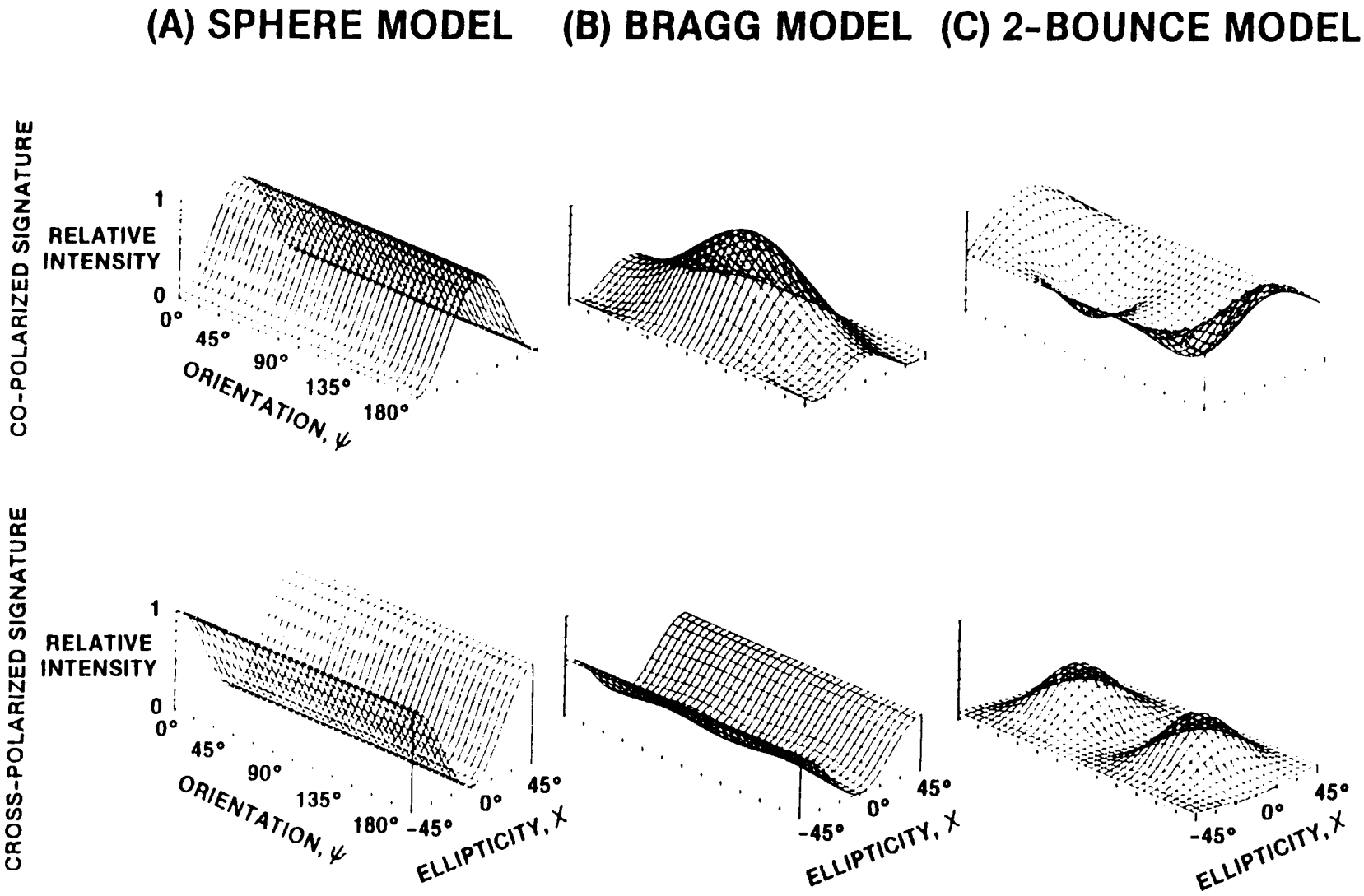


Figure 1. Plots corresponding to the isotropic sphere

Figure 2. Polarimeter images of San Francisco. The data shown were processed by synthesizing a set of linear, copolarized antennas and applying them to data collected over San Francisco, California

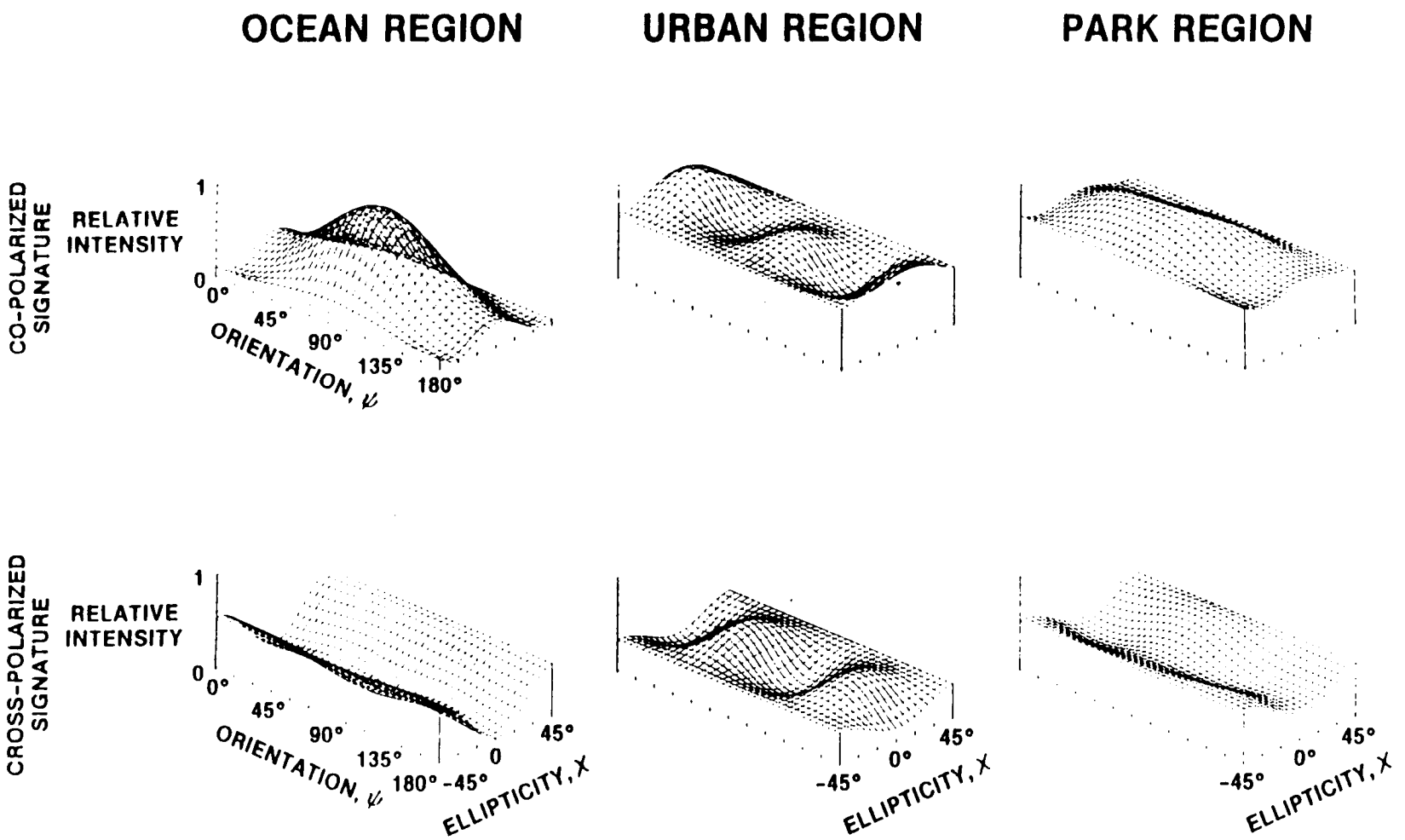


Figure 3. Complete polarization signatures

# RADAR SIGNATURE DETERMINATION : TRENDS AND LIMITATIONS

J. A. Richards
Centre for Remote Sensing, and
School of Electrical Engineering and Computer Science
The University of New South Wales
Kensington NSW, Australia

## I. INTRODUCTION

Knowledge of the backscattering characteristics of earth surface features is essential for reliable interpretation of radar image data, particularly if tonal discrimination, as against structural interpretation, is required. Information on backscattering behavior can be derived from measurements or by constructing and utilizing models of the interaction of radar incident energy with cover types of interest. An appealing aspect of the latter approach is that a suitably derived model might be invertible, allowing significant physical properties of a surface to be determined using radar remote sensing data as an input. Several different approaches may be adopted in endeavoring to derive backscatter models, including the use of a theoretical framework based upon propagation and scattering theory or the adoption of regression fits to experimental data. One can also adopt a phenomenological approach in which an apparently complicated situation can be viewed as a set of readily handled components.

Modelling studies, as means for assessing what could be called radar signatures, are a part of two radar remote sensing research programs with which the author is affiliated. First, at the University of New South Wales, assessment of SIR-B data is being undertaken for a number of purposes including its value in arid land geomorphological and geological studies, forest and crop assessment, and mapping. A number of early results have been reported [1-6]; however modelling aspects are still at an early stage. Secondly, the author recently spent 6 months working on SIR-B invertible forest canopy modelling in the Department of Geography at the University of California, Santa Barbara. Results from this work are outlined in the following; fuller details will be found in Richards, Sun and Simonett [7].

## II. SIMPLE FOREST BACKSCATTER MODELLING AT L-BAND

A forest stand, particularly at L-band, is a composite scattering environment. In establishing a model one may need to account therefore for volume scattering from the foliage, scattering from the underlying surface or understory and scattering from the branches, branchlets and trunks. There is also ample evidence to suggest that significant radar return can result from bistatic scattering from tree elements onto the surface, followed by specular reflection from the surface to the sensor [6,8]. Guided by tractability and invertibility considerations, those components considered important need to be realised as a model and then aggregated with forest statistical data to form a model of a forest stand.

The simplified model adopted in the current treatment is shown in Figure 1, consisting of four components that are easily described. A simple exponential dependence of diffuse surface backscatter was chosen for the soil component, modified suitably for two way path loss in the canopy. An order of magnitude of 0.1 $Npm^{-1}$ was chosen for the attenuation coefficient, with other parameters chosen from Figure 11.98 of Ulaby et al. [9]. A simple water cloud model was chosen for the foliage [10] while the work of Engheta and Elachi [11] was used to account for backscattering via multiple reflection from the foliage and surface. Parameter values for these were established from Attema and Ulaby, and from the chosen value of the attenuation coefficient.

The fourth component adopted is strong reflection via the trunk and surface, with the trunk viewed as a lossy dielectric cylinder standing on a lossy plane. However, rather than using available expressions for bistatic scattering from cylinders [12], considerations of computational speed and the need to keep the model simple if inversion is to be entertained, led to representing the trunk/ground combination as a simple planer dihedral corner reflector. An expression for the radar cross section for this structure is available. In the work undertaken [7] this was modified to account for Fresnel reflections at the trunk and ground and for the two way path loss through the canopy. A correction factor was also incorporated to match the reflection from the dihedral arrangement to that for a cylinder over a plane.

Figure 2 shows simulated levels of backscatter versus incidence angle for 20 trees of 20m height, added incoherently. Both the individual backscattering components and the composite value are shown, suggesting that at L band with the parameter values chosen, the trunk/ground component is dominant over the midrange of incidence angles.

The importance of the trunk term is also evident in the results of Figure 3. These compare simulated backscatter to measured (SIR-B) backscatter of a region of the Klamath forest in the Mt. Shasta region of northern California for 6 different natural stands and two plantations of Ponderosa Pine; the stands were of differing heights and densities. Owing to the uncalibrated nature of SIR-B, it was necessary to match the simulated and measured values for one experimental site. As seen, when contribution from the trunk is included there is a much better match of simulated and measured results.

## III. CONCLUDING REMARKS

Development of the forest canopy model is continuing at the University of California, Santa Barbara. Present intentions are to incorporate generalizations to other wavebands and polarization configurations, which almost certainly will require better models for canopy scattering. The trunk scattering term however is easily adjusted for these different conditions.

In the Australian experiment it is intended to modify the trunk term to account for the different morphologies of native Eucalypts. In addition however it is planned to extend the nature of the model to allow simulations of backscatter from sugar cane plantations.

ACKNOWLEDGMENTS

The author is grateful to Professor D. S. Simonett of the University of California, Santa Barbara, for the opportunity to work on forest stand modelling with Sun Guoqing under NASA/JPL contract #JPL 956887. The Australian project is supported by the Australian Research Grants Scheme.

REFERENCES

1. J. A. Richards, B. C. Forster, G. R. Taylor, J. C. Trinder and A. K. Milne. Preliminary results from an Australian multi-experimental assessment of SIR-B. IEEE International Geoscience and Remote Sensing Symposium, Amherst, Mass. 1985.

2. G. J. Lynne and G. R. Taylor. Geological assessment of SIR-B imagery of the Amadeus Basin, central Australia. IEEE Transactions on Geoscience and Remote Sensing (in press).

3. G. R. Taylor and G. J. Lynne. Pattern recognition and geological interpretation of SIR-B images of central Australia. Proc. ERIM 5th Thematic Conference (Remote Sensing for Exploration Geology). Reno, Nevada. September 1986.

4. G. J. Lynne and G. R. Taylor. Integration of SIR-B imagery with geological and geophysical data in central Australia. Proc. ERIM 5th Thematic Conference (Remote Sensing for Exploration Geology). Reno, Nevada. September 1986.

5. J. C. Trinder, The use of SIR-B and LFC image for mapping. International Seminar on Photogrammetry and Remote Sensing, Delhi, India. March 1986.

6. A. K. Skidmore, P. W. Woodgate and J. A. Richards. Classification of the Riverina forests of S. E. Australia using co-registered Landsat MSS and SIR-B radar data. Symposium of Commission VII, International Society of Photogrammetry and Remote Sensing. The Netherlands, October 1986.

7. J. A. Richards, G. Sun and D. S. Simonett. L-band radar backscatter modelling of forest stands. Submitted for publication to IEEE Transactions on Geoscience and Remote Sensing.

8. J. P. Ormsby, B. J. Blanchard and A. J. Blanchard. Detection of lowland flooding using active microwave systems. Photogrammetric Engineering and Remote Sensing, 51, 1985, pp. 317-328.

9. F. T. Ulaby, R. K. Moore and A. K. Fung. Microwave Remote Sensing: Active and Passive, Vol. 2, Massachusetts. Addison Wesley, 1982.

10. E. P. W. Attema and F. T. Ulaby. Vegetation modeled as a water cloud. Radio Science, 13, 1978, pp. 357-364.

11. N. Engheta and C. Elachi. Radar scattering from a diffuse vegetation layer over a smooth surface. IEEE Transactions on Geoscience and Remote Sensing, GE-20, 1982, pp. 212-216.

12. G. T. Ruck, D. E. Barrick, W. D. Stuart and C. K. Kirchbaum. Radar Cross Section Handbook, New York: Plenum 1970.

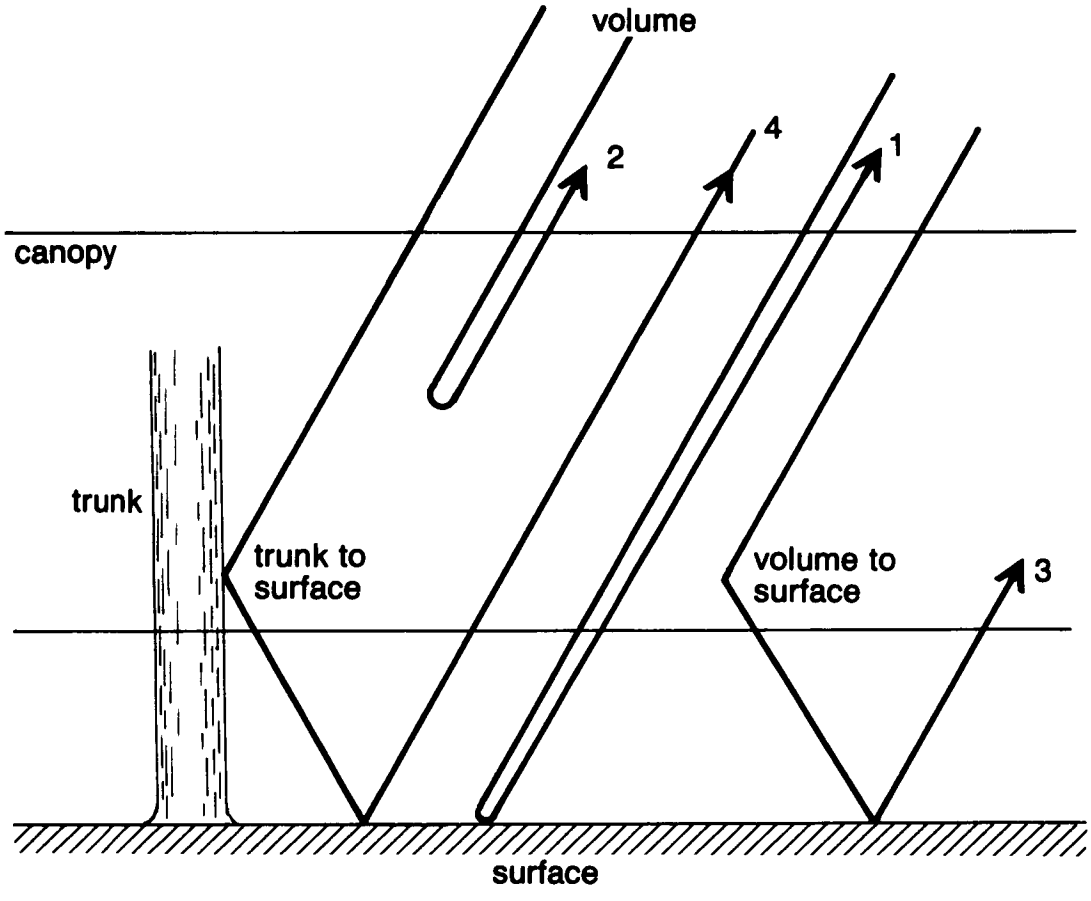


Figure 1. Components of forest backscatter considered in the model.

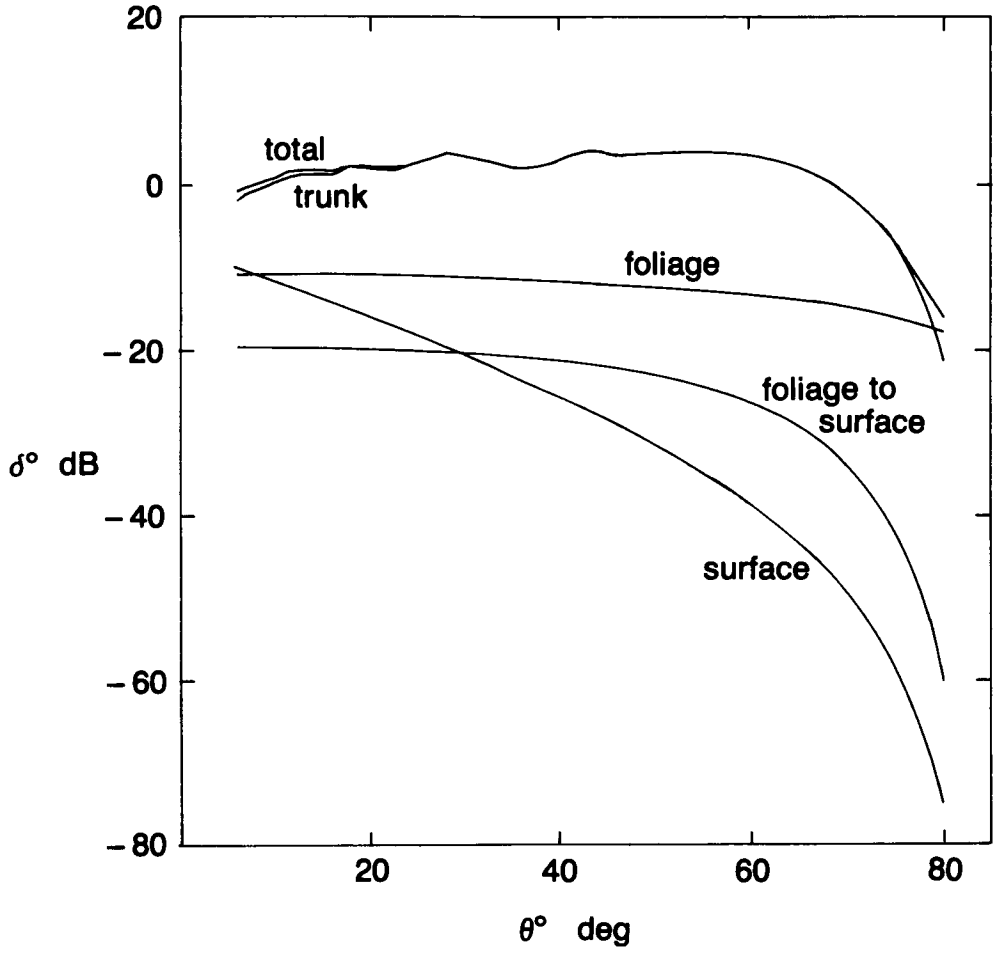


Figure 2. Simulated backscattering coefficient as a function of incidence angle for each of the four components of forest scattering and for their aggregate (from Ref. 7).

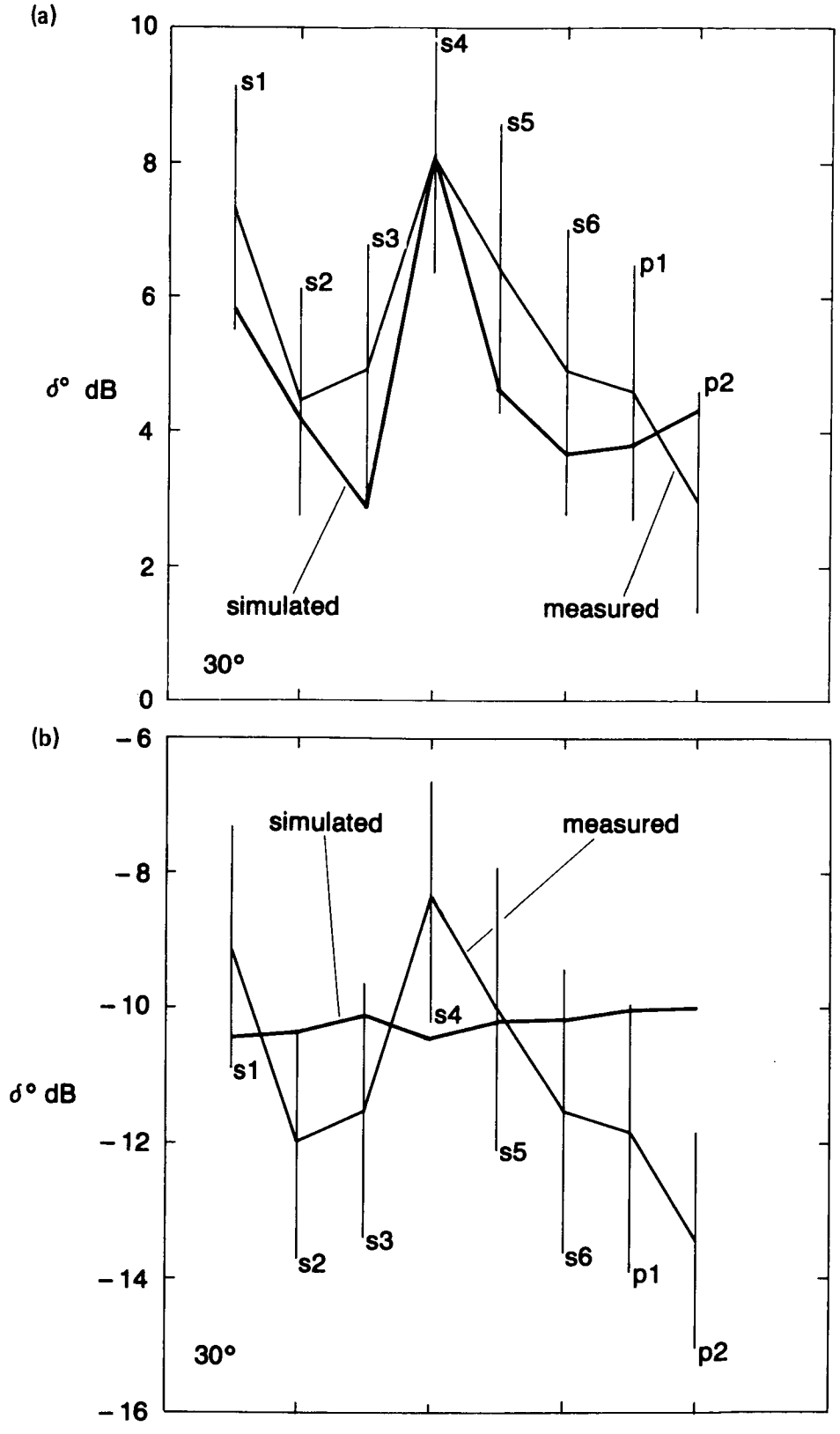


Figure 3. Comparison of measured and simulated forest backscattering coefficient for six natural stands and two plantations of Ponderos Pine (a) with trunk term included (b) without the trunk term (from Ref. 7).

# SIR-B MEASUREMENTS AND MODELING OF VEGETATION

Fawwaz T. Ulaby and M. Craig Dobson
University of Michigan
Ann Arbor, Michigan

## I. INTRODUCTION

This paper presents a summary of the results derived from analysis of six SIR-B data takes over an agricultural test site in west-central Illinois. The first part of the paper describes the procedure used to calibrate the SIR-B imagery, the second part pertains to the observed radar response to soil moisture content, and the last part examines the information derivable from multiangle observations.

## II. SIR-B CALIBRATIONS

Five calibrated receivers distributed over an area extending approximately 20 km in both range and azimuth directions were used to record the azimuth pattern of the SIR-B antenna beam for each of six shuttle passes over the test site. A typical pattern is shown in Fig. 1(a). In addition to measuring the shape of the pattern, the transmitter power-gain product $P_t G_t$ was determined also. The values recorded by the various receivers on the six data takes were then combined to establish the range pattern of the SIR-B antenna[1].

The second objective of the calibration task was to develop a transfer function that relates the digital number DN of a given pixel to the scattering coefficient $\sigma^\circ$ of that pixel. To this end, two types of calibration targets were used: (a) six Active Radar Calibrators (ARCs), and (b) approximately 80 distributed targets. The ratio of the signal from an ARC to that from the background pixel in which it was deployed was typically 15 dB. The distributed targets were uniform agricultural fields whose scattering coefficients were measured by calibrated truck-mounted scatterometers within $\pm$2 hours of the shuttle overpass. The result of this calibration study is shown in Fig. 1(b) for one of the data takes (Orbit 97.2). Another curve (with no data points shown) is given for Orbit 49.2 to indicate the level of change that existed between data takes due to changes in transmitter power.

## III. SOIL-MOISTURE RESPONSE

Two predawn ascending data takes by SIR-B were used to evaluate the effect of soil moisture on the scattering coefficient. The two images were separated in acquisition date by three days and were obtained at the same local angle of incidence ($\theta$ = 30°) but with opposite azimuth viewing directions.

Figures 2(a) and 2(b) show linear regressions of the scattering coefficient measured by SIR-B versus soil moisture content for bare fields and fields planted with corn, respectively. The corn plants had an average maximum height of 280 cm and an average water content of 2.12 kg/m$^2$. We observe that $\sigma^\circ$ exhibits a strong sensitivity to soil moisture content for both cases. This result is not surprising when considered alone because it would imply that

the canopy is quasi-transparent, but the fact that the level of the $\sigma^\circ$ response is about 5.5 dB higher than that of the bare-soil response presents a problem. Ordinarily, a high $\sigma^\circ$ level for corn would be attributed to volume scattering by the corn canopy, but such a strong scattering medium would also be a highly lossy medium, thereby resulting in poor sensitivity to soil moisture. This problem was resolved by modeling the canopy backscattering as the sum of three terms: (a) volume backscattering by the canopy, (b) soil backscatter attenuated by the canopy, and (c) a new term related to soil-volume interaction. This last term accounts for forward scatter by the soil followed by reflection by the stalks, as well as the inverse process. The results of this analysis [2] are shown in Fig. 3, which shows that the soil-volume interaction term is the dominant term among the three.

## IV. INFORMATION FROM MULTIANGLE OBSERVATIONS

In any assessment of the information content of multiangle SIR-B observations, it is important to understand that all observations are also separated in the time domain and may be derived from distinctive azimuthal viewing geometries. Hence, composite images of multiangle observations contain information related both to sensor/scene geometric properties and to scene dynamics. The SIR-B observations of the Illinois test site consist of two ascending and four descending data takes occurring predawn and early afternoon respectively at the viewing geometrics listed in Table 1.

Table 1. SIR-B Data Takes

| Data Take | Date | Local Time | Incidence Angle | Look Direction |
|---|---|---|---|---|
| 38.1 | October 7 | 2:25 PM | 17° | NE |
| 49.2 | October 8 | 6:23 AM | 30° | NW |
| 54.1 | October 8 | 2:08 PM | 38° | NE |
| 70.1 | October 9 | 1:52 PM | 50° | NE |
| 86.1 | October 10 | 1:34 PM | 59° | NE |
| 97.2 | October 11 | 5:32 AM | 30° | SE |

The test site consists of an agricultural region of well-drained silt loams (loess) with small vertical relief. Soil moisture conditions ranged from 0.2 to 0.3 $g/cm^3$ over the observation period in response to a prolonged period of cloud cover with associated light rain and ground fog. Of the agricultural portion of the site, 45% had been planted to corn and 45% to soybeans; the remaining 10% primarily contained alfalfa, sorghum, and pasture. Both the corn and soybeans were generally in harvest-ready conditions and during the experimental period approximately 10% of the corn and 30% of the soybeans were harvested. Thus, approximately 5% of the agricultural area experienced a dramatic change in surface cover due to harvest/tillage operations over any 24 hour period.

An example color composite of multiangle and multidate imagery is shown in figure 4, using data obtained at the maximum, median, and minimum incidence angle limits for SIR-B. The familiar checker-board pattern of agricultural fields is displayed in a wide variety of additive colors as related to both the magnitude of radar backscatter $\sigma^\circ$ as a function of incidence angle $\theta$ for time-constant target conditions and to field-specific tillage/harvest history over the four-day period. Unharvested corn produces a bright return at all three angles and is observed as a variety of bright additive colors wherein hue is related to subtle differences in canopy condition (biomass, stage of growth, etc.). The progress of the corn harvest can be readily mapped on a daily basis as freshly harvested corn appears as bright blue or blue-green depending upon the date of harvest. Other crop canopies appear generally dark with image brightness proportional to surface roughness and canopy biomass conditions. Fields which have been roughened by plowing or disking tend to express themselves as various shades of green, yellow, and orange and have moderate intensity depending upon the date and nature of the tillage operation. No row direction effects are observed, which is to be expected for azimuth view angles of approximately 45° with respect to crop row direction.

The effects of gentle relief and scene dynamics on stereo imaging are illustrated by figure 5. Stereo coverage was provided by the sidelap region of the two ascending data takes both at 30° incidence angle but with a 180° difference in illumination direction and a three-day time difference. Figure 5(a) shows the additive color composite of the two data takes; the image intensity for each data take has been radiometrically calibrated to $\sigma^\circ$ via log linear transfer functions established by active radar calibrators and by truck scatterometer observations. Yellow would indicate equivalent $\sigma^\circ$ on both dates; the generally orange hue of the image is the result of an average increase in $\sigma^\circ$ of 2 to 3 dB over the three day period as a consequence of daily rainfall leading to a 0.05 to 0.1 $g/cm^3$ increase in near surface soil moisture. Since the area is not irrigated, bright red fields can only be attributed to surface roughness changes due to tillage ($\Delta\sigma^\circ$ = 3 to 5 dB) while green areas correspond to the harvest of corn over the three-day period.

Stereo separation of the topographic effects (3° to 5° local slopes) and scene change are enhanced by differencing the magnitudes of the two calibrated images. Figure 5(b) is a pseudo-color presentation of the difference in $\sigma^\circ$ between the two ascending data takes. The differential illumination of local slopes along both sides of drainages allow ready discrimination of the drainage network even in areas of only 10 to 20 m net relief. In addition to the field specific changes in $\sigma^\circ$ related to changes in agronomic conditions, the regional change in $\sigma^\circ$ is found to correlate well with the rainfall patterns recorded by an informal network of 56 gauges. Hence, appropriate filtering of calibrated change detection can yield thematic maps of agronomic changes (i.e., harvest, no change, plowing) and contour maps of soil moisture change which are more nearly independent of field specific canopy and roughness conditions.

## V. CONCLUSIONS

This study demonstrated that it is possible to establish a calibration transfer function for a space SAR with an accuracy of about $\pm 0.9$ dB. Moreover, because the SIR-B imagery wave calibrated into $\sigma^\circ$ units, it was possible to conduct a quantitative analysis of the radar response to soil moisture and to extend theoretical models accordingly.

The use of multiangle observations -- either in incidence, azimuth, or both -- has been found to provide valuable topographic information, and change detection provides information on agronomic conditions and soil moisture variations.

In a related study involving multipolarization airborne observations made coincident with SIR-B, a model was developed relating the phase difference between HH and VV backscattered signals from corn to the dielectrics and geometric properties of the corn canopy [3].

## REFERENCES


[1] Dobson, M. C., F. T. Ulaby, D. R. Brunfeldt, and D. N. Held, "External Calibration of SIR-B Imagery with Area-Extended and Point Targets," IEEE Trans. Geoscience and Remote Sensing, Vol. GE-24, No. 4, 1986.

[2] Dobson, M. C., and F. T. Ulaby, "Preliminary Evaluation of the SIR-B Response to Soil Moisture, Surface Roughness, and Crop Canopy Cover," IEEE Trans. Geoscience and Remote Sensing, July, 1986.

[3] F. T. Ulaby, D. Held, M. C. Dobson, and K. McDonald, "Relating Polarization Phase Difference of SAR Signals to Scene Properties," IEEE IGARSS Special Issue, November, 1986.

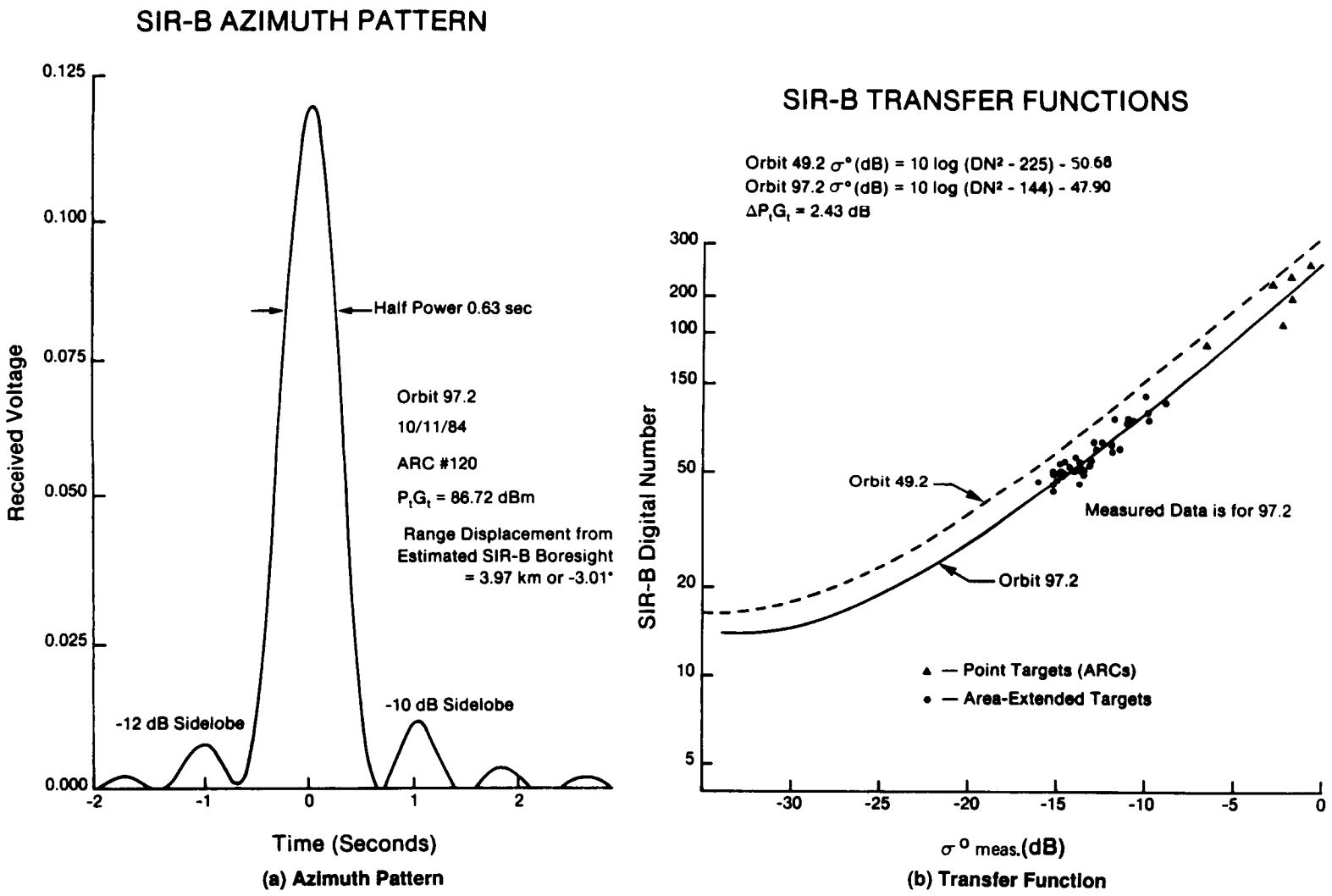


Figure 1. Measured (a) azimuth pattern of SIR-B antenna and (b) SIR-B transfer function.

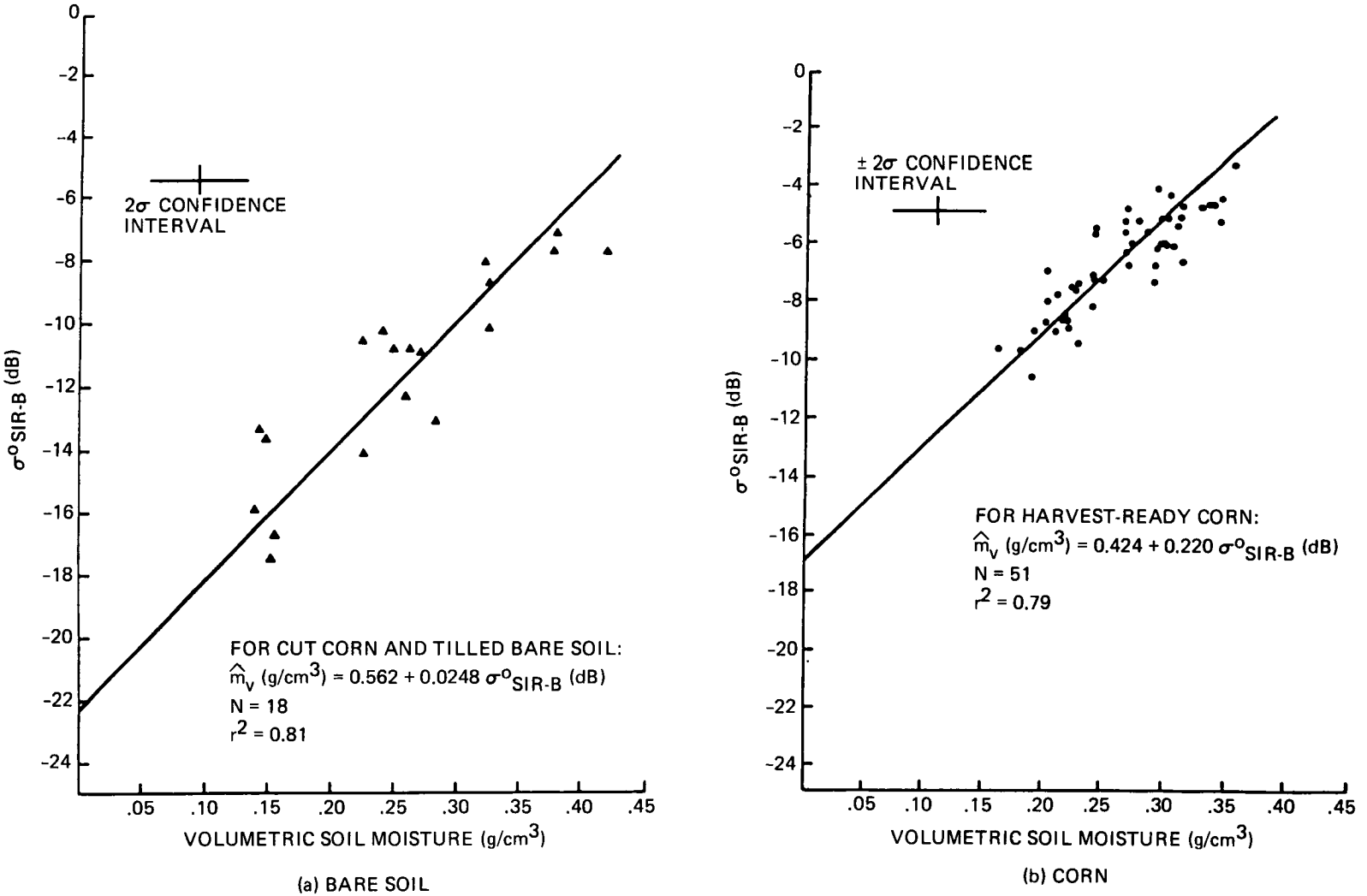


Figure 2. Measured SIR-B response to soil moisture for (a) bare soil and (b) corn canopies.

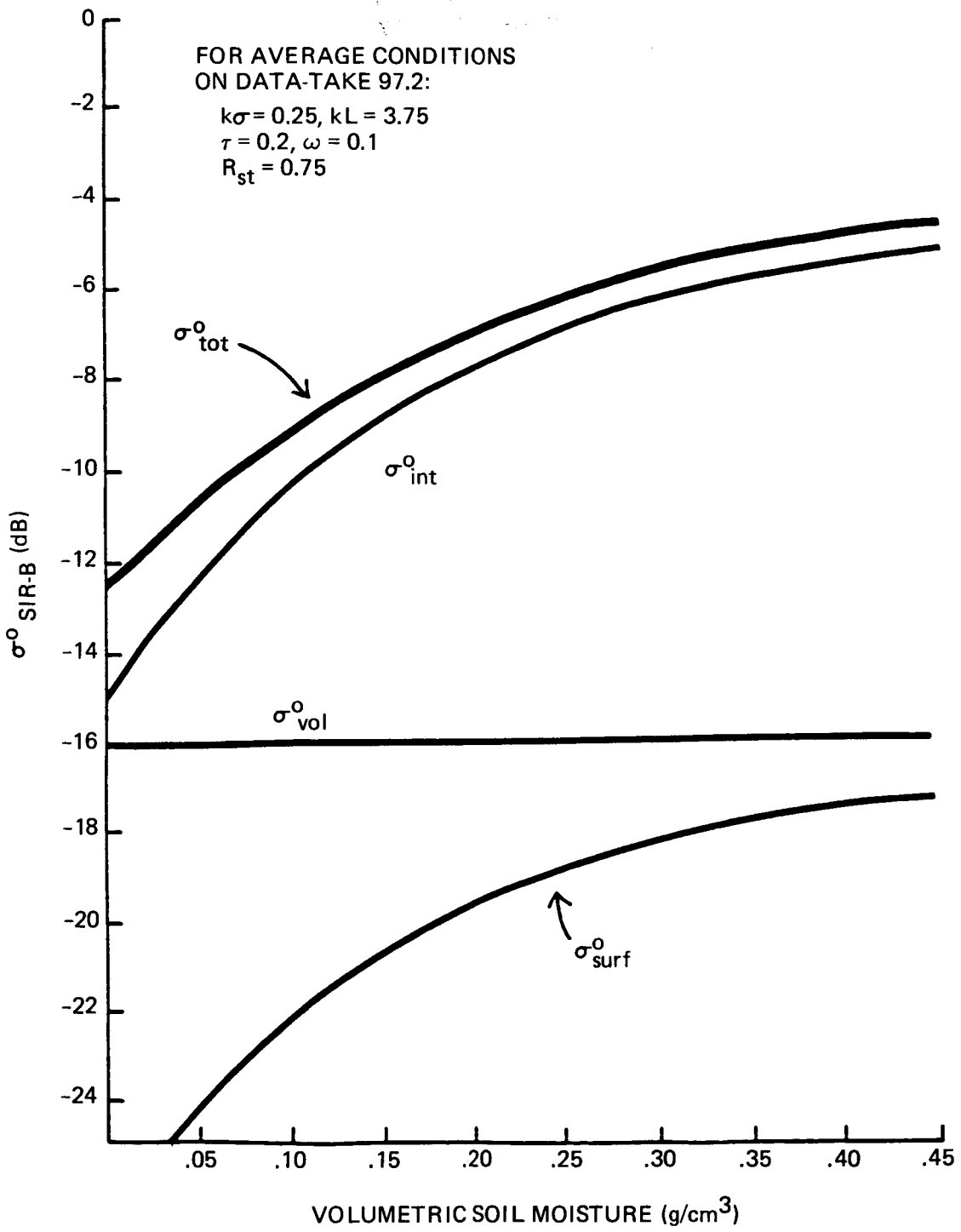


Figure 3. Backscattering contributions of the soil surface, corn canopy, and surface-stalk interactions.

ORIGINAL PAGE IS
OF POOR QUALITY

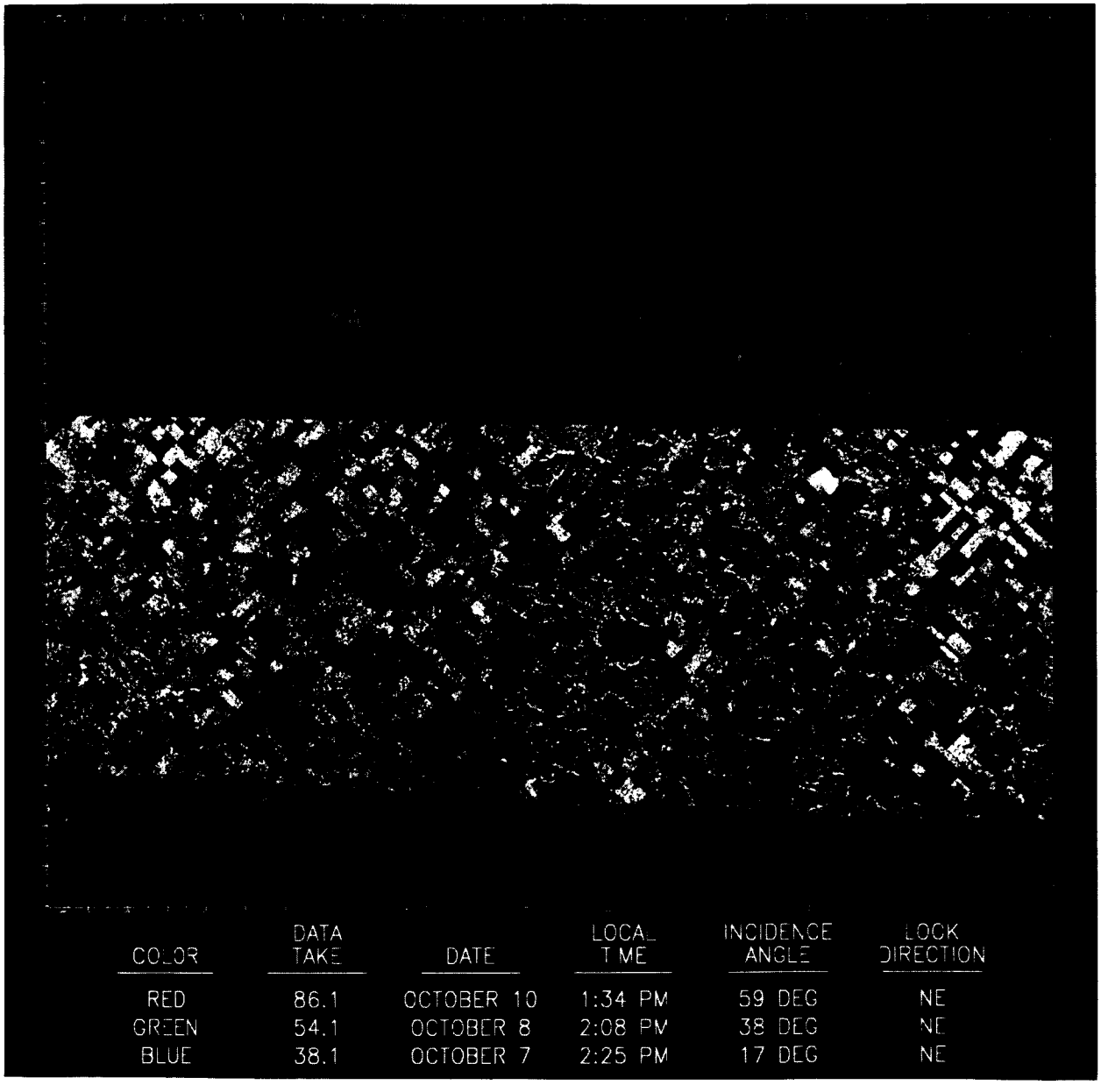


Figure 4. Color composite of multiangle and multidata SIR-B imagery of the Illinois test site. (This image was orignally produced in color.)

Figure 5(a). Color composite of calibrated SIR-B stereo images at 30° incidence angle. (This image was originally produced in color.)

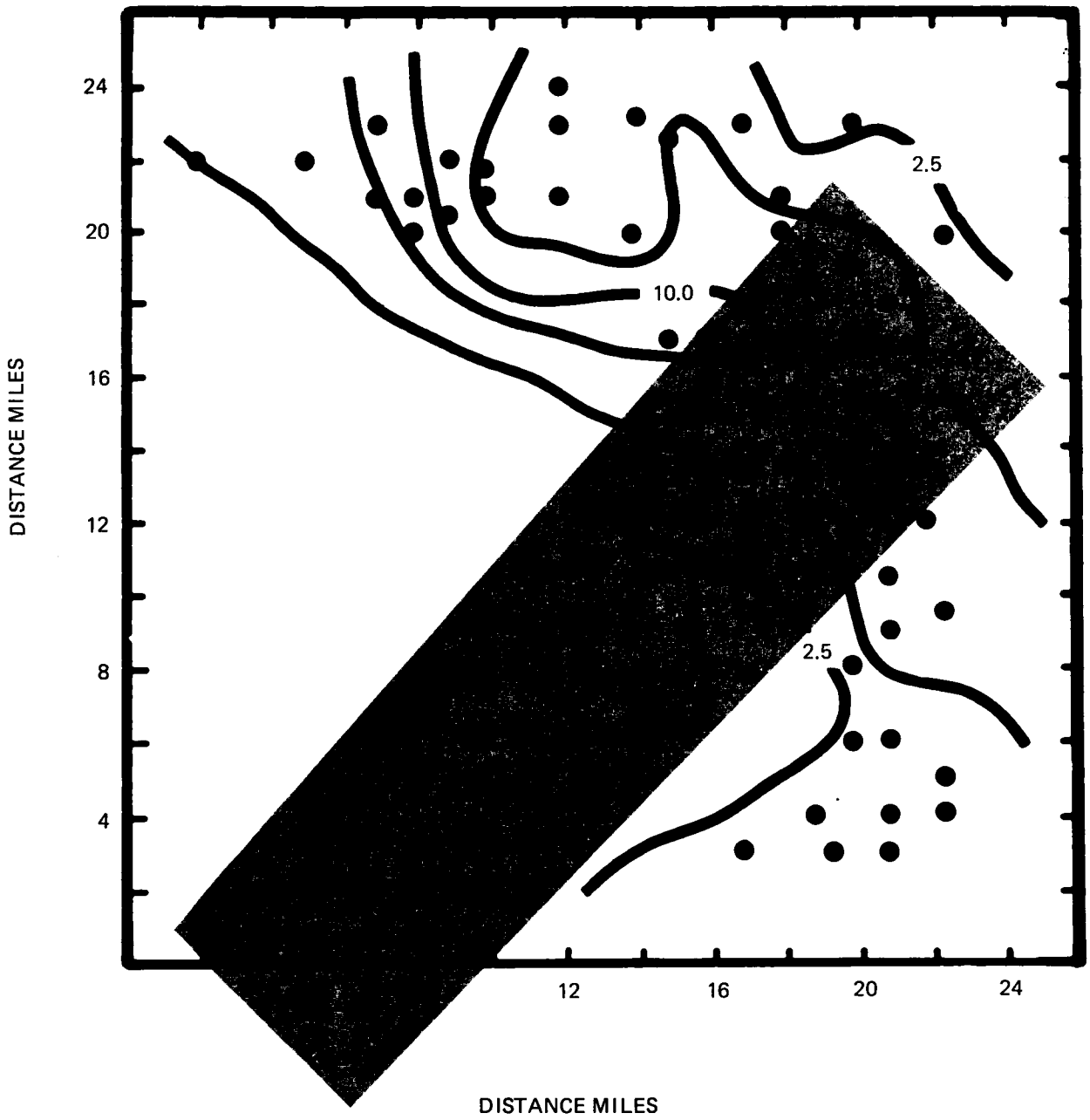


Figure 5(b). Rain gauge locations at Illinois SIR-B test site. Change in calibrated backscatter at 30° incidence over three days and associated cumulative rainfall (in millimeters) on October 9 and 10. Red, yellow, green, and blue correspond to $\Delta\sigma°$ of $\leq$ -2 dB, $\leq$ 0 dB, $\leq$ +4 dB, and $>$ 4 dB, respectively. (This image was originally produced in color.)

# SIR-B Reflight, SIR-C, and XSAR Planning

# SIR-C, THE NEXT GENERATION SPACEBORNE SAR

E. R. Caro
Jet Propulsion Laboratory, California Institute of Technology
Pasadena, California

## I. INTRODUCTION

The decade between 1976 and 1986 has seen a period of steady development in the use of a Synthetic Aperture Radar (SAR) in remote sensing applications. The technology which was originally developed for airborne use was extended to space with the launch of Seasat in June 1978, followed by the Shuttle Imaging Radar-A (SIR-A) in November, 1981 and SIR-B in October 1984. These three SAR missions had a common heritage: Seasat, a free flyer, which demonstrated for the first time the feasibility of operating a SAR at orbital altitudes, thus setting the stage for acquiring SAR data on a global scale. SIR-A and SIR-B were derivatives of the SEASAT technology which was adapted for the Space Shuttle era and capitalized heavily on the original hardware design. All three featured a single wavelength: 23.5 cm (1.27 GHz), single polarization: HH (Horizontal transmit and receive), and a corporate fed, passive planar array antenna. The parameters which differed for the three missions were: look angle: 20° for Seasat, 45° for SIR-A and 15° to 60° for SIR-B (by means of a mechanical antenna tilt mechanism); range bandwidths which were 19 MHz, 6 Hz and 12 MHz respectively; and data handling: analog link for Seasat, on-board Optical Recorder for SIR-A and Digital Data link and recorder for SIR-B.

Advances in technology in recent years now make it appropriate to take the next evolutionary step in expanding the capabilities of the next generation Spaceborne SAR. What follows is a description of the SIR-C instrument, its major elements and the capabilities which have been incorporated into the design in response to the requirements and goals identified by the SIR-C Science Steering Committee and stated in the SIR-C Science Plan[1].

## II. SYSTEM DESCRIPTION

SIR-C takes a significant departure from the previously flown SAR systems in several areas.

Firstly: it is a multiple frequency sensor system capable of operating in L-Band (1.2 GHz), C-Band (5.3 GHz), or both simultaneously.

Secondly: Each frequency can transmit and receive in either or both of two polarizations: Horizontal and Vertical. This feature permits acquisition of SAR data in the quad-polarization mode, i.e., transmit alternating pulses in H and V and receive like-polarized echoes; HH and VV as well as the cross-polarized echoes HV and VH. Recent work by H. Zebker[2] at JPL, based on similarly acquired SAR data with an airborne SAR demonstrated a technique for synthesizing any arbitrary polarization, given the data set obtained in the quad-polarization mode. This method makes possible the use of polarization effects for SAR data extraction and image interpretation.

Thirdly: The SIR-C antenna is an active aperture phased array or distributed SAR. The antenna contains individual transmitter/receiver modules mounted directly behind the radiating elements. The array geometry can thus be tailored to optimize system performance. There is an additional benefit which results from this configuration: the ability to steer the beam electronically.

In addition to the L- and C-Band systems described above, a third system operating at X-Band will fly along with SIR-C, provided jointly by the German Space Agency, DFVLR, and the Italian Space Agency, CNR/PSN. XSAR will use a passive waveguide array antenna with vertical polarization. The cost of implementing the distributed SAR concept at X-Band is prohibitive with the current state of technology, but could be considered for the EOS time frame.

## III. PAYLOAD CONFIGURATION

SIR-C is being configured similarly to SIR-A and SIR-B. The electronic assemblies will be mounted on a pallet in the cargo bay of the Space Shuttle. The main difference is the size of antenna: 4.2 m x 12.0 m (SIR-B was 2.1 m x 10.7 m). To reduce the space occupied in the cargo bay, the 12 meter length of the antenna is divided into 3 segments, each 4 meters long with two fold hinges. The 4.2 meter width of the folded antenna will span across the cargo bay from sill to sill. Figure 1 shows the SIR-C payload configuration. Although the L-Band and C-Band arrays both have the capability of electronically pointing the beam, a mechanical tilt mechanism has been included in the design of the antenna mount to provide a means of pointing the antenna in elevation without perturbing the Shuttle's attitude. This latter feature was deemed necessary to accommodate XSAR which has a fixed beam and in consideration of other earth viewing sensors which may be flying along with SIR-C.

## IV. SYSTEM CAPABILITIES

SIR-C has been designed to meet the requirements and goals identified in the SIR-C Science Plan to the extent allowed by the present state of the art. The system's characteristics are presented in Table I. Aside from the conventional modes of operation in either single, dual or quad-polarization modes at either or both frequencies, the ability to steer the antenna beam electronically will permit collecting SAR data in several unconventional ways. These are listed below along with a brief description of each mode.

Squint Mode - In this mode, the antenna beam is electronically steered to a fixed azimuth angle other than broadside either forward or rearward relative to the line of flight.

Scan-SAR Mode - In this mode, the antenna beam is sequentially stepped in elevation (cross-track) over a set of up to four positions within one synthetic aperture in order to illuminate a wider strip and thus increase swath beyond the antenna elevation beam limit. The trade-off of course is a slight degradation in azimuth resolution in direct proportion to the increase in swath.

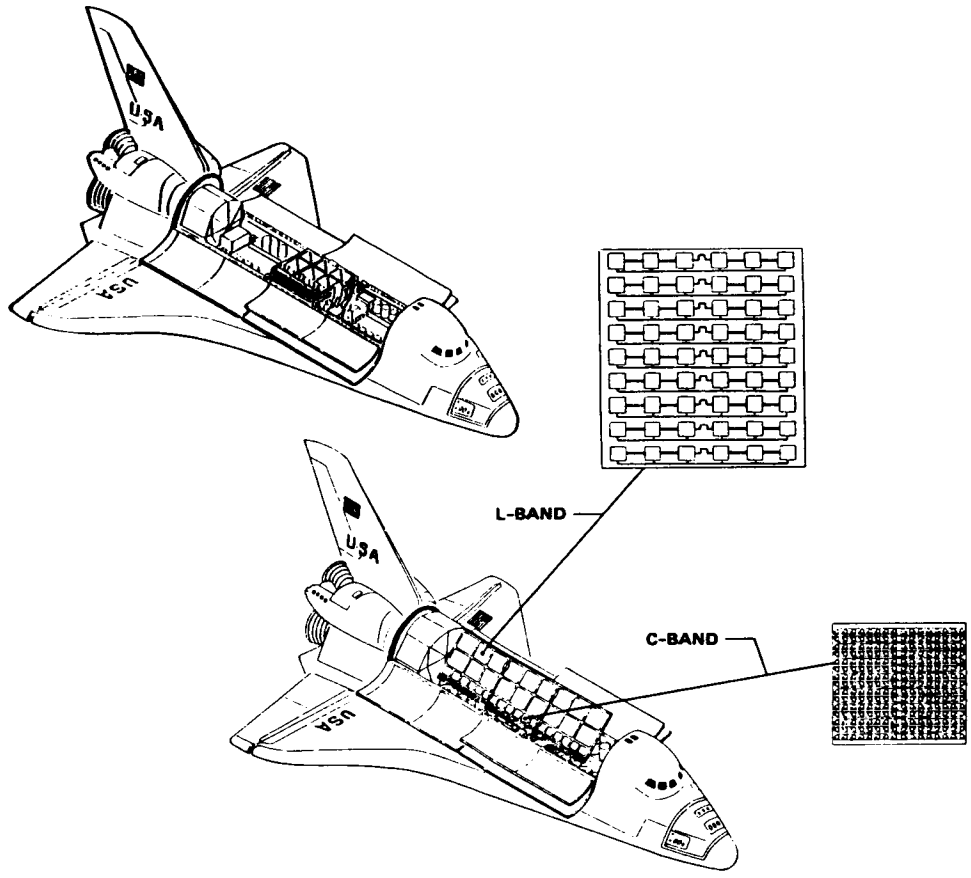


Fig. 1. SIR-C payload configuration: upper, stowed; lower, deployed

Extended Aperture Mode - This is a mode which uses electronic beam steering in azimuth to extend the time that a scene is kept in the antenna beam. This technique will increase the available number of azimuth looks which will improve image quality. Figure 2 depicts the various imaging modes for SIR-C.

## V. ANTENNA SUBSYSTEM

The SIR-C antenna aperture has been partitioned so as to accommodate the three frequencies L-, C-, and X-Band with similar elevation beamwidths. The ratios of the antenna widths are thus scaled to the ratio of the frequencies. The array lengths for all three frequencies are identical: 12 meters. Since the ultimate single look resolution for a SAR is equal to 1/2 the antenna length, each of the SARs will have the same azimuth resolution: 6 meters.

Table I. SIR-C instrument characteristics

| Parameter | SIR-C | |
|---|---|---|
| | L-band | C-band |
| Transmitter power | 3600 W peak+ | 2235 W peak+ |
| Modulation | Linear FM pulse | Linear FM Pulse |
| Pulse width | 33 μs | 33 μs |
| RF center frequency | 1248, 1254 MH | 5298, 5304 MHz |
| Bandwidth | 10, 20 MHz | 10, 20 MHz |
| Rcvr noise temperature | 366 K+ | 417 K+ |
| Rcvr gain | 56 to 101 dB+ | 56 to 101 dB+ |
| Antenna size | 12.08 x 2.92 m | 12.08 x 0.75 m |
| Polarization | HH, HV, VV, VH | HH, HV, VV, VH |
| Antenna gain* | 37 dBi | 43.2 dBi |
| Mechanical antenna pointing to nadir | 15 to 60° | 15 to 60° |
| Electronic-beam steering | ±23° El, ±2° Az | ±23° El, ±2° Az |
| Recording | Digital | Digital |
| Number of high-rate record channels | 4 | 4 |
| Bit rate/channel | 45 Mbits/s | 45 Mbits/s |
| Data processing | Digital | Digital |
| Range resolution | 8.6 to 58 m | 8.6 to 58 m |
| Azimuth resolution | 25 m | 25 m |
| Number of azimuth looks | 4 | 4 |

*Referenced to antenna port at sensor electronics.
+Referenced to antenna element feedthrough points.

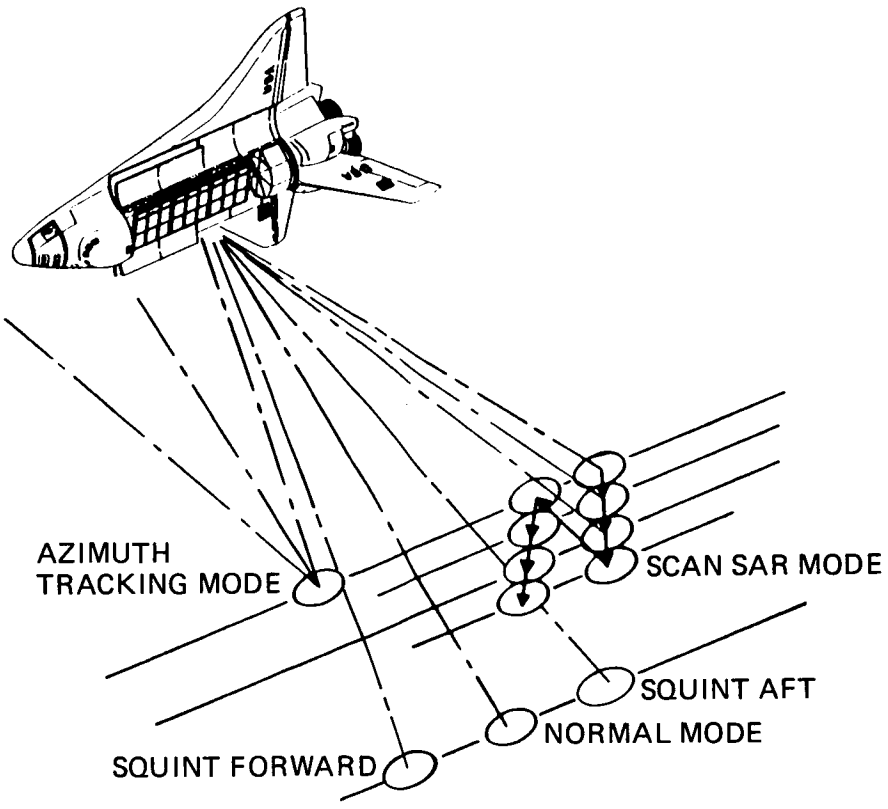


Fig. 2. SIR-C imaging modes

The L- and C-Band arrays are of microstrip design with square radiating elements with orthogonal feed points for H and V polarization. The isolation between the H and V ports of the array will be 20 dB or better. Figure 3 shows a layout of a typical L-Band and C-Band dual polarized subarray. Figure 4 shows the partitioning of the antenna area in panels. For ease of manufacturing, all L-Band panels are identical and interchangeable. The same is true for C-Band.

The array geometry chosen for SIR-C results in a uniformly illuminated aperture in azimuth. In elevation, a staircase approximation of cosine squared weighting is used. This is accomplished with use of power dividers as shown in Figure 5. The predicted patterns are shown in Figure 6 and Figure 7. Several advantages result from configuring SIR-C as a distributed SAR. First is the elimination of the feed losses between the transmitter/receiver and the radiating elements. This pays off both in a more efficient use of transmitter power and an increase in sensitivity by reducing the losses in front of the low noise amplifiers. The noise temperature predicted for SIR-C is 366 K for L-Band and 417 K for C-Band. The array gains are 37 dBi and 43.2 dBi, respectively. These correspond to G/T (gain over temperature) figures of 11.37 dB and 17 dB and EIRP (Effective Isotropic Radiated Power) of 72.5 dBw for L-Band and 76.3 dBw for C-Band. These factors play an important role in acquiring cross-polarized data. Cross-polarized returns are typically 1 dB weaker than like-polarized returns. To achieve the same performance, a conventional SAR would need about 10 times the transmitter power of a distributed SAR.

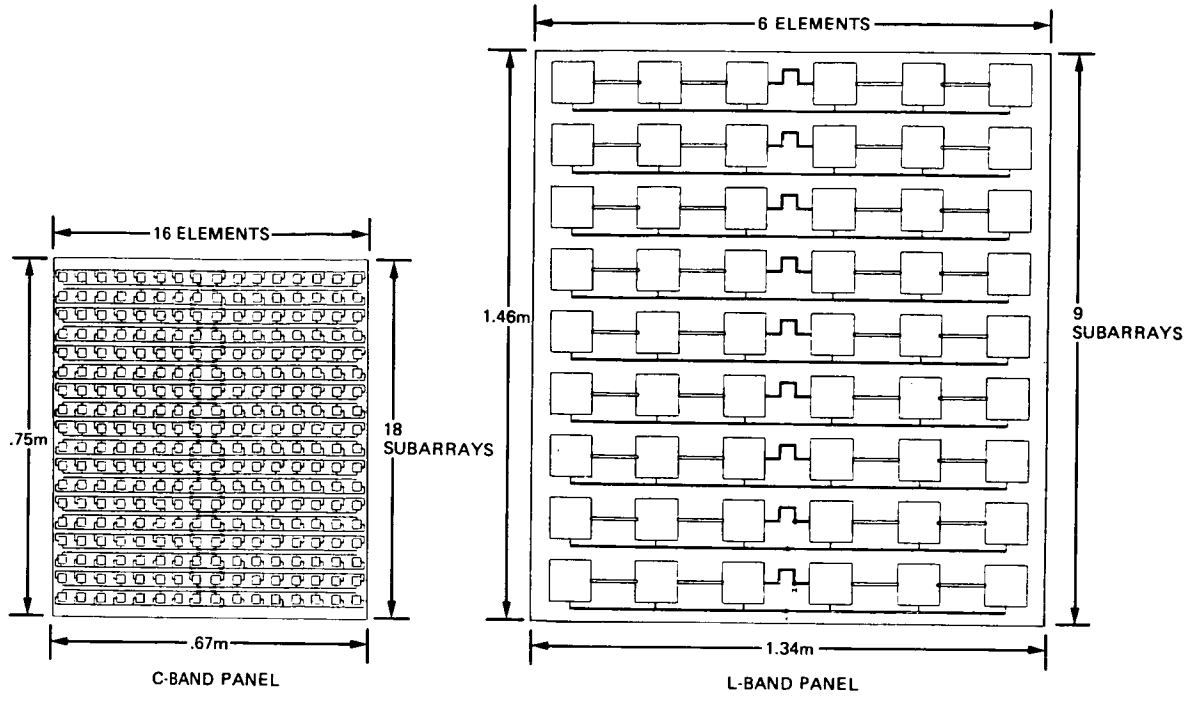


Fig. 3. C-Band and L-Band panel geometry

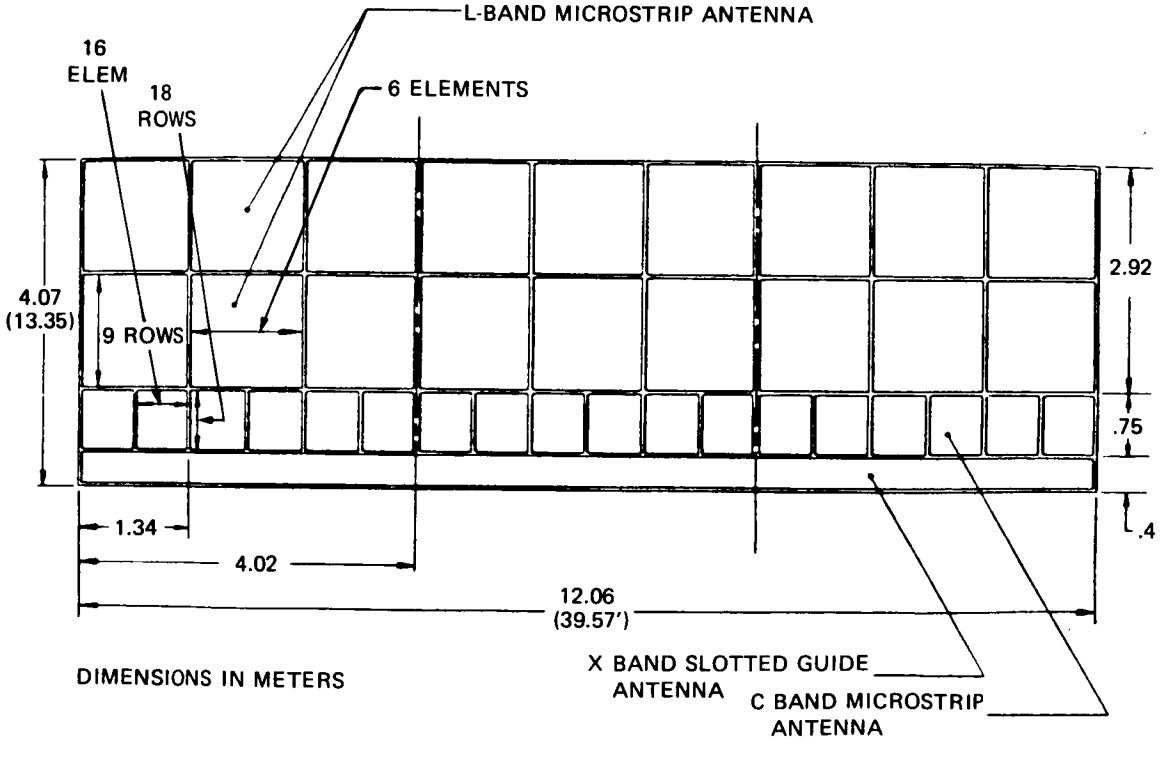


Fig. 4. SIR-C aperture partitioning

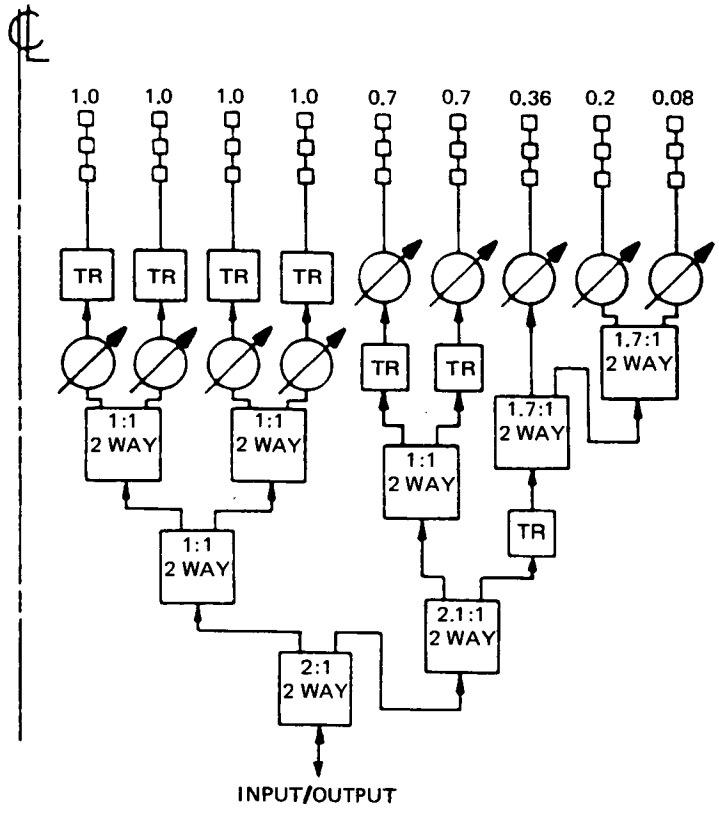


Fig. 5. Elevation aperture weighting

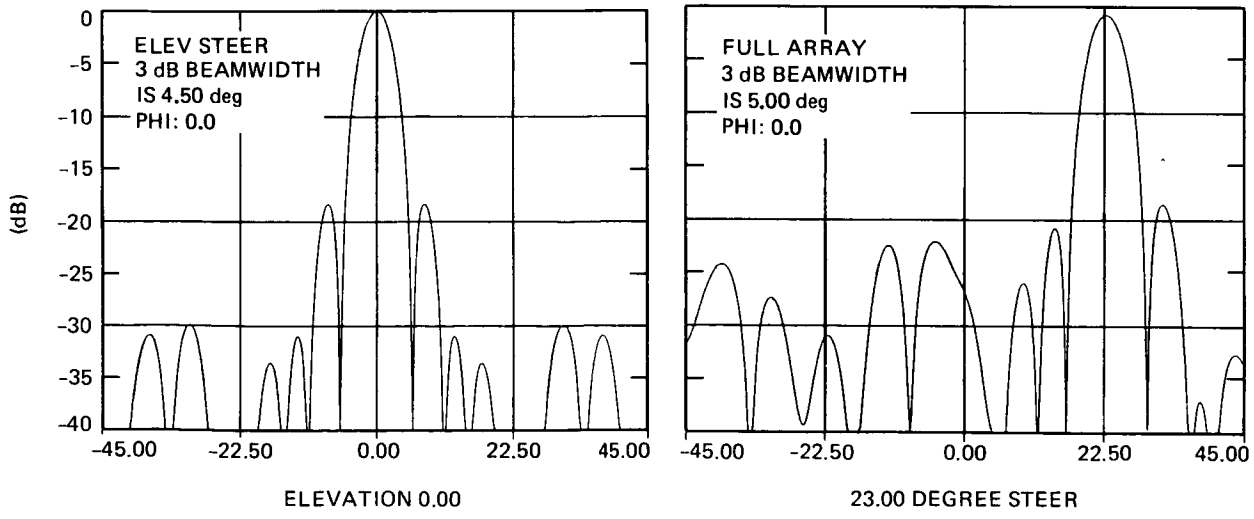


Fig. 6. Typical L- and C-Band weighted pattern in elevation: left, broadside; right, 23° steering

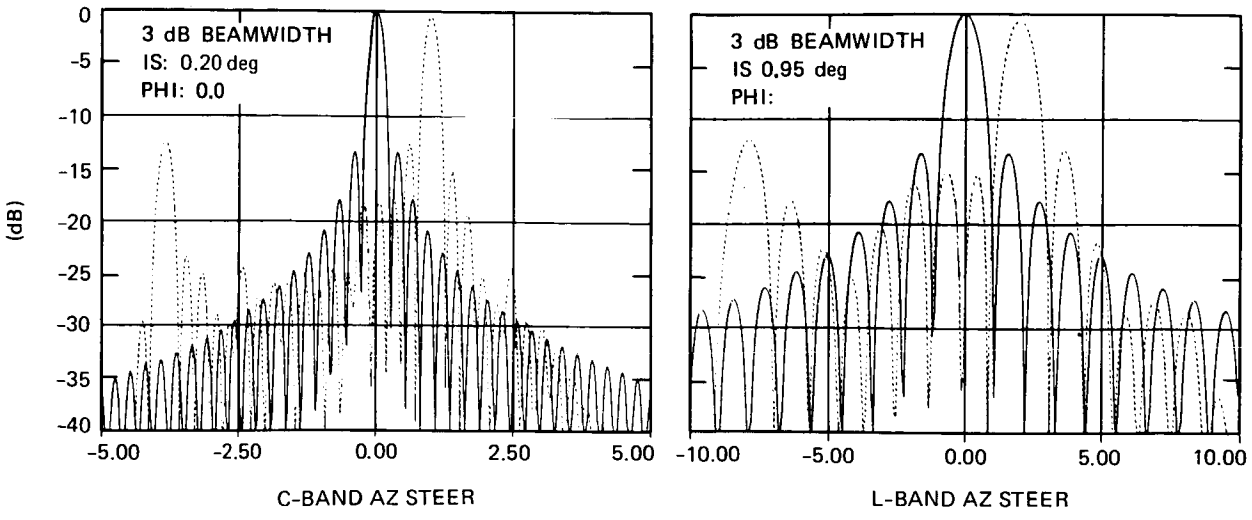


Fig. 7. Typical azimuth broadside and steered patterns: left, C-Band; right, L-Band

Another advantage of a distributed SAR is its inherent tolerance to random failures in the T/R modules. Loss of 10% of the T/R modules only degrades the performance by less than 1 dB.

Finally, the ability to steer the antenna beam electronically increases the flexibility of operating in a variety of unconventional modes previously described. In addition, electronic control of the phase of the antenna elements allows control of the antenna elevation beamwidth to optimize the swath illumination over the full range of look angles from 15 to 60 degrees. Figure 8 shows a set of beamwidths achievable with phase control.

## VI. RF ELECTRONICS SUBSYSTEM

The RF electronics subsystem for the L- and C-Band SAR are based on a common design. The exciter chain produces a linear FM pulse. SIR-C will have two selectable chirp bandwidths: 10 MHz and 20 MHz with corresponding range resolutions of 15 and 7.5 meters. The chirp signals will be amplified to a level sufficient to drive the T/R modules on the antenna. There are four receiver channels designated L-Horizontal, L-Vertical, C-Horizontal, and C-Vertical. Again, common designs are shared by both frequencies with appropriate up and down converters. A functional diagram of the SIR-C Flight Instrument is shown in Figure 9.

## VII. DIGITAL ELECTRONICS SUBSYSTEM

The SIR-C digital electronics data subsystem is an upgraded version of the SIR-B design with two significant improvements. First is the upgrading of the ADC from 6 bits to 8 bits. Second is the incorporation of a Block Floating Point Quantizer (BFPQ). The increase from 6 to 8 bits in the ADC results in a 12 dB improvement in dynamic range.

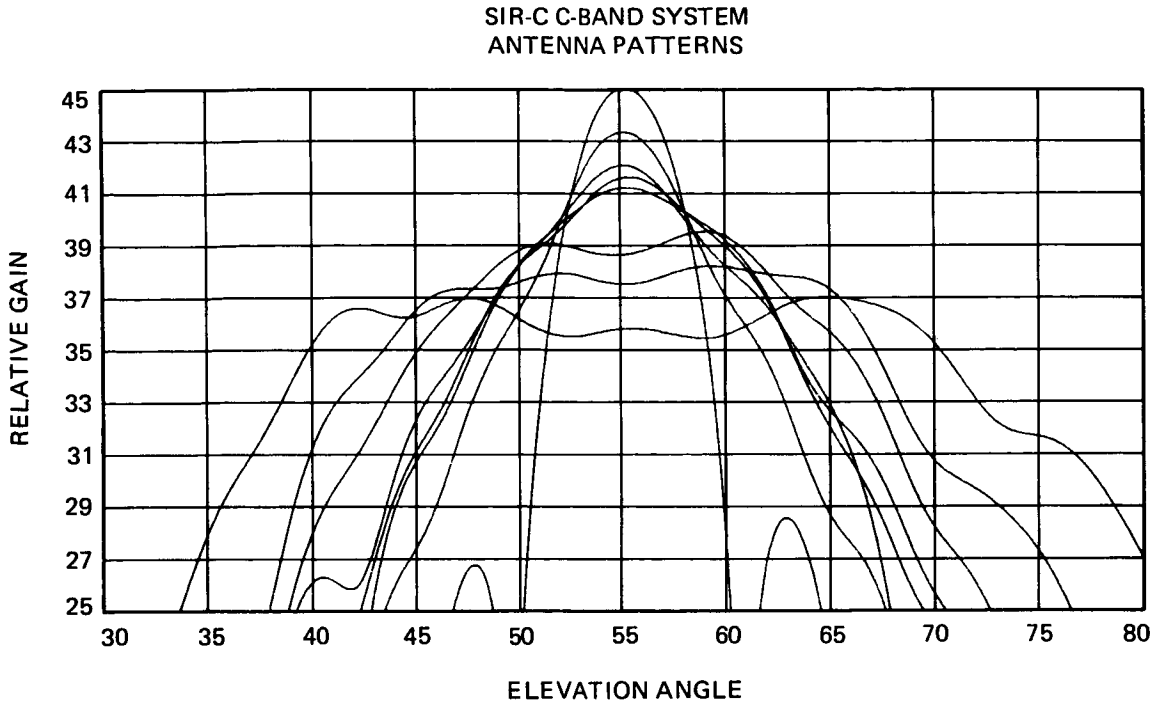


Fig. 8. Elevation beam broadening by phase control

Dynamic Range can be approximated by: [6(N-1)+3] dB where N = the number of ADC quantization bits.

The dynamic ranges for a 6 and 8 bit ADC are thus:

6 (6-1) + 3 = 33 dB for N = 6

6 (8-1) + 3 = 45 dB for N = 8

For a data rate limited system (limited by the present shuttle Ku-Band link to 50 MBPS and on-board data recorders to 50 MBPS per channel), an increase in quantization bits from 6 to 8 would result in a 33% reduction in image swath width.

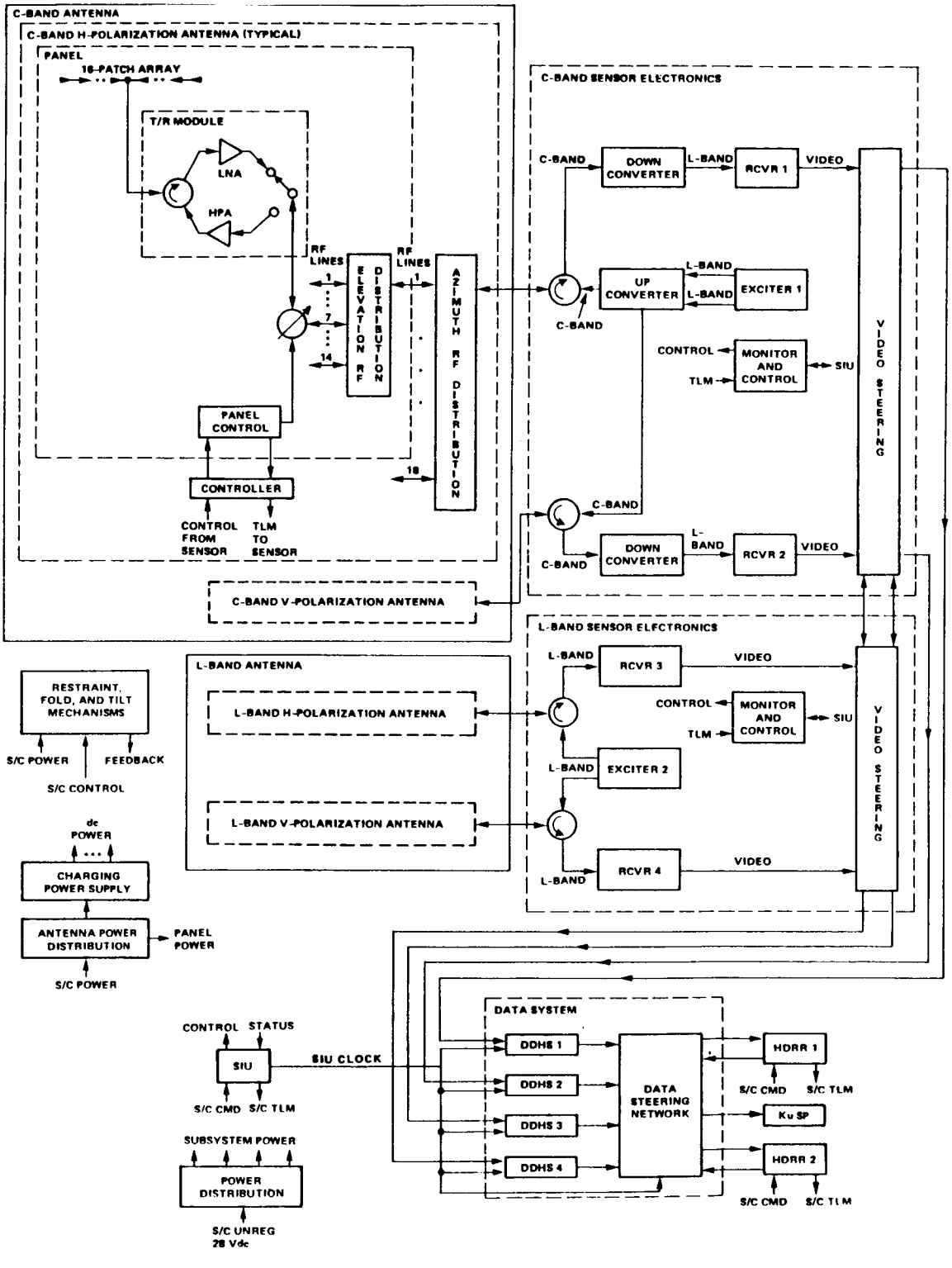


Fig. 9. SIR-C Flight Instrument functional diagram

The BFPQ overcomes this swath width penalty with a data compression scheme which acts as an adaptive scaler. The digitized 8 bits are statistically compared to a predetermined set of thresholds in memory and only the most significant bits along with the appropriate multiplier are sent to the output formatter. In SIR-C, the format chosen is 8 bits reduced to 4 significant bits plus multiplier. An 8 bit error protected code for the multiplier is included in each data block and represents the scaling factor to be applied to that particular block. Data block lengths of 256 to 2048 have been simulated with very good results. The multiplier overhead is thus very low. What results is an output data rate equivalent to a 4 bit system which approaches the dynamic range of an 8 bit system without sacrificing swath. J. Curlander[3] and Q. Nguyen[4] have described this scheme in detail in the reference. Figure 10 shows a functional diagram of an 8/4 BFPQ. Figure 11 shows a comparison between the signal to distortion noise ratios of an 8 bit uniform quantizer, a four bit uniform quantizer and an 8 to 4 bit BFPQ. The 8/4 BFPQ has a broad region of nearly constant noise level with a 20 dB SNR while retaining the intrinsic wide dynamic range of the 8 bit ADC. This results in a higher degree of tolerance to system gain setting errors or large variations in the backscatter intensity in the image scene. The SIR-C Digital Data Subsystem will provide the investigator a commandable option of formatting the data in 8 bits uniform, 4 bits uniform or 8/4 BFPQ.

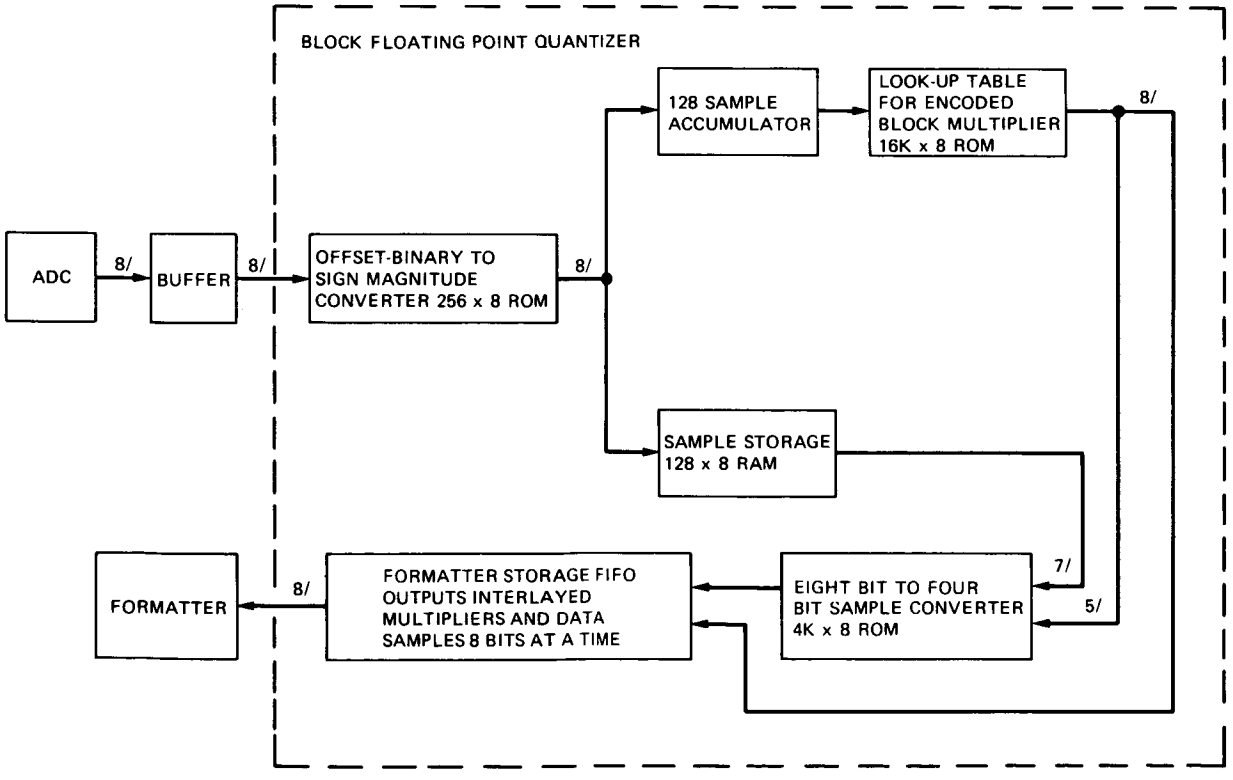


Fig. 10. Functional diagram 8 to 4 Bit Block Floating Point Quantizer

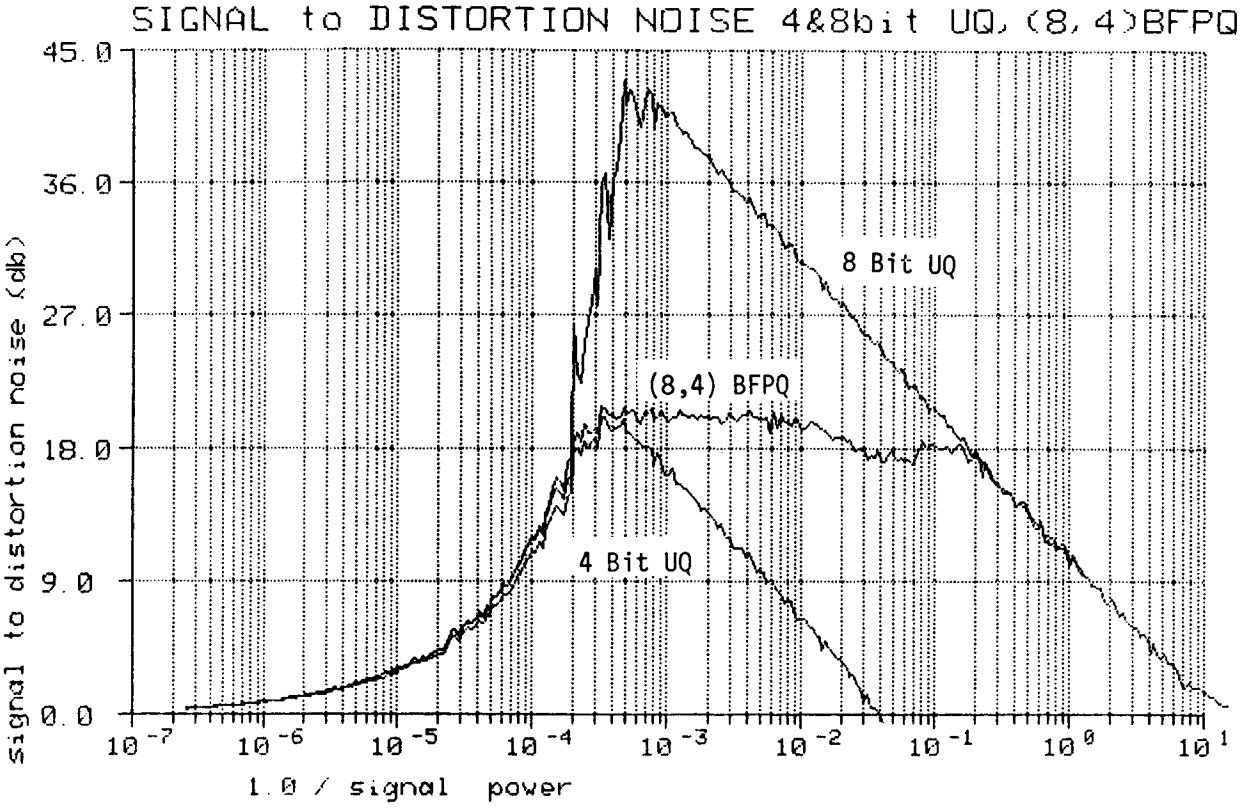


Fig. 11. Comparison between the Signal to Distortion Noise Ratio of an 8 Bit Uniform Quantizer, a 4 Bit Uniform Quantizer, and an 8 to 4 Bit Block Floating Point Quantizer. Note the broad region of nearly constant Signal to Distortion Noise Ratio exhibited by the 8/4 BFPQ over a wide range of signal power.

Four Digital Data Handling Assemblies (DDHA) will digitize and format the receiver outputs at a rate of 45 Megabits per second per channel. The four serial data streams will be routed to a Data Steering Network (DSN) which will then deliver the data to High Data Rate Recorders. The DSN can selectively route any one of the serial data streams to the Ku-Band link for real-time transmission via TDRS to a ground station. The Data Recorders for SIR-C will be located in the crew cabin in order to give the orbiter crew access to the recorders for tape changing. A functional diagram of the SIR-C Digital Electronics Subsystem is shown in Figure 12.

## VIII. SHUTTLE INTERFACES

SIR-C has five major interfaces with the Space Shuttle. These are: mechanical, thermal, power, command, and telemetry. The mechanical interfaces are dictated by the physical mounting of the payload in the cargo bay. The thermal interfaces involve an active coolant loop to dissipate the heat produced by the electronics assemblies. D.C. power will be supplied primarily by the orbiter 28 volt bus via the Standard Interface Panels (SIP). Ground command will be through the Payload Signal Processor (PSP) and telemetry will be monitored on the ground via the Payload Data Interleaver (PDI). All of the above are part of the standard accommodations available to payloads which fly in the Space Shuttle. Figure 13 shows the electrical interfaces between SIR-C and the orbiter.

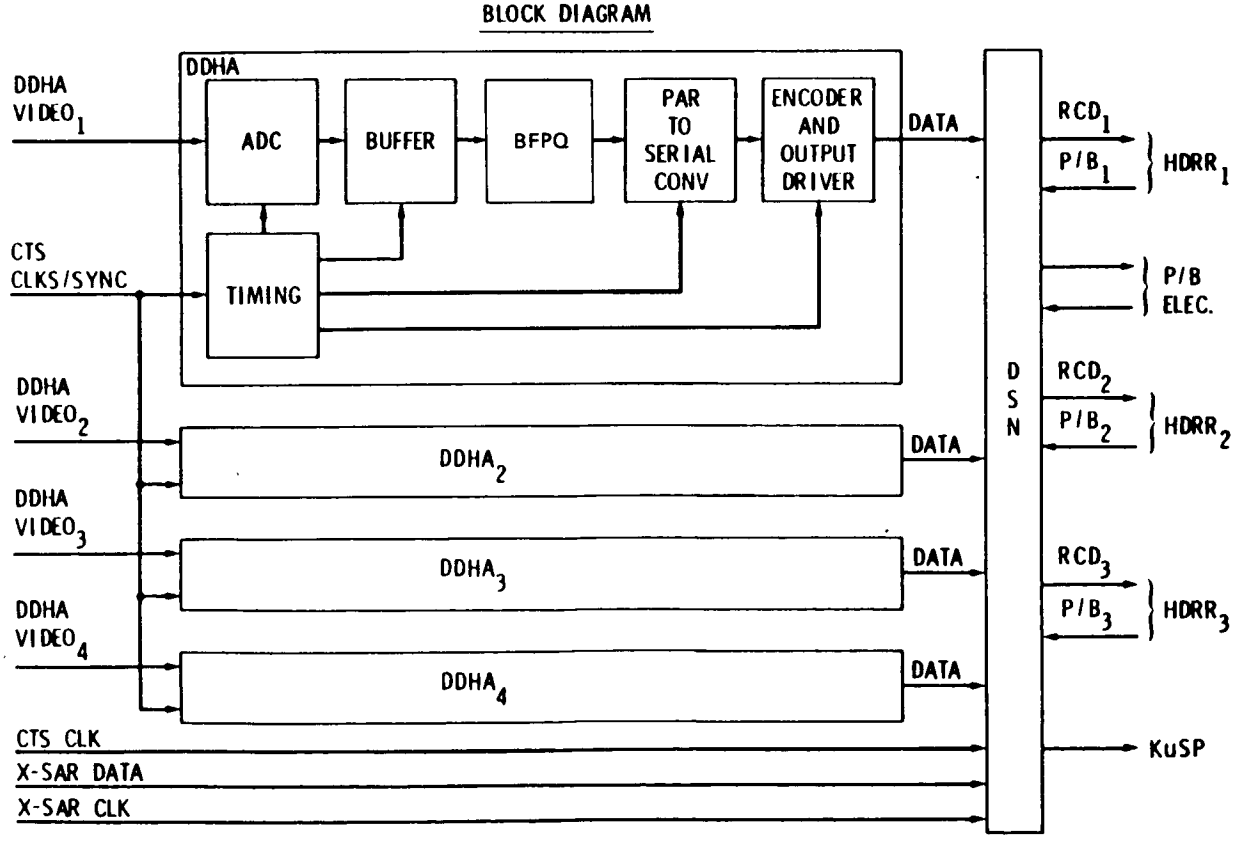


Fig. 12. SIR-C Digital Electronics Subsystem functional diagram

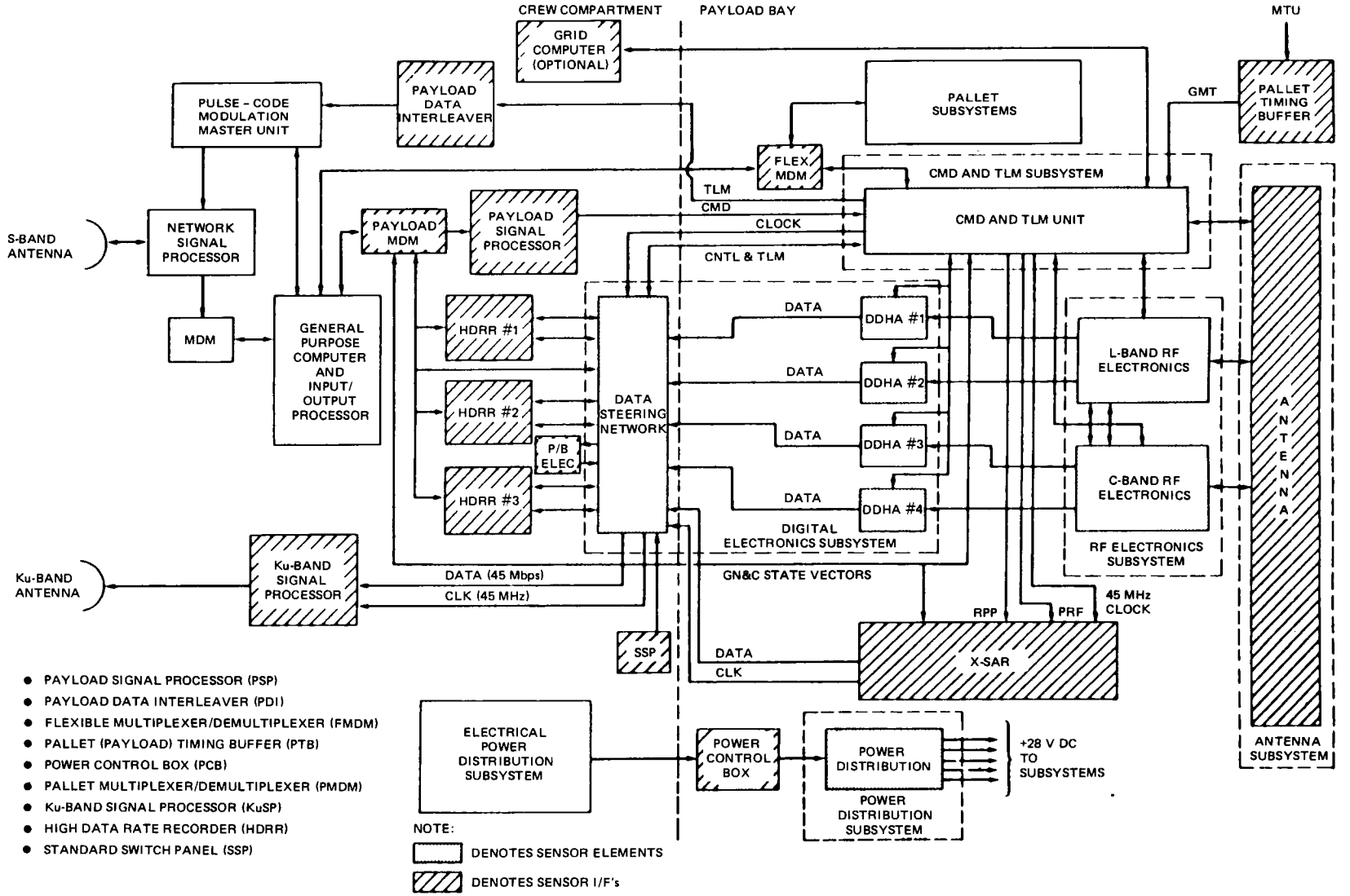


Fig. 13. SIR-C/Orbiter electrical interfaces

## IX. SUMMARY

SIR-C represents a significant advance in spaceborne SAR system capabilities. The design approach is responsive to the requirements identified by the Science Steering Committee. The multimode features of the sensor will provide science investigators with new dimensions in acquiring and interpreting scientific data. The flexibility of the SIR-C design will provide a core instrument which will meet the needs of SAR data users into the 1990's and serve as a foundation for ultimate incorporation into the EOS platform.

## ACKNOWLEDGMENT

The contribution of the SIR-C team and Ball Aerospace Systems Division to this effort is gratefully acknowledged. In particular, the author wishes to thank the following for material and data presented here: R. Jordan, J. Curlander, J. Klein, M. Paller, B. Huneycutt and Q. Nguyen, all of JPL.

This work is being undertaken under the auspices of the Office of Space Science and Application (OSSA), National Aeronautics and Space Administration.

## REFERENCES

1. SIR-C Science Plan, K. Carver et al., July 1986, Jet Propulsion Laboratory, July 1986.

2. H. Zebker, "Imaging Radar Polarimetry by Wave Synthesis," in this volume.

3. J. Curlander, "Why Does SIR-C Need a Block Floating Point Quantizer," JPL Interoffice Memorandum, Ref: 3348-85-099. (JPL internal document.)

4. Q. Nguyen, "Study of (8,4) BFPQ," JPL Interoffice Memorandum, Ref: 3348-86-040. (JPL internal document.)

# THE X-SAR SYSTEM

Herwig Öttl
Institut für Hochfrequenztechnik, DFVLR
Oberpfaffenhofen, Germany

## I. INTRODUCTION

During the past few years, there has been significant progress made in the planning for an X-band SAR /1/, designed to fly in the shuttle together with the SIR-C system of NASA/JPL. New work and studies have been initiated to enable the goal of two missions in 1990 to be met.

The antennas of X-SAR and SIR-C will be placed side-by-side on a pivoted steerable foldable structure, which will allow antenna movement without changing the attitude of the shuttle (fig. 1). This figure also shows the pallet, underneath the antenna structure, which houses the electronic sub-systems of both radars. Although the two radar systems, X-band SAR and the L- and C-band SAR of SIR-C, have different technical designs /2,3/, their overall system performance, in terms of image quality, is expected to be similar.

This paper details the current predicted performance of the X-SAR system based on results of the continuing Phase B studies /2/. Differences between the performance parameters of X-SAR and those of SIR-C are only detailed in as far as they affect planning decisions to be made by experimenters.

The X-SAR system is a joint German/Italian project, financially supported by BMFT/DFVLR[1] in Germany and PSN[1] in Italy. Project Scientists are Dr. Herwig Öttl on the German side and Prof. Francesco Valdoni on the Italian side. The role of the Project Scientist is to assist in optimizing the system performance to the scientific requirements subject to tight funding constraints.

## II. KEY X-SAR SPECIFICATIONS

The shuttle is a unique space vehicle capable of fulfilling many varying requirements for differing experiments. Nevertheless, spaceborne radars have such high power requirements and generate very large data rates, which tax even the shuttle's resources. The combined X-SAR/SIR-C equipment will fully use the available on-board power (X-SAR alone uses 1.4 kW) and one radar channel will be sufficient to fully occupy the data transmitting capability of approx. 46 Mbits/s. Data from the other radar channels will have to be stored on tape on-board.

[1] BMFT = Ministry for Research and Technology.
DFVLR = German Aerospace Research Agency.
PSN = National Space Plan (Agency).

The constraints of power, bandwidth and physical size of the cargo-bay, together with a desire to have a large swath width of up to 50 km or more, dictated the following specifications:

| | |
|---|---|
| Frequency | 9.6 GHz |
| Polarization (transmit/receive) | vertical/vertical |
| Geometric resolution | ca. 25 m in azimuth (4 looks) and range |
| Swath width | 10 km - 45 km |
| Radiometric resolution /4/ | 2.5 dB at $\sigma^\circ$ = -18 dB (4 looks) with 6 bit I / 6 bit Q quantization[2] |
| Off-nadir angle | 15° - 60° |

The predicted performance changes with the off-nadir angle and is derived in the following section.

It should be noted that X-SAR does not have the multi-polarization capability of SIR-C and that the X-SAR antenna (12 x 0.4 m) has a fixed beamwidth of 5.8° in elevation and 0.13° in azimuth, whereas SIR-C has a phased array antenna. A phased array antenna which permits the beamwidth to be changed, allows the swath coverage to be selected. There is a trade-off between swath width and resolution due to data rate limitations in the datalink or the on-board recorder. The X-SAR antenna has a gain >43 dBi.

## III. EXPECTED PERFORMANCE

The high power amplifier is designed to generate more than 3 kW peak power. The low noise amplifier is expected to have a noise figure of less than 2 dB. A dynamic range window of 20 dB, adjustable in 2 dB steps (gain setting), can be selected from the 60 dB receiver dynamic available.

The Pulse Repetition Frequency (PRF) is variable in 16 steps between 1234 Hz and 1802 Hz. The exact setting depends on the shuttle configuration, orbit height (nominal 255 km) and off-nadir angle, and is chosen to minimize range ambiguity effects. The transmitted pulse has a linear chirp of length 40 µs and a bandwidth of 19 MHz or 12 MHz.[3] These bandwidths give slant range resolutions of 10 m and 16 m respectively.

Figure 2 shows some of the more important system parameters. The top four curves in the upper half of the figure give the swath width as a function of off-nadir angle, resolution mode, and radiometric resolution. The swath width is constrained by the elevation beamwidth at low off-nadir angles and by the data rate at high off-nadir angles. Note here that the high resolution modes refer to the 10 m slant range resolution case.

[2] 4 bit I/4 bit quantization is also possible.
[3] This may be changed to 19 MHz and 9.5 MHz, the figures planned for SIR-C.

The range ambiguity level, represented by the curve in the lower part of fig. 2, has been derived using the following assumptions:

- the antenna sidelobes in elevation are at least 20 dB below the mainlobe,

- $\sigma^\circ$ is constant across the whole elevation pattern.

The ambiguity level is calculated as the ratio of the desired reflected signal within one range bin to the sum of all extraneous reflections whose returns lie within the same range bin or time interval.

The bounds on the system sensitivity area, also shown in the lower part of fig. 2, are given by the two radiometric resolution values of 2.5 dB and 3 dB and the illuminated swath width.

It should be noted that a 3 dB margin, to cover possible additional losses arising in the X-SAR design and construction stage, has been included in fig. 2 whose figures, in any case, represent conservative values.

## IV. CALIBRATION, SURVEY PROCESSOR

As part of the internal calibration philosophy of X-SAR, it is planned to monitor the phase and amplitude stability of the chirp by passing a replica of the transmitted pulse through the receiving chain. Distortions introduced by the High Power Amplifier, such as a amplitude ripple, are measured separately.

Parallel to the X-SAR sensor itself, a real-time survey processor is also being developed. This processor will be used to verify system performance, for quick look processing during the mission, and in selecting the scenes for full precision processing.

## V. SCIENTIFIC GOALS

A summary of the prime scientific objectives of the X-SAR mission, in both land and sea applications, is given in /5/.

Experiments will be selected by Spring 1987, based on the response to the announcement of opportunity due to be issued shortly. The mission planning will then be tailored to the selected experiments.

## ACKNOWLEDGMENTS

I would like to thank Mr. H. Schüssler, Mr. W. Gilg and Dr. H. M. Braun for supplying some of the system parameters and computations, and Mr. T. K. Pike for technical discussions and assistance with the manuscript.

## REFERENCES


1. Öttl, H. and M. Werner, 1984. German Synthetic Aperture Radar Activities for Shuttleborne Missions. Proceedings of the Fourteenth International Symposium on Space Technology and Science, pp. 1031-1306, AGNE Publishing, Inc., Tokyo.

2. Dornier System, SELENIA SPAZIO, 1986. X-SAR Phase B Design Review, BMFT/DFVLR, CNR/PSN.

3. Caro, E. R., B. L. Huneycutt and R. L. Jordan, 1986. SIR-C/XSAR Phase B2 Review, Presentation to BMFT/DFVLR - DORNIER SYSTEMS, CNR/PSN - SELENIA SPAZIO.

4. Pike, T. K., 1985. SAR Image Quality: A Review. DFVLR-Mitt. 85-07, p. 26.

5. Öttl, H. and F. Valdoni et al. 1985. The X-SAR Science Plan. DFVLR-Mitt. 85-17.

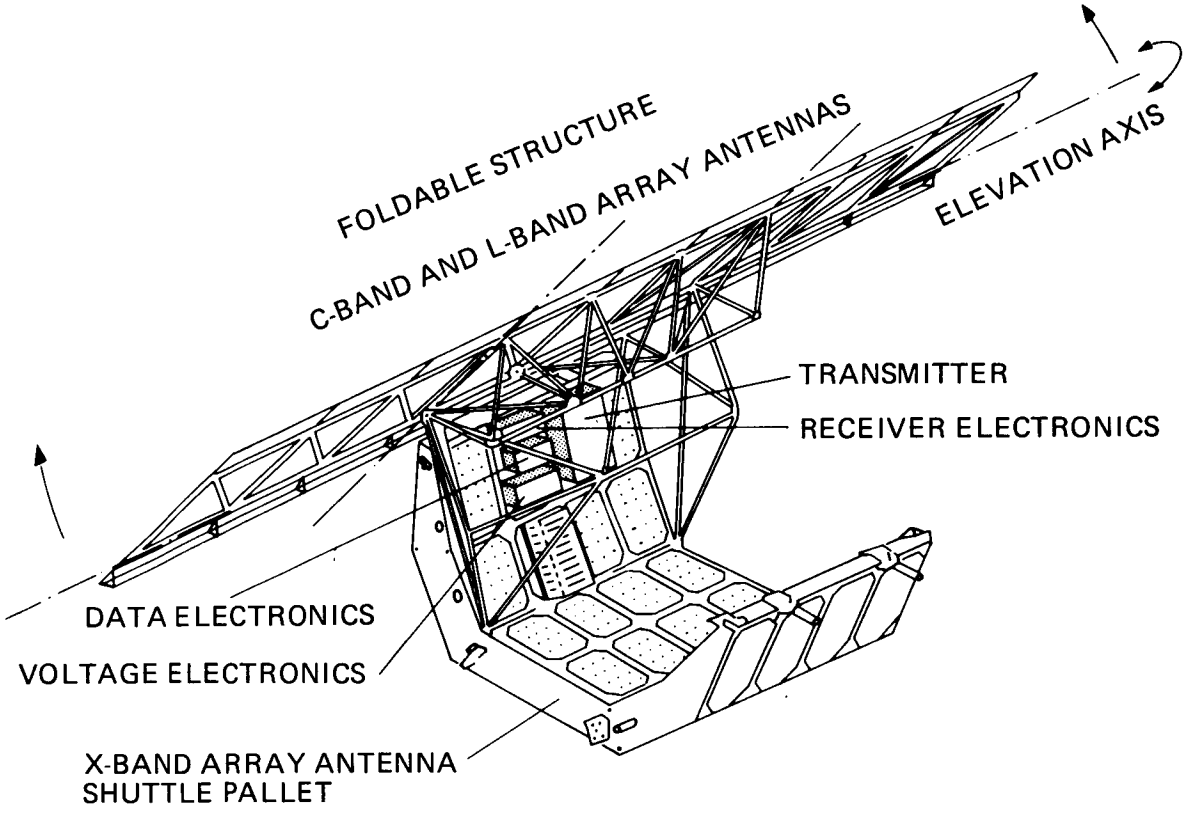


Figure 1. X-band, C-band and L-band antenna mounted above the shuttle structure. Only the containers for X-SAR electronics are shown.

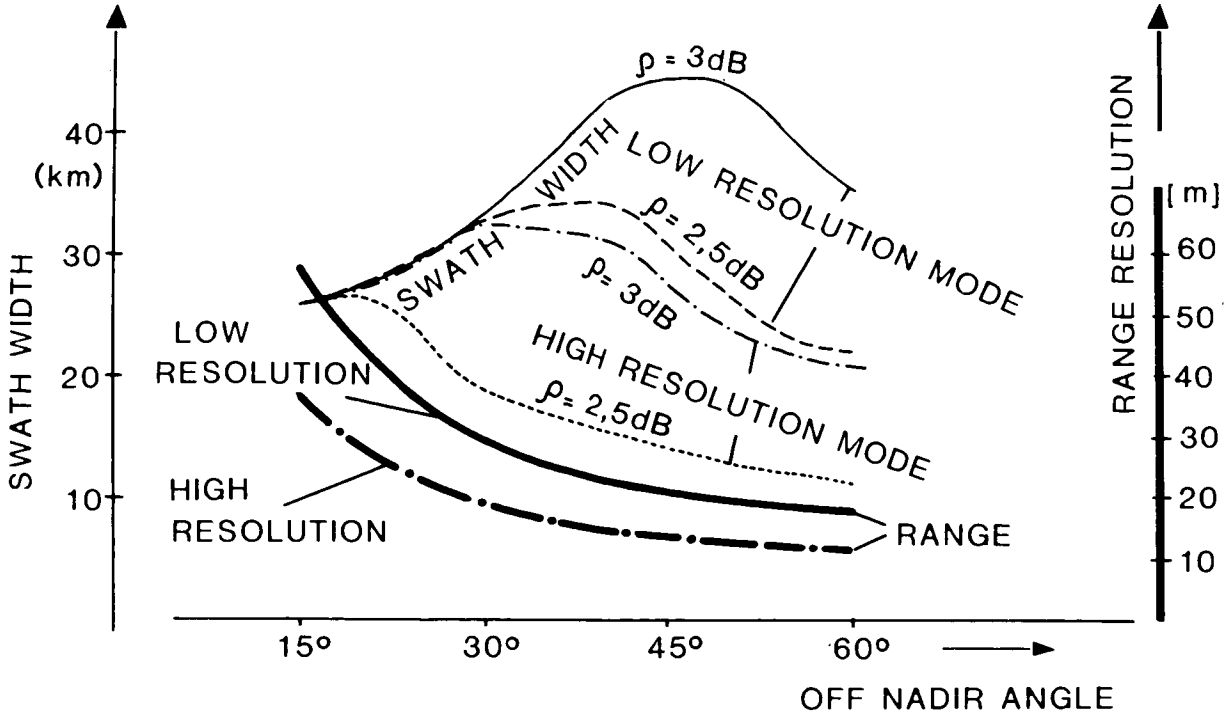


Figure 2a. Swath width and range resolution.

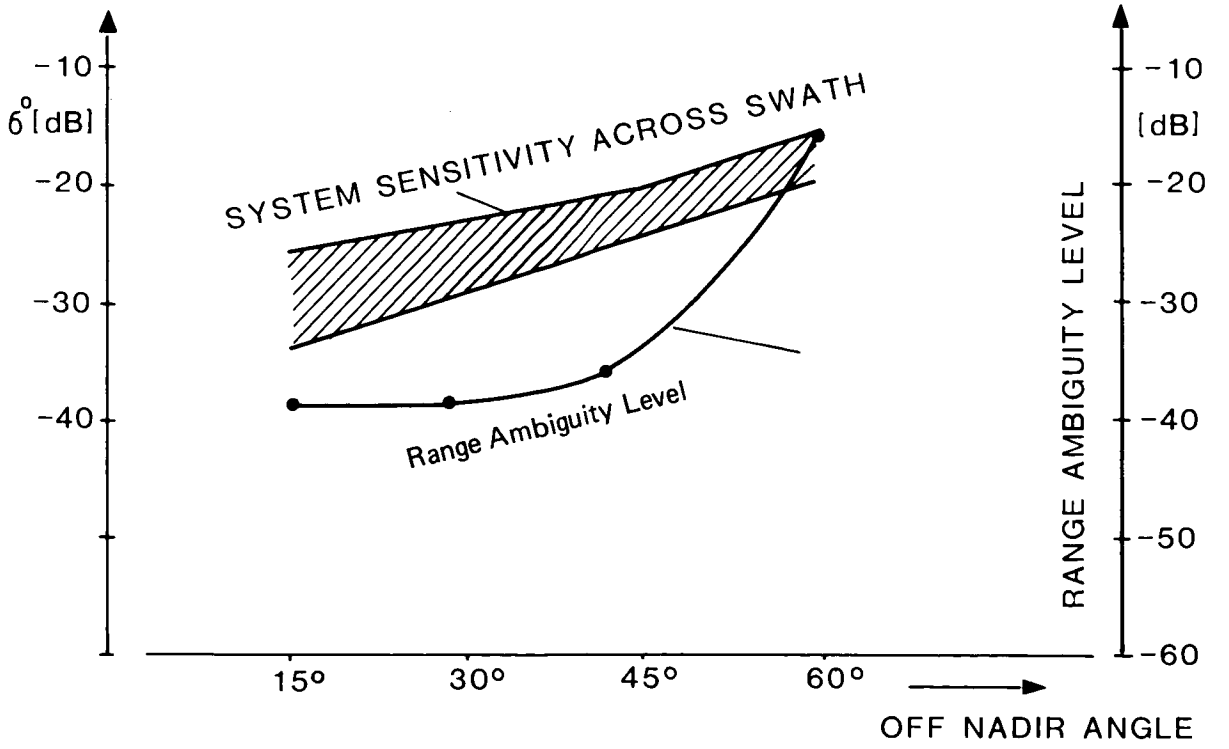


Figure 2b. System sensitivity and range ambiguity level.